Reliable Estimation of Horizontal Stress Magnitudes from Borehole Breakout Data

Reliable Estimation of Horizontal Stress Magnitudes from Borehole Breakout Data

Huasheng Lin

A thesis in fulfilment of the requirements for the degree of

Doctor of Philosophy

School of Minerals and Energy Resources Engineering

Faculty of Engineering

April 2020

Thesis/Dissertation Sheet

Surname/Family Name	:	Lin
Given Name/s	:	Huasheng
Abbreviation for degree as give in the University calendar	:	PhD
Faculty	:	Faculty of Engineering
School	:	School of Minerals and Energy Resources Engineering
Thesis Title	:	Reliable estimation of horizontal stress magnitudes from borehole breakout data

Abstract 350 words maximum: (PLEASE TYPE)

As mining depths increase to meet the global demand for minerals and conditions become more arduous at many underground mines, understanding of the state of in-situ stresses will be increasingly important to ensure the workplace safety. However, current stress measurement techniques experience difficulties in obtaining reliable results at low costs. Borehole breakout is a drilling-induced phenomenon due to the local stress concentration and its geometries are dependent on in-situ stresses. In Australia, breakout data is freely accessible as geological and geophysical logging is mandatory. Therefore, developing a horizontal stress estimation technique using borehole breakout is not only pivotal for the safety of underground operations, but also economically beneficial to the mining and petroleum industries.

Breakout tests conducted in this study revealed that breakout geometries are influenced by three principal stresses, indicating the intermediate stress should be considered in horizontal stress magnitude estimation. The investigation of laboratory data and analytical solutions suggested breakout geometries are not dependent factors, so that estimation of both horizontal stress magnitudes is viable. Results also showed that the borehole size has significant influence on breakout geometries and an investigation was carried out using normal compression tests. An empirical relationship was proposed to predict the breakout initiation stress at various borehole sizes.

Numerical simulation using Particle Flow Code was conducted to study breakout development and borehole size effect. The modelling results revealed that breakout angular span forms at the early stage of breakout, followed by substantial breakout elongation. The borehole size simulation indicated breakout initiated at the borehole wall with stress re-distribution from micro-cracking. The study also showed that breakout initiation stress decreases with increasing temperature, and larger breakouts were observed under high stress conditions when the temperature was over 300 °C.

An estimation technique for horizontal stress magnitudes was proposed based on an Artificial Neural Network model and Mogi–Coulomb failure criterion. Using 26 field data, the technique estimated the minimum and maximum horizontal stress magnitudes at average error rates of 15.05% and 7.62%. Considering its reliability, simplicity and cost, this model is valuable for in-situ stress evaluation and can help improve safety in underground operations.

ORIGINALITY STATEMENT

‘I hereby declare that this submission is my own work and to the best of my knowledge it contains no materials previously published or written by another person, or substantial proportions of material which have been accepted for the award of any other degree or diploma at UNSW or any other educational institution, except where due acknowledgement is made in the thesis. Any contribution made to the research by others, with whom I have worked at UNSW or elsewhere, is explicitly acknowledged in the thesis. I also declare that the intellectual content of this thesis is the product of my own work, except to the extent that assistance from others in the project's design and conception or in style, presentation and linguistic expression is acknowledged.’

Signed ……………………………………………..............

Date ……………………………………………..............

COPYRIGHT STATEMENT

'I hereby grant the University of New South Wales or its agents the right to archive and to make available my thesis or dissertation in whole or part in the University libraries in all forms of media, now or hereafter known, subject to the provisions of the Copyright Act 1968. I retain all proprietary rights, such as patent rights. I also retain the right to use in future works (such as articles or books) all or part of this thesis or dissertation.

I also authorise University Microfilms to use the 350 word abstract of my thesis in Dissertation Abstract International (this is applicable to doctoral theses only). I have either used no substantial portions of copyright material in my thesis or I have obtained permission to use copyright material; where permission has not been granted I have applied/will apply for a partial restriction of the digital copy of my thesis or dissertation.'

Signed ………………………………………………..........................

Date ………………………………………………..........................

AUTHENTICITY STATEMENT

'I certify that the Library deposit digital copy is a direct equivalent of the final officially approved version of my thesis. No emendation of content has occurred and if there are any minor variations in formatting, they are the result of the conversion to digital format.'

Signed ………………………………………………..........................

Date ………………………………………………..........................

INCLUSION OF PUBLICATIONS STATEMENT

UNSW is supportive of candidates publishing their research results during their candidature as detailed in the UNSW Thesis Examination Procedure.

Publications can be used in their thesis in lieu of a Chapter if:

- The candidate contributed greater than 50% of the content in the publication and is the "primary author", ie. the candidate was responsible primarily for the planning, execution and preparation of the work for publication
- The candidate has approval to include the publication in their thesis in lieu of a Chapter from their supervisor and Postgraduate Coordinator.
- The publication is not subject to any obligations or contractual agreements with a third party that would constrain its inclusion in the thesis

Please indicate whether this thesis contains published material or not:

☐ This thesis contains no publications, either published or submitted for publication
(if this box is checked, you may delete all the material on page 2)

☐ Some of the work described in this thesis has been published and it has been documented in the relevant Chapters with acknowledgement
(if this box is checked, you may delete all the material on page 2)

☒ This thesis has publications (either published or submitted for publication) incorporated into it in lieu of a chapter and the details are presented below

CANDIDATE'S DECLARATION

I declare that:

- I have complied with the UNSW Thesis Examination Procedure
- where I have used a publication in lieu of a Chapter, the listed publication(s) below meet(s) the requirements to be included in the thesis.

Candidate's Name	Signature	Date (dd/mm/yy)
Huasheng Lin		

POSTGRADUATE COORDINATOR'S DECLARATION *To only be filled in where publications are used in lieu of Chapters*

I declare that:

- the information below is accurate
- where listed publication(s) have been used in lieu of Chapter(s), their use complies with the UNSW Thesis Examination Procedure
- the minimum requirements for the format of the thesis have been met.

PGC's Name	PGC's Signature	Date (dd/mm/yy)
Ryan Armstrong		

Details of publication #1:

Full title: A review of in situ stress measurement techniques

Authors: Huasheng Lin, Joung Oh, Hossein Masoumi, Ismet Canbulat, Chengguo Zhang

Journal or book name: Coal Operators 2018

Volume/page numbers: 95-102

Date accepted/published: Feb 2018

Status	*Published*	×	*Accepted and In press*		*In progress (submitted)*	

The Candidate's Contribution to the Work

The candidate conducted literature review and wrote the whole manuscript.

Location of the work in the thesis and/or how the work is incorporated in the thesis: Chapter 2 was extended based on the publication.

PRIMARY SUPERVISOR'S DECLARATION

I declare that:

- the information above is accurate
- this has been discussed with the PGC and it is agreed that this publication can be included in this thesis in lieu of a Chapter
- All of the co-authors of the publication have reviewed the above information and have agreed to its veracity by signing a 'Co-Author Authorisation' form.

Primary Supervisor's name	**Primary Supervisor's signature**	**Date (dd/mm/yy)**
Joung Oh		

Details of publication #2: *Full title:* Experimental and analytical investigations of the effect of hole size on borehole breakout geometries for estimation of in situ stresses *Authors:* Huasheng Lin, Joung Oh, Ismet Canbulat, Thomas Stacey *Journal or book name:* Rock Mechanics and Rock Engineering *Volume/page numbers:* 53:781-798 *Date accepted/published:* August 2019						
Status	*Published*	×	*Accepted and In press*		*In progress (submitted)*	
The Candidate's Contribution to the Work The candidate designed and conducted experiments, carried out analysis and wrote the whole manuscript.						
Location of the work in the thesis and/or how the work is incorporated in the thesis: The publication is fully incorporated in Section 3.1 in Chapter 3.						
PRIMARY SUPERVISOR'S DECLARATION I declare that: • the information above is accurate • this has been discussed with the PGC and it is agreed that this publication can be included in this thesis in lieu of a Chapter • All of the co-authors of the publication have reviewed the above information and have agreed to its veracity by signing a 'Co-Author Authorisation' form.						
Primary Supervisor's name **Joung Oh**		**Primary Supervisor's signature**			**Date (dd/mm/yy)**	

Details of publication #3: *Full title:* Estimation of in-situ maximum horizontal principal stress magnitudes from borehole breakout data using machine learning *Authors:* Huasheng Lin, Won Hee Kang, Joung Oh, Ismet Canbulat *Journal or book name:* International Journal of Rock Mechanics and Mining Sciences *Volume/page numbers:* 126 *Date accepted/published:* Jan 2020						
Status	*Published*	×	*Accepted and In press*		*In progress (submitted)*	
The Candidate's Contribution to the Work The candidate collected experimental and field data, conducted analysis, constructed model and wrote the whole manuscript.						
Location of the work in the thesis and/or how the work is incorporated in the thesis: The publication is fully incorporated in Chapter 4.						
PRIMARY SUPERVISOR'S DECLARATION I declare that: • the information above is accurate • this has been discussed with the PGC and it is agreed that this publication can be included in this thesis in lieu of a Chapter • All of the co-authors of the publication have reviewed the above information and have agreed to its veracity by signing a 'Co-Author Authorisation' form.						
Primary Supervisor's name **Joung Oh**		**Primary Supervisor's signature**			**Date (dd/mm/yy)**	

Details of publication #4:

Full title: Experimental study on borehole size effect and prediction of breakout initiation stress

Authors: Huasheng Lin, Joung Oh, Ismet Canbulat, Bruce Hebblewhite, Hossein Masoumi, Stuart Walsh

Journal or book name: International Journal of Rock Mechanics and Mining Sciences

Volume/page numbers: N/A

Date accepted/published: N/A

Status	*Published*		*Accepted and In press*		*In progress (submitted)*	×

The Candidate's Contribution to the Work

The candidate designed and conducted experiments, carried out analysis and wrote the whole manuscript.

Location of the work in the thesis and/or how the work is incorporated in the thesis:

The publication is fully incorporated in Section 3.2 in Chapter 3.

PRIMARY SUPERVISOR'S DECLARATION

I declare that:

- the information above is accurate
- this has been discussed with the PGC and it is agreed that this publication can be included in this thesis in lieu of a Chapter
- All of the co-authors of the publication have reviewed the above information and have agreed to its veracity by signing a 'Co-Author Authorisation' form.

Primary Supervisor's name	**Primary Supervisor's signature**	**Date (dd/mm/yy)**
Joung Oh		

<table>
<tr><td colspan="7">Details of publication #5:
Full title: Numerical simulation on borehole breakout and borehole size effect using discrete element method
Authors: Huasheng Lin, Won Hee Kang, Joung Oh, Ismet Canbulat, Bruce Hebblewhite
Journal or book name: International Journal of Mining Science and Technology
Volume/page numbers: N/A
Date accepted/published: N/A</td></tr>
<tr><td>Status</td><td>Published</td><td>×</td><td>Accepted and In press</td><td></td><td>In progress (submitted)</td><td></td></tr>
<tr><td colspan="7">The Candidate's Contribution to the Work
The candidate designed and conducted numerical simulation, carried out analysis and wrote the whole manuscript.</td></tr>
<tr><td colspan="7">Location of the work in the thesis and/or how the work is incorporated in the thesis:
The publication is fully incorporated in Chapter 5.</td></tr>
<tr><td colspan="7">PRIMARY SUPERVISOR'S DECLARATION
I declare that:
• the information above is accurate
• this has been discussed with the PGC and it is agreed that this publication can be included in this thesis in lieu of a Chapter
• All of the co-authors of the publication have reviewed the above information and have agreed to its veracity by signing a 'Co-Author Authorisation' form.</td></tr>
<tr><td colspan="2">Primary Supervisor's name
Joung Oh</td><td colspan="3">Primary Supervisor's signature</td><td colspan="2">Date (dd/mm/yy)</td></tr>
</table>

<table>
<tr><td colspan="7">Details of publication #6:
Full title: A combined approach for estimating horizontal principal stress magnitudes from borehole breakout data via Artificial Neural Network and Rock failure criterion
Authors: Huasheng Lin, Sarvesh Singh, Joung Oh, Ismet Canbulat, Won Hee Kang, Bruce Hebblewhite, Thomas Stacey
Journal or book name: International Journal of Rock Mechanics and Mining Sciences
Volume/page numbers: N/A
Date accepted/published: N/A</td></tr>
<tr><td>Status</td><td>Published</td><td></td><td>Accepted and In press</td><td></td><td>In progress (submitted)</td><td>×</td></tr>
<tr><td colspan="7">The Candidate's Contribution to the Work
The candidate designed and conducted experiments, carried out analysis and wrote the whole manuscript.</td></tr>
<tr><td colspan="7">Location of the work in the thesis and/or how the work is incorporated in the thesis:
The publication is fully incorporated in Chapter 6.</td></tr>
<tr><td colspan="7">PRIMARY SUPERVISOR'S DECLARATION
I declare that:
the information above is accurate
this has been discussed with the PGC and it is agreed that this publication can be included in this thesis in lieu of a Chapter
All of the co-authors of the publication have reviewed the above information and have agreed to its veracity by signing a 'Co-Author Authorisation' form.</td></tr>
<tr><td colspan="2">Primary Supervisor's name
Joung Oh</td><td colspan="3">Primary Supervisor's signature</td><td colspan="2">Date (dd/mm/yy)</td></tr>
</table>

ABSTRACT

As mining depths increase to meet the global demand for minerals and conditions become more arduous at many underground mines, understanding of the state of in-situ stresses will be increasingly important to ensure the workplace safety. However, current stress measurement techniques experience difficulties in obtaining reliable results at low costs. Borehole breakout is a drilling-induced phenomenon due to the local stress concentration and its geometries are dependent on in-situ stresses. In Australia, breakout data is freely accessible as geological and geophysical logging is mandatory. Therefore, developing a horizontal stress estimation technique using borehole breakout is not only pivotal for the safety of underground operations, but also economically beneficial to the mining and petroleum industries.

Breakout tests conducted in this study revealed that breakout geometries are influenced by three principal stresses, indicating the intermediate stress should be considered in horizontal stress magnitude estimation. The investigation of laboratory data and analytical solutions suggested breakout geometries are not dependent factors, so that estimation of both horizontal stress magnitudes is viable. Results also showed that the borehole size has significant influence on breakout geometries and an investigation was carried out using normal compression tests. An empirical relationship was proposed to predict the breakout initiation stress at various borehole sizes.

Numerical simulation using Particle Flow Code was conducted to study breakout development and borehole size effect. The modelling results revealed that breakout angular span forms at the early stage of breakout, followed by substantial breakout elongation. The borehole size simulation indicated breakout initiated at the borehole wall with stress re-distribution from micro-cracking. The study also showed that breakout initiation stress decreases with increasing temperature, and larger breakouts were observed under high stress conditions when the temperature was over 300 °C.

An estimation technique for horizontal stress magnitudes was proposed based on an Artificial Neural Network model and Mogi–Coulomb failure criterion. Using 26 field data, the technique estimated the minimum and maximum horizontal stress magnitudes at average error rates of 15.05% and 7.62%. Considering its reliability, simplicity and

cost, this model is valuable for in-situ stress evaluation and can help improve safety in underground operations.

ACKNOLEDGEMENT

The past three years of my PhD research was a challenging but exciting chapter of my life and I truly enjoyed every minute of it. The completion of this thesis would not have been possible without the support from many people.

First and foremost, I would like to express my sincere gratitude to my primary supervisor Dr Joung Oh, who guided and motivated me throughout this thesis, and provided invaluable advices as an outstanding researcher and a great father. I would like to appreciate Professor Ismet Canbulat, my joint supervisor for his great contribution to this research, particularly on processing field data and sharing his practical knowledge with me. I would also, like to thank my co-supervisor Dr Won Hee Kang from Western Sydney University, for helping me to develop the machine learning model. Dr Won Hee Kang spent significant amount of time on sharing his machine learning knowledge with me, a mining student who had no clue at the beginning. All of my supervisors were always supportive and available for discussions whenever I needed.

I would like to extend my gratitude to Professor Thomas Stacey from University of Witwatersrand, for his help on developing the constitutive model. I appreciate Professor Bruce Hebblewhite for his supervision and support on the associated industry projects.

I am very grateful to my former supervisor Dr Hossein Masoumi from Monash University, who helped me get into PhD and provided critical recommendations to my laboratory work.

My special thanks to Technical officers Mr Kanchana Gamage and Mr Mark Whelan for their time in preparing specimens and conducting tests. I would also like to thank Dr Stuart Walsh from Monash University and Dr Hamid Roshan for allowing me to use the optical scans.

I appreciate the geotechnical engineers and management teams from mine sites, for supplying field data and providing technical consultations for my study.

It was a great pleasure to spend past three years in the PhD office. I enjoyed the quality research discussions and had fun with everyone.

I acknowledge the financial support from UNSW Sydney and Australian Coal Association Research Program (ACARP).

Finally, I would like to thank my parents for their endless love and support. I am deeply indebted to my wife Sunnie Cheuk and my son Jonathan Lin for their love, encouragement and tolerance. I would not have been able to complete my PhD without the support from all my family members.

TABLE OF CONTENTS

LIST OF FIGURES

LIST OF TABLES

1 INTRODUCTION

1.1 BACKGROUND

Knowledge of the state of in-situ stress is a precursor to any underground design and stability analysis. With the presence of major geological features, horizontal stress magnitudes and orientations can alter significantly (Zoback and Healy 1992). These changes in horizontal stress can adversely affect the ground conditions and increase the likelihood of catastrophic failures, including coal burst. Therefore, it is critical to obtain reliable horizontal stress magnitudes and orientations for underground operations to identify high risk zones and implement sufficient ground control.

Currently, the most reliable and popular stress measurement techniques for underground operations are hydraulic fracturing and overcoring. Hydraulic fracturing utilises the hydraulic fluid to induce tensile fractures around the borehole in a sealed section to measure the in-situ stress state. Fractures are produced along the least resistance direction, i.e. the plane that is perpendicular to the minimum horizontal stress direction. Based on the pressures recorded in multiple hydraulic fracturing cycles, both horizontal stress magnitudes can be estimated. This method provides direct measurement of the minimum horizontal stress, whereas the maximum horizontal stress needs to be calculated subsequently given the value of minimum horizontal stress (Haimson and Cornet 2003). On the other hand, the overcoring technique predicts the in-situ stress by monitoring the deformation of the borehole during overcoring activities. Based on the readings from strain gauges and rock mechanical properties gathered from cored samples at the measurement location, both horizontal stress magnitudes can be determined (Gray and See 2007).

Due to increasing urbanisation and infrastructure growth, mineral resources near the surface are being exhausted and mining operations are inevitably taking place at deeper locations to meet the increasing global demand (Nickless 2016). As mining depths increase and conditions become more difficult at many underground mines, knowledge of the state of in-situ stresses will be increasingly important to ensure the safety of the working environment (Yokoyama and Ogawa 2016). Current stress measurement techniques, including hydraulic fracturing and overcoring, suffer from measuring reliable stress magnitudes while maintaining low cost (Ljunggren et al. 2003; Gaines et al. 2012), as these techniques require the measurement locations in the borehole and cored samples to be elastic. This is generally difficult to achieve in deep mining locations or weak strata, where cored samples and the borehole wall are likely to fracture prior to stress measurements (Fairhurst 2003; Ljunggren et al. 2003). However, horizontal stress magnitudes and orientations in such rock strata are particularly important for excavation and support designs since they indicate the high risk zones.

Borehole breakout, named by Babcock (1978), is a drilling-induced phenomenon that is observed in layers where the rock fracture occurs due to the local stress concentration, particularly in weak rock strata (Lee et al. 2016). As the tangential stress at the wall exceeds the rock strength, rock failures will take place around the borehole. The fractures will propagate along the minimum horizontal stress direction and eventually result in symmetrical V-shaped void spaces (Gough and Bell 1982; Zoback et al. 1985), as displayed in Figure 1.1. For this reason, borehole breakout has been widely used as a reliable indicator of horizontal stress orientation since the 1980s (Stock et al. 1985; Zoback et al. 2003; Lin et al. 2010; Ask et al. 2015).

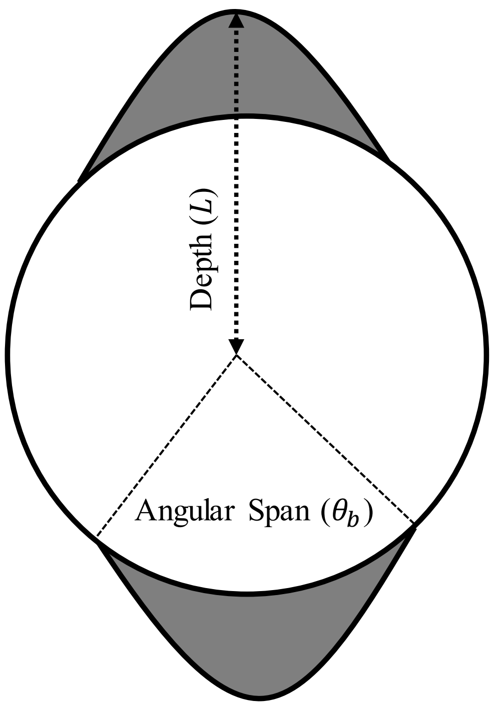

Figure 1.1 Borehole breakout

Many researchers have also argued that the breakout geometric attributes, i.e. angular span and depth, are dependent on horizontal stress magnitudes and rock strength (Zoback et al. 1985; Haimson and Herrick 1989; Haimson and Lee 2004; Lee et al.

2016). Experimental studies investigated breakout behaviours by changing the maximum horizontal stress while keeping minimum horizontal and vertical stresses constant. Results suggested both geometries increase with increasing maximum horizontal stress, although the definitive relationship remains unknown (Haimson and Herrick 1986; Herrick and Haimson 1994; Lee and Haimson 2006).

Given the rapid advancement of borehole imaging technology, using such phenomenon to estimate horizontal stress magnitudes has also received significant attention (Gaines et al. 2012). Early researchers who attempted to determine the horizontal stress magnitudes from breakout geometries were Zoback et al. (1985). They combined the Kirsch solution and Mohr–Coulomb failure criterion to define the initial failure zone of the breakout. Barton et al. (1988) extended the model and used breakout angular span as the input parameter to predict maximum horizontal stress given the magnitude of the minimum horizontal stress and uniaxial compressive strength. This approach has been successfully used for horizontal stress estimation (Barton et al. 1988; Zoback et al. 2003; Chang et al. 2010; Nian et al. 2016; Kim et al. 2017; Molaghab et al. 2017) and has been modified by numerous researchers based on different failure criteria (Vernik and Zoback 1992; Song and Haimson 1997; Haimson and Chang 2002; Chang et al. 2010). The contemporary approach for horizontal stress estimation from borehole breakout is the stress polygon method. The technique is based on the model proposed by Barton et al. (1988) and Anderson’s faulting mechanism (Anderson 1951), which is capable of providing ranges of both horizontal stress magnitudes based on breakout angular span, vertical stress and relevant rock information (Zoback et al. 2003; Chang et al. 2010; Kim et al. 2017). However, none of the approaches provide exact values of two horizontal stresses from borehole breakout data. Hence, there is a need to improve the current understanding of breakout mechanisms and relationship with horizontal stress magnitudes for the purpose of horizontal stress prediction.

Since breakouts can be found in weak strata under high stress conditions, it can overcome the limitations of existing stress measurement techniques. Rather than point stress measurements provided by overcoring or hydraulic fracturing at pre-determined layers, a local stress profile along the depth can be constructed if there is sufficient breakout data observed in different locations. Since every borehole in Australia is geologically and geophysically logged, breakout data and associated rock information are freely accessible. This means using this technique to estimate horizontal stress magnitudes does not incur any additional cost, which is attractive compared to other approaches. Therefore, developing a horizontal stress measurement technique from borehole breakout data is not only pivotal for the safety of underground operations, but also economically beneficial to the mining, petroleum and civil industries.

1.2 Problem Statement

Despite the efforts of researchers (Zoback et al. 1985; Barton et al. 1988; Brudy et al. 1997; Zoback et al. 2003; Chang et al. 2010; Song and Chang 2018), the accurate estimation of two horizontal stress magnitudes from borehole breakout geometric attributes is still a problem with no universally accepted solution. This is mainly because the current techniques only use breakout angular span as the input while neglecting the breakout depth. The primary reason preventing the use of breakout depth is the belief there is a unique relationship between two breakout geometries, which is insensitive to horizontal stress magnitudes. This belief led to the conclusion that both horizontal stress magnitudes cannot be derived solely from two dependent breakout geometries (Sahara et al. 2017). However, this claim was based on experimental observations (Haimson and Herrick 1989; Haimson et al. 1991; Herrick and Haimson 1994; Haimson and Lee 2004; Lee and Haimson 2006), and was not derived from a solid theoretical background. Therefore, it is essential to clarify the relationship between the two geometries from experimental and analytical investigation.

Recent experimental studies on breakout have suggested that higher maximum horizontal stress always leads to longer and wider breakouts given the constant minimum horizontal and vertical stress magnitudes (Haimson and Herrick 1986; Haimson and Herrick 1989; Haimson et al. 1991; Herrick and Haimson 1994; Haimson and Lee 2004; Lee and Haimson 2006; Lee et al. 2016). On the other hand, the influences of the other two stresses have rarely been investigated. In reality, in-situ stress is three dimensional and it is believed that each of the three principal stress components plays an important role in rock failure (Mogi 1971; Al-Ajmi and Zimmerman 2005; Rahimi and Nygaard 2015). Hence, the relationship between breakout geometries and minimum horizontal and vertical stresses should be explored to develop a horizontal stress estimation technique from breakout data.

During the experimental observations, a number of researchers also pointed out that the stress required for borehole breakout initiation is inversely proportional to the borehole size (radius), especially under laboratory conditions (Haimson and Herrick 1989; Carter 1992; Cuss et al. 2003; Elkadi and Van Mier 2006; Meier et al. 2013). To model this borehole size effect, various theories have been proposed, including the stress averaging concept (Lajtai 1972; Carter 1992), fracture mechanics (Bažant et al. 1993) and the pressure-dependent linear elastic model (Santarelli et al. 1986; Santarelli and Brown 1989). Due to the experimental limitation, it is not feasible to monitor stress change and fracture initiation within a rock sample precisely in the laboratory. Thus, it is difficult to examine the validity of each theory. Although there is a significant body of research on the borehole size effect on breakout initiation stress (Carter et al. 1991; Van den Hoek et al. 1994; Van den Hoek 2001; Dresen et al. 2010; Papanastasiou and Thiercelin 2010; Meier et al. 2013), the influence of borehole size on breakout geometries has not been studied. This is particularly important for breakout research at the laboratory scale since it contributes to the relationship between breakout geometries and horizontal stress magnitudes.

As briefly discussed in Section 1.1, there have been a series of modified model versions of Barton et al. (1988) to construct the relationship between breakout angular span and horizontal stress magnitudes based on various failure criteria (Vernik and Zoback 1992; Song and Haimson 1997; Haimson and Chang 2002; Chang et al. 2010). However, there is no thorough analysis to identify the most reliable failure criterion and the determination of whether the intermediate stress should be considered. This lack of universal agreement on selecting the failure criterion can lead to poor or misleading estimation results when using the model. Hence, it is necessary to compare the effects of failure criteria on prediction models and examine their performances on experimental and field data.

Overall, a number of critical research gaps have been identified in breakout research. This thesis proposes a combined approach including experimental study, numerical simulation, analytical investigation, machine learning and field data validation to address these problems and develop a better understanding of borehole breakout.

1.3 Research Objectives

The main objective of the thesis research is to develop a technique that can be used to estimate the magnitude of horizontal stress based on borehole breakout data. To achieve this goal, it is important to solve the problems addressed in Section 1.2. The sub-objectives are to:

- Validate the conclusion drawn by previous researchers on the unique relationship between breakout geometries that is not influenced by horizontal stress magnitudes. Breakout data observations are collected from experimental work in this thesis and from the literature. The breakout geometric relationship under various horizontal stress combinations is investigated experimentally and analytically.
- Determine the effect of minimum horizontal and vertical stresses on breakout geometries.
- Investigate the borehole size effect on breakout initiation stress. This is achieved both experimentally and numerically. Breakout initiation stress is monitored and recorded under normal compression tests and a number of approaches are proposed to model this relationship. Particle Flow Code (PFC) is a powerful tool which can simulate rock behaviour under various conditions. Based on its measurement functions, the validity of borehole size effect models is examined.
- Investigate the influence of temperature on breakout geometries and the breakout propagation under the same stress condition.
- Propose an approach that can estimate horizontal stress magnitudes from borehole breakout data. This technique is examined against experimental and field data.

1.4 Thesis Structure

This thesis has eight chapters in total:

Chapter 1: Introduction

Chapter 1 provides an overview of current stress measurement techniques and the potential to predict horizontal stress from borehole breakout. The research gaps in borehole breakout study and the thesis objectives are addressed.;

Chapter 2: Literature Review

Chapter 2 presents a literature review of the thesis topic in four sections. The first section discusses the procedures and mechanisms of available stress measurement techniques, together with their advantages and disadvantages. The second section reviews the mechanisms of borehole breakout, borehole size effect and the existing constitutive models to estimate horizontal stress from borehole breakout. It is followed by a review of numerical simulation techniques on borehole breakout. The last section reviews machine learning techniques and their applications in rock mechanics.

Chapter 3: Experimental Study on Borehole Breakout and Borehole Size Effect

Chapter 3 has two sections. Section 3.1 presents the investigation of the maximum horizontal stress and borehole size influences on breakout geometries based on a series of borehole breakout tests using a specially designed true triaxial test apparatus. Then, the relationship between breakout angular span and depth is explored. To obtain a better understanding of breakout initiation stress under various borehole sizes, normal compression tests are conducted and the results presented in Section 3.2. A number of methodologies on predicting breakout initiation stress are also compared.

Section 3.1 has been published in *Rock Mechanics and Rock Engineering* (Lin et al. 2020a) and Section 3.2 has been submitted to *International Journal of Rock Mechanics and Mining Sciences* (Lin et al. 2020b).

Chapter 4: Estimation of Maximum Horizontal Stress Magnitudes from Kriging

Chapter 3 found that the relationship between breakout geometries is not unique, such that both breakout angular span and depth can be used to estimate horizontal stress magnitudes. Chapter 4 first presents the experimental data and field data collected from published articles and a mine site. Then, a machine learning technique, Kriging, is introduced to predict the maximum horizontal stress magnitudes based on both breakout geometries. The model is trained by laboratory data and validated against both laboratory and field data. In addition, the limitation of the experimental dataset and Kriging application to minimum horizontal stress estimation is discussed.

Chapter 4 has been published in *International Journal of Rock Mechanics and Mining Sciences* (Lin et al. 2020c).

Chapter 5: Numerical Simulation on Breakout Development and Borehole Size Effect

Chapter 5 presents the numerical simulation results on borehole breakout and borehole size effect using Particle Flow Code. The breakout progressive development is initially observed during simulation, and breakout geometries under various stress combinations are compared to experimental results in Chapter 3. The theories which explain the borehole size effect on breakout initiation are also examined based on the stress–strain change and micro-cracking monitored from Particle Flow Code. The influence of temperature on breakout geometries and initiation stress is simulated and discussed.

Chapter 5 has been submitted to *International Journal of Mining Science and Technology* (Lin et al. 2020d).

Chapter 6: Experimental Study and Combined Horizontal Stress Magnitude Estimation from Artificial Neural Network and Constitutive Modelling

The review of borehole breakout in Chapter 2 found that the influences of minimum horizontal and vertical stresses on breakout geometries have not been studied explicitly. Hence, Chapter 6 investigates the two parameters by conducting breakout tests. Based on the experimental results and data collected from Chapter 4, a comparison between constitutive models on minimum and maximum horizontal stress estimations is conducted. Results show that it is not feasible to predict minimum horizontal stress using constitutive models. To overcome this limitation, an Artificial Neural Network (ANN) is implemented to model the relationship between breakout angular span and minimum horizontal stress. Based on this analysis, a combined constitutive–ANN model is proposed to estimate both horizontal stress magnitudes from borehole breakout geometries. This model is then validated against field data and a sensitivity analysis on modelling parameters is also conducted.

Chapter 6 has been submitted to *International Journal of Rock Mechanics and Mining Sciences* (Lin et al. 2020e).

Chapter 7: Applicability of the developed models to field cases: additional data collection and validation

Chapter 7 provides the procedures for processing downhole logging data to extract breakout geometries and relevant rock information from mine sites. Further against the extracted data is conducted to examine the applicability of models proposed in Chapters 4 and 6 in various field cases.

Chapter 8: Conclusions and Recommendations

Chapter 8 summarises the conclusions drawn from each chapter to estimate borehole breakout and provides recommendations for future research.

1.5 PUBLICATIONS

1.5.1 Journal articles

Lin H, Oh J, Canbulat I, Stacey T (2020a) Experimental and analytical investigations of the effect of hole size on borehole breakout geometries for estimation of in situ stresses. *Rock Mechanics and Rock Engineering* 53:781–798. doi: https://doi.org/10.1007/s00603-019-01944-z.

Lin H, Kang W-H, Oh J, Canbulat I (2020c) Estimation of in-situ maximum horizontal principal stress magnitudes from borehole breakout data using machine learning. *International Journal of Rock Mechanics and Mining Sciences* 126:104199. doi: https://doi.org/10.1016/j.ijrmms.2019.104199.

Lin H, Kang W-H, Oh J, Canbulat I, Hebblewhite B (2020d) Numerical simulation on borehole breakout and borehole size effect using discrete element method. *International Jounral of Mining Science and Technology*. https://doi.org/10.1016/j.ijmst.2020.05.019.

Lin H, Kang W-H, Oh J, Canbulat I, Hebblewhite B (2020b) Experimental study on borehole size effect and prediction of breakout initiation stress. *International Journal of Rock Mechanics and Mining Sciences* (under review).

Lin H, Singh S, Oh J, Canbulat I, Kang W-H, Hebblewhite B, Stacey T (2020e) A combined approach for estimating horizontal principal stress magnitudes from borehole breakout data via Artificial Neural Network and rock failure criterion. *International*

Journal of Rock Mechanics and Mining Sciences (under review).

1.5.2 Conference papers

Lin H, Oh J, Canbulat I, Masoumi H, Zhao Y(2018a) Experimental investigation on borehole breakout and its implication on stress magnitudes. In: 4th Australasian Ground Control in Mining Conference 2018. University of New South Wales (Sydney, Australia).

Lin H, Oh J, Masoumi H, Canbulat I, Zhang C, Dou L (2018b) A Review of In-situ Stress Measurement Techniques. In: Coal Operators Conference. University of Wollongong (Wollongong, Australia).

1.5.3 Technical report

Oh J, Canbulat I, Hebblewhite B, Masoumi H, Lin H (2019) Reliable Estimation of Horizontal Stress Magnitudes from Borehole Breakout Data. Australian Coal Research Industry Program (ACARP).

2 LITERATURE REVIEW

Knowledge of the state of in-situ stresses is required for underground design and stability analysis. With the presence of major geological features, stress magnitudes and their orientations vary accordingly (Zoback and Healy 1992). Changes in stress can adversely influence ground conditions and increase the risk of major failures, including coal burst. To identify high-risk zones and implement appropriate controls in underground operations, reliable estimation of horizontal stress magnitudes is essential.

As the mining depth increases, obtaining accurate horizontal stress magnitudes is more challenging. The two most popular stress measurement techniques, hydraulic fracturing and overcoring, are difficult for horizontal stress estimation in weak strata because these techniques require the testing section of the borehole and cored samples to be elastic (Ljunggren et al. 2003), whereas rock fracture is likely to occur in weak strata, particularly at deep locations where in-situ stress is higher. Therefore, it is essential to develop a horizontal stress measurement technique that is suitable for these conditions.

Borehole breakout usually occurs in weak strata, typical creating V-shaped voids in the vicinity of the borehole along the minimum horizontal stress direction. As breakout geometries are stress dependent (Zoback et al. 1985; Haimson and Herrick 1989) and can be easily obtained from existing downhole logging data, they can be used to overcome the shortcomings of current stress measurement techniques.

This chapter aims to demonstrate the importance of developing such technique and provides a state-of-the-art borehole breakout study. The chapter has four sections. Section 2.1 reviews current stress measurement techniques, including benefits and limitations. Section 2.2 focuses on breakout formation mechanisms and the relationship between breakout geometries and horizontal stress magnitudes. Section 2.3 reviews numerical simulation and its application to borehole breakout. Section 2.4 presents a review of machine learning and its application to rock mechanics problems. Machine learning is used in later chapters to estimate horizontal stress magnitudes from breakout geometries.

2.1 REVIEW OF STRESS MEASUREMENT TECHNIQUES

Estimating in-situ stress magnitudes is vital for geotechnical and mining engineers. This section reviews existing stress measurement techniques, including the mechanisms and their advantages and disadvantages. Based on the review, the need to develop a horizontal stress estimation technique from borehole breakout is discussed.

2.1.1 Hydraulic fracturing

Hydraulic fracturing is one of the commonly used methods for stress measurements. It was initially used for reservoir productivity stimulation and was applied to stress measurement in the early 1960s (Ljunggren et al. 2003). The technique has two major types: conventional hydraulic fracturing and hydraulic tests on pre-existing fractures (HTPF).

2.1.1.1 Conventional hydraulic fracturing

Conventional hydraulic fracturing measurement utilises hydraulic pressure from the fluid injection to create tensile fractures around the borehole. To measure the stress at the desired depth, a sealed section of the borehole at the location is isolated by the impression straddle packer. Fluid is then slowly injected into this interval to apply pressure on the borehole sidewall. When the pressure induced tangential tensile stress overcomes the tensile strength of the surrounding rock, two fractures will form in opposite directions and penetrate along the plane perpendicular to the minimum principal stress direction, see Figure 2.1. This is because fluid will break rock in the direction where the resistance is lowest. The pressure at this point is called 'breakdown pressure, P_b'.

Once the fracture is initiated and penetrates through rock, the fluid pressure will decrease rapidly. On the termination of fluid injection, the pressure is carefully monitored to obtain the steady pressure point, which is called 'instantaneous shut in pressure (ISIP), P_{ISIP}'. To close the fractures and prepare for the second hydraulic cycle, pressure is released from the system. Fluid is then re-pumped into the sealed borehole section to re-open the fractures (P_r), followed by the same shut-in process. Multiple cycles are usually conducted to improve the accuracy of pressure records and hence stress estimation. Figure 2.2 illustrates the hydraulic fracturing process.

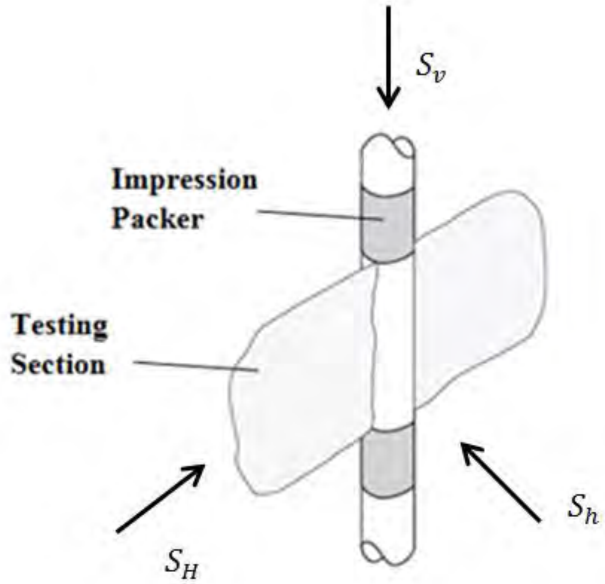

Figure 2.1 Conventional hydraulic fracturing after Lakirouhani et al. (2016)

As postulated by Hubbert and Willis (1957), if the borehole is drilled vertically and parallel to one of the principal stresses, the minimum horizontal principal stress magnitude can be calculated as:

$$\boldsymbol{\sigma_h = P_{ISIP}} \tag{2.1}$$

This is because, at the shut-in point, the pressure required to keep the fractures open can be roughly equal to the fracture-normal stress, σ_h (Haimson and Cornet 2003).

Based on the Kirsch solution (Kirsch 1898), the tangential stress (σ_θ) at the fracture initiation point around the borehole can be expressed as:

$$\boldsymbol{\sigma_\theta = 3\sigma_h - \sigma_H - P_0} \tag{2.2}$$

where σ_H = maximum horizontal principal stress and P_0 = pore pressure. Since the fractures occur along the borehole wall, the radial stress (σ_r) at the location can be neglected. Hence, to induce hydraulic fracture, the tangential stress has to overcome the rock tensile strength (T), i.e.

$$T = \sigma_H - 3\sigma_h + P_0 \qquad (2.3)$$

By taking account of breakdown pressure (P_b) from the system and minimum horizontal stress estimated from shut-in pressure, σ_H can be obtained:

$$\sigma_H = 3\sigma_h + T - P_b - P_0 \qquad (2.4)$$

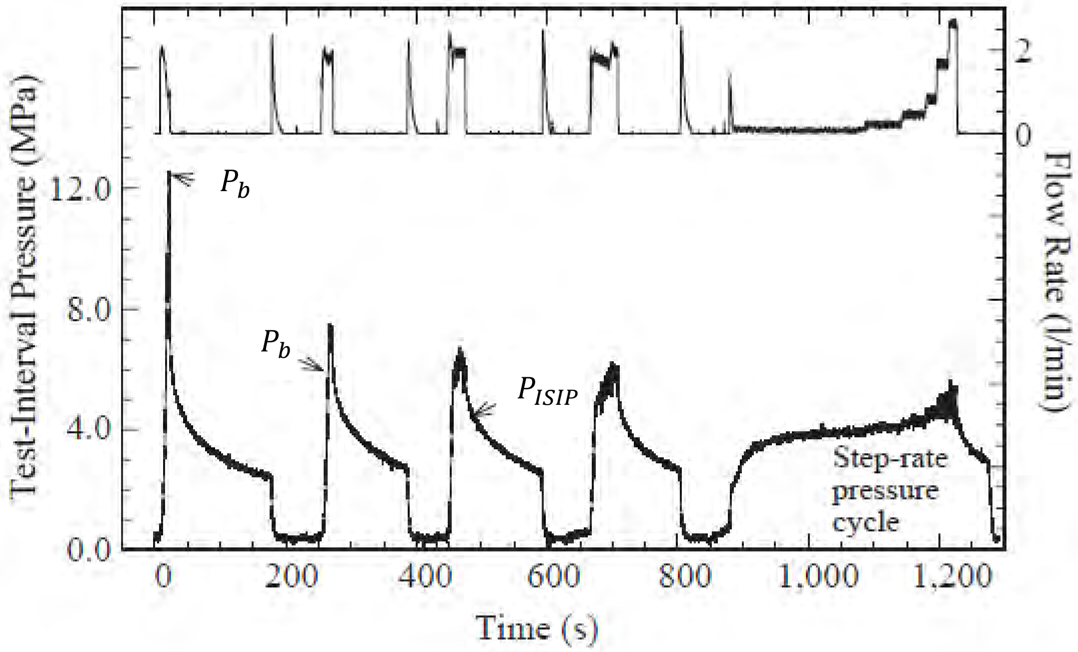

Figure 2.2 Hydraulic fracturing process after Haimson and Cornet (2003)

Based on Eq. (2.4), it is clear that the tensile strength of the sealed section is required. However, cored samples can be fractured during collection and the tensile strength gathered in the laboratory may not be representative of the field due to the scale effect (Haimson and Cornet 2003). To overcome this issue, an alternative was proposed, where two or more cycles of the process are repeated to determine the pressure that re-opens the fracture (P_r). This is because the tensile strength of rock is very low and therefore can be neglected after the initial fracture in the first cycle (Bredehoeft et al. 1976). In this case, Eq. (2.4) can be simplified as:

$$\sigma_H = 3\sigma_h - P_r - P_0 \qquad (2.5)$$

Conventional hydraulic fracturing provides a simple way to measure horizontal stress magnitudes, so that advanced knowledge of rock properties, such as Young's modulus and Poisson's ratio, is not essential. This method also offers a very reliable and direct measurement of minimum horizontal principal stress at an accuracy of ± 5% (Ljunggren et al. 2003). Another advantage of the method is its application to deep locations. In theory, hydraulic fracturing can be conducted at any depth as long as the surrounding rock is elastic and brittle (Haimson and Cornet 2003). For instance, Hung et al. (2009) successfully conducted hydraulic fracturing stress measurement at a depth below 1 km. Horizontal stress orientations can be determined because the fracture propagation is perpendicular to the minimum principal stress direction.

However, one inevitable shortcoming of this technique is the accuracy of the maximum horizontal principal stress calculation. As the fractures occur on opposite sides of the borehole, the stress concentration at the fracture orientation around the borehole is no longer elastic and cannot be represented by the Kirsch solution; and the remaining apertures at the start of each cycle (Cornet 1993) can cause imprecise recording of the re-opening pressure. The variation in estimation can be over ± 20% (Ljunggren et al. 2003).

When there are pre-existing weaknesses around the testing section, the injected fluid re-opens and penetrates through pre-existing fractures instead of the plane perpendicular to the minimum principal stress direction since the resistance is much lower along pre-existing fractures. This disturbance of pre-existing weaknesses can result in misleading pressure recording and false stress estimation. Hence, the technique is not suitable for pre-existing weaknesses or thinly laminated strata. Hydraulic fracturing is also limited by the faulting mechanism. For instance, if the stress field is controlled by reverse faulting, where vertical stress is the minimum principal stress as is common in shallow coal mines, fractures will be formed in the horizontal plane (Haimson and Cornet 2003). In this case, horizontal stress magnitudes or orientations cannot be estimated (Gaines et al. 2012). As hydraulic fracturing is a horizontal stress measurement technique, no information about the magnitude of vertical stress can be calculated. In addition, if the tensile strength is too high and the fluid cannot induce any fracture, horizontal stress magnitudes cannot be estimated.

2.1.1.2 Hydraulic tests on pre-existing fractures

Hydraulic tests on pre-existing fractures (HTPF) were initially proposed by Cornet and Valette (1984) to overcome some shortcomings of the conventional hydraulic fracturing method. HTPF has similar procedures as the traditional method. The only difference is that it uses the hydraulic pressure to re-open the pre-existing fractures around the borehole rather than inducing fractures from intact conditions. This technique calculates the in-situ stress field based on the normal stresses acting perpendicular to pre-existing fractures at different orientations, where the normal stresses are determined from the re-opening process of HTPF. Similar to conventional hydraulic fracturing, the magnitude of normal stress is equal to the instantaneous shut-in pressure. Accordingly, it is important to gather precise locations and orientations of fractures before starting fluid injection. This is usually done by borehole imaging techniques, such as the Mosnier tool (Haimson and Cornet 2003). HTPF is shown in Figure 2.3.

Since HTPF does not induce fractures, it is less limited by geological conditions compared to the conventional method. In weak strata, there are more pre-existing fractures that may influence the reliability of conventional hydraulic fracturing. In this condition, HTPF can effectively use the pre-existing fractures to estimate the principal stress magnitudes. By conducting sufficient tests, the 3D stress field can also be computed using the method.

However, due to strict requirements on fracture locations and a large number of tests, HTPF is more time intensive than the conventional method. In general, at least 18 to 20 successful tests are required for a reliable 3D stress interpretation (Ljunggren et al. 2003). Therefore, HTPF is based on the assumption that the fracture orientation is persistent. Distorted fractures can lead to overestimation of shut-in pressure which results in inaccurate evaluation of principal stress magnitudes.

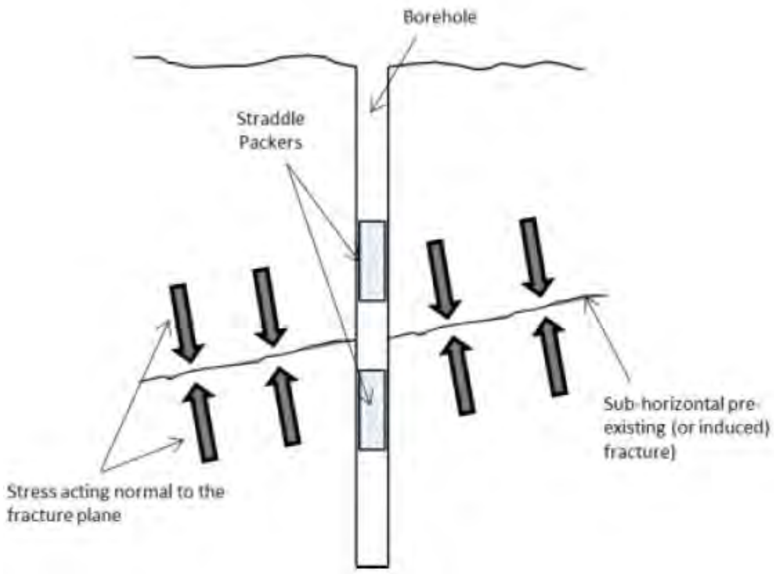

Figure 2.3 Schematic of HTPF (Gaines et al. 2012)

2.1.2 Overcoring

Overcoring is a widely used stress measurement technique in underground excavations. The estimation is based on the strain or radial change of a hole during the overcoring process. Using various designs and specifications, a range of methods was developed with similar procedures and the same principle of linear elasticity and the Kirsch solution. Depending on instrumentations and requirements of pilot holes, these methods can be divided into three types (Ljunggren et al. 2003):

- Soft inclusion cells (strain change)
- Radial deformation cells
- Overcoring without pilot holes.

2.1.2.1 Soft inclusion cells

The concept of soft inclusion cells is to solve the stress matrix based on the local stress tensor, where this stress tensor is gathered from the strain changes in the axial direction (along the borehole axis), circumferential direction, and 45° above and below the circumferential direction around the borehole due to the stress relief. By attaching highly sensitive strain gauges to the rock around the borehole using temperature-specific gluing packs, gauges can rapidly become part of the rock and experience similar behaviours during overcoring.

A borehole is initially drilled to the desired measurement depth. A pilot hole is then advanced from the bottom of the borehole at the centre using a barrel. At the completion of pilot hole drilling, strain gauges are installed in the hole and glued onto the side of the wall at different orientations and angles, so they will experience similar deformation of the rock. By then, the equipment is retrieved together with cored rock samples. The rock samples are transported to the laboratory for testing to obtain properties including Young's modulus and Poisson's ratio. Overcoring commences from the bottom of the borehole towards the pilot hole to remove rock and induce strain change. This change is continuously monitored by the strain gauges. Once the process is completed, the strain readings from the strain gauges are collected and used for stress estimation. Figure 2.4 illustrates overcoring.

Soft inclusion cell instruments include CSIR, CSIRO HI cell, SCT ANZI cell and Borre Probe. Depending on the instrument, calculation equations are slightly different but they are all based on the Kirsch solution and elastic parameters. For example, CSIRO HI cell incorporates its own correction factors during the stress estimation (Ask 2006):

$$\boldsymbol{\varepsilon_\theta = \frac{1}{E}\{K_1(\sigma_x + \sigma_y) - 2(1 - v^2)[(\sigma_x - \sigma_y)cos2\phi + 2\tau_{xy}sin2\phi]K_2 - vK_4\sigma_z\}} \tag{2.6}$$

$$\boldsymbol{\varepsilon_z = \frac{1}{E}[\sigma_z - v(\sigma_x + \sigma_y)]} \tag{2.7}$$

$$\boldsymbol{\varepsilon_{45/135^\circ} = \frac{1}{E}[\varepsilon_z + \varepsilon_\theta \pm \frac{4K_3}{E}(1 + v)(\tau_{yz}cos\phi - \tau_{zx}sin\phi)]} \tag{2.8}$$

where σ_x, σ_y, σ_z, τ_{xy}, τ_{zx}, τ_{yz} are the local stress tensors around the borehole based on the chosen coordinate system, as shown in Figure 2.5, ϕ = angle from σ_x direction according to the coordinate, v = Poisson's ratio, E = Young's modulus, and K_1 to K_4 are correction factors that take into account the influence of the glue between the contact of gauges and rock, which are usually near 1.

The soft inclusion cell determines the stress field within one borehole measurement only, which is better than most of the techniques, including radial deformation cell measurement. This technique provides direct stress measurements for both horizontal principal stresses at high accuracy and is considered the most reliable underground stress measurement technique (Reinecker et al. 2008). Compared to other overcoring methods, soft stress cells offer 3D stress estimation rather than 2D through a rotational and continue logging, except for CSIR. Unlike other soft stress cells, Borre Probe can be applied to deep boreholes, even with water infill (Gaines et al. 2012). In addition, the CSIRO HI cell can be recovered and re-used to reduce the prohibitive cost (Cai and Blackwood 1987; Cai and Thomas 1991).

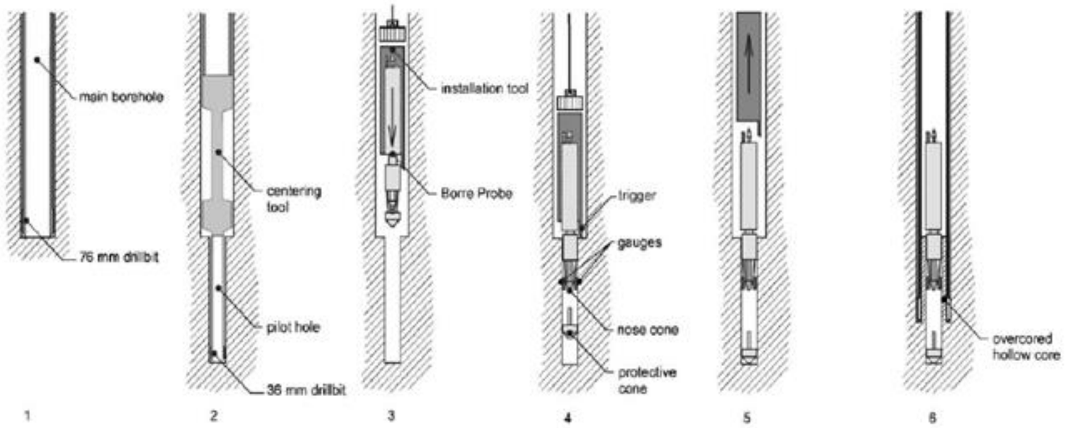

Figure 2.4 Overcoring procedures (Hakala et al. 2003)

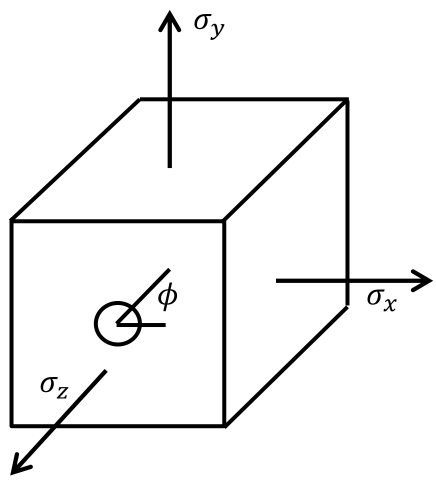

Figure 2.5 Stress orientation around the borehole

The soft inclusion cell technique also has a number of disadvantages. Unlike radial deformation cells, soft stress cells are difficult to recover from the field. Epoxy based glue cannot be used in humid and dusty environments, including coal mines (Coetzer 1997). The thickness of glue and its associated temperature effect may influence the accuracy of the measurement. Unbroken long cores of at least 40–60 cm are required for successful measurements (Ljunggren et al. 2003), but these can be difficult to obtain in high stress zones due to core discing or pre-existing fractures, especially for Borre Probe measurement where the measurement location is deep. As the technique assumes the rock is elastic and deforms linearly, any discontinuity including joints or a failed borehole wall can disturb the measurement and yield unreliable results.

2.1.2.2 Radial deformation cells

The operating procedures for deformation cells are similar to soft inclusion cells, where the deformation of the pilot hole is monitored throughout the overcoring process. Instead of recording strain gauges, deformation cells calculate the horizontal stress magnitudes based on the recording of borehole radial change at various orientations during overcoring via cantilevers or pins. By considering the stresses around the borehole in the x–y plane, as shown in Figure 2.5, the borehole radial displacement can be expressed as below (Leeman 1967):

$$\boldsymbol{u_r = \frac{r}{E}\left[(\sigma_x + \sigma_y) + 2(1 - v^2)(\sigma_x - \sigma_y)cos2(\phi - \alpha) - v\sigma_z\right]} \tag{2.9}$$

where u_r = radial deformation, r = radius, α = the angle between the σ_x direction and the radial measurement. Since multiple radial changes are recorded at different angles, the simultaneous equations can be obtained from Eq. (2.9). In conjunction with the Young's modulus and Poisson's ratio obtained from cored samples under laboratory testing, horizontal principal stresses and their orientations can be derived. The two most common measurement instruments are the US Bureau of Mine cell (USBM) and SIGRA in-situ stress testing (IST). In the Australian coal industry, the most used instrument is SIGRA IST.

Similar to soft inclusion cells, radial deformation cells also provide direct stress measurements (Amadei and Stephansson 1997). SIGRA IST has an average success rate of 70% over 600 measurements (Gray and See 2007). Cells used in this technique are also recoverable and can be used for multiple tests. Since cables are not connected from cells to a computer and the monitoring data is extracted after overcoring (Gray 2003), theoretically it is not limited by depth.

However, the technique also has shortcomings. Similar to soft inclusion cells, unbroken long cores are required for laboratory testing to collect rock information. Given the continuity of the cored sample under high stress conditions, this method is in practice only suitable at shallow depths. A single measurement can only provide 2D stress measurement rather than 3D. To obtain a complete 3D in-situ stress field, at least three non-parallel boreholes are required (Ljunggren et al. 2003), which is more time consuming and economically less favourable compared to soft inclusion cells.

2.1.2.3 Overcoring without pilot holes

Doorstopper is a special overcoring method which does not require a pilot hole. Instead, the borehole bottom has to be carefully polished to ensure it is flat so that the strain gauges can be glued and attached to the rock. Atomic Energy of Canada Ltd. modified this instrument for deep measurement, called the Deep Doorstopper Gauge System (DDGS) (Thompson and Chandler 2004). Figure 2.6 illustrates the process of DDGS. Instead of 'overcoring' the rock around the pilot hole, the doorstopper method 'undercores' the rock below the gauges, i.e. the borehole is extended downwards to induce strain relief, see step 5 in Figure 2.6. Although the procedures are different, it is similar to other overcoring techniques which record the deformation of rock induced by drilling and rock removal.

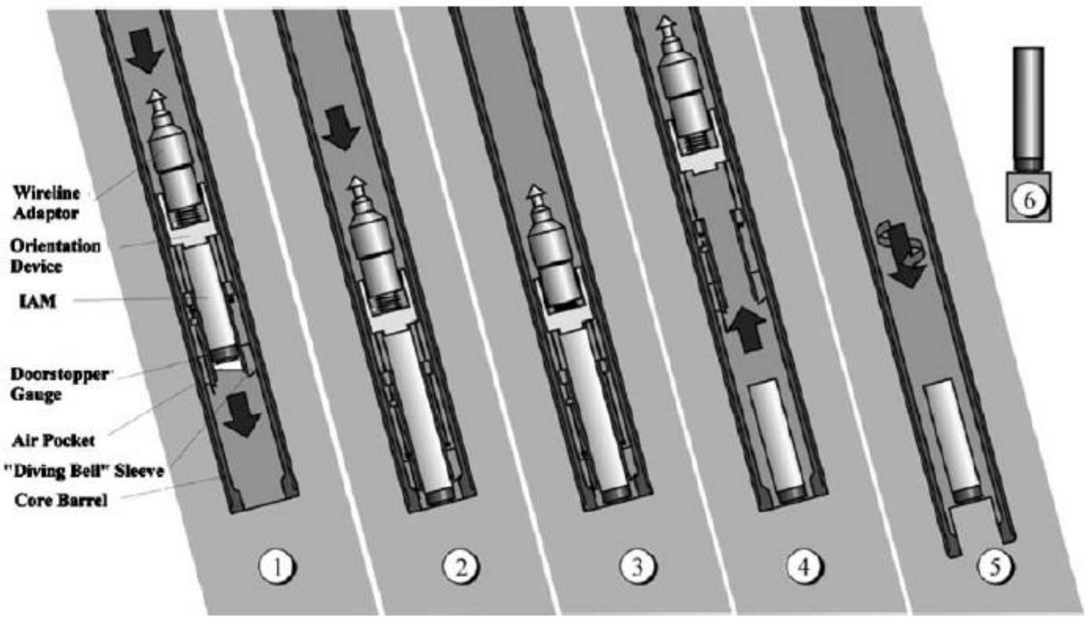

Figure 2.6 Deep Doorstopper Gauge System (DDGS) procedures (Fairhurst 2003)

Overcoring methods with pilot holes generally require more than 30 cm overcoring length, whereas the doorstopper only needs 5 cm (Amadei and Stephansson 1997). As a result, the doorstopper is more applicable for deep locations where stress concentration near the borehole is high. It also has a more successful measurement rate in relatively weak or broken rock conditions, because a pilot hole is not necessary. With modifications, DDGS can be implemented in deep, water filled boreholes (Ljunggren et al. 2003).

Although a pilot hole is not necessary for the doorstopper, polishing and preparing the borehole bottom is essential. This can be quite challenging considering the stress measurement is conducted at very deep locations. Three boreholes are generally required to obtain a complete stress field (Amadei and Stephansson 1997). The doorstopper also experiences the same issues as other overcoring methods under pre-existing fractures and only provides a 2D in-situ stress field.

2.1.3 Core discing

Core discing is a phenomenon occurring at the coring bit–rock interface due to the tensile stress induced from drilling. When drilling takes place, stress is concentrated across the core which results in fractures. If stresses are high enough and the rock is brittle, the core is disced into thin chips, as shown in Figure 2.7a. 'Saddle-shaped' discs are indicative of horizontal stress orientations, in which the convex axis is aligned with the minimum horizontal stress direction (Jaeger and Cook 1963; Dyke 1989), see Figure 2.7b. Hence, core discing has been used in horizontal stress orientation determination.

Since core discing is a result of drilling and horizontal stress magnitudes, many attempts have been made to correlate the in-situ stress magnitudes with core discing (Obert and Stephenson 1965; Dyke 1989; Ishida and Saito 1995; Haimson and Song 1995; Kaga et al. 2003; Lim and Martin 2010). Obert and Stephenson (1965) conducted drilling tests on cylindrical specimens under triaxial conditions to investigate the relationship between stress magnitudes and core disc thickness. The experimental results on six rock types highlighted that discs are thinner under higher stress combinations than under lower stress combinations, suggesting the disc thickness can be used for horizontal stress indication.

By analysing the experimental results, Obert and Stephenson (1965) also proposed that the minimum axial stress required for core discing initiation should have the following relationship with radial stress:

$$\boldsymbol{\sigma_r = k_1 + k_2\sigma_z} \tag{2.10}$$

where σ_r = radial stress applied to the specimen, σ_z = axial stress applied to the specimen, k_1 and k_2 are empirical constants that can be derived from experimental data. This study also argued that to achieve core discing in the field, two in-situ stress conditions should be satisfied: i) the vertical stress should be the least principal stress; and ii) the horizontal stress should be high compared to the rock strength.

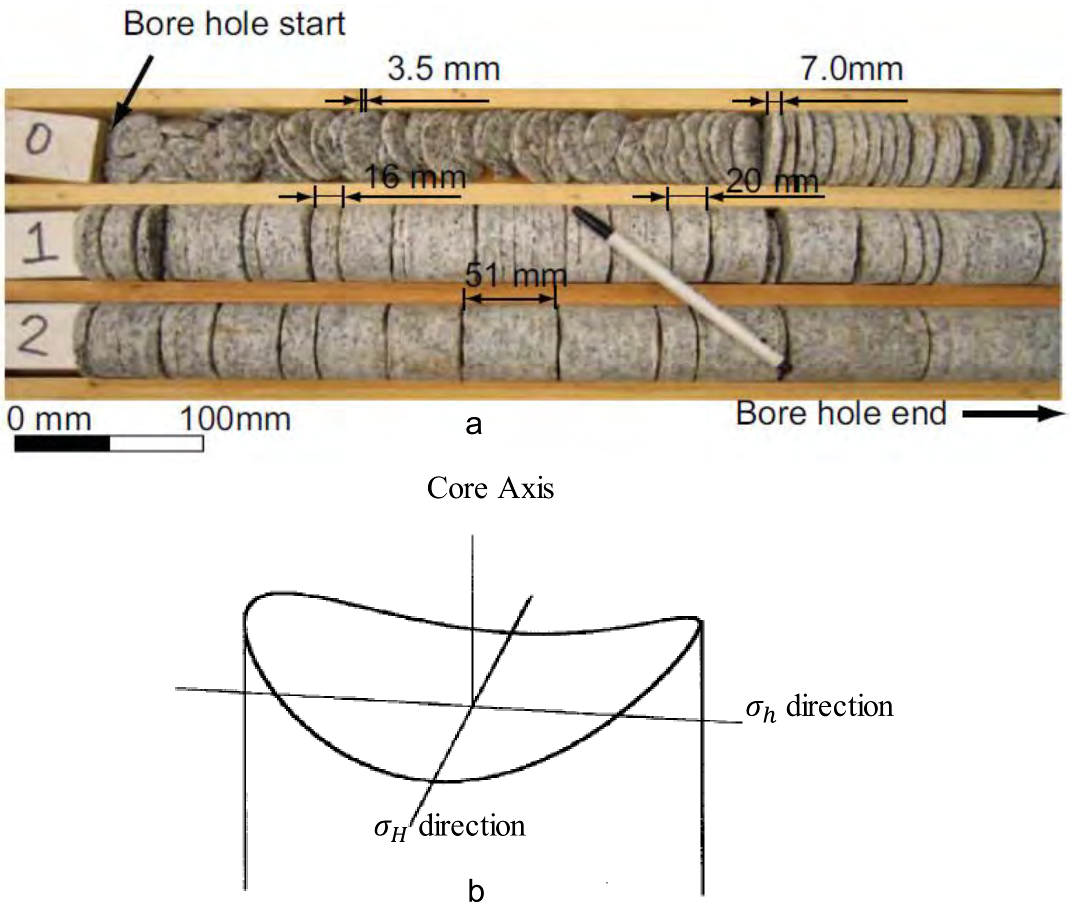

Figure 2.7 a) Core discing (Lim and Martin 2010); b) stress orientation after Matsuki et al. (2004)

Kaga et al. (2003) conducted 77 stress scenarios on an HQ core through finite element analysis. Based on simulation results, Kaga et al. (2003) found that greater depth would lead to shorter disc lengths and therefore introduced a new core discing criterion considering tensile strength (T):

$$\boldsymbol{T = -A'\sigma_m + B'\sigma_x - C'(\frac{\sigma_x^2}{\sigma_m}) - D'(\sigma_x - \sigma_y)} \tag{2.11}$$

where A', B', C' and D' are constants that can be derived from curve-fitting. σ_m = mean stress, σ_x and σ_y are horizontal principal stresses. This criterion was validated against the experimental results in Sugawara et al. (1978) and Haimson (1995). Based on the least-squares method, Kaga et al. (2003) also suggested a relationship between disc thickness (t) and core length (L):

$$\boldsymbol{L/R = \frac{t}{R}/[1 + 0.0261\left(\frac{t}{R}\right)^{-4.37}] - 0.0716} \tag{2.12}$$

where R = core radius. Lim and Martin (2010) analysed the core discing data of Lac du Bonnet granite collected from underground excavations. Based on observation, they suggested that the core discing initiates if the ratio between maximum horizontal stress and tensile strength is over 6.5. A classification system was also introduced by the researchers to divide core discing into three categories according to different disc thickness, which can be used to estimate maximum horizontal stress, see Figure 2.8.

Overall, this methodology uses a naturally occurring event during coring, which does not incur any additional costs. As core discing is observed in high stress concentration zones at deep locations, it is usually used as a stress indication tool (Fairhurst 2003) and it is useful for the later drilling process (Ljunggren et al. 2003). Because of its shape alignment with horizontal stresses, it can also be used to determine horizontal stress orientation (Bankwitz and Bankwitz 1997).

The major disadvantage of core discing is that the technique cannot consistently provide reliable estimation and can only be used as a stress indicator (Ljunggren et al. 2003). Coring is not conducted in every borehole which means the critical data might not be available. Furthermore, core discing only occurs in limited conditions where the tensile strength is overcome by the stress concentration, so that it can only be considered a complementary technique.

Term	Core photo	Description	Disk thickness t/D	Stress condition σ_1/σ_t
Core disking		Crushed disking: The disks are crushed due to the extremely high stress	<0.05	>11
		Very thin disking: The majority of the disks are intact but a few are crushed	0.05–0.12	9–11
		Thin disking: The shape and spacing of the core disks are uniform	0.12–0.2	8–9
		Medium disking: The shape and spacing of the core disks are uniform. Most commonly observed disk thickness	0.2–0.4	7–8
		Thick disking: The shape of the core disks is uniform	0.4–2.2	6.5–7
Partial disking		Partially disking: Distinct white lines appear at regular spacings, similar to that observed when the complete disks form, but the core remains intact. Spacing between these lines is similar to that of Medium disking	0.2–0.4	6–7
No disking		No disking: Solid core but the core maybe microcracked which can be seen with the naked eye	–	–

Figure 2.8 Core discing thickness vs the maximum horizontal stress/tensile strength with three categories (Lim and Martin 2010)

2.1.4 Borehole slotter

Borehole slotter is a 2D stress relief method developed by Bock and Foruria (1984). It has the same principles as overcoring to monitor the strain change of rock (Becker and Werner 1994). Instead of overcoring the pilot hole, the borehole slotter cuts slots into the wall at different orientations. A half-moon shaped radial slot approximately 1 mm wide and 25 mm deep is initially cut into the wall of a borehole using a diamond saw, while the variation in tangential strain during cutting is recorded by the strain sensor mounted in the saw, see Figure 2.9. By cutting three slots that are 120° apart, three tangential strain recordings can be collected and the in-situ stresses can be calculated with the elastic rock properties.

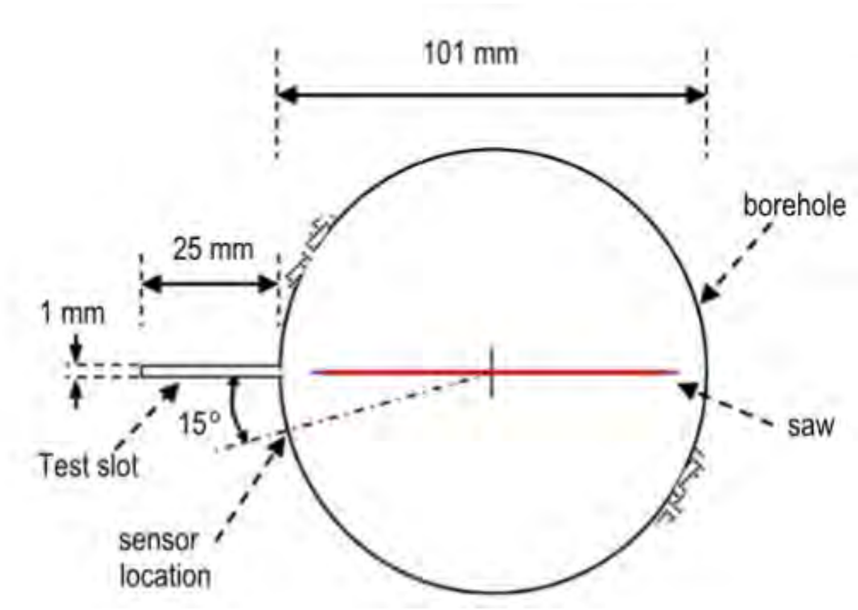

Figure 2.9 Plan view of borehole slotter (Saati and Mortazavi 2011)

The primary advantage of the technique is that overcoring is not required for the stress measurements. Since the system is connected, the equipment is recoverable and can be re-used, while the strain data is continuously recorded during the cutting process. The strain sensor is also recoverable and each test only takes around 40 minutes (Bock 1993).

The method has some limitations. Once the first slot is cut, the stress field around the borehole is disrupted, so the Kirsch solution does not represent the stress field around the borehole anymore. This can yield some uncertainties within the estimation. The borehole slotter only provides 2D stress measurement and the equipment is designed to work for boreholes with diameters over 95 mm, which constrains its applicability to a few drill bits such as HQ or PHD bits. In addition, it cannot be implemented in wet boreholes and has only been tested in shallow depths (Ljunggren et al. 2003). Similar to overcoring, it requires the borehole wall to be elastic to obtain the rock mechanical properties.

2.1.5 Acoustic emission

Acoustic emission is a technique developed from the Kaiser effect which was initially reported by Kaiser (1953). The theory suggested that when the rock is re-stressed to its original stress conditions under uniaxial compression, there is substantial increase in acoustic emission activities which can be detected by sensors. The typical acoustic emission data is shown in Figure 2.10. This indicates the maximum stress that the rock was subjected to underground. To determine the in-situ stress from acoustic emission, a series of experimental and field studies have also been carried out (Kurita and Fujii 1979; Kanagawa et al. 1981; Pestman and Van Munster 1996; Lavrov 2003; Chen et al. 2006).

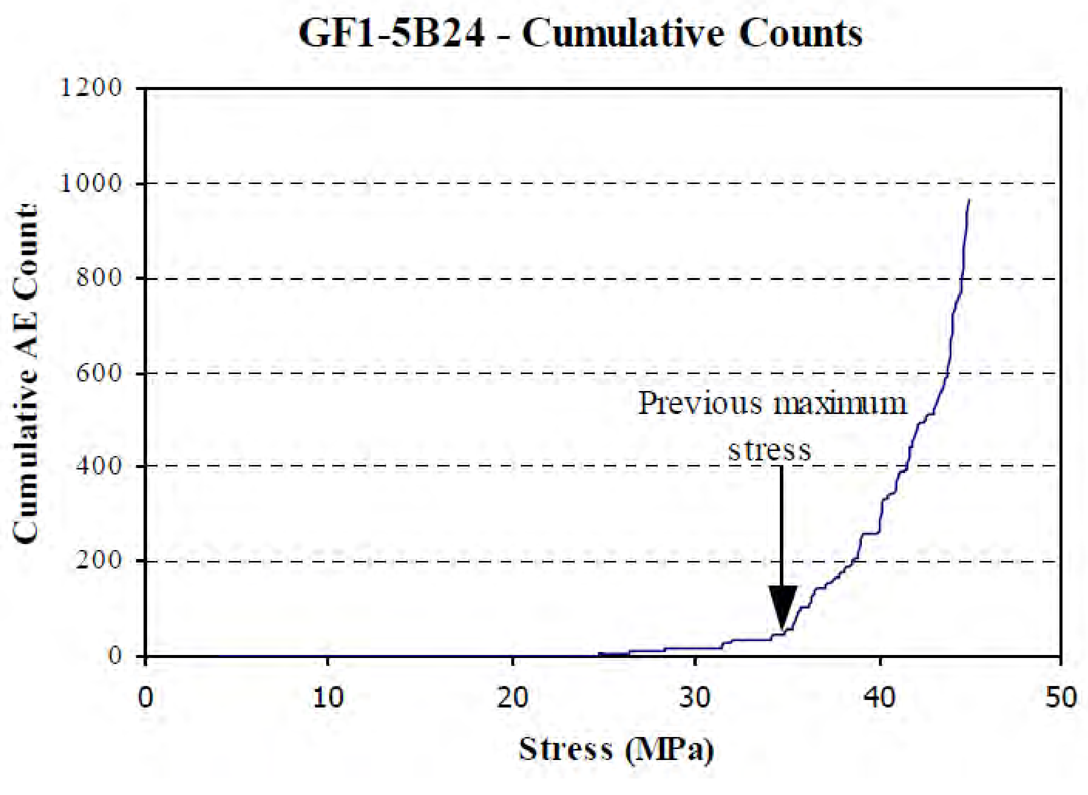

Figure 2.10 Typical acoustic emission cumulative count of core sample vs stress (Villaescusa et al. 2002)

Once the core is attained from the borehole, a secondary core is drilled in the middle of the core to obtain the sample for testing. The laboratory test is conducted on the sample while acoustic emission sensors are attached to the sample for data recording, as shown in Figure 2.11. The critical time at which the rate of acoustic emission significantly increases can be found and thus the corresponding stress (take-off point) can be determined.

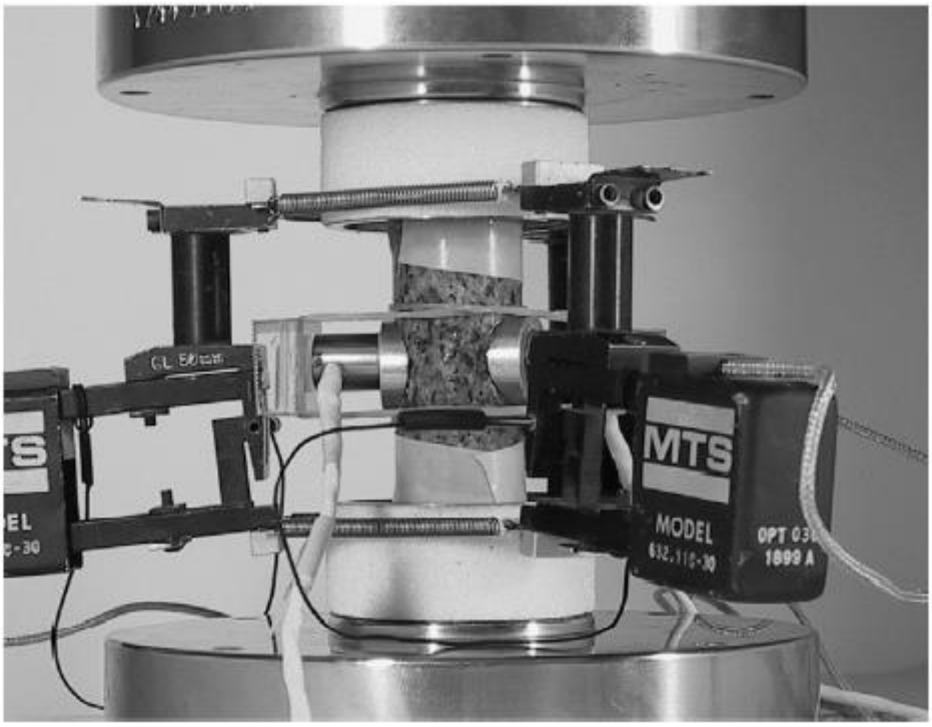

Figure 2.11 Uniaxial compression test with acoustic emission recording (Lehtonen et al. 2012)

The main advantage of this method is that the test is conducted in laboratory conditions, where data is monitored and collected carefully with high precision. Conducting measurement in the field also avoids field based borehole drilling errors in overcoring (Lehtonen et al. 2012). Conducting the measurement in the laboratory is also time-saving, as multiple measurements can be made within one day. As the measurement only requires the secondary core, the primary core can also be used for other purposes, including sampling.

Although some researchers have reported stress estimation from this approach was in line with the results from experiments and field measurements (Yamshchikov et al. 1991; Pestman and Van Munster 1996; Seto et al. 1997; Villaescusa et al. 2002; Lehtonen et al. 2012), the application of this technique is still limited. This is because the explicit relationship between acoustic emission and in-situ stress magnitudes is not justifiable. Thereby, the critical time of the change in acoustic emission is not a precisely definable point, so that numerous tests may be required to optimise the stress result. Since a number of laboratory tests need to be conducted to determine in-situ stress, it is essential to have coring samples with good conditions, i.e. elastic and undamaged. These conditions are generally difficult to obtain in weak rock strata under high stress, particularly in deep locations.

2.1.6 Flat jack

Flat jack is a cost effective method conducted at the surface of the excavation. It was developed in the 1950s by Mayer et al. (1951) and Tincelin (1951) for rock mechanics application and then adapted for structural engineering in the early 1980s (Gregorczyk and Lourenço 2000). The concept is to calculate the stress based on the pressurisation of a flat jack in a slot. Two points, A and B, are selected and measured continuously by strain gauges, followed by a nearby slot cutting. Afterwards, a flat jack is inserted into the slot and pressurised until the distance between A and B is back to the original distance. The pressure at this point, the cancellation pressure, is assumed to be the average normal stress across the slot. Based on the normal stresses acquired from numerous tests, the in-situ stress field can be interpreted. A simple illustration is shown in Figure 2.12.

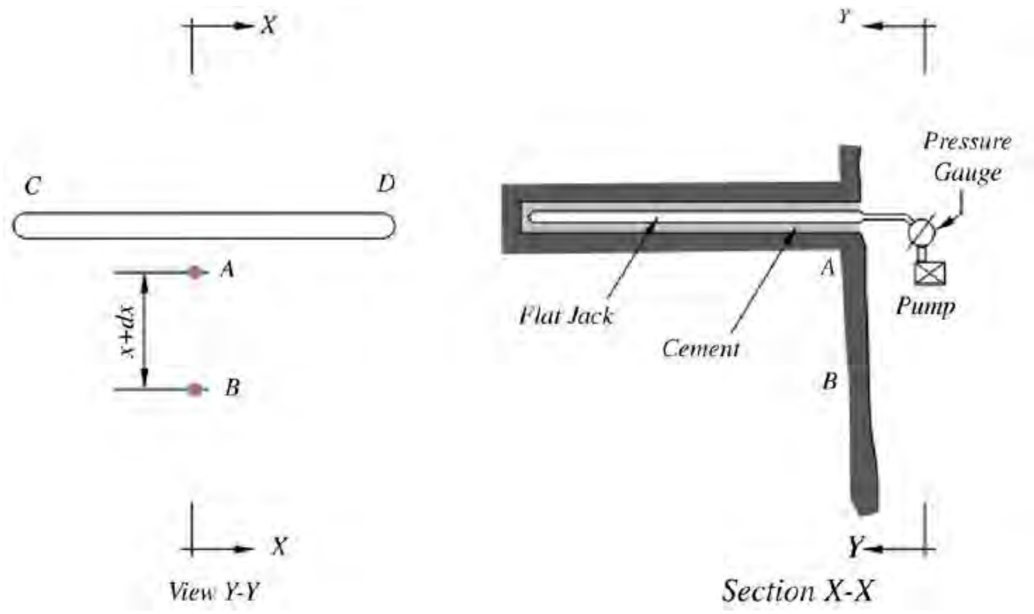

Figure 2.12 Flat jack (Fairhurst 2003)

The flat jack method is simple, cheap and easy to carry out which rock information is not required. It is commonly used in large rock mass and measures the in-situ stress magnitudes with the nearby discontinuities (Li and Cornet 2004), which is more representative than laboratory testing (Vogler et al. 1976; Faiella et al. 1983; KIM 1993; Rao 1998). It has been successfully implemented in deep mining operations by performing a flat jack on the rib (Ageton 1967). Other than measuring stress magnitudes, flat jack can also be used to calculate the in-situ rock deformation modulus (Li and Cornet 2004; Hoek and Diederichs 2006; Kavur et al. 2015).

Flat jack is only applicable at the surface of the excavation, where the stress is concentrated and likely to induce fracture, which may lead to unreliable estimation of stress. This also limits this technique in measuring stress in exploration boreholes and rock strata with some distance over and below the excavation. To overcome these limitations, Jaeger and Cook (1964) introduced a modified flat jack which attempted to extend the measurement to 7 m distance from the rock surface. Due to the practical and technical difficulties, this method was not successful and abandoned (Fairhurst 2003).

2.1.7 Summary

Reviewing popular in-situ stress measurement techniques including their advantages and disadvantages shows that hydraulic fracturing is the most suitable method in petroleum or hard rock conditions, where the vertical stress is usually not the least principal stress, whereas overcoring is widely used in the coal mining industry due to its applicability and reliability. However, most methods need the borehole conditions to be elastic and require rock information from cored samples. These conditions are generally difficult to obtain in weak strata where stress is high, especially at deep mining depths. To overcome the limitations of these methods as mining operations are getting increasingly deeper, there is a need to develop a new stress measurement technique.

Borehole breakout is a drilling induced phenomenon which occurs due to stress concentration. It has been argued this phenomenon can be used for horizontal stress estimation (Zoback et al. 1985; Barton et al. 1988; Zoback et al. 2003). In Australia, every borehole drilled has to be geologically and geophysically logged, which means associated breakout information is easily accessible at no cost. The formation mechanism also means it is suitable for high stress and weak strata conditions as it is not constrained by the depth of measurement and does not induce any damage to the borehole, which is advantageous compared to other methods. As breakout can occur at multiple layers, a stress profile along depths can also be extracted if a reliable estimation technique is available. Hence, there is the possibility of predicting horizontal stress magnitudes from borehole breakout data.

The next section reviews borehole breakout and its potential for horizontal stress estimation.

2.2 REVIEW OF BOREHOLE BREAKOUT

Drilling a borehole into a rock mass can disturb the in-situ stress field and re-distribute the stresses around the borehole. According to the Kirsch solution (Kirsch 1898; Jaeger et al. 2009), the maximum stress concentration for a vertical borehole occurs along the minimum horizontal principal stress (σ_h) direction and gradually decreases towards the maximum horizontal principal stress (σ_H) direction. If the horizontal stress magnitudes are high, such that the rock strength is not sufficiently strong to withstand the stress concentration, rock failures will take place around the borehole. The fractures will propagate along the minimum horizontal principal stress direction and eventually result in symmetrical V-shaped void spaces (Gough and Bell 1982; Zoback et al. 1985; Zheng et al. 1989 Haimson and Song 1995), as shown in Figure 2.13.

This phenomenon was reported by Cox (1970), who observed the elongation in the borehole diameter in Alberta wells using a four-armed dipmeter. Since the 1960s, borehole scanning techniques have advanced significantly and have been widely implemented in the petroleum and mining industries (Zemanek et al. 1969; Nelson et al. 2005; Fowler and Weir 2007; Yaghoubi and Zeinali 2009; Chang et al. 2010; Molaghab et al. 2017). This has enabled more detailed and accurate interpretation of borehole conditions and breakout shapes compared to results obtained from dipmeters or callipers. Borehole breakout has been used as a reliable indicator of horizontal stress orientations in sub-vertical boreholes due to its depth alignment with the minimum horizontal stress direction (Stock et al. 1985; Zoback et al. 2003; Lin et al. 2010; Ask et al. 2015; Malinverno et al. 2016).

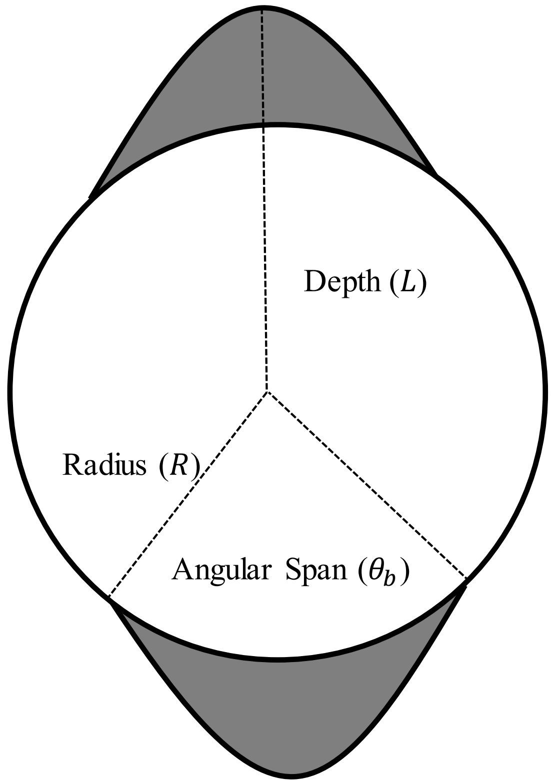

Figure 2.13 Borehole breakout and its geometries

As illustrated in Figure 2.13, a borehole breakout has two geometries: depth (L) and angular span (θ_b). Many researchers have suggested that both geometries are dependent on horizontal stress magnitudes (Zoback et al. 1985; Haimson and Herrick 1986; Barton et al. 1988; Haimson and Herrick 1989; Haimson et al. 1991; Haimson and Song 1993; Herrick and Haimson 1994; Haimson and Lee 2004; Lee and Haimson 2006; Lee et al. 2016; Sahara et al. 2017). Although a significant body of research has been conducted in the field, there is no universally accepted method for horizontal stress estimation from breakout geometries.

To identify the research gap and estimate horizontal stress magnitudes from borehole breakout, breakout shapes, formation mechanisms, experimental findings and existing constitutive modelling are reviewed.

2.2.1 Breakout shape

Although a V-shaped breakout is the most common breakout type, two other types of breakout shapes are observed in the laboratory: fracture-like and spiral-shaped breakout. These three breakout categories are used to review borehole breakout.

2.2.1.1 V-shaped breakout

A V-shaped breakout or 'dog ear' shaped breakout, the first type of breakout discovered by researchers, is the most common breakout shape appearing in the field as well as in laboratories. It was initially found in a series of sedimentary lithology from Devonian to Cretaceous, in Alberta, Canada, where boreholes had resembled elongations in different wells. A typical cross sectional view of a V-shaped breakout is shown in Figure 2.13.

2.2.1.1.1 Breakout formation mechanism

Babcock (1978) named this phenomenon 'borehole breakout' and observed that the direction of maximum breakout elongation is consistent within the region regardless of depth of lithology. Based on the field observation, Babcock (1978) also argued that the formation of breakouts was due to the pre-existing joints encountered by drilling bits, since orientations of both breakouts as well as joints were at similar angles. Schafer (1979) reached the same conclusion from field observation at Austin Chalk, Texas. The limitation of Babcock (1978) was discussed by Bell and Gough (1979), as the proposed mechanism cannot explain the non-parallelism between breakouts and other equally prominent joint sets. Based on stress analysis around the borehole using the Kirsch solution (Kirsch 1898), Bell and Gough (1979) suggested breakout formation was due to the stress concentration rather than pre-existing joint sets, in the location where the in-situ stress field has large horizontal stress magnitudes. This theory was further extended by Gough and Bell (1981), who advocated that breakout may infer the horizontal stress orientation, which has since been used extensively (Stock et al. 1985; Qian and Pedersen 1991; Amato et al. 1995; Zoback et al. 2003; Li et al. 2018). In addition, Gough and Bell (1981) reported time-dependency behaviour of borehole breakouts in a few Canadian wells, with some breakouts propagated along the minimum horizontal stress direction. The time-dependency of breakout geometries was later investigated by numerous researchers (Mastin 1984; Kessels 1989; Zheng et al. 1989; Schoenball et al. 2014).

Gough and Bell (1982) attempted to explain the breakout formation through the Mohr–Coulomb failure criterion, with the mechanism suggesting that breakout initiates at the wall and forms a set of shear fractures towards the minimum horizontal stress direction. Shear fractures eventually meet at an intersection and the distance from this intersection to the borehole wall is the breakout depth, see Figure 2.14. This hypothesis has been observed in numerous experimental studies (Guenot 1990; Haimson and Song 1993; Cuss et al. 2003).

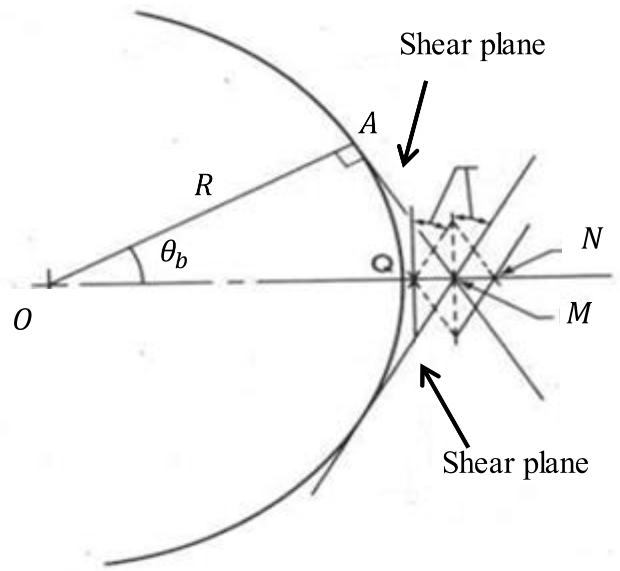

Figure 2.14 Breakout depth after Gough and Bell (1982)

The theory suggested that the angular span is governed by the friction angle (ϕ), such that breakout depth and line OA forms a right angle; breakout depth can therefore be calculated in terms of angular span and borehole radius:

$$\boldsymbol{L = R\sec(\theta_b)} \tag{2.13}$$

As discussed by Gough and Bell (1982), breakout depth developed under this concept generally should be less than 1.08–1.1 times the borehole radius, which did not fully represent field observations.

Based on Gough and Bell (1982), Zoback et al. (1985) also argued that breakout is a result of compressive shear failure. The study proposed a constitutive relationship from the Kirsch solution and Mohr–Coulomb failure criterion, and reported 'flat-bottomed' shaped borehole breakouts in the field, see Figure 2.15. It was also suggested that this 'flat-bottomed' breakout is the initial shape at breakout formation, whereas a V-shaped breakout is the subsequent propagation due to either inelastic deformation or time-dependency behaviour.

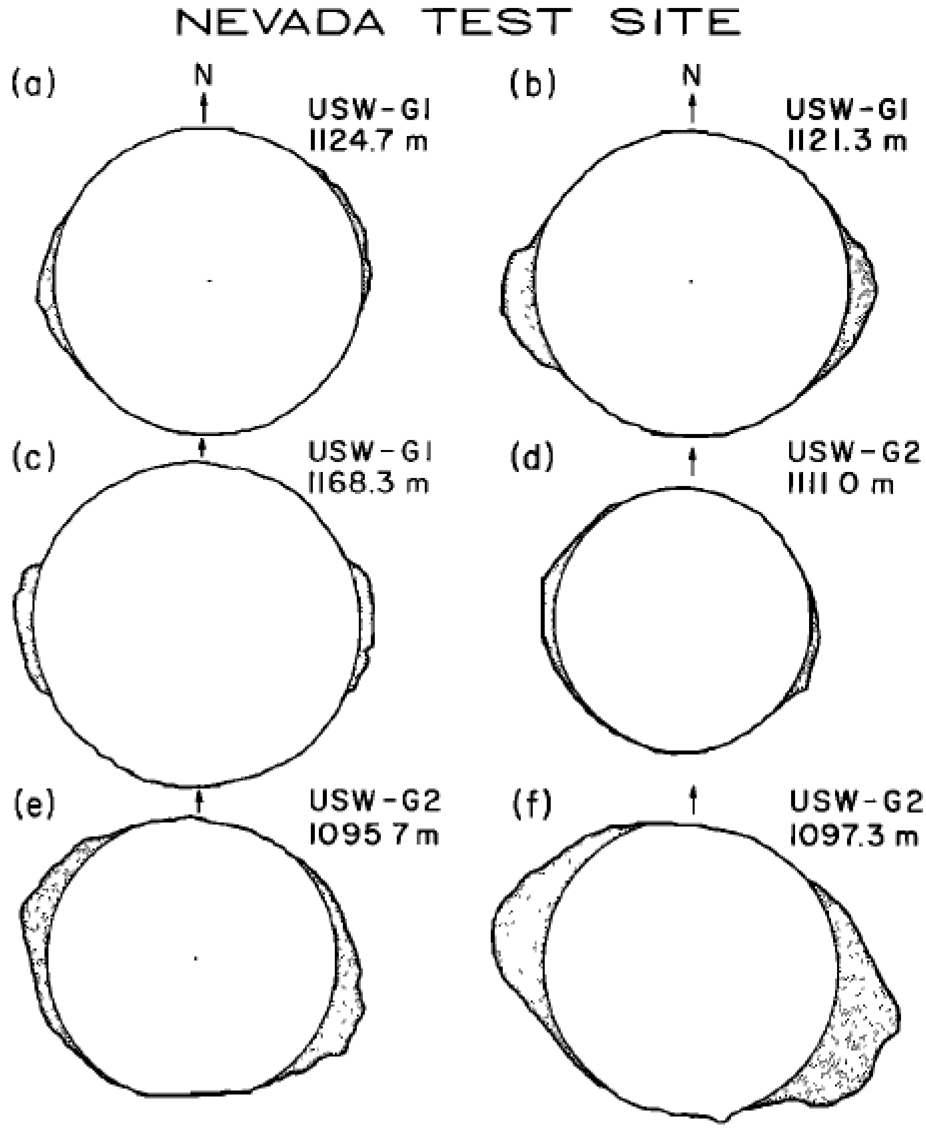

Figure 2.15 'Flat-bottomed' borehole breakouts (Zoback et al. 1985)

Another failure mode proposed by researchers is tensile spalling (Mastin 1984; Zheng et al. 1989; Bažant et al. 1993). The theory suggested that breakout is initiated by extensile splitting near the borehole that is parallel to the maximum horizontal stress direction. Following the sequential rock spalling and slabbing outwards from the borehole, the void zone eventually leads to a pointed V-shaped breakout (Lee and Haimson 1993). An illustration is shown in Figure 2.16.

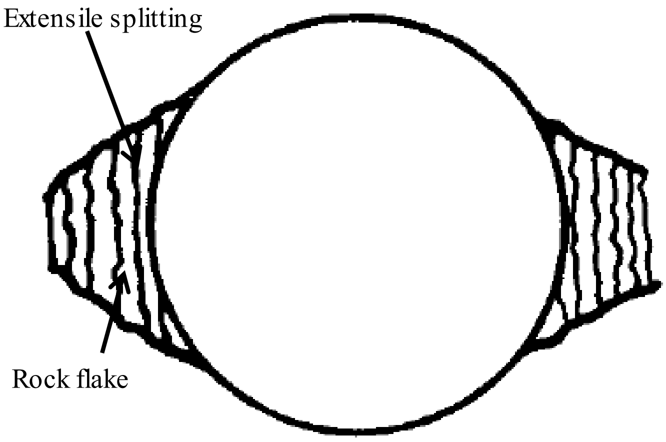

Figure 2.16 Extensile splitting of borehole breakout after Bažant et al. (1993)

A series of researchers have attempted to explain the tensile spalling of rock under a high compressive stress zone. Based on uniaxial compressive tests conducted on sandstone, Gallagher Jr et al. (1974) addressed the phenomenon from the grain level. They suspected that under the uniaxial compressive test, each grain is loaded similarly to the Brazilian test, such that grains will split along the direction and form a tensile fracture. In the vicinity of the borehole, rock can also be considered to be under a uniaxial compressive condition since the tangential stress is high and radial stress is negligible. This enables arrays of grains splitting that are parallel to the maximum horizontal stress direction, where an individual grain is split parallel to the minimum horizontal stress direction. The grain-splitting concept was observed and supported by Haimson and Herrick (1986) from their laboratory investigation. Freudenthal (1977) provided another explanation of extensile splitting based on shear dilatancy caused in high compressibility and low shear modulus rock. Under high shear stress around the borehole, shear dilatancy may produce radial tensile stress, which leads to tensile fracture in the region.

At the same time, a pressure-dependent elastic model was introduced by Santarelli et al. (1986). The model postulated that due to the change in Young's modulus with confinement, breakout initiation should occur at some distance from the borehole wall rather than at the borehole wall. Santarelli and Brown (1989) later extended this model by considering the micro-cracking model proposed by Zaitsev (1985) to represent two failure modes. The study stated that, depending on the toughness of the micro-structure, micro-cracking can either occur across grains and the matrix (intragranular cracking) or solely along the matrix (intergranular cracking). If intragranular cracking takes place given the toughness of grains and matrix are similar, the coalescence of micro-fractures will result in extensile splitting. On the other hand, if the toughness of the matrix is lower than that of the grain, the intersections between intergranular cracks will lead to shear fractures at the macro-scale. Figure 2.17 illustrates the different failure types due to micro-fractures. This model has been examined and supported by a series of experimental and numerical studies (Haimson and Song 1993; Lee and Haimson 1993; Haimson and Lee 2004; Lee et al. 2016). In addition, Van den Hoek (2001) used bifurcation theory to explain the fracture mode preference between tensile spalling and shear failure and concluded that tensile failure is favoured in stronger and more dilatant rock with larger boreholes, whereas weak and non-dilatant rock with a smaller borehole is prone to shear failure.

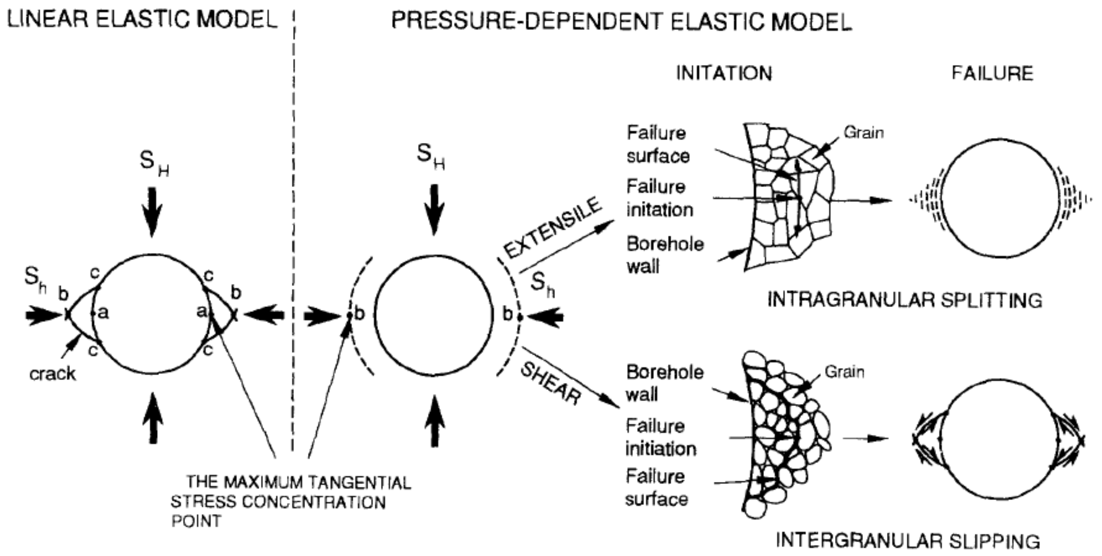

Figure 2.17 Linear elastic model vs pressure-dependent elastic model on borehole breakout (Haimson and Song 1993)

Another failure mechanism was reported by Haimson and Herrick (1986) in their experimental study, which found that breakout formation was a combination of tensile and shear failures in Indiana limestone. Based on the thin section analysis, it was revealed that tensile rupture occurred in the vicinity of the borehole that was sub-parallel to the maximum horizontal stress direction, followed by the rock slabbing as a result of shear failure. This phenomenon has also been observed in other studies (Shen et al. 2002; Cuss et al. 2003; Haimson 2007).

2.2.1.1.2 Laboratory studies on breakout geometries and horizontal stress magnitudes

Since the 1980s, a significant body of experimental studies on borehole breakout and its relationship with horizontal stress magnitudes have been conducted, particularly at the University of Wisconsin (Haimson and Herrick 1986; Haimson and Herrick 1989; Haimson et al. 1991; Herrick and Haimson 1994; Haimson and Lee 2004; Lee and Haimson 2006; Lee et al. 2016).

Haimson and Herrick (1986) conducted true triaxial tests on Indiana limestone and confirmed that borehole breakouts are symmetrical in opposite zones of the borehole along the minimum horizontal stress direction. Based on various horizontal stress combinations, Haimson and Herrick (1986) also advised that both the breakout depth and angular span are directly proportional to horizontal stress magnitudes, so that it is possible to derive horizontal stress from breakout data. Findings were further supported by the experimental results obtained on Indiana limestone and Alabama limestone from Haimson and Herrick (1989).

While the previous experiments used pre-drilled rock specimens with subsequent triaxial loading, Haimson et al. (1991) upgraded the experimental apparatus so that drilling could be conducted during triaxial loading. Although results also suggested that both breakout geometries are stress-dependent, Haimson et al. (1991) suspected that there is a unique relationship between breakout depth and angular span, which may be insensitive to horizontal stress magnitudes, see Figure 2.18. Results indicated that it might not be feasible to determine two horizontal stress magnitudes solely from breakout geometries. This observation has also been reported by a number of researchers, which all suggested it is not viable to estimate both horizontal stress magnitudes solely from breakout data (Herrick and Haimson 1994; Haimson and Lee 2004; Lee and Haimson 2006; Sahara et al. 2017).

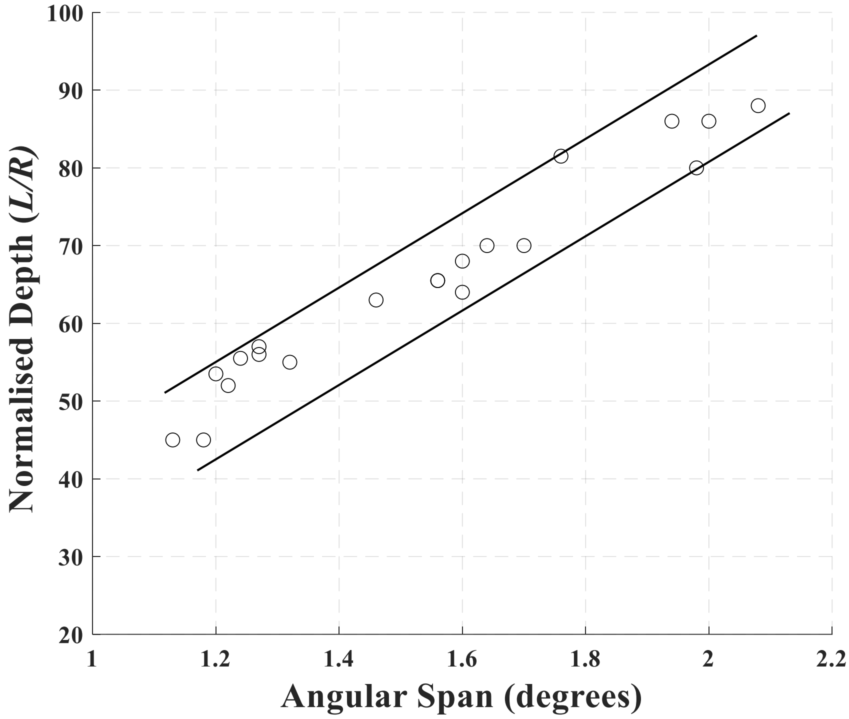

Figure 2.18 The relationship between breakout angular span and depth after Haimson et al. (1991)

Haimson and Lee (2004) and Lee and Haimson (2006) conducted experiments on Tablerock sandstone and Tenino sandstone. Results revealed that the increasing maximum horizontal stress will always result in deeper and wider breakout under constant minimum horizontal and vertical principal stresses. The study also showed the importance of the horizontal stress ratio, in which the rates increase in breakout geometries with higher minimum horizontal and vertical stresses, see Figure 2.19. The implication here is that breakout geometries are also influenced by other two principal stresses. With the implementation of acoustic emission, Haimson and Kovacich (2003) and Haimson and Lee (2004) were able to monitor breakout development and stabilisation throughout the experimental process and determine the appropriate stop time for each test. Lee et al. (2016) later used scanning electron microscope (SEM) equipment with backscattered scanning electrons (BSE) to observe the micro-cracking mechanism of breakouts generated in Tablerock and Tenino sandstones. The investigation pointed out that although breakout shapes under the two series of experiments were the same (V-shaped breakouts), the micro-cracking modes were vastly different. Tablerock sandstone showed intra- and transgranular micro-cracks, whereas Tenino sandstone had intergranular cracks. The numerical simulation by Lee et al. (2016) also verified the observations.

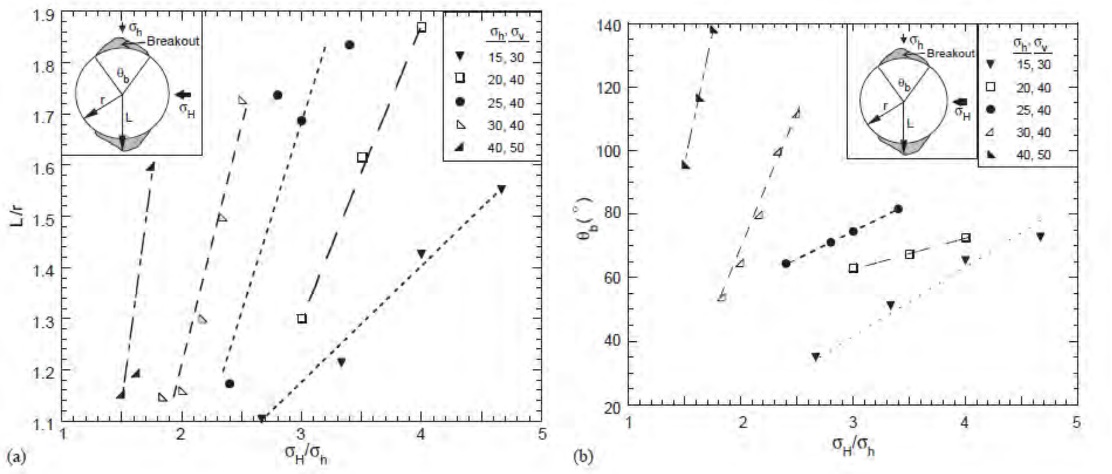

Figure 2.19 Relationships between breakout geometries and horizontal stress ratio (Haimson and Lee 2004)

2.2.1.2 Fracture-like breakout

Haimson and Song (1998) conducted breakout tests on high porosity (22.5%) Berea sandstone and found a distinctive breakout shape. This 'fracture-like' breakout appeared in a narrow slot orthogonal to the maximum horizontal stress direction with constant width from the borehole to the breakout tip, see Figure 2.20. Haimson and Song (1998) suspected that this was due to the weak bonding material (matrix) between quartzitic grains, as indicated by the high porosity. Under high anisotropic horizontal stress conditions, quartz grains are deboned and spall off. This redistributes stress concentration behind the breakout area and leads to progressive breakout failure, and eventually forms fracture-like breakout.

Olsson (1999) suggested that this fracture-like breakout might be due to the empty compaction band where grains were washed away by circulating drilling fluid. The compaction band was first found by Mollema and Antonellini (1996) in Navajo sandstone, where the rock was subjected to pure compaction but zero offset or shear, with substantial porosity deduction. Haimson (2001) used micro-graphs to analyse the results in Berea sandstone and discovered the compaction band ahead of the breakout tip, where a narrow layer of grains was compacted with fewer spaces in-between compared to grains in other locations. The fracture-like breakout formation mechanism from the compaction band has been supported by numerous studies (Katsman et al. 2009; Katsman and Haimson 2011; Rahmati et al. 2019; Wang et al. 2020).

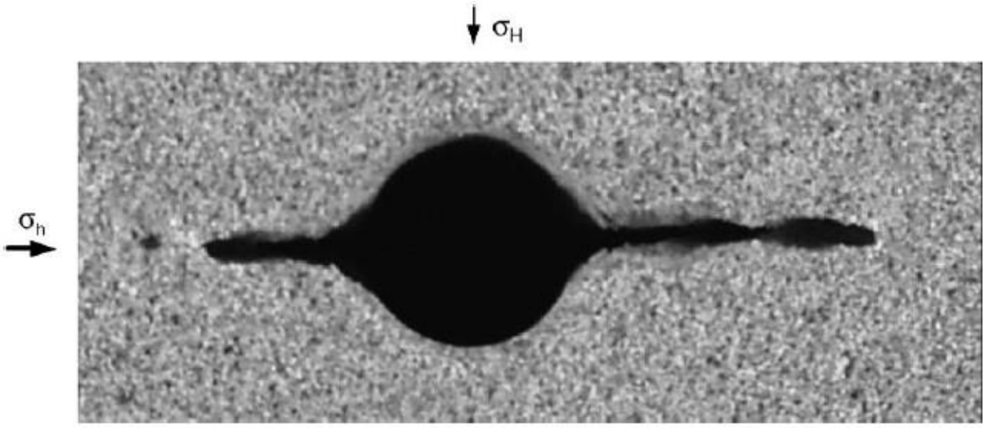

Figure 2.20 Fracture-like breakout (Haimson and Kovacich 2003)

As V-shaped breakout had been investigated extensively under experimental conditions, Haimson and Kovacich (2003) conducted a parametric study on fracture-like breakout, including horizontal stress conditions and borehole radius etc. Similar to V-shaped breakout, experimental results revealed that the fracture-like breakout depth is strongly dependent on horizontal stress magnitudes. The increasing maximum horizontal stress always led to deeper breakout depth, providing constant minimum and vertical stresses. The finding showed it can be indicative of horizontal stress magnitudes (Haimson and Lee 2004; Lee and Haimson 2006). Unlike breakout depth, breakout angular span was relatively constant (3.3 ± 0.3 mm) and insensitive to the change in horizontal stress magnitudes, confirming that the phenomenon is due to the compaction band. The study also showed that the larger borehole radius resulted in longer normalised breakout while the drilling rate and fluid rate had no effect on breakout geometries.

Haimson and Lee (2004) reported a different behaviour of breakout angular span under various horizontal stress magnitudes. Rather than a constant angle, the angular span varied between 15–45° and approached a consistent angle (15–25°) under a higher horizontal stress ratio. In addition, due to the narrow angular span range, Haimson and Lee (2004) suggested that it was not possible to determine a clear relationship between angular span and in-situ stress.

2.2.1.3 Spiral-shaped breakout

Haimson and Song (1993) reported another breakout shape under uniform horizontal stress ($\sigma_H = \sigma_h$) in Cordova Cream limestone. Under this condition, fractures initiated around the borehole surface and extended along high shear stress lines outwards; followed by the inwards cracking back to the borehole, shown as a ‘spiral fracture path’, see Figure 2.21a. Figure 2.21b shows the final breakout shape from the experiment, with randomly distributed breakouts along the borehole exhibiting no obvious bedding effect. Haimson (2007) later found that under uniform horizontal stress, three breakouts were generated around the borehole in Cordova Cream limestone which were approximately 120° apart and St Meinrad sandstone, as shown in Figure 2.22a. This breakout shape was very similar to the shapes observed in Haimson and Song (1993) (Figure 2.21b), which were classified as the same breakout shape.

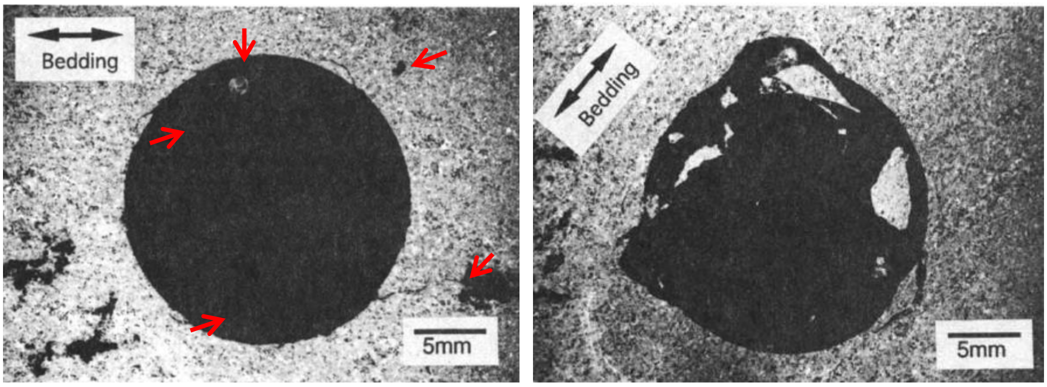

a b

Figure 2.21 a) Breakout initiation under uniform horizontal stresses = 30 MPa; b) breakout generated under uniform horizontal stresses = 40 MPa; after Haimson and Song (1993)

Based on a series of hollow cylinder tests (uniform horizontal stress), Van den Hoek (2001) noticed a ‘spiral-shaped’ breakout in weak artificial sandstone. The early formation of fractures was similar to that in Haimson and Song (1993) and Haimson (2007), where cracks spiralled outwards with shear banding from the borehole. However, the individual fracture line did not extend inwards at the later stage of breakout development and eventually stabilised with spring lines near the borehole, as illustrated in Figure 2.22b. In addition, the high confinement pressure applied would cause borehole closure (Van den Hoek 2001; Meier et al. 2013).

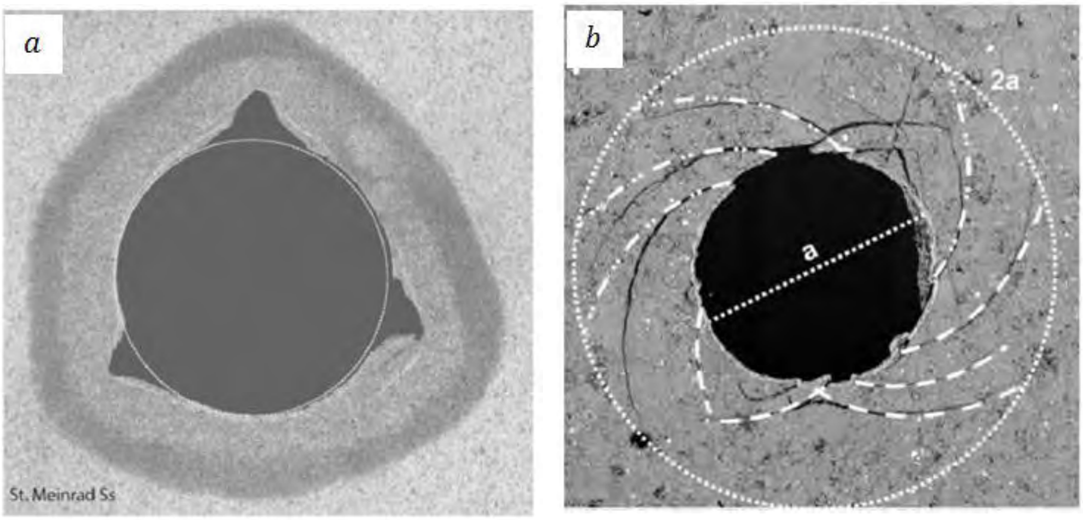

Figure 2.22 a) Three randomly distributed breakouts generated under uniform horizontal stress (Haimson 2007); b) spiral shaped breakout (Meier et al. 2013)

Crook et al. (2003) argued that both breakouts in Figure 2.22 can be considered a spiral-shaped breakout as the fracture mechanisms are essentially the same under uniform horizontal stress. Based on the simulation results, the study suggested that the different shapes were due to the ratio between specimen radius to borehole radius. A higher ratio (10:1) would lead to 'spiral-lines' (spiral-shape 2), whereas the former shape (spiral-shape 1) was a result of a lower ratio (3:1). Another explanation was provided by Meier et al. (2013), who suggested that the fracture line (shear band) was governed by the frictional coefficient, see Figure 2.23. A higher frictional coefficient would result in the shear plane moving close to the borehole and forming spiral-shape 1, while a lower frictional coefficient would cause a wider angle between the shear plane and borehole and induce spiral-shape 2.

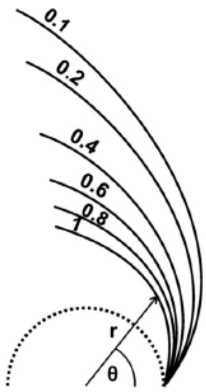

Figure 2.23 Frictional coefficient controlled fracture plane (Meier et al. 2013)

Recently, Duan and Kwok (2016) were able to reproduce both spiral-shaped breakouts using a discrete element model with the same synthetic rock, see Figure 2.24. The only difference between the two breakouts in the numerical model was particle size distribution; and this parameter had negligible influence on rock mechanical properties based on a comparative analysis. Simulation results show that spiral-shape 1 was due to particle size heterogeneity (maximum to minimum particle size ratio = 1.8) and spiral-shape 2 can be produced by more uniform particle size (maximum to minimum particle size ratio = 1.4).

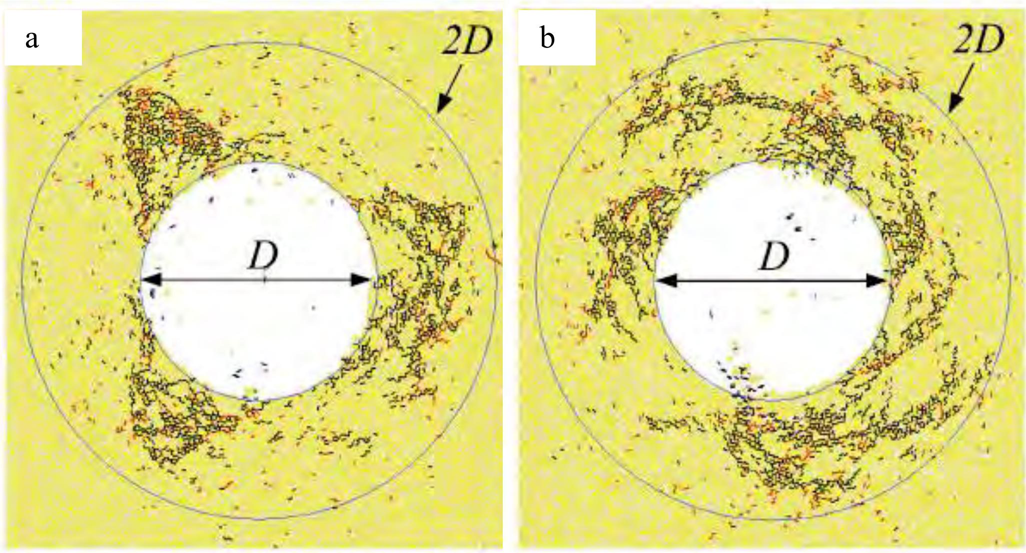

Figure 2.24 a) maximum to minimum particle size ratio = 1.4; b) maximum to minimum particle size ratio = 1.8 (Duan and Kwok 2016)

Figure 2.25 shows the stress analysis around the borehole wall, indicating that the heterogeneous model has more tangential stress fluctuation compared to the uniform model. Such fluctuation can induce crack localisation and create spiral-shape 1 under uniform horizontal stress conditions. Nevertheless, the spiral-shaped breakout formation requires uniform horizontal stress conditions, which generally will not be encountered in the field condition. It is difficult to derive meaningful horizontal stress information due to the randomness of the breakout shape.

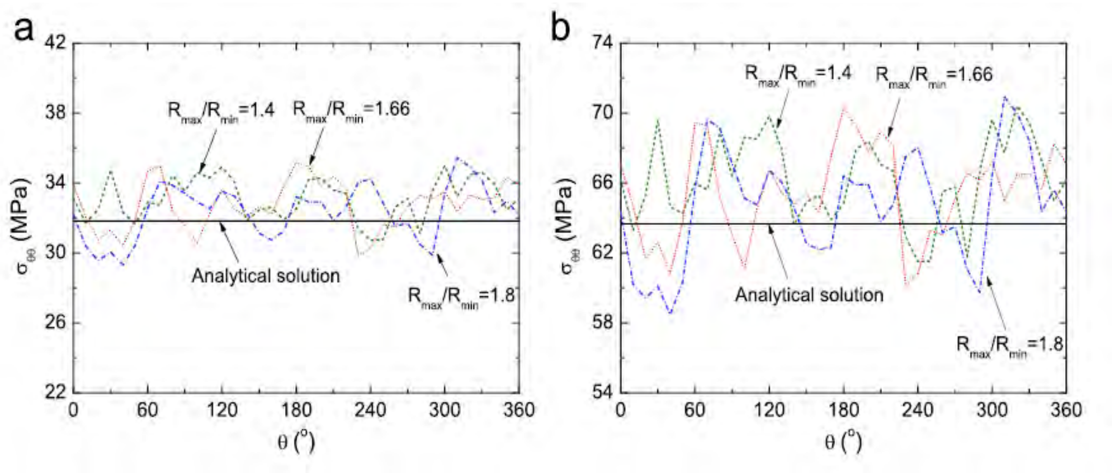

Figure 2.25 Tangential stress around the borehole at different angles with various particle size models: a) horizontal stress magnitudes = 20 MPa; b) horizontal stress magnitudes = 40 MPa (Duan and Kwok 2016)

2.2.2 Existing constitutive models for horizontal stress estimation from borehole breakout

Determining horizontal stress magnitudes from borehole breakout geometries (V-shaped breakout) is an important topic in rock engineering that has been investigated in the past four decades. However, there has not yet been a universally accepted method. This section reviews the existing approaches of horizontal stress estimation from borehole breakout.

2.2.2.1 Mohr–Coulomb

As briefly discussed in Section 2.2.1.1, Zoback et al. (1985) was a pioneering study which attempted to determine horizontal stress magnitudes from breakout geometries. The study calculated stress magnitudes around the borehole at every point using the Kirsch solution (Kirsch 1898):

$$\boldsymbol{\sigma_\theta} = \frac{1}{2}(\boldsymbol{\sigma_H} + \boldsymbol{\sigma_h})\left(\mathbf{1} + \frac{\boldsymbol{R^2}}{\boldsymbol{r^2}}\right) - \frac{1}{2}(\boldsymbol{\sigma_H} - \boldsymbol{\sigma_h}) \times \left(\mathbf{1} + \mathbf{3}\frac{\boldsymbol{R^4}}{\boldsymbol{r^4}}\right)\boldsymbol{cos2\theta} + \frac{\boldsymbol{\Delta PR^2}}{\boldsymbol{r^2}} \quad (2.14)$$

$$\boldsymbol{\sigma_r} = \frac{1}{2}(\boldsymbol{\sigma_H} + \boldsymbol{\sigma_h})\left(\mathbf{1} - \frac{\boldsymbol{R^2}}{\boldsymbol{r^2}}\right) + \frac{1}{2}(\boldsymbol{\sigma_H} - \boldsymbol{\sigma_h}) \times \left(\mathbf{1} - \mathbf{4}\frac{\boldsymbol{R^2}}{\boldsymbol{r^2}} + \mathbf{3}\frac{\boldsymbol{R^4}}{\boldsymbol{r^4}}\right)\boldsymbol{cos2\theta} + \frac{\boldsymbol{\Delta PR^2}}{\boldsymbol{r^2}} \quad (2.15)$$

$$\tau_{r\theta} = -\frac{1}{2}(\sigma_H + \sigma_h)\left(1 + \frac{R^2}{r^2}\right)\left(1 + 2\frac{R^2}{r^2} - 3\frac{R^4}{r^4}\right) sin2\theta \tag{2.16}$$

where $\tau_{r\theta}$ = tangential shear stress, σ_θ = tangential stress and σ_r = radial stress, R = radius of the borehole, r = distance from the centre of the borehole (L = breakout depth), θ = azimuth measured from the maximum horizontal principal stress direction, as illustrated in Figure 2.26, ΔP = difference between mud pressure and pore pressure (P_0).

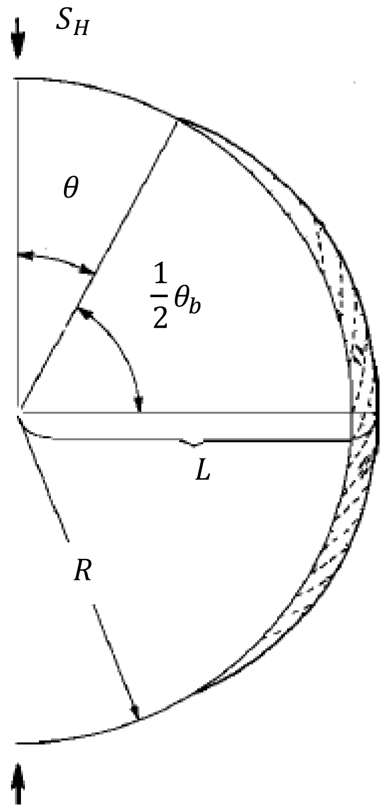

Figure 2.26 Half a borehole breakout after Zoback et al. (1985)

Zoback et al. (1985) then combined the Kirsch solution and Mohr–Coulomb failure criterion to govern the breakout geometries. In other words, the radius of the Mohr circle (R_M) should be equal to the distance from the centre of the Mohr circle to the failure envelope at breakout boundaries, as shown in Figure 2.27.

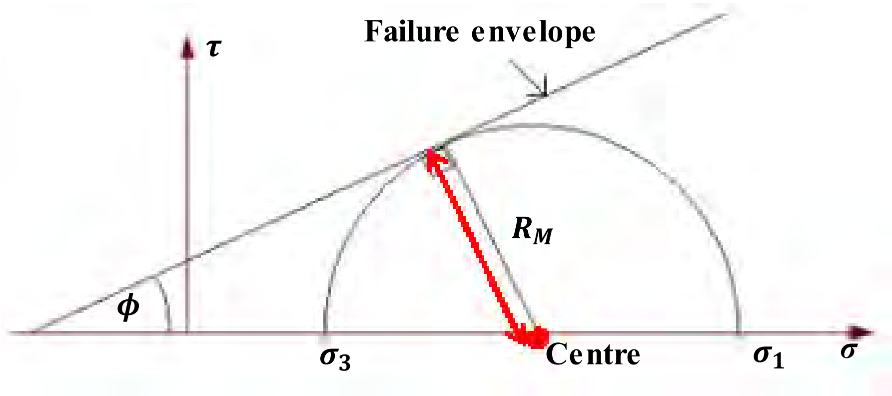

Figure 2.27 Mohr–Coulomb failure criterion after Zoback et al. (1985)

The radius of the Mohr circle can be simply expressed based on the Kirsch solution:

$$[\left(\frac{\sigma_\theta - \sigma_r}{2}\right)^2 + \tau_{r\theta}{}^2]^{\frac{1}{2}} \tag{2.17}$$

whereas the distance from the centre of the Mohr circle to the failure envelope can also be calculated:

$$\frac{\mu \times (\frac{\sigma_\theta + \sigma_r}{2} + \sigma_\theta)}{\sqrt{\mu^2 + 1^2}} \tag{2.18}$$

At the breakout boundary, these two equations should be equalised:

$$[\left(\frac{\sigma_\theta - \sigma_r}{2}\right)^2 + \tau_{r\theta}{}^2]^{\frac{1}{2}} = \frac{\mu \times \frac{\sigma_\theta + \sigma_r}{2} + \tau_0}{\sqrt{\mu^2 + 1^2}} \tag{2.19}$$

in which μ = coefficient of friction, τ_0 = cohesive strength. Assuming the Navier Coulomb failure criterion applies, Eq. (2.19) can be re-expressed as:

$$\tau_0 = (1 + \mu^2)^{1/2}[(\frac{\sigma_\theta - \sigma_r}{2})^2 + \tau_{r\theta}{}^2]^{1/2} - \mu(\frac{\sigma_\theta + \sigma_r}{2}) \tag{2.20}$$

For particular rock strata, the cohesive strength should be the same. Therefore, Eq. (2.20) at breakout depth and angular span (θ_b = 180° - 2θ) should be equal to each other, i.e.

$$\tau_0(R, \theta) = \tau_0(L, \pi/2) \tag{2.21}$$

As the difference between the pore pressure and mud pressure (ΔP) is relatively low, they were neglected during estimation. By substituting Eq. (2.14)–(2.16) into Eq. (2.21), the following relationships can be rearranged:

$$\boldsymbol{\tau_0(R,\theta) = \frac{1}{2}(a\sigma_H + \sigma S_h)} \tag{2.22}$$

$$\boldsymbol{\tau_0(L,\pi/2) = \frac{1}{2}(c\sigma_H + d\sigma_h)} \tag{2.23}$$

where

$$\boldsymbol{a = [(1+\mu^2)^{\frac{1}{2}} - \mu](1 - 2cos2\theta)}$$

$$\boldsymbol{b = [(1+\mu^2)^{\frac{1}{2}} - \mu](1 + 2cos2\theta)}$$

$$\boldsymbol{c = -\mu + (1+\mu^2)^{\frac{1}{2}} - \frac{R^2}{L^2}\left[(1+\mu^2)^{\frac{1}{2}} + 2\mu\right] + \frac{3R^4}{L^4}(1+\mu^2)^{\frac{1}{2}}}$$

$$\boldsymbol{d = -\mu - (1+\mu^2)^{\frac{1}{2}} + \frac{R^2}{L^2}\left[3 \times (1+\mu^2)^{\frac{1}{2}} + 2\mu\right] - \frac{3R^4}{L^4}(1+\mu^2)^{\frac{1}{2}}}$$

Although the above equations seem complex, the only parameters required are breakout geometries, cohesion and the coefficient of friction. By solving simultaneous equations Eq. (2.22) and Eq. (2.23), the horizontal principal stress ratio and magnitudes can be obtained below:

$$\boldsymbol{\sigma_h = 2\tau_0(\frac{a-c}{ad-bc})} \tag{2.24}$$

$$\boldsymbol{\sigma_H = 2\tau_0(\frac{d-b}{ad-bc})} \tag{2.25}$$

$$\boldsymbol{\frac{\sigma_H}{\sigma_h} = \frac{d-b}{a-c}} \tag{2.26}$$

Based on Eq. (2.26), the relationship between horizontal stress ratio and breakout geometries can be graphically presented, as shown in Figure 2.28.

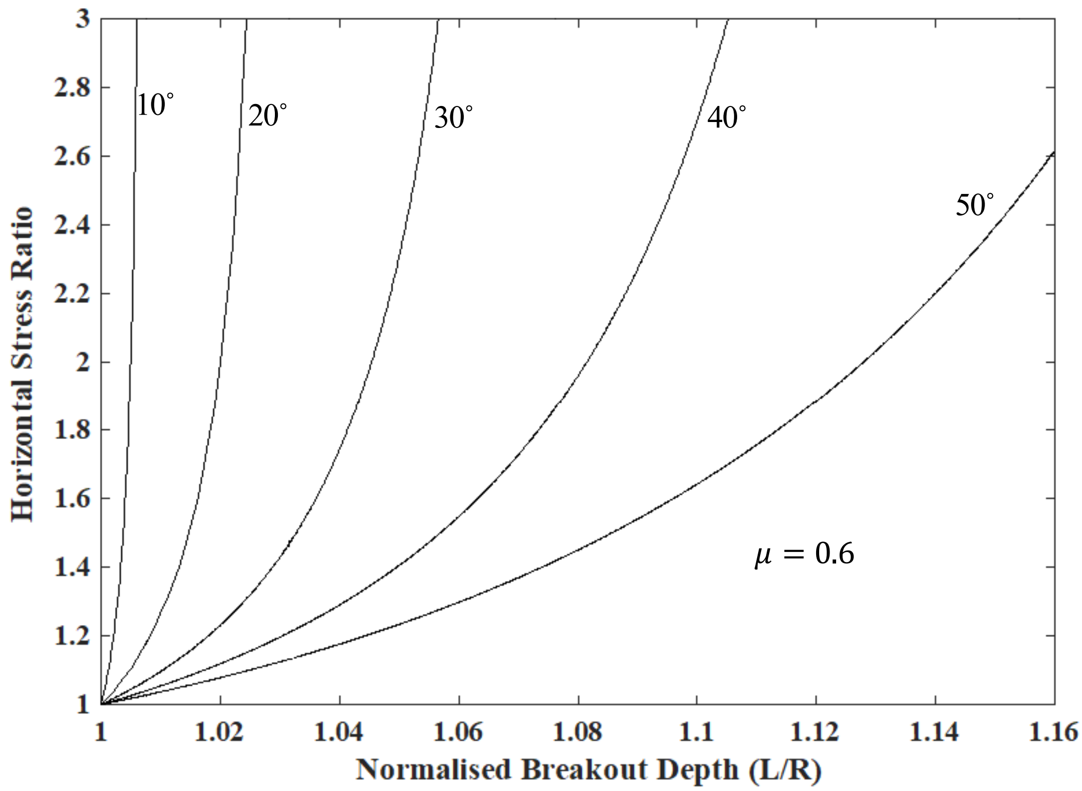

Figure 2.28 Mohr–Coulomb model after Zoback et al. (1985)

As discussed by Zoback et al. (1985), this model was only applicable at the initial stage of breakout, where breakout was 'flat-bottomed' rather than V-shaped. It was also limited to the shear failure mechanism, without considering tensile spalling or a combination of both. Inelastic deformation and time-dependency creeping behaviour may also influence the estimation results (Zoback et al. 1986; Zheng et al. 1989). However, this model built a strong theoretical base for horizontal stress estimation using breakout geometries, which was critical for later model developments.

2.2.2.2 Stress polygon

Since breakout depth involves some uncertainty, Barton et al. (1988) used only breakout angular span to estimate maximum horizontal stress given the minimum horizontal stress (usually from hydraulic fracturing). The model assumed that breakout angular span does not widen after the initial failure as the nearby circumferential stress decreases (Mastin 1984; Zoback et al. 1985), such that the stress conditions at the maximum angle of breakout initiation ($\frac{R}{r} = 1$) can be computed by the Kirsch solution:

$$\boldsymbol{\sigma_r = 0} \tag{2.27}$$

$$\boldsymbol{\sigma_\theta = (\sigma_H + \sigma_h) - 2(\sigma_H - \sigma_h)cos2\theta} \tag{2.28}$$

$$\boldsymbol{\tau_{r\theta} = 0} \tag{2.29}$$

Since the rock along the wall only exerted uniaxial compressive stress, at the breakout angular span, the tangential stress applied should be equal to the uniaxial compressive strength of the rock (UCS), i.e.

$$\boldsymbol{UCS = (\sigma_H + \sigma_h) - 2(\sigma_H - \sigma_h)cos2\theta} \tag{2.30}$$

By rearranging the equation, the maximum horizontal stress can be calculated as follows:

$$\boldsymbol{\sigma_H = \frac{UCS}{(1 - 2cos2\theta)} - \sigma_h \frac{(1 + 2cos2\theta)}{(1 - 2cos2\theta)}} \tag{2.31}$$

This simple and effective approach has been implemented in numerous field cases, although it does not take the vertical stress into consideration (Barton et al. 1988; Brudy 1995; Zoback et al. 2003; Yaghoubi and Zeinali 2009; Nian et al. 2016). It is also the basis of the current stress polygon technique which can constrain horizontal stress magnitudes from breakout angular span and rock information (Vernik and Zoback 1992; Zoback and Healy 1992; Lund and Zoback 1999; Zoback et al. 2003; Chang et al. 2010; Song and Chang 2018). A number of modified versions have been introduced to address the influence of vertical stress. The modifications were achieved by changing the failure criterion which considers the intermediate stress effect, including the Wiebols–Cook (Vernik and Zoback 1992), Nadai (Song and Haimson 1997), Mogi–Coulomb (Song and Haimson 1997; Haimson and Chang 2002) and Modified Wiebols–Cook criterion (Chang et al. 2010).

Based on Anderson’s faulting theory (Anderson 1951), where the frictional strength of a fault is controlled by the state of stress, Zoback et al. (1986) derived the boundary equation of in-situ stress:

$$\boldsymbol{\sigma_1/\sigma_3 = \left[(1 + {\mu_f}^2)^{\frac{1}{2}} + \mu_f\right]^2} \tag{2.32}$$

where σ_1 and σ_3 are the major and minor principal stresses and μ_f = coefficient of friction of the fault, which is usually assumed to be 0.6 (Byerlee 1978); pore pressure was not considered for simplicity. According to different faulting mechanisms, both principal stresses can be either vertical or horizontal. With unknown faulting condition and given vertical principal stress, the horizontal principal stresses at the depth can be governed and constrained within the polygon by Eq. (2.32), as presented in Figure 2.29.

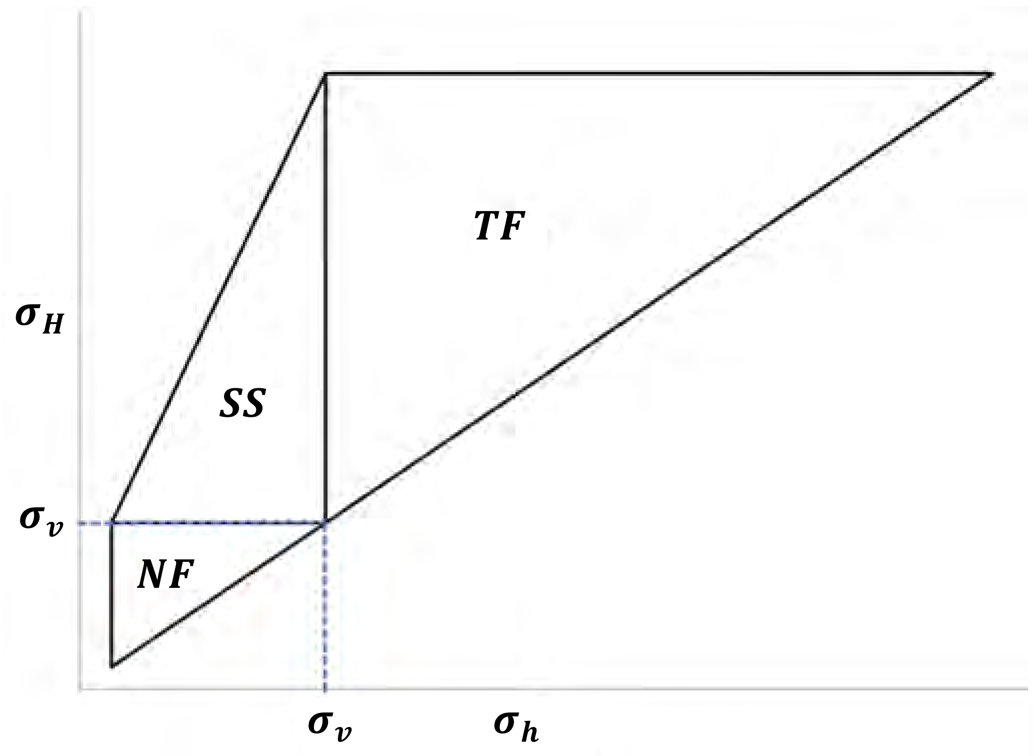

Figure 2.29 Stress conditions under different faulting: NF = normal faulting, SS = strike-slip faulting and TF = reverse faulting after Zoback et al. (1986)

Zoback et al. (2003) combined the approaches from Barton et al. (1988) and Zoback et al. (1986) and provided a 'stress polygon method', see Figure 2.30. As illustrated in the figure, horizontal stresses should always be on the red line (Barton's equation) and match in pairs (e.g. σ_{H1} and σ_{h1}), The highest and lowest values of horizontal stresses are bounded in small regions between σ_{H1} to σ_{H2} and σ_{h1} to σ_{h2} providing the faulting mechanism is reverse faulting. Hence, with appropriate knowledge of rock information and breakout angular span, possible ranges of horizontal stress magnitudes can be estimated.

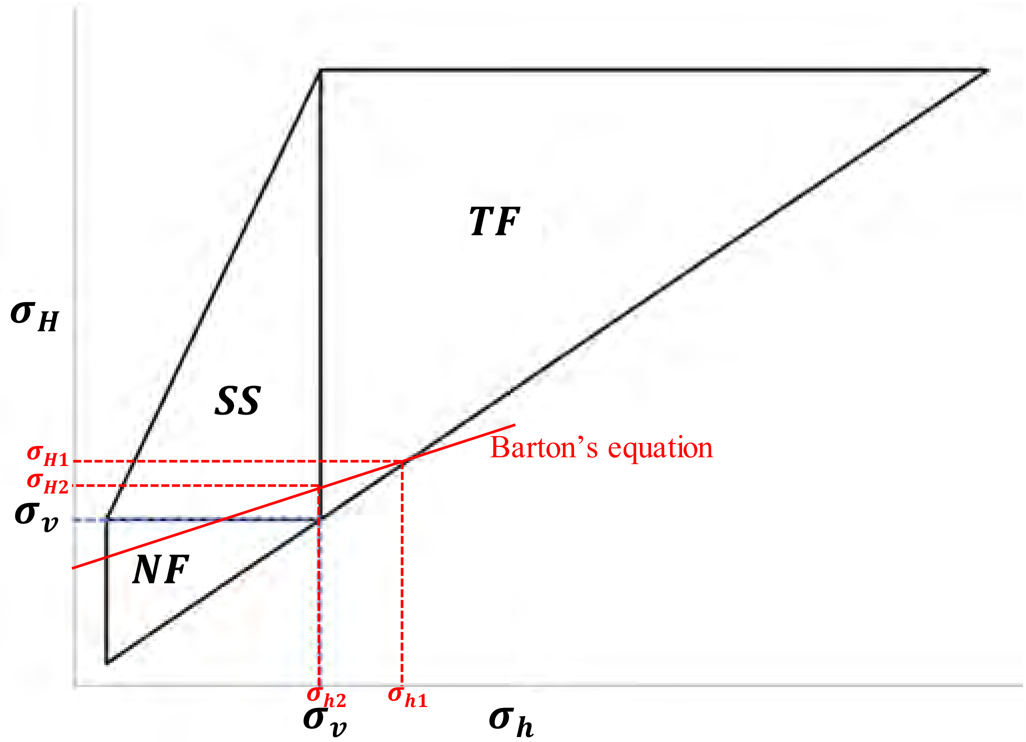

Figure 2.30 Stress polygon example

This stress polygon approach is the most common and reliable technique in determining horizontal stress ranges from borehole breakout. Based on the different breakout governing equations with different failure criteria, as discussed earlier, various versions of stress polygons have also been introduced and applied successfully in the field to constrain horizontal stress magnitudes (Barton et al. 1988; Brudy 1995; Lund and Zoback 1999; Zoback et al. 2003; Chang et al. 2010; Lin 2014; Lee and Ong 2018; Song and Chang 2018).

2.2.3 Borehole size effect

During laboratory investigation of borehole breakout, it was found that the horizontal stress ratio applied to induce breakout can be as high as 18 (Haimson and Herrick 1986; Haimson and Herrick 1989). This does not truly reflect field conditions as the horizontal stress ratios in the field are generally below 3 (Zoback et al. 1985; Walton et al. 2015). A series of experimental studies conducted using normal compression tests and hollow cylinder tests found that the critical stress required for breakout initiation is higher with smaller borehole radius (borehole size), called the borehole size effect (Haimson and Herrick 1989; Carter 1992; Cuss et al. 2003; Papanastasiou and Thiercelin 2010; Dresen et al. 2010; Meier et al. 2013). To quantify the relationship between borehole size and critical stress required for breakout initiation, a review on borehole size effect is presented.

2.2.3.1 Stress averaging

Carter (1992) attempted to explain the borehole size effect by considering the stress averaging concept proposed by Lajtai (1972). Lajtai (1972) postulated that when rock is subject to high stress gradient, stress within the region will be redistributed and averaged over a distance ($2d$) through micro-cracking or plastic deformation (Labuz et al. 1985; Ortiz 1988; Carter et al. 1991), see Figure 2.31. This stress averaging distance is regarded as a material constant which can be determined by data-fitting. Lajtai (1972) calculated the average stress along the fracture length as follows:

$$\boldsymbol{\sigma_d = \sigma_m + d \times (\frac{\partial \sigma}{\partial R})_{R=r}} \quad (2.33)$$

where σ_d = the averaged stress over the distance, σ_m = the maximum tangential stress at the borehole wall, $(\frac{\partial \tau}{\partial R})_{R=r}$ = the stress gradient at the borehole wall and it was assumed to be linear over the distance, $2d$. If the rock failure is in tension, the equation can be expressed as:

$$\boldsymbol{T = \sigma_m + d \times (\frac{\partial \sigma}{\partial R})_{R=r}} \quad (2.34)$$

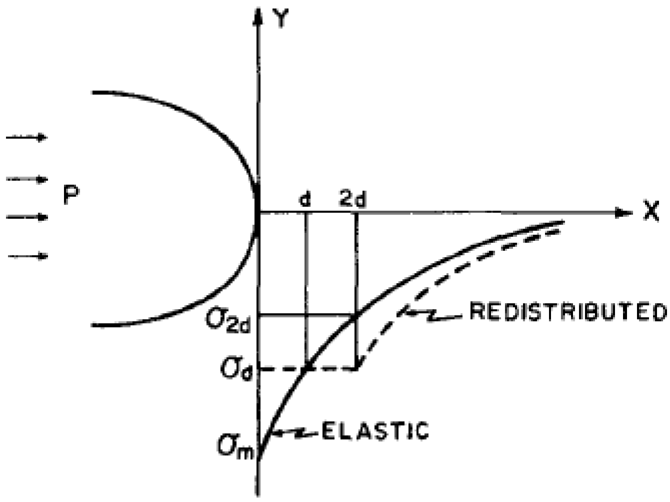

Figure 2.31 Stress averaging over $2d$ (Lajtai 1972)

Considering the fracture at the borehole wall along the maximum horizontal stress direction, which was later discovered to be drilling-induced tensile fractures (Brudy and

Zoback 1999; Zoback et al. 2003; Chang et al. 2010), the stress condition at the location can be represented by the Kirsch solution:

$$\boldsymbol{T} = (\frac{\boldsymbol{5d}}{\boldsymbol{R}} - \boldsymbol{1})\boldsymbol{\sigma_H} + (\boldsymbol{3} - \frac{\boldsymbol{7d}}{\boldsymbol{R}})\boldsymbol{\sigma_h} \tag{2.35}$$

Under a normal compression test (uniaxial compression on block samples), where σ_h = 0, Eq. (2.35) can be rearranged as:

$$\boldsymbol{P_T} = \boldsymbol{\sigma_H} = \frac{\boldsymbol{T}}{(\frac{\boldsymbol{5d}}{\boldsymbol{R}} - \boldsymbol{1})} \tag{2.36}$$

where P_T is the critical axial stress required for tensile fracture initiation, as a function of borehole size (R). Nesetova and Lajtai (1973) also extended this theory to calculate the critical stress required for compressive failure at the borehole along the minimum horizontal stress direction, which was later seen as the breakout initiation. Carter (1992) pointed out that the assumption of linearised stress gradient was not appropriate, since the tangential stress decreases non-linearly from the borehole wall into the rock (see Eq. (2.14) and Figure 2.31). Hence, Carter (1992) calculated the stress gradient by integrating the Kirsch solution and simplified the failure criterion as the uniaxial compressive condition, because the radial stress near the borehole is small compared to tangential stress. The critical axial stress (σ_P^*) required for breakout initiation under the normal compression test can be estimated as:

$$\boldsymbol{\sigma_P^*} = \frac{\boldsymbol{d} \times \boldsymbol{UCS}}{(\boldsymbol{R} + \boldsymbol{d})(\boldsymbol{1} - \frac{\boldsymbol{R^2}}{\boldsymbol{2(R + d)^2}} - \frac{\boldsymbol{R^4}}{\boldsymbol{2(R + d)^4}})} \tag{2.37}$$

Elkadi and Van Mier (2006) also implemented the stress averaging concept and the Kirsch solution on the hollow cylinder test and estimated the critical confining pressure (σ_c^*) required for breakout initiation:

$$\boldsymbol{\sigma_c^*} = \boldsymbol{UCS} \times \frac{\boldsymbol{d(b^2 - R^2)}}{\left(\boldsymbol{d} + \boldsymbol{R} - \frac{\boldsymbol{R^2}}{\boldsymbol{R + d}}\right)\boldsymbol{b^2}} \tag{2.38}$$

where b = radius of the hollow cylinder sample.

2.2.3.2 Fracture energy release

Bažant et al. (1993) explained the borehole size effect based on the principle of conservation of energy, such that the loss in potential energy during breakout formation is equal to the energy dissipated in the fracturing process. This study considered that breakout is created by parallel and equidistant cracks splitting in the axial direction, which undergoes a buckling process, as shown in Figure 2.32.

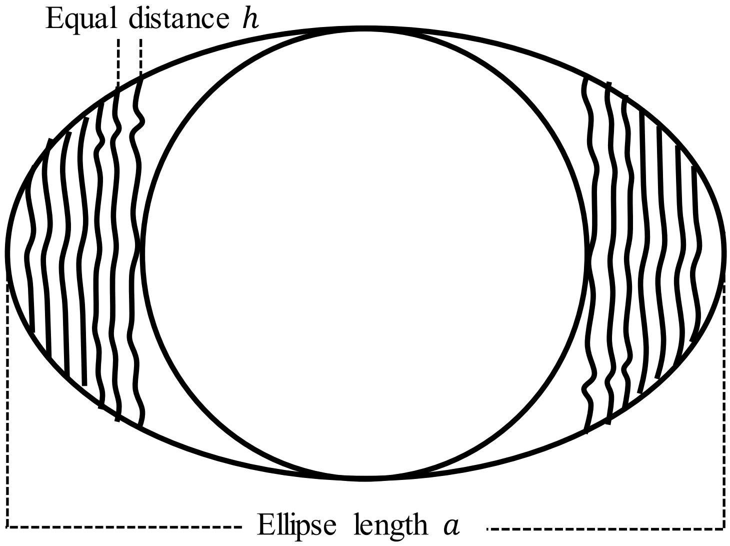

Figure 2.32 Breakout formation under fracture energy release with equidistant fracture space after Bažant et al. (1993)

Based on Eshelby's theory (Eshelby 1957), the potential energy released from no cavity to an ellipse ($\Delta\Pi_1$) can be estimated as:

$$\Delta\boldsymbol{\Pi}_1 = -\boldsymbol{\pi}/2\boldsymbol{E}'[(\boldsymbol{a}+2\boldsymbol{R})\boldsymbol{R}\boldsymbol{\sigma}_h^2 + (2\boldsymbol{a}+\boldsymbol{R})\boldsymbol{R}\boldsymbol{\sigma}_H^2 - 2\boldsymbol{aR}\boldsymbol{\sigma}_H\boldsymbol{\sigma}_h] \quad (2.39)$$

where $E' = \frac{E}{1-v^2}$ = plain strain modulus. Eq. (2.39) calculates the work done given σ_H within the ellipse is reduced to zero. When σ_H is reduced to σ_{cr}, the equation can be written in the form of:

$$\Delta\boldsymbol{\Pi}_1' = -\boldsymbol{\pi}/2\boldsymbol{E}'[(\boldsymbol{a}+2\boldsymbol{R})\boldsymbol{R}\boldsymbol{\sigma}_h^2 + (2\boldsymbol{a}+\boldsymbol{R})\boldsymbol{R}\boldsymbol{\sigma}_H^2 - 2\boldsymbol{aR}\boldsymbol{\sigma}_H\boldsymbol{\sigma}_h - 2\boldsymbol{a}^2\boldsymbol{\sigma}_{cr}^2] \quad (2.40)$$

where $\sigma_{cr} = -\pi^2/l^2(\frac{E'h^2}{12} - \frac{h}{\lambda}G)$, λ = empirical constant, G = shear modulus, and $l = kR$ = length of buckling, where k = empirical constant < 1. The potential energy change from no cavity to circular cavity ($\Delta\Pi_0$) can be computed as:

$$\Delta\boldsymbol{\Pi}_0 = -\boldsymbol{\pi}\boldsymbol{R}^2/2\boldsymbol{E}'(3\boldsymbol{\sigma}_h^2 + 3\boldsymbol{\sigma}_H^2 - 2\boldsymbol{\sigma}_H\boldsymbol{\sigma}_h) \quad (2.41)$$

As there is still residual strain energy ($\Delta\Pi_{cr}$) stored in the buckling area, it should also be considered:

$$\Delta\boldsymbol{\Pi}_{cr} = \frac{\pi R(a-R)}{2E'}\left(\frac{\pi^2 E' h^2}{12k^2R^2} + \frac{h}{\lambda}G\right)^2 \tag{2.42}$$

By assuming borehole breakout as a rough elliptical shape, the potential energy required for breakout development ($\Delta\Pi$) can be expressed as:

$$\Delta\boldsymbol{\Pi} = \Delta\boldsymbol{\Pi}_1 + \Delta\boldsymbol{\Pi}_{cr} - \Delta\boldsymbol{\Pi}_0 \tag{2.43}$$

Bažant et al. (1993) also calculated the energy dissipation due to fracturing (ΔW_f) by summing the energy required for all axial splitting cracks:

$$\Delta W_f = \frac{(\pi aR - \pi R^2)G_f}{h} \tag{2.44}$$

where $G_f = K_{IC}^2/E'$ = fracture energy of rock and K_{IC} = stress intensity factor. Due to the principle of conservation of energy, $-\Delta\Pi = \Delta W_f$. By differentiating both sides of the equation with respect to a:

$$-\frac{\partial(\Delta\boldsymbol{\Pi})}{\partial a} = \frac{\partial(\Delta W_f)}{\partial a} \tag{2.45}$$

Since the primary interest is breakout initiation stress, $a = R$, Eq. (2.45) can be expressed as:

$$\sigma_h^2 + 5\sigma_H^2 - 2\sigma_H\sigma_h - 4\sigma_{cr}^2 = \left(\frac{\pi^2E'h^2}{12k^2R^2} + \frac{h}{\lambda}G\right)^2 + \frac{2E'G_f}{h} \tag{2.46}$$

Since the remote effective applied stress (σ_{eff}) can be replaced by a single variable:

$$\sigma_{eff} = \sigma_H\left(1 - \frac{2\sigma_h}{5\sigma_H} + \frac{\sigma_h^2}{5\sigma_H^2}\right)^{\frac{1}{2}} \tag{2.47}$$

Eq. (2.47) may be simplified as:

$$\sigma_{eff}^2 = \left(\frac{\pi^2 E' h^2}{12k^2R^2} + \frac{h}{\lambda}G\right)^2 + \frac{2E'G_f}{5h} \tag{2.48}$$

The applied effective stress is now a function of h. Bažant et al. (1993) then differentiated the equation with respect to h to find the minimum stress required for breakout initiation:

$$\frac{\partial(\sigma_{eff}^2)}{\partial h} = \frac{5\pi^4 E'^2}{72k^4 R^4} h^5 + \frac{11\pi^2 E' G}{12k^2 R^2 \lambda} h^4 + \frac{5G^2}{\lambda^2} h^3 - E' G_f = 0 \tag{2.49}$$

For small R, the second and third terms of the differentiation become negligible, such that:

$$h = C_s R^{\frac{4}{5}} \tag{2.50}$$

and $C_s = \left(\frac{72k^4 G_f}{5\pi^4 E'}\right)^{\frac{1}{5}}$. Conversely, if R is large:

$$h = \left(\frac{E'^{G_f}\lambda^2}{5G^2}\right)^{\frac{1}{3}} \tag{2.51}$$

By substituting h from the two above equations into Eq. (2.48), the critical stress required for breakout initiation for both small and large R can be obtained respectively:

$$\sigma_{eff,small} = C_1 R^{-\frac{2}{5}} \tag{2.52}$$

$$\sigma_{eff,large} = 3\left(\frac{GE'G_f}{5\lambda}\right)^{\frac{1}{3}} = C_0 \tag{2.53}$$

where $C_1 = \left(\frac{\pi^2 5^{\frac{1}{2}}}{48k^2} E'^3 G_f^2\right)^{\frac{1}{5}}$. From Eq. (2.52), it is clear that the stress required for breakout initiation is inversely proportional to borehole size for small radius; and becomes constant with large radius, according to Eq. (2.53). As the solutions do not provide an equation for intermediate stress, Bažant et al. (1993) combined the two equations and provided an approximation equation:

$$\sigma_{eff} = C_1 R^{-\frac{2}{5}} + C_0 \tag{2.54}$$

2.2.3.3 Pressure-dependent

Based on a series of triaxial compression tests, Santarelli et al. (1986) found that Young's modulus is proportional to the confinement (σ_3). Thus, the study argued that the stress–strain relationship around the borehole is not only linear elastic, but also depends on the pressure. As the radial stress gradually increases from zero given the location is moving away from the borehole, this will result in increased Young's modulus at more distant locations. In this way, the maximum tangential stress is not concentrated at the borehole wall, but shifted to some distance into the rock. This will lead to breakout initiation away from the borehole (Santarelli and Brown 1989), see Figure 2.17. A number of researchers have also observed this phenomenon in the laboratory (Zaitsev 1985; Lee and Haimson 1993; Cuss et al. 2003).

Since the approach does not provide direct estimation of critical stress for breakout initiation, Dresen et al. (2010) and Meier et al. (2013) extended the theory by considering a breakout initiation distance (Δr) and simply used the Kirsch solution to represent the stress condition at the location. Since then, studies have attempted to calculate the critical stress under the hollow cylinder test by examining a number of failure criteria. Although predictions showed promising accuracy against experimental results, the determination of parameters including Δr and initial defect length is challenging and dubious.

2.3 NUMERICAL SIMULATION

Numerical modelling is a powerful tool which has been implemented in the rock mechanics field in the past few decades to provide simulations and solve complex geotechnical problems (Oettl et al. 2004; Lu et al. 2011; Zhou et al. 2016) or investigate laboratory rock behaviour at the micro-scale (Liu et al. 2002; Liu et al. 2007). This methodology is particularly useful to study the mechanisms and development of breakout, since it is practically impossible to observe progressive breakout failure during an experiment due to the limitations of experimental apparatus with a sealed frame with pressure applied in all dimensions. A significant body of research has been carried out to model the breakout phenomenon and study the geometrical relationship with horizontal stress magnitudes (Zheng et al. 1989; Shen et al. 2002; Schoenball et al. 2014; Lee et al. 2016; Sahara et al. 2017).

In general, numerical modelling can be classified into two groups: continuum and discontinuum approaches.

2.3.1 Continuum approach to borehole breakout

The continuum model treats the synthetic rock as a continuous body, such that it cannot be fractured into pieces and spalled off unless there are pre-existing discontinuities. The most commonly used numerical methods include Finite Element Method (FEM), Finite Difference Method (FDM) and Boundary Element Method (BEM).

Mastin (1984) was one of the first researchers to use numerical simulation to study borehole breakout. Based on BEM, Mastin (1984) observed that breakout initiated in a 'flat-bottom' shape and progressively elongated along the minimum horizontal stress direction, as shown in Figure 2.33. This study also found that stress redistributed during each stage and angular span did not widen after breakout initiation. Zheng et al. (1989) extended the work by Mastin (1984) and simulated the evolution of breakout from initiation until stabilisation with extensile splitting only, which agreed with Mastin (1984) on the constant angular span over the breakout development. However, Zheng et al. (1989) stated that, although breakout geometries are dependent on horizontal stress, estimation of the absolute magnitudes can still be difficult and will require additional information.

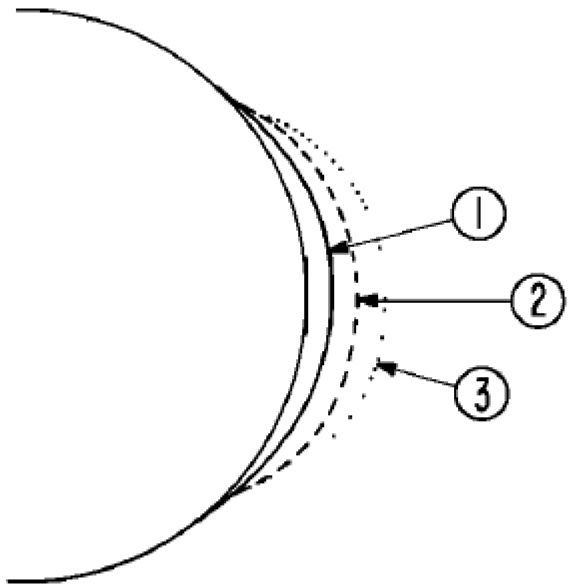

Figure 2.33 Progressive breakout failure (Mastin 1984; Zoback et al. 1985)

Zhou (1994) developed a linear elastic model with various failure criteria in Formula Translator (Fortran) program and attempted to model breakout under different faulting mechanisms and stress combinations. Results showed that the breakout orientation was not always aligned with the minimum horizontal stress direction under the Mohr–Coulomb failure criterion, which Zhou (1994) suggested this was due to the faulting mechanism. In addition, Zhou (1994) suggested that the breakout geometries generated under the Mohr–Coulomb criterion were greater than breakout predicted under other failure criteria that considered the effect of intermediate stress. This implies the importance of vertical stress in borehole breakout study.

Shen et al. (2002) investigated the breakout mechanism using their own BEM software – Fracture Propagation Code (FRACOD). The researchers implemented the modified energy release rate criterion, F-criterion (Shen and Stephansson 1994), in the software to govern rock failure, which was capable of simulating both shear and tensile cracking modes. Numerical results revealed that breakout formation was a combination of tensile and shear failures, which supported the argument of Haimson and Herrick (1986). However, the numerical simulation on FRACOD was limited because it could not induce fracture initiation, and 'artificial fractures' had to be introduced around the borehole before the start of each simulation. Shen (2008) later conducted breakout simulation on an updated FRACOD, which overcame this limitation. Shen tried to correlate the horizontal stress magnitudes with breakout geometries based on breakouts produced under different stress combinations in numerical simulation. Two empirical equations were derived from the results and showed promising predictions against field data. The software was also used by Kim et al. (2017) to determine the maximum horizontal stress in the field. This was achieved by matching the numerically created breakout with field observation based on given rock information and minimum horizontal stress obtained from hydraulic fracturing.

Schoenball et al. (2014) studied the time-dependency behaviour of breakout geometries through Abaqus (FEM), which was based on the time-dependent brittle creep model proposed by Amitrano and Helmstetter (2006). Simulation found that breakout quickly widened and became stable in the early stage of formation followed by the subsequent elongation over time, resulting in a V-shaped breakout. This supports the argument from previous studies on time-dependent breakout propagation (Zoback et al. 1985; Barton et al. 1988).

2.3.2 Discontinuum approach to borehole breakout

The discontinuum model can simulate materials varying from large scale rock mass with pre-existing fractures to micro-scale grain-to-grain contacts. In contrast to the continuum model, it enables the detachment of rock pieces along boundaries and can explicitly model the response of fractured rock mass under various conditions. Three frequently used discontinuum approaches are the Discrete Element Method (DEM), Discrete Fracture Network (DFN) and Discontinuous Deformation Analysis (DDA). In general, DEM is the most commonly used approach for modelling borehole breakout.

Santarelli et al. (1992) investigated breakout behaviour under pre-existing fractures based on Universal Distinct Element Code (UDEC). Results showed that both the stress concentration near the borehole and the breakout elongation direction altered noticeably with joint sets. The conclusions in this study were confirmed by Rawlings et al. (1993) using UDEC and by Du (1997) through the Displacement Discontinuity Method (DDM). Du (1997) conducted additional numerical simulation on borehole size effect which suggested that the breakout initiation stress was proportional to the crack length. This crack length was also dependent on the borehole size: the larger the borehole size, the longer the crack length. Therefore, longer borehole radius would lead to lower breakout initiation stress.

Fakhimi et al. (2002) tried to replicate the experimental breakout from Berea sandstone via Particle Flow Code (PFC). Good agreement was found between the laboratory and simulation results. The study concluded that it is more advantageous to model breakout behaviour based on DEM as the grain movements and crack extensions can be explicitly captured without further mesh generation. Li et al. (2006) successfully simulated all three types of breakout using the same software with the consideration of fluid flow. They suggested that V-shaped breakout would be created if rock is competent and not likely to fail in localised compaction, whereas fracture-like breakout was due to the compaction band. However, there was no porosity reduction monitored at the breakout tip, which was different from that reported in the laboratory (Mollema and Antonellini 1996; Haimson 2001). In addition, the spiral-shaped breakout created in the simulation was unclear, as it did not show any apparent shear failures around the borehole. As PFC only allows bond breakage and does not enable the breakage of particles, Rahmati (2013) implemented a 'grain crushing' scheme to model both failure modes. Simulation results suggested that grain crushing and repacking were the main contributors to fracture-like breakout, in which the depth was closely related to applied stress magnitudes. On the other hand, the angular span remained relatively constant with change in stress applied, which was consistent with the laboratory observations (Haimson and Kovacich 2003; Haimson and Lee 2004). In addition, Rahmati (2013) stated that the bonding strength (matrix strength) was an important parameter that can influence the shape of breakout. The stronger matrix strength would increase the possibility of fracture-like breakout, whereas the lower matrix strength would lead to V-shaped breakout.

Lee et al. (2016) further studied the mechanisms of V-shaped breakout based on PFC and a 'grain crushing' scheme. By simulating the experimental results on two types of sandstone, Lee et al. (2016) found that breakout forms either due to intergranular cracking or intra- and transgranular cracking depending on grain and matrix strengths, see Figure 2.34. This confirms the earlier argument on breakout formation mechanism proposed by Santarelli and Brown (1989). The numerical simulation showed that breakout angular span is dependent on horizontal stress magnitudes, and formed quickly at an early stage of borehole breakout, followed by progressive elongation in the minimum horizontal stress direction (Barton et al. 1988; Zheng et al. 1989). Hence, breakout angular span can be used as a reliable parameter for horizontal stress estimation (Lee et al. 2016).

Duan and Kwok (2016) analysed various aspects of borehole breakout using PFC, including horizontal stress magnitudes, borehole size, particle size distribution and rock anisotropy. Based on the simulation results, breakout geometries increased with constant horizontal stress ratio but increasing stress magnitudes. This indicates that the breakout geometries are dependent on the absolute horizontal stress magnitudes, rather than the horizontal stress ratio. Thereby, the borehole size effect investigation showed consistent results with laboratory studies, where the smaller borehole size requires more stress for breakout initiation (Haimson and Herrick 1989; Carter 1992; Dresen et al. 2010; Meier et al. 2013). Duan and Kwok (2016) were also able to simulate two types of spiral-shaped breakouts on the same rock type, as discussed in Section 2.2.1.3. In addition, anisotropic synthetic rock was achieved by introducing a smooth joint model. Duan and Kwok (2016) showed that the anisotropy has significant influence on breakout orientation and shapes, such that the parameter of bedding plane should be considered in field breakout studies.

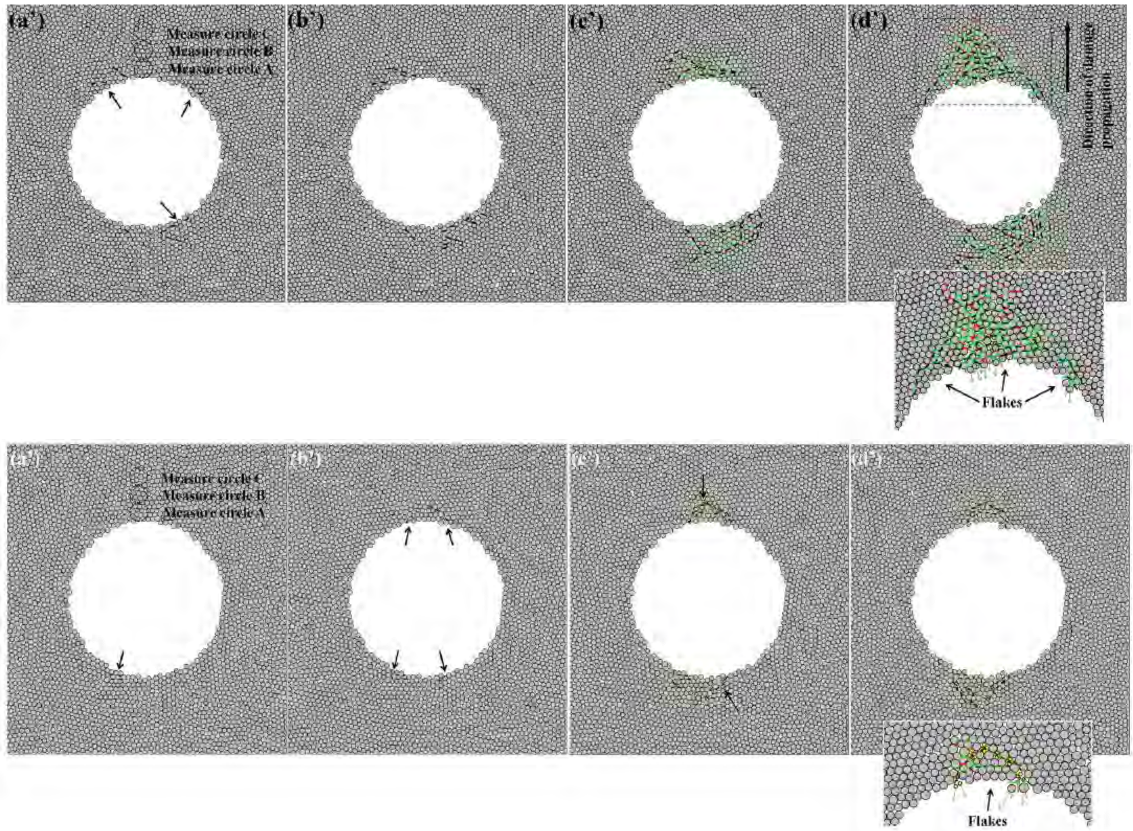

Figure 2.34 Breakout development over timesteps under two types of mechanisms, top: intergranular cracking, bottom: intra- and transgranular cracking (Lee et al. 2016), green lines mean tensile failure in bond, red lines represent shear failure in bond, black lines indicate micro-crack coalescence, yellow particles mean grain breakage

2.4 MACHINE LEARNING

In the rock mechanics field, the primary goal of many studies is to determine the relationship between unknown values, such as in-situ stress or factor of safety, from a series of observable variables, such as rock strength or depth of cover. However, due to the complexity of problems and the number of input parameters, it is sometimes not possible to derive a closed-form solution. Machine learning, a computer based algorithm, provides an alternative to solve the problem.

Machine learning is a method that enables computers to predict unknown responses based on past experiences. The technique learns and recognises the patterns between the input parameters and unknown responses based on sample data, also known as 'training data'. The constructed machine learning model is capable of improving the prediction accuracy by training with additional sample data. In the past few decades, it has been implemented extensively in rock mechanics (Hampson et al. 2001; Singh et al. 2001; Yilmaz and Yuksek 2008; Zain et al. 2010; Khandelwal and Monjezi 2013; Chou and Thedja 2016).

There are many types of machine learning models depending on their mathematical foundations. Popular techniques include Support Vector Machine (SVM), Kriging, Artificial Neural Network (ANN) and Regression. This section reviews two particular approaches, Kriging and ANN, because of their prevalence in mining and geotechnical engineering applications.

2.4.1 Kriging

Kriging is a semi-parametric interpolation method that provides predictions based on a number of inputs. The technique was initially developed by Krige (1951) in mining to estimate resources and was improved by Matheron (1973). Prediction using Kriging was not common until the pioneering work of Sacks et al. (1989); since then, it has been widely applied to estimate unknown responses in many disciplines.

The performance function (G(x)) of Kriging is expressed as (Sacks et al. 1989):

$$\mathbf{G}(\mathbf{x}) = \mathbf{F}(\mathbf{x}, \mathbf{b}) + \mathbf{Z}(\mathbf{x}) \tag{2.55}$$

where x is a vector of random variables, F(x, b) is the deterministic mean function of responses from the dataset, which describes the tendency of the model and can be represented by a regression equation:

$$\mathrm{F}(\mathbf{x}, \mathbf{b}) = \mathbf{f}(\mathbf{x})^T \mathbf{b} \tag{2.56}$$

where f(x) is a vector with $[f_1(\mathrm{x}), \dots, f_k(\mathrm{x})]^{\mathrm{T}}$ and b is the vector of regression coefficient corresponding to x. Z(x) is the stationary Gaussian process function with zero mean and auto-covariance:

$$\mathbf{Z}(\mathbf{x}) = \boldsymbol{\sigma}_{\mathbf{Z}}^{\mathbf{2}} \boldsymbol{R}(\mathbf{x}, \mathbf{x}'; \boldsymbol{\theta}) \tag{2.57}$$

where σ_Z^2 is the process variance and $R(\mathbf{x}, \mathrm{x}')$ is the auto-correlation function, and θ is the parameter that defines the auto-correlation function. The auto-correlation function is quantified based on a semi-variogram (see Figure 2.35), which is constructed by the covariance of all pairs of points in the training dataset (Bigg 1991). A 'best-fit' model will then be selected to represent the data trend of the semi-variogram (red dots), i.e. the auto-correlation function, which can be in a polynomial, exponential or Gaussian form

(Koehler and Owen 1996). Based on the determined auto-correlation function, the nearby training data (where the distance from the predicting point from the training data is less than the range) and their corresponding weight can be determined. Subsequently, the unknown response can be predicted from Kriging.

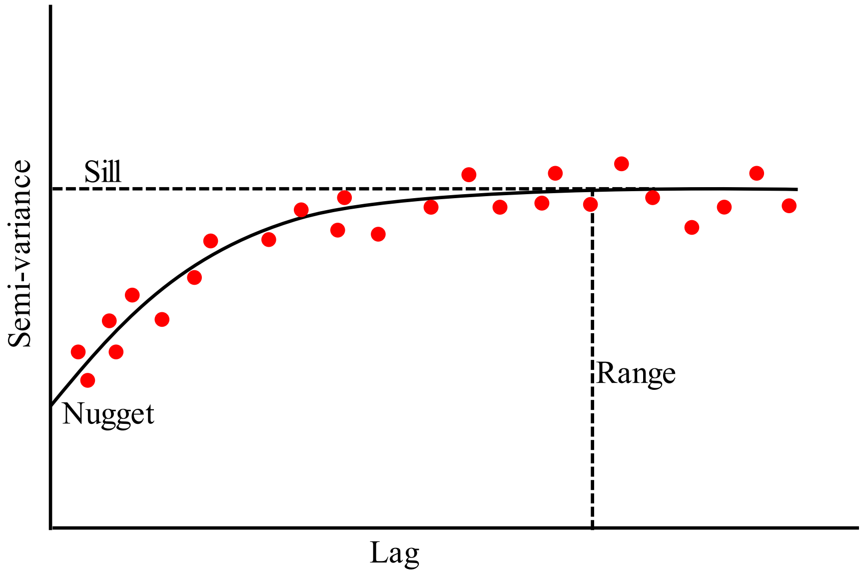

Figure 2.35 Semi-variogram

Kriging modelling has been used in various mining and geotechnical conditions. Yao et al. (1999) predicted porosity in rock from seismic data via Kriging. Choi and Lee (2007) successfully used the approach to estimate the Rock Mass Rating (RMR) from field data including geophysical and borehole surveys for tunnel design. Webber et al. (2013) attempted to estimate coal quality from downhole logging data through the technique. Abdideh et al. (2014) were able to estimate the uniaxial compressive strength of rock in deep locations from petrophysical information. Given its wide application and success in sophisticated problems, Kriging can be considered a useful tool for predicting horizontal stress from borehole breakout geometries.

2.4.2 Artificial Neural Network

Artificial Neural Network (ANN) is a major type of machine learning technique, inspired by biological neural networks (Chen et al. 2019). Composed of mathematical functions (activation functions) in its neurons, ANN aims to replicate the human brain and learn patterns based on training data (Salchenberger et al. 1992). In general, the network architecture of an ANN is divided into three layers of an input layer, hidden layer and output layer (Srinivasulu and Jain 2006), as shown in Figure 2.36. The input layer is at the beginning of the modelling process and receives input parameters for processing. The hidden layer consists of a number of parallel neurons that are connected by edges, which have a weight for computation (Bashir and El-Hawary 2009). The hidden layer can be further divided into multiple sub-hidden layers depending on the complexity of the problem. The output layer produces the final estimation and is formed by a weighted summation of outputs from the last hidden layer (Phung and Bouzerdoum 2007).

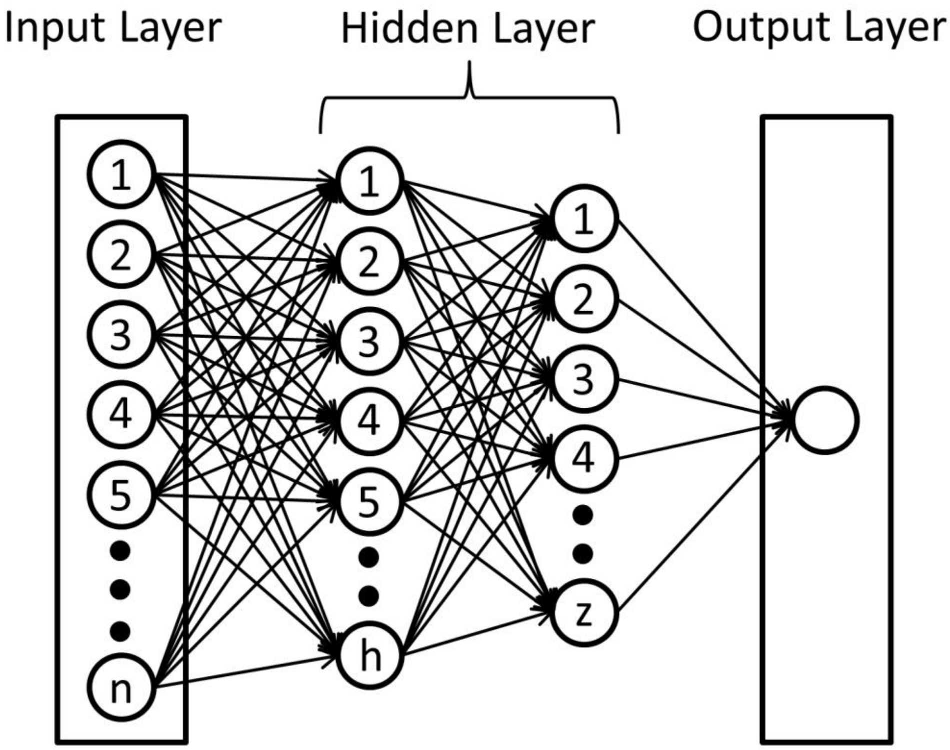

Figure 2.36 General ANN architecture, where n = number of inputs, h and z = number of neurons in each hidden layer

Many types of ANN models are available, such as feedforward, radial basis and multilayer perceptron. Among these models, the most popular technique for ANN models is the backpropagation (learning) technique from a multilayer feedforward ANN (Dougherty 1995; Tu 1996; Sonmez et al. 2006; Khosravi et al. 2011). Backpropagation, a stochastic descent method, calculates the gradient of loss functions corresponding to the weight of ANN layers from the last layer back to the first layer (Amari 1993). As the gradient calculation from the current layer can be partially used in the next layer (i.e.

the layer before the current layer in the ANN model, as the backpropagation process is going backwards), it can save significant computation time (Chen and Jain 1994; Tu 1996).

Similar to many other machine learning techniques, an ANN model is also built on the learning process from a sample dataset. The dataset is randomly divided into three groups: training, validation and testing. The ANN model is initially constructed based on the training data, which is adjusted based on the obtained mean square error (MSE). The inputs from the validation data then feed into the developed ANN model to predict the outputs and these predicted outputs are compared to the known output from the validation data. Based on the difference between prediction outputs and known values, an error signal can be calculated and backpropagated through the ANN model (McClelland and Rumelhart 1988; Zurada 1992). The error signal is a mathematical factor which is used to adjust the weights of elements in the developed ANN model, such that the future estimation based on similar input parameters as the validation dataset can be more accurate (Tu 1996). This repetitive training process is undertaken to minimise the error. Finally, the trained ANN model is further examined against the test data to measure its performance. The entire process is repeated again until the error in all three datasets is optimised to a minimum.

The ANN model is one of the most attractive techniques in geo-engineering due to its reliability and applicability to sophisticated multivariate problems (Sonmez et al. 2006). Recently, it has also been implemented widely in mining and geotechnical engineering fields (Esfe et al. 2019; Nguyen et al. 2019). Singh et al. (2001) attempted to predict rock strengths from petrographic information via ANN. Ocak and Seker (2012) used the technique to estimate the Young's modulus of intact rock. Surface roughness was also calculated from 68 experimental data points by Mia and Dhar (2016). The importance of ANN model applications in rock engineering and mineral processing has been recognised by Kapageridis (2002).

2.5 Conclusions

This chapter reviewed existing stress measurement techniques. It is clear that the most popular stress measurement methods in practice are hydraulic fracturing and overcoring, which can estimate both absolute stress magnitudes and orientation. However, they are neither effective nor reliable in measuring in-situ stress in weak strata under high stress conditions, where the borehole and cored samples are likely to be fractured. This condition will be encountered more frequently due to deeper mining activities.

Borehole breakout, resulted from borehole drilling activities, usually occurs in the weak strata where the stress is concentrated and its geometries are influenced by horizontal stress magnitudes. In Australia, every borehole requires geophysical and geological logging, which means breakout data is easily accessible at no cost. Based on extensive experimental observation, it has been argued that breakout geometries are dependent on each other such that estimation of both horizontal stress magnitudes is not feasible. The current models are only capable of either estimating maximum horizontal stress from minimum horizontal stress or constraining the magnitudes of two horizontal stresses, whereas the absolute magnitudes remain unsolved. However, this is purely based on laboratory results and lacks a solid theoretical background. Detailed investigation is necessary to examine the argument while exploring the possibility of deriving two horizontal stress magnitudes.

The majority of the experimental studies focused on the influence of maximum horizontal stress on breakout geometries, whereas the minimum horizontal and vertical stresses were rarely considered. In the field, in-situ stress is always three-dimensional and the intermediate stress plays a critical role in rock failure. Therefore, it is critical to study the effect of the other two stresses on breakout geometries. In addition, borehole size is an important parameter that substantially affects the breakout geometries in the laboratory. It should also be considered in experimental investigation.

Numerical simulation provides a method to study breakout development and mechanisms which cannot be achieved in the laboratory. Based on the review of numerical models, it can be concluded that the continuum approach is not suitable to analyse laboratory-scaled breakout simulation, especially grain movements due to micro-cracking. On the other hand, Particle Flow Code has shown promising breakout simulation results and ability to model such behaviour.

The machine learning technique, particularly Kriging and Artificial Neural Network modelling, has been implemented in many rock mechanics problems, including those which cannot be solved by a closed-form solution. These problems include predicting rock mechanical properties and estimating resources. As the relationship between borehole breakout geometries and horizontal stress magnitudes is unclear and sophisticated due to the complex breakout formation mechanism, it is required to use advanced computer algorithms to model this relationship. This thesis studies the application of machine learning on horizontal stress estimation from borehole breakout in conjunction with the traditional rock mechanics approach.

3 EXPERIMENTAL STUDY ON BOREHOLE BREAKOUT AND BOREHOLE SIZE EFFECT

Understanding the influence of in-situ stress on breakout geometries is vital for developing a horizontal stress measurement technique from borehole breakout data. Previous laboratory studies have confirmed that the increasing maximum horizontal stress leads to wider and deeper breakout given the constant minimum horizontal and vertical stresses (Lee and Haimson 2006). Based on the experimental results, researchers have also argued that there is a unique relationship between the two geometries, so that estimating two horizontal stress magnitudes from borehole breakout is not possible (Haimson et al. 1991; Herrick and Haimson 1994; Haimson and Lee 2004; Lee and Haimson 2006; Sahara et al. 2017).

The literature review in Chapter 2 indicated that this conclusion is tentative as this claim is purely from experimental observations. Section 3.1 provides a detailed study of this hypothesis, which is based on a series of breakout experiments, using the true triaxial testing machine designed by the University of NSW. The experiments investigate the correlation between breakout geometries and horizontal stress magnitudes. The study also considered the effect of borehole size on breakout geometries, which were not explored in previous experiments (Haimson and Herrick 1986; Haimson et al. 1991; Herrick and Haimson 1994; Haimson and Lee 2004; Lee and Haimson 2006; Lee et al. 2016).

Borehole size can significantly influence the stress required for breakout initiation and its geometries under laboratory conditions. In previous studies, either a constant ratio between the borehole radius and specimen size or a constant specimen size was used in each laboratory study during sample preparation, particularly in normal compression tests (Haimson and Herrick 1989; Carter 1992), while there were no direct comparisons between the same borehole radius under different specimen sizes. As a larger specimen size generally has lower UCS value due to the scale effect (Bažant and Xi 1991; Bažant and Yavari 2005), it might also influence the breakout initiation stress results. Section 3.2 investigates whether the specimen size influences breakout initiation stress through two series of normal compression tests. Based on experimental results, Section 3.2 also provides a number of methods to predict the stress required for breakout initiation due to the borehole size effect.

3.1 BOREHOLE BREAKOUT TEST

3.1.1 Experimental procedures

True triaxial tests were conducted on Gosford sandstone specimens, which were collected from a quarry located in the Sydney Basin. According to the rock property testing, the uniaxial compressive strength and Young's modulus of the specimen are 42.3 MPa and 7.5 GPa, respectively; the Poisson's ratio and tensile strength are 0.18 and 2.8 MPa; and the cohesion and internal friction angle are 12.9 MPa and 35°.

To simulate the in-situ stress conditions in Australia ($\sigma_H > \sigma_h > \sigma_v$), a customised apparatus was designed for this purpose as shown in Figure 3.1a. The rock specimen (120 × 120 × 120 mm^3) with a pre-drilled hole was placed in the middle of the equipment, with the hole aligned in the y-direction. Biaxial stresses (σ_h and σ_v) were then applied by tightening the nuts shown in Figure 3.1a, with the stress magnitudes monitored by the load cells connected between the outer and inner plates, as shown in Figure 3.1b.

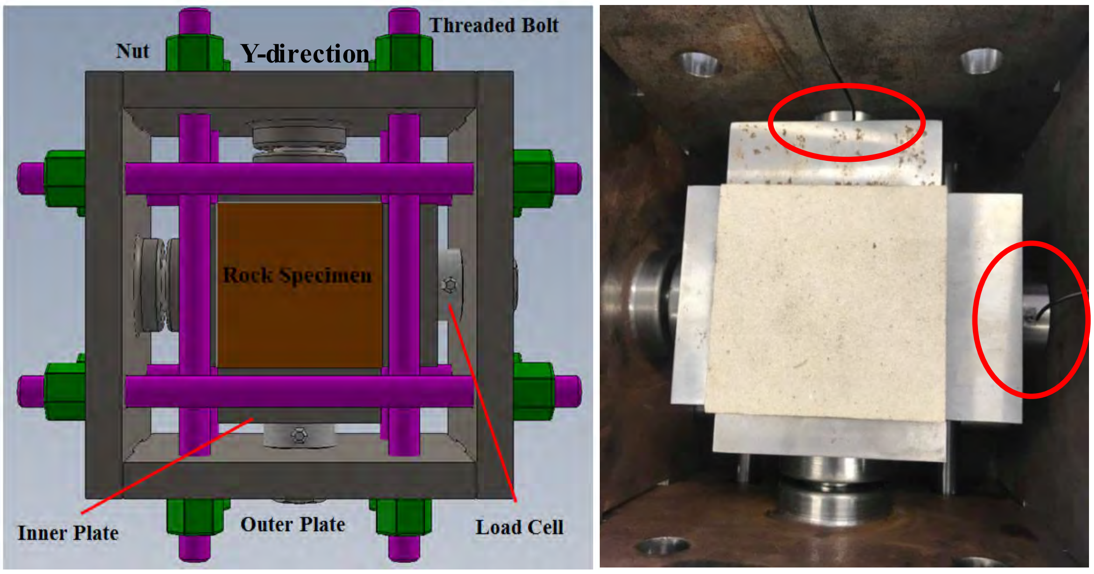

a b

Figure 3.1 UNSW variable confinement cell

Once the desired stress levels were reached, the rock specimen was loaded by the tertiary stress from the MTS machine, see Figure 3.2. To ensure the full development and stabilisation of the breakout phenomenon, the specimen was held under the same stress condition for another 30 minutes (Haimson et al. 1991; Haimson and Kovacich 2003; Lee et al. 2016). Rock specimens with three hole sizes (8 mm, 11 mm and 15 mm) were tested under the same stress conditions to observe the influence of borehole size on borehole breakout geometries.

The conventional technique to measure the cross-sectional geometry uses infilled epoxy materials along the length of the borehole (Haimson and Song 1998; Haimson and Lee 2004; Katsman et al. 2009; Lee et al. 2016). However, this may not be very accurate considering the hole size (radius) is only 11 mm, where a 1% variation in breakout depth is 0.11 mm, and both angular span and breakout depth show some variation along the borehole length. It is important to take account of these variations to obtain precise measurements for later studies. Therefore, the optical scanning technique was implemented to measure breakout geometries with higher accuracy, as shown in Figure 3.3b. The rock specimen was first cut in half along σ_H such that the breakout profile would not be damaged, but well preserved. The inner faces were then sprayed to cover shiny particles to ensure good scanning quality. Afterwards, scanning was undertaken to capture the full breakout profile from top to bottom, see Figure 3.3a. Breakout geometries were obtained by determining the average values of the scanning data along the borehole axis.

Figure 3.2 True triaxial test

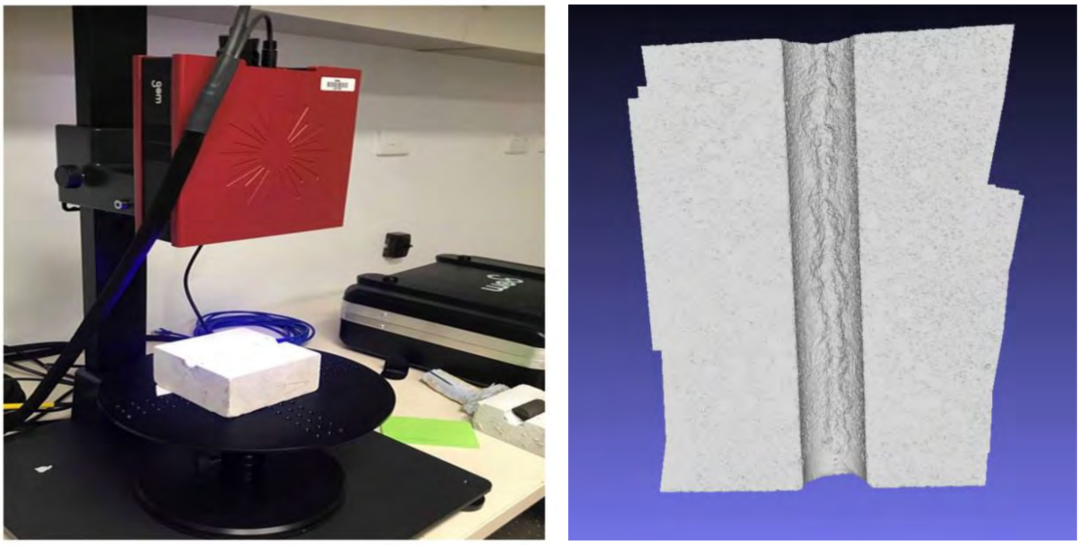

a b

Figure 3.3 Optical scanning

3.1.2 *Results and discussion*

To investigate breakout geometries and the influence of borehole sizes, three sets of experiments with different hole sizes were carried out under various σ_H conditions, with constant σ_h = 10 MPa and σ_v = 5 MPa applied. Results showed a good alignment between breakout depth and σ_h direction. This confirmed that breakout is indeed a reliable tool for stress orientation determination. Figure 3.4 presents a clear V-shaped borehole breakout obtained from the experiments, where σ_H = 60 MPa and the hole size is 11 mm.

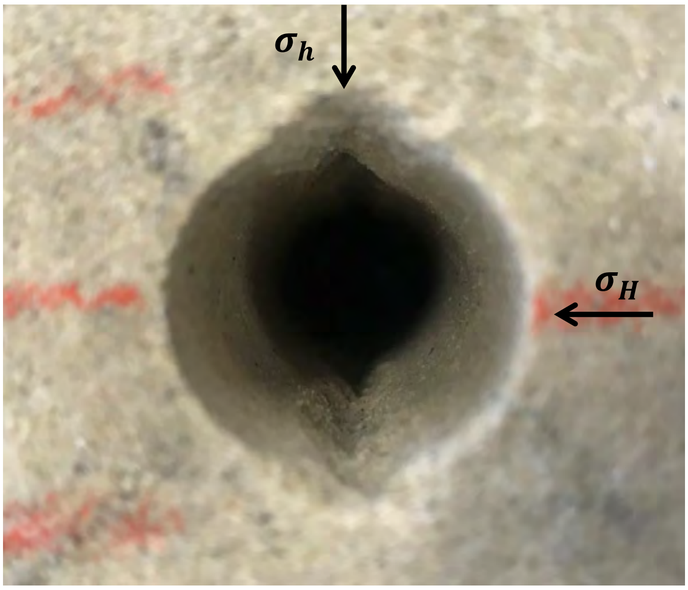

Figure 3.4 Experimental borehole breakout

3.1.2.1 Breakout geometries and horizontal stress magnitudes

Figure 3.5 and Figure 3.6 show strong stress dependencies on breakout geometries. For the same hole size, both normalised breakout depth (L/R) and angular span increase with the increasing horizontal stress ratio; in particular, they both increase with σ_H as σ_h and σ_v were all kept constant during the experiments. Clear linear trends can also be observed based on the figures, in which both parameters increase at relatively steady rates; except for the 15 mm hole size, where the gradients for breakout geometries are sharper. Experimental results obtained from this study agree with previous experimental studies conducted by earlier researchers (Haimson and Herrick 1986; Haimson and Herrick 1989; Haimson and Song 1993; Herrick and Haimson 1994; Haimson and Lee 2004; Lee and Haimson 2006; Lee et al. 2016), suggesting that there are correlations between breakout geometries and horizontal stress magnitudes.

Figure 3.7 shows the relationships between the two breakout geometries. Based on experimental results, it is observed that the normalised breakout depth is strongly dependent on the angular span (Gough and Bell 1982; Zheng et al. 1989), the wider breakout always being deeper for the same hole size. This trend can be bounded in a narrow increasing region as shown in Figure 3.7. Haimson et al. (1991) observed similar results in their experiments, in which they aruged that, due to the dependency between breakout geometries, they are redundant factors for horizontal stress estimation. Therefore, deriving two horizontal stresses from two redundant breakout geometries is not viable.

3.1.2.2 Breakout geometries and hole sizes

Previous experiments focus heavily on the horizontal stress magnitudes, the hole size used being quite consistent, with radii in the 10–11 mm range. Three different hole sizes are studied here.

Figure 3.5 and Figure 3.6 illustrate that, under the same stress conditions, a larger hole size actually results in a wider angular span and deeper normalised breakout depth. For each hole size, the gradients of the breakout geometries and increasing horizontal stress ratio show similar relationships as observed in previous studies without considering the hole size. The indication here is that hole size is crucial for borehole breakout geometries and has to be explicitly analysed.

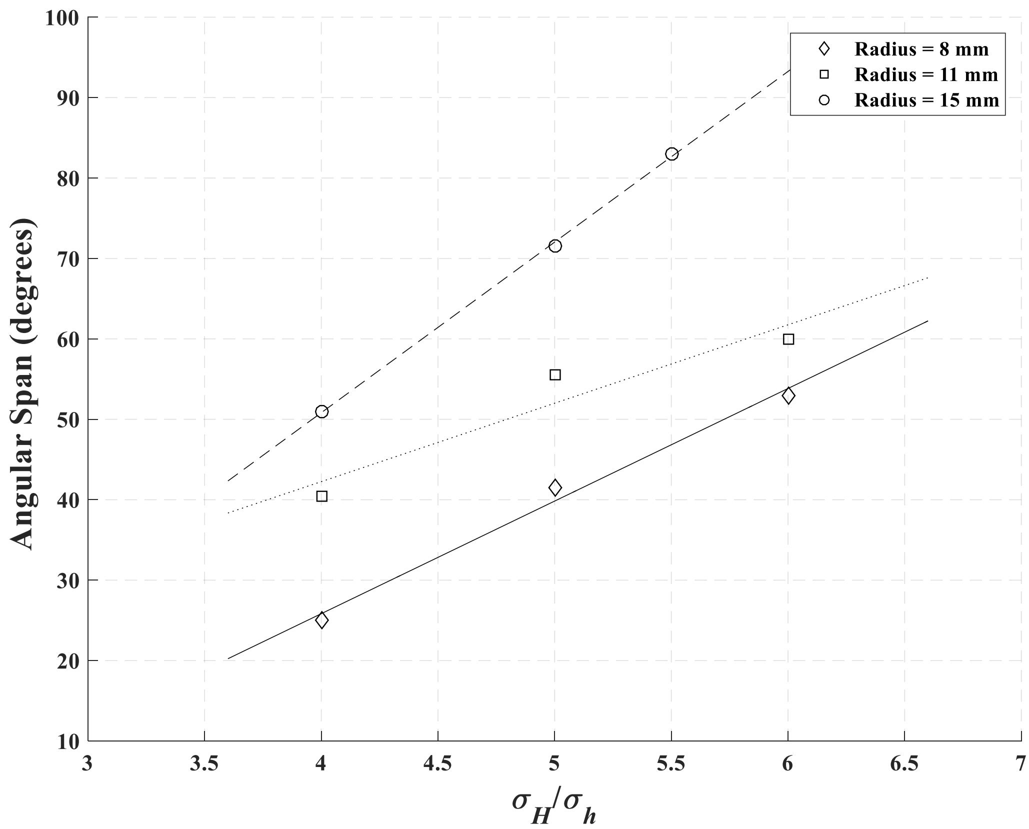

Figure 3.5 σ_H/σ_h vs angular span (θ_b)

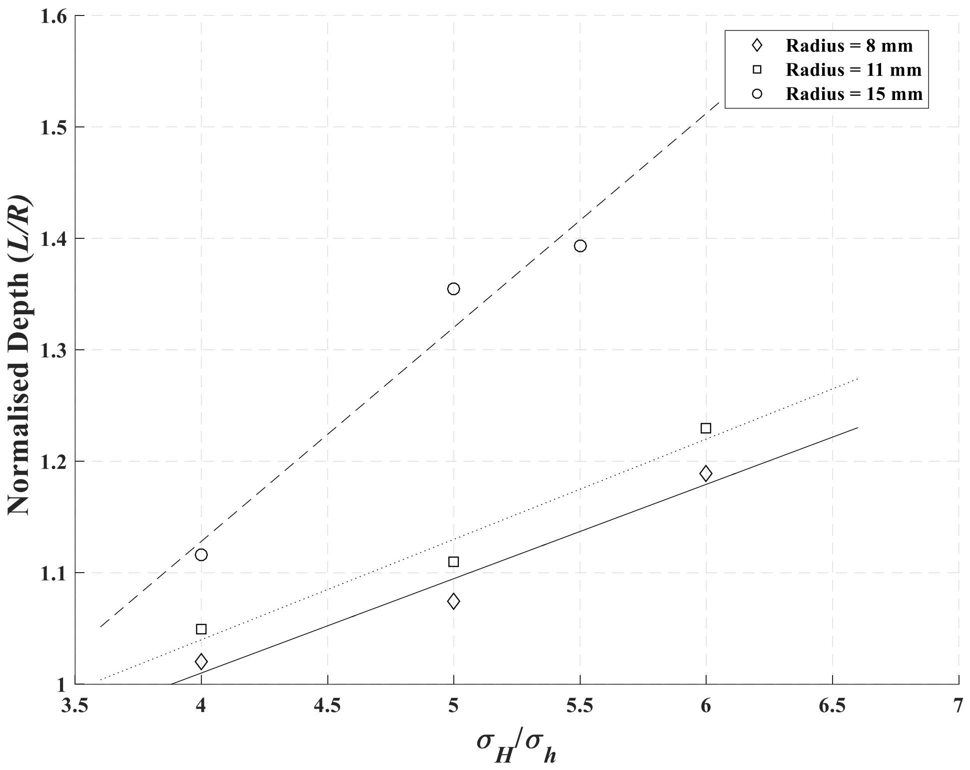

Figure 3.6 σ_H/σ_h vs normalised depth (L/R)

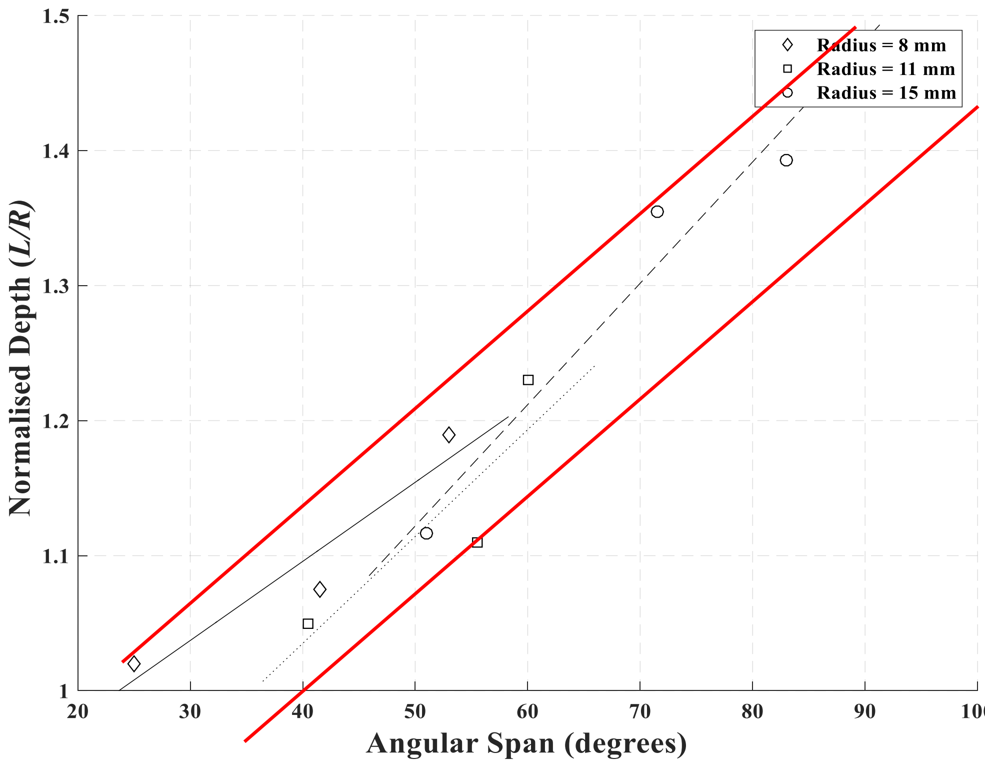

Figure 3.7 θ_b vs L/R

According to the Kirsch solution, the stress concentration around a circular cavity can be calculated from the in-situ stress field, given elastic conditions (Jaeger et al. 2009):

$$\boldsymbol{\sigma_r = \frac{1}{2}(S_H + S_h)\left(1 - \frac{R^2}{r^2}\right) + \frac{1}{2}(S_H - S_h)\left(1 - 4\frac{R^2}{r^2} + 3\frac{R^4}{r^4}\right)cos2\theta + \Delta P\frac{R^2}{r^2}} \quad (3.1)$$

$$\boldsymbol{\sigma_\theta = \frac{1}{2}(S_H + S_h)\left(1 + \frac{R^2}{r^2}\right) - \frac{1}{2}(S_H - S_h)\left(1 + 3\frac{R^4}{r^4}\right)cos2\theta - \Delta P\frac{R^2}{r^2}} \quad (3.2)$$

$$\boldsymbol{\tau_{r\theta} = -\frac{1}{2}(S_H + S_h)\left(1 + 2\frac{R^2}{r^2} - 3\frac{R^4}{r^4}\right)sin2\theta} \quad (3.3)$$

where σ_r = radial stress around the circular hole, σ_θ = tangential stress around the circular hole, $\tau_{r\theta}$ = shear stress around the circular hole, S_H and S_h = maximum and minimum effective horizontal principal stresses, R = hole size, r = distance from the centre of the borehole to the location of interest; $\frac{R}{r}$ = 1/normalised breakout depth, 2θ = 180 – breakout angular span, and ΔP = the difference between fluid pressure and the pore pressure.

The Kirsch solution uses the normalised breakout depth and angular span (θ_b) as inputs, which means that the stress concentrations should be identical at a certain location around the borehole regardless of the hole size; and, under the same stress conditions, breakout geometries should be the same for any hole size. However, the above experimental results show a substantial discrepency between the breakout geometries for different hole sizes.

Based on the Kirsch solution, Barton et al. (1988) proposed a model which introduced a relationship between horizontal stress magnitudes and angular span. It is the basis of the current stress polygon technique using borehole breakout and has been implemented in numerous field conditions (Barton et al. 1988; Zoback and Healy 1992; Brudy et al. 1997; Lund and Zoback 1999; Zoback et al. 2003; Valley and Evans 2015). The model assumes plane strain, where the rock around the borehole is subjected to resultant stresses from horizontal stresses only. For the sake of simplification, ΔP is assumed to be zero. Along the borehole, the stress conditions can be calculated as:

$$\boldsymbol{\sigma_r = 0} \quad (3.4)$$

$$\boldsymbol{\sigma_\theta = S_H + S_h - 2(S_H - S_h)cos2\theta} \tag{3.5}$$

$$\boldsymbol{\tau_{r\theta} = 0} \tag{3.6}$$

The above equations show that, along the borehole, the radial stress and shear stresses can be neglected. Therefore, under the plane strain assumption the rock at the borehole wall should experience only uniaxial compressive stress. At breakout angular span, UCS should be equal to σ_θ from Eq. (3.5):

$$\boldsymbol{UCS = \sigma_\theta = S_H + S_h - 2(S_H - S_h)cos2\theta} \tag{3.7}$$

The breakout angular span hence can be estimated as:

$$\boldsymbol{2\theta_b = 180^\circ - cos^{-1}\left(\frac{S_H + S_h - UCS}{2(S_H - S_h)}\right)} \tag{3.8}$$

in which the angular span, $2\theta_b$ = 180 – 2θ and S_H and S_h are assumed to be equal to σ_H and σ_h.

$$\boldsymbol{2\theta_b = 180^\circ - cos^{-1}\left(\frac{\sigma_H + \sigma_h - UCS}{2(\sigma_H - \sigma_h)}\right)} \tag{3.9}$$

Based on the horizontal stress magnitudes and UCS, angular spans from experiments can be estimated. Given that the analytical solution does not account for the influence of hole size, the angular span it predicts should be the same for any hole size for the same stress conditions. Figure 3.8 shows the predictions and the experimental results, and it can be seen that the prediction has a less steep gradient compared with experimental results for the 15 mm hole size, although they all exhibit an increasing trend with increasing horizontal stress ratio. In addition, a considerable discrepancy between the prediction and the closest set of experimental results can be seen, which again indicates that hole size should be used as a parameter when investigating the breakout geometries under experimental scenarios.

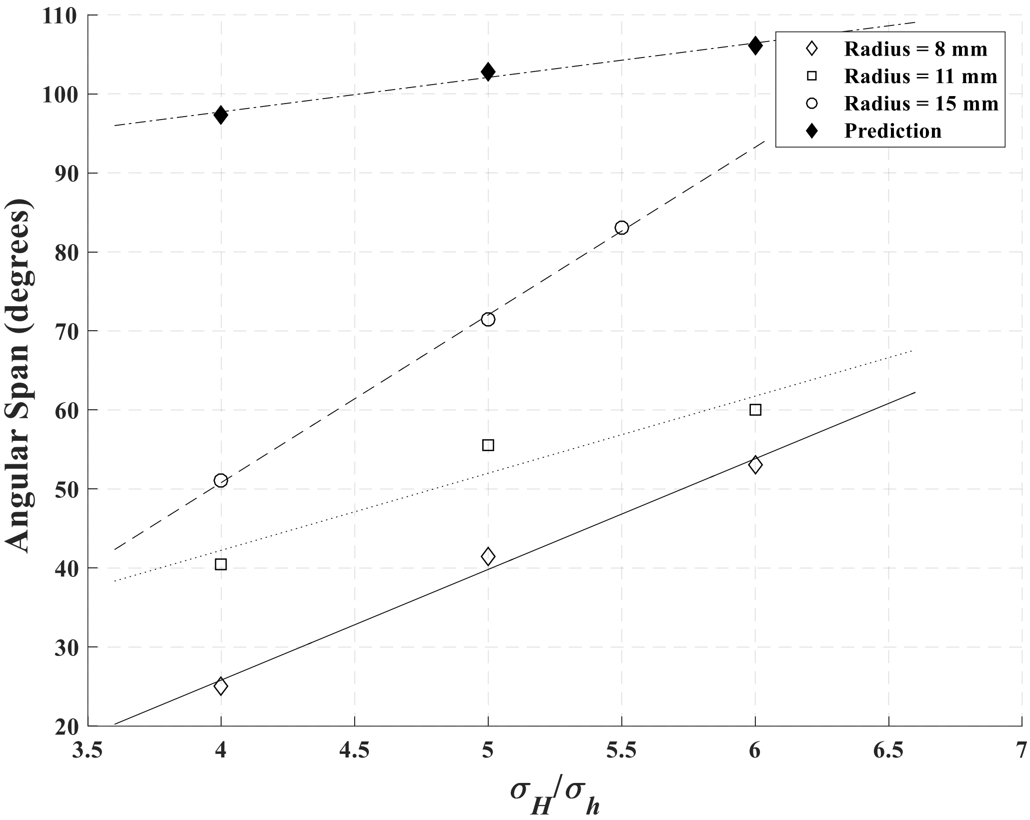

Figure 3.8 Prediction of experimental results

3.1.2.3 Hole size effect

As observed and demonstrated by many researchers from uniaxial tests on pre-drilled prisms and hollow cylinder tests (Lajtai 1972; Ingraffea 1979; Mastin 1984; Ewy and Cook 1989; Haimson and Herrick 1989; Carter et al. 1991; Elkadi and Van Mier 2006; Dresen et al. 2010; Meier et al. 2013), the hole size has substantial influence on fracture initiation under laboratory conditions. The fracture initiation is detected by strain gauges or acoustic emission and assumed to first occur at the borehole wall along σ_h, namely the sidewall (θ = 90°).

If the hole size is small, the required stress concentration for fracture initiation at the sidewall was observed to be as large as three times the UCS, where stress concentration is calculated from Eq. (3.2) and simplified as $\sigma_\theta = 3\sigma_H - \sigma_h$. As the hole size gradually increases, the fracture initiation stress decreases dramatically and eventually equals the UCS. Walton et al. (2015) and LeRiche et al. (2017) named this intensification of borehole wall as 'borehole wall strength (BWS)'. In this research, as the experiment was under conditions similar to the uniaxial tests, the only difference was the true triaxial loading on rock specimens. This is perhaps the primary reason for discrepancies between the analytical model and experimental observations.

The stress averaging concept was initially proposed by Lajtai (1972) to explain fracture initiation along the maximum horizontal stress direction along the borehole (for tensile fracture). Lajtai (1972) suggested that even brittle material can have 'ductile behaviour' under high stress gradient. The stress will redistribute and be averaged over a certain distance, $2d$ (Ortiz 1988). This distance is assumed to be a material property and can be determined based on data fitting. As the rock around the borehole is subjected to high stress gradient, Lajtai (1972) assumed this gradient to be linear and the average stress is equal to:

$$\boldsymbol{\sigma_d = \sigma_m + d \times (\frac{\partial \sigma}{\partial r})_{r=R}} \tag{3.10}$$

where σ_d = the average stress over the distance, σ_m = the maximum tangential stress at the borehole wall, $(\frac{\partial \tau}{\partial r})_{r=R}$ = the stress gradient at the borehole wall, assumed to be linear over the distance of $2d$. If σ_d = the tensile strength of rock (T), fracture will initiate at the point:

$$\boldsymbol{T = \sigma_m + d \times (\frac{\partial \sigma}{\partial r})_{r=R}} \tag{3.11}$$

Based on the Kirsch solution, Eq. (3.11) can be derived in terms of the horizontal stresses applied:

$$\boldsymbol{T = (\frac{5d}{R} - 1)\sigma_H + (3 - \frac{7d}{R})\sigma_h} \tag{3.12}$$

For the uniaxial compressive condition, where σ_h = 0, the equation can be rearranged as:

$$\boldsymbol{P_T = \sigma_H = \frac{T}{(\frac{5d}{R} - 1)}} \tag{3.13}$$

where P_T is the required uniaxial compressive stress for fracture initiation along the direction of applied stress (θ = 0°). Nesetova and Lajtai (1973) implemented the same concept to explain the stress initiation at the borehole sidewall by using the Coulomb failure criterion, as the stresses at the location are compressive stresses. The same approach was used as discussed above and the equation for the compressive condition derived as:

$$\boldsymbol{P_S} = \frac{\mathbf{2} \times \boldsymbol{\tau_s}}{\mathbf{3} - \mathbf{10}\frac{\boldsymbol{d}}{\boldsymbol{R}}} \tag{3.14}$$

where P_S = the applied uniaxial stress required for fracture initiation at the sidewall and τ_s = rock shear strength. As the stress concentration around the borehole clearly does not drop linearly, Carter (1992) later considered the true stress gradient over the distance by integrating the Kirsch solution into the gradient calculation and simplified the failure criterion to the uniaxial compressive condition:

$$\boldsymbol{P_S} = \frac{\boldsymbol{d} \times \boldsymbol{UCS}}{(\boldsymbol{R} + \boldsymbol{d})(\mathbf{1} - \frac{\boldsymbol{R}^2}{\mathbf{2}(\boldsymbol{R}+\boldsymbol{d})^2} - \frac{\boldsymbol{R}^4}{\mathbf{2}(\boldsymbol{R}+\boldsymbol{d})^4})} \tag{3.15}$$

Due to the stress averaging, the stress concentration that rock around the hole is subjected to is considerably lower than predicted by the Kirsch solution. This in turn requires more stress to be applied to the rock specimen to induce fracture initiation. The stress concentration around the borehole can be represented by the Kirsch solution and its input is the normalised depth (L/R). For the stress averaging concept, the stress concentration is averaged in the distance (d/R). Since d does not change and R varies between experiments, a larger R will lead to a shorter normalised stress averaging distance (d/R). Consequently, the higher stress concentrates within a shorter averaging distance for a larger hole size compared to a smaller hole size, which eventually results in wider and deeper breakouts. To be more specific, d is assumed to be 2 mm for the explanation. For the breakout experiment, where σ_H = 40 MPa, σ_h = 10 MPa and σ_v = 5 MPa, the tangential stress and the stress averaging values can be calculated based on Eq. (3.2) and plotted in Figure 3.9. From the figure, it is clear that the larger hole size has a higher averaging tangential stress. If the rock strength is the same, the higher tangential stress undoubtedly will produce more fractures, thus larger breakouts.

Bažant et al. (1993) explained this borehole wall strengthening using the principle of conservation of energy, in which the potential energy loss due to breakout formation from a circular borehole is equal to the energy dissipation of rock fracturing which forms a breakout. In their study, Bažant et al. (1993) assumed that borehole breakout is formed by parallel and equidistant axial splitting of cracks which undergo the buckling process, see Figure 3.10. The potential energy loss is evaluated by Eshelby's theorem

(Eshelby 1957), in which the potential energy can be calculated as the difference between the energies required to generate an elliptical cavity and a circular hole in a vacuum that is subjected to a biaxial stress field; the energy dissipation is calculated by the fracture energy release from vertical cracks within the breakout region.

$$\boldsymbol{BWS = \sigma_{ef} \approx C_1 R^{-\frac{2}{5}} + C_0} \tag{3.16}$$

where $C_1 = (\frac{\pi^2 5^{1/2}}{48k^2} E'^3 G_f^2)^{1/5}$ and $C_0 = 3(\frac{GE'G_f}{5\lambda})^{\frac{1}{3}}$. $E' = E/(1-v^2)$, E = Young's modulus and v = Poisson's ratio, $G_f = K_{IC}^2/E'$, in which K_{IC} = fracture toughness, k = empirical positive constant that is less than 1, and λ = empirical length (material property). According to the equation, it is also clear that, as the hole size increases, BWS decreases. Papanastasiou and Thiercelin (2010) proposed a calibration process for Bažant et al. (1993) to determine the parameters required under experimental data.

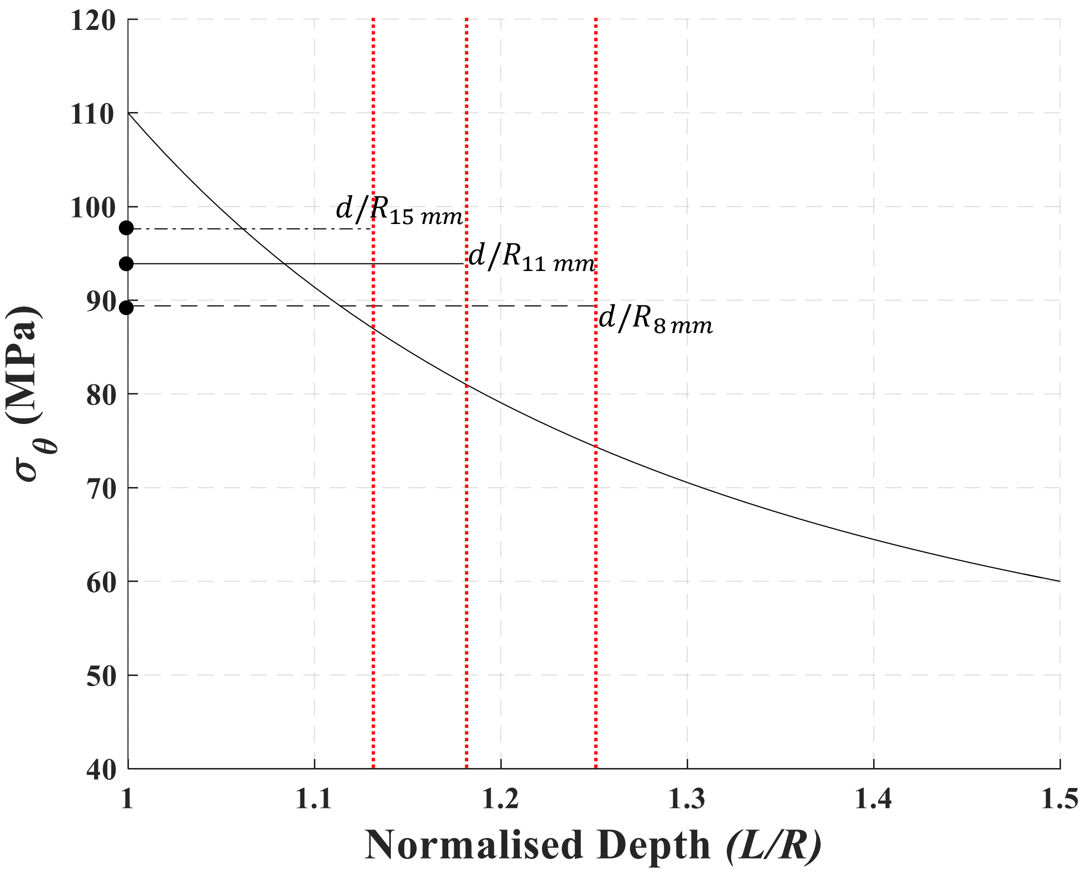

Figure 3.9 σ_θ along the σ_h direction and stress averaging under σ_H = 40 MPa, σ_h = 10 MPa and σ_v = 5 MPa

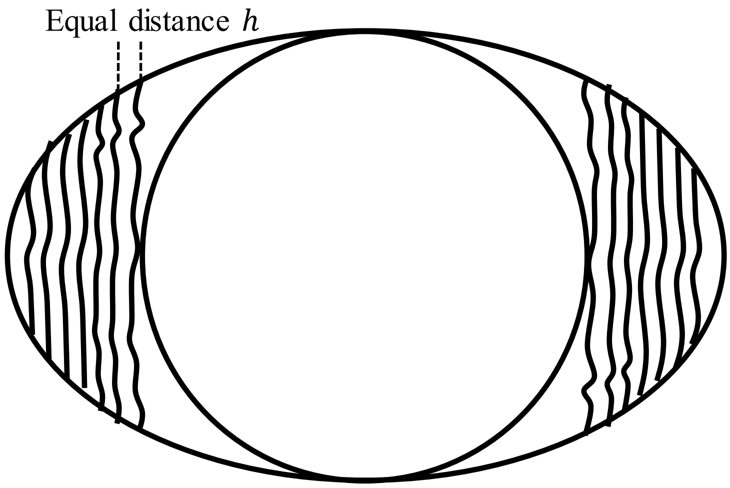

Figure 3.10 Illustration of Bažant et al. (1993)

The aforementioned methods require additional experimental work to determine the BWS for each rock type, which is sometimes difficult to implement due to lack of experimental data. As the conventional stress estimation from borehole breakout has difficulties in obtaining the absolute magnitudes, a machine learning algorithm has been developed by Lin et al. (2020). The model is trained based on the experimental data and validated against field data which are all from the literature. The parameters used in the training process include breakout depth, angular span and BWS. Since the previous data are from different rock types and do not contain the information to use the above techniques for BWS, it is not feasible to use either technique for the general determination of BWS. Therefore, Lin et al. (2020) collected existing uniaxial test data (Haimson and Herrick 1989; Carter 1992) on pre-drilled blocks, see Figure 3.11, and derived an empirical relationship between BWS and borehole size:

$$\boldsymbol{BWS} = (\mathbf{0.0005}\boldsymbol{R}^{\mathbf{2}} - \mathbf{0.0638}\boldsymbol{R} + \mathbf{2.7885}) \times \boldsymbol{UCS} \tag{3.17}$$

The equation is only applicable to the determination of BWS for the experimental cases and primarily for model training, where the borehole radius is below 15 mm. Due to the similarity of rock properties between this experiment and the collected data, this empirical relationship was used directly for the BWS calculation of Gosford sandstone. The estimated BWS of radii 8 mm, 11 mm and 15 mm are 97.72 MPa, 90.83 MPa and 82.23 MPa, respectively. Eq. (3.9) is again used to predict angular span with the newly estimated BWS, and results are shown in Figure 3.12.

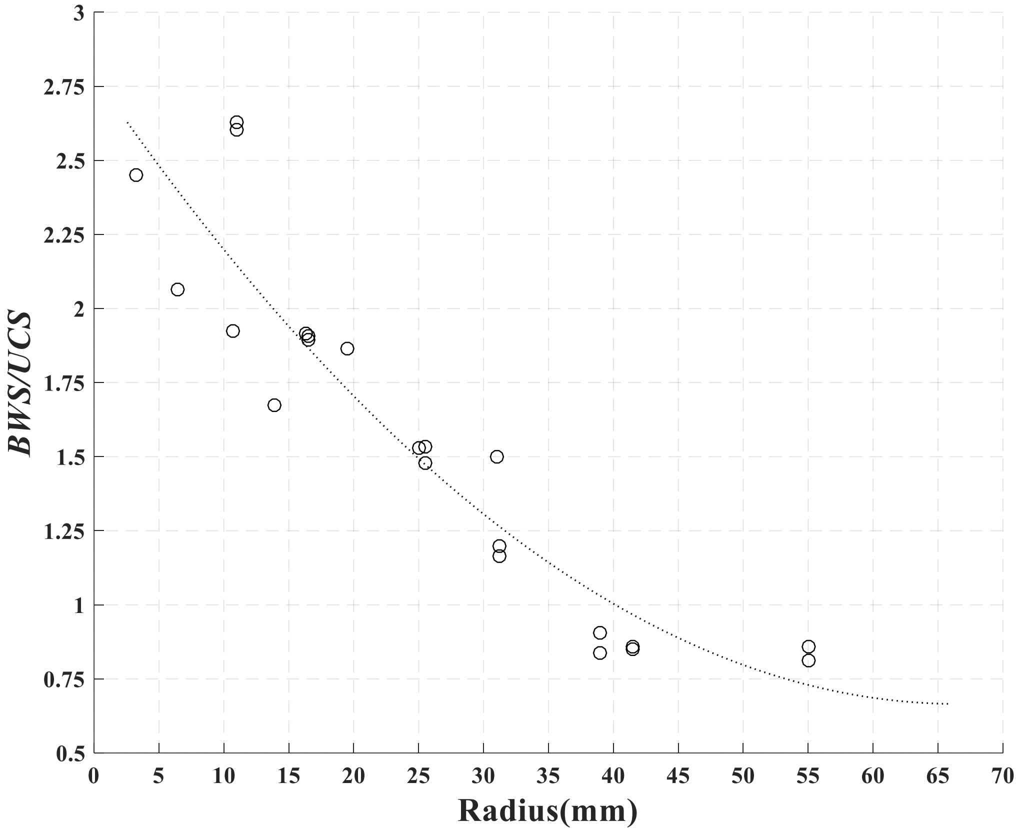

Figure 3.11 BWS/UCS vs borehole radius after Lin et al. (2020)

Based on the results, it can be observed that predictions are more reasonable than before. In particular, for a 15 mm borehole size, the prediction is very accurate compared with the experimental results. Barton et al. (1988)'s model overestimated the angular spans for both 8 mm and 11 mm borehole radii, with the 8 mm hole size having the largest discrepancy between predicted and experimental results. This indicates that the larger the hole size, the better the prediction the Barton et al. (1988) model would produce. However, the discrepancies may also likely be due to the lack of data for smaller hole sizes. As displayed in Figure 3.11, the majority of the data have hole sizes over 10 mm. In this case, the empirical relationship might not yield a very accurate estimation for BWS for hole sizes below 10 mm. Collecting more BWS data would improve the empirical relationship.

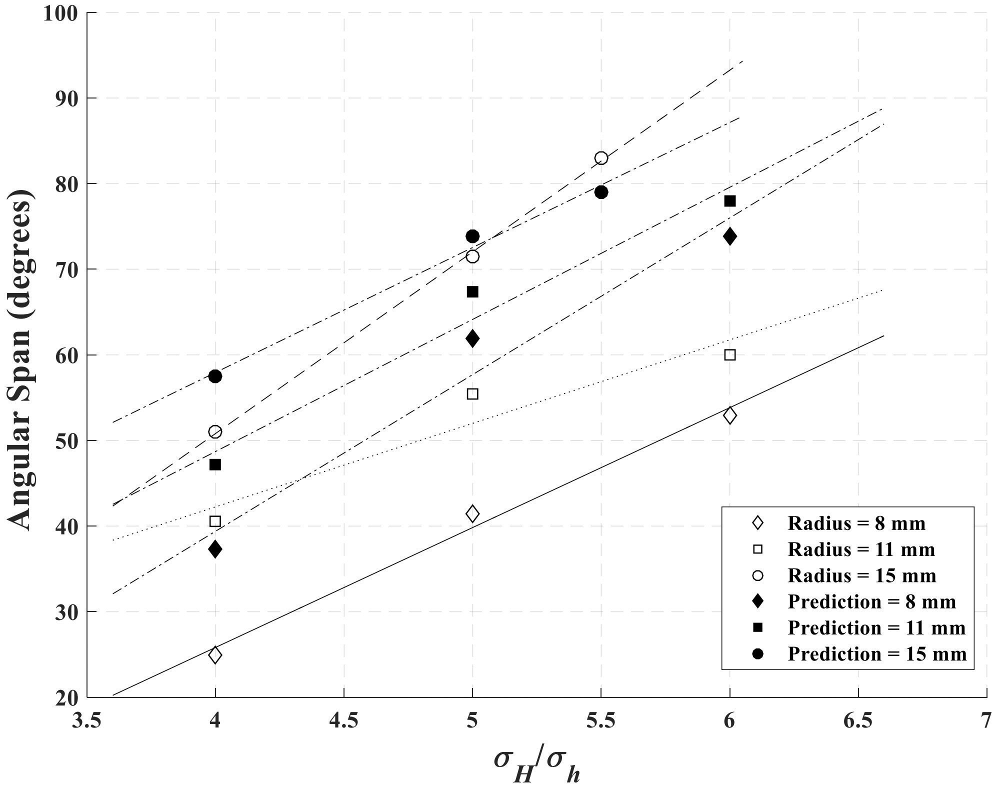

Figure 3.12 Experimental results with predictions including borehole size effect

3.1.2.4 Further investigation on breakout geometries

3.1.2.4.1 Breakout angular span

Angular span is the most crucial parameter for in-situ stress estimation as it is reported to form quickly and not to widen (Mastin 1984; Zoback et al. 1985; Zheng et al. 1989; Schoenball et al. 2014). However, many studies have argued that the breakout angular span increases with σ_H for constant σ_h and σ_v (Haimson and Herrick 1986; Haimson and Herrick 1989; Haimson et al. 1991; Haimson and Song 1993; Herrick and Haimson 1994; Haimson and Lee 2004; Lee and Haimson 2006; Lee et al. 2016), and therefore it is considered to be worthwhile to re-investigate the trend of angular span with respect to horizontal stresses.

$$\boldsymbol{2\theta_b = 180^{\circ} - cos^{-1}(\frac{a\sigma_h + \sigma_h - BWS}{2(a\sigma_h - \sigma_h)})} \tag{3.18}$$

The model proposed by Barton et al. (1988) is analysed here for the relationship between angular span and horizontal stress ratio in a vertical borehole. For the same rock property, to examine whether the angular span increases with increasing horizontal stress ratio, σ_H, σ_h should be kept as a constant rather than a parameter. Thus, $\sigma_H = a\sigma_h$, where a is the horizontal stress ratio; and Eq. (3.9) can be rearranged as:

$$\boldsymbol{f(a) = 2\theta_b = 180^\circ - cos^{-1}(\frac{a\sigma_h + \sigma_h - UCS}{2(a\sigma_h - \sigma_h)})} \tag{3.19}$$

The first order derivative of the function with respect to a can indicate the angular span change with respect to the horizontal stress ratio:

$$\boldsymbol{\frac{df(a)}{da} = \frac{UCS - 2\sigma_h}{2\sigma_h(a-1)^2\sqrt{1 - \frac{(a\sigma_h - UCS + \sigma_h)^2}{4(a\sigma_h - \sigma_h)^2}}})} \tag{3.20}$$

Since the horizontal stress ratio, (a) is always greater than 1, $(a-1)^2$ and $\sqrt{1 - \frac{(a\sigma_h - UCS + \sigma_h)^2}{4(a\sigma_h - \sigma_h)^2}}$ should be greater than 0, which means the denominator of Eq. (3.20) is positive. Thus, the term that defines the relationship between angular span and horizontal stress ratio is the numerator, i.e. $UCS - 2\sigma_h$.

If $UCS > 2\sigma_h$, then the function has a positive first order derivative, which means the breakout width increases with the horizontal stress ratio and σ_H. This agrees with the prevailing argument.

If $UCS = 2\sigma_h$, the derivative is zero, which means there is an extremity occurring, which can also be considered as the transitional point.

If $UCS < 2\sigma_h$, a negative derivative is obtained. Given the increase in horizontal stress ratio, the breakout angular span can be narrower at constant σ_h and σ_v. This indicates that there may be an 'unconventional trend' between the angular span and the increasing horizontal stress ratio, which has not been observed in breakout depth in experimental conditions (Haimson et al. 1991; Herrick and Haimson 1994; Haimson and Lee 2004; Lee and Haimson 2006; Sahara et al. 2017). Figure 3.13 shows the previous experimental observations which satisfy this stress–strength condition and constant σ_h and σ_v.

Interestingly, a growth in angular span with increasing horizontal stress ratio is still observed regardless of the UCS of specimens, which disagrees with the explanation above. Nevertheless, this can be explained by the hole size effect discussed in the previous section, in which the borehole wall strength is significantly amplified for smaller hole size. To take account of the hole size effect, data reported by Lee and Haimson (2006) is carefully analysed. Based on Eq. (3.17), the BWS of the rock specimen is converted to 75.28 MPa. Thereby, according to Eq. (3.5), σ_θ along the hole at different angles can be estimated and is depicted together with its UCS and BWS in Figure 3.14. If σ_θ is greater than the rock strength, breakout should occur at that angle, i.e. the region of the stress curve that is above the UCS or BWS line.

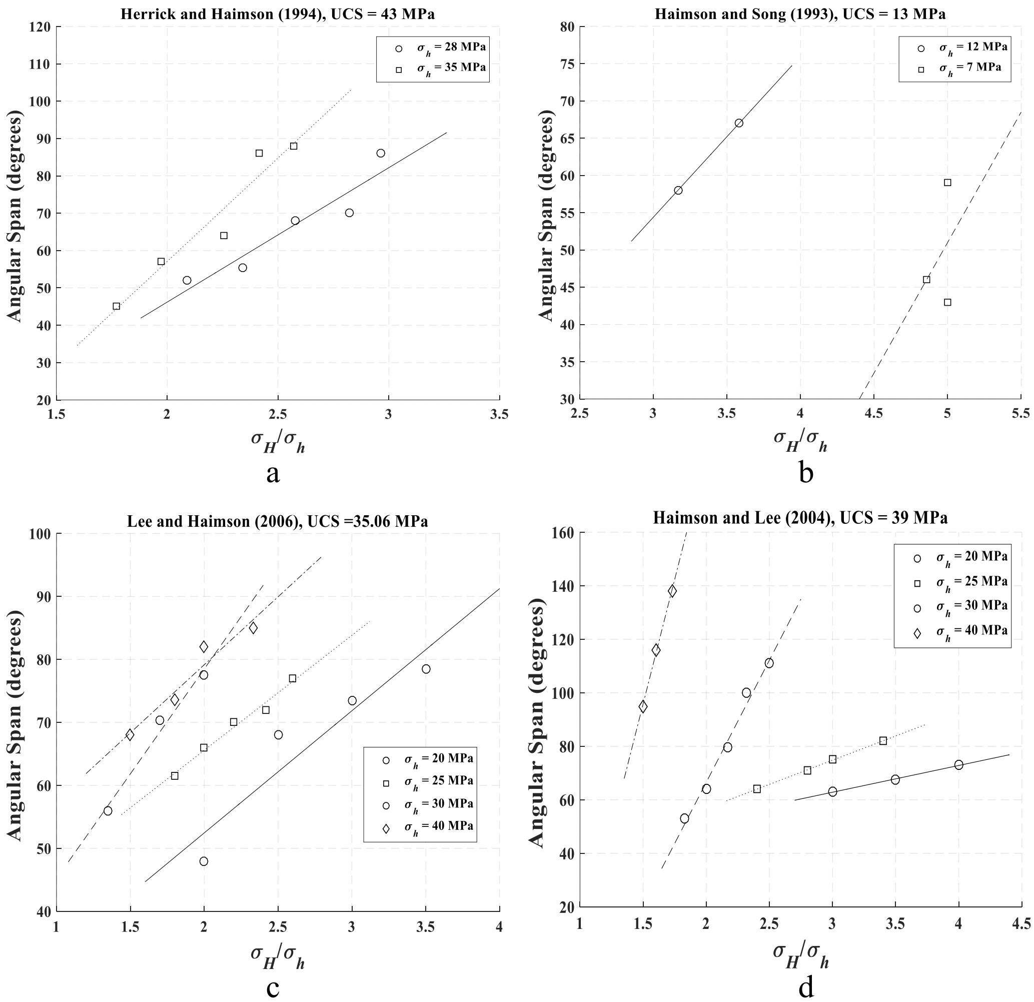

Figure 3.13 Previous experimental data where $UCS < 2\sigma_h$

From Figure 3.14, it can be seen that σ_θ is higher for a higher horizontal stress ratio until the angular span is at 120°. After this angle, a reverse trend can be observed such that the increasing horizontal stress ratio will result in a lower σ_θ thus narrower angular span. At 120°, σ_θ can be expressed from Eq. (3.5):

$$\sigma_\theta = S_H + S_h - 2(S_H - S_h)cos60^\circ = 2S_h \tag{3.21}$$

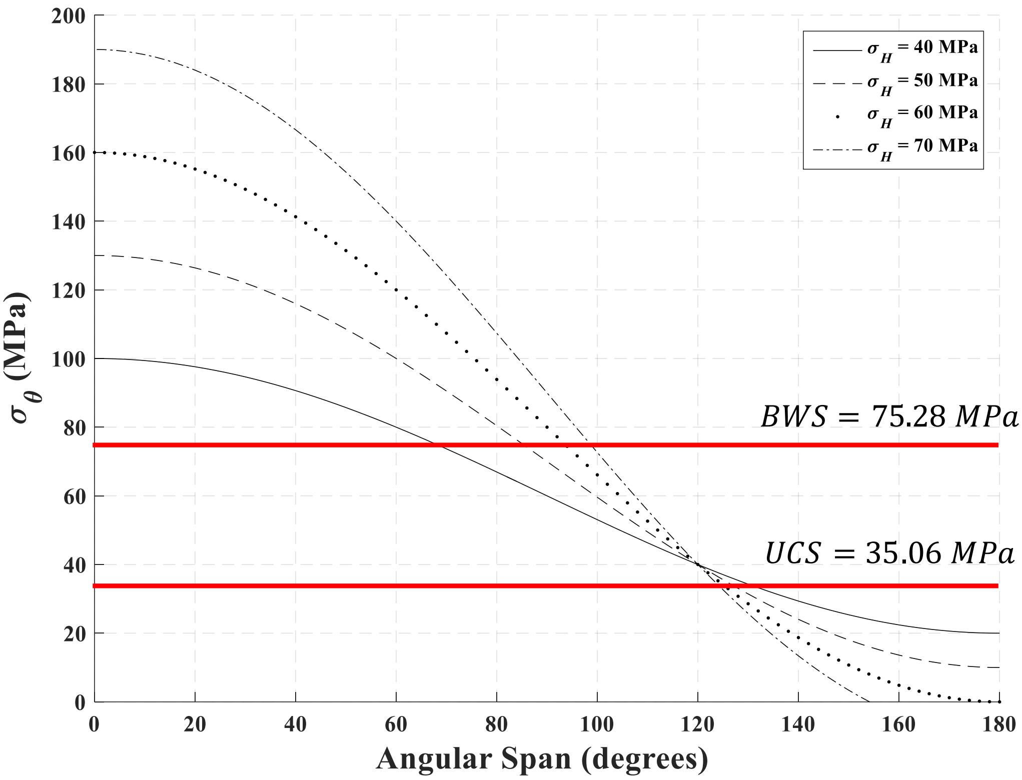

Figure 3.14 Tangential stress along the borehole, where σ_h = 20 MPa

Assuming S_h is constant, σ_θ at 120° should always be the same regardless of σ_H. This also indicates that if the rock strength is equal to $2S_h$, the breakout angular span produced should be 120°, see Figure 3.14 and Figure 3.15.

Although the experimental conditions satisfied the unconventional trend requirement, $UCS < 2\sigma_h$, the actual hole strength BWS is three times more than σ_h because of the small hole size tested. As $BWS > 2\sigma_h$, this is still under the conventional scenario in which the higher stress ratio yields a wider angular span, as shown in Figure 3.13. In this case, Eq. (3.9) should be re-expressed in terms of BWS:

$$2\theta_b = 180^\circ - cos^{-1}(\frac{a\sigma_h + \sigma_h - BWS}{2(a\sigma_h - \sigma_h)}) \tag{3.22}$$

It is also noted that there is one set of data, σ_h = 40 MPa in Lee and Haimson (2006), where $BWS < 2\sigma_h$, but the unconventional trend is still not observed in that data. As discussed earlier, this might be due to the limitation of the empirical relationship, which may underestimate the BWS value for smaller hole sizes. Another possible explanation is the influence of the vertical stress confinement. In the their experiment, the strike-slip faulting mechanism ($\sigma_H > \sigma_v > \sigma_h$) was considered, to keep σ_v as the intermediate stress, σ_v had to increase with σ_h in different tests, which can apply more confinement to the rock around the hole (Song 1998; Chang et al. 2010). It is hence suggested that under experimental conditions for breakout analysis, the influence of BWS and σ_v should be considered.

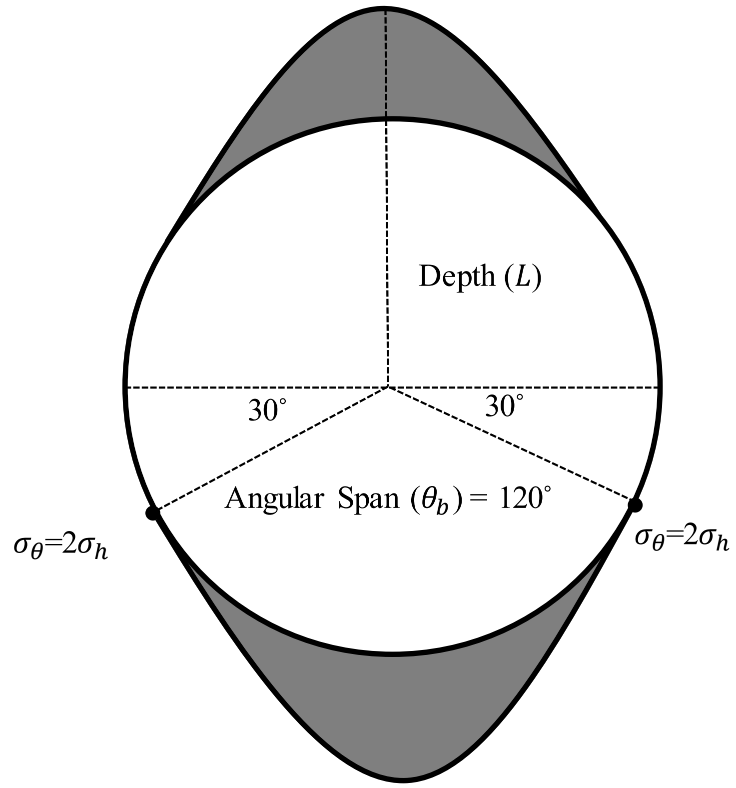

Figure 3.15 Tangential stresses at breakout = 120°

3.1.2.4.2 Breakout depth

Unlike the angular span, breakout depth is more complicated and difficult to predict by an analytical solution. This is mainly because of its inelastic deformation and time dependent propagation behaviour observed in the field and numerically (Mastin 1984; Barton et al. 1988; Kessels 1989; Schoenball et al. 2014). Another reason is that the stress condition is not simply in the rock along the borehole wall.

Gough and Bell (1982) attempted to use angular span to compute the breakout depth based on the Mohr–Coulomb criterion. They assumed that breakout commences at the wall and forms into a V-shape with the intersection of two major shear fracture planes at the breakout tip, as shown in Figure 3.16. However, since the breakout formation and propagation involve both shear and tensile fractures (Tronvoll and Fjaer 1994; Cuss et al. 2003; Lee et al. 2016), a simple shear failure model does not solve the problem.

Zoback et al. (1985) combined the Kirsch solution and Mohr–Coulomb criterion and postulated a model in which the breakout depth can be calculated with given horizontal stress magnitudes and Mohr–Coulomb parameters. For the same reason as Gough and Bell (1982) and the breakout propagation beyond the elastic condition, the model significantly underestimates the breakout depth. Haimson and Herrick (1986) revealed that although the model underestimates the breakout depth compared with experimental results, the prediction of breakout depth follows a similar trend as was observed in experiments.

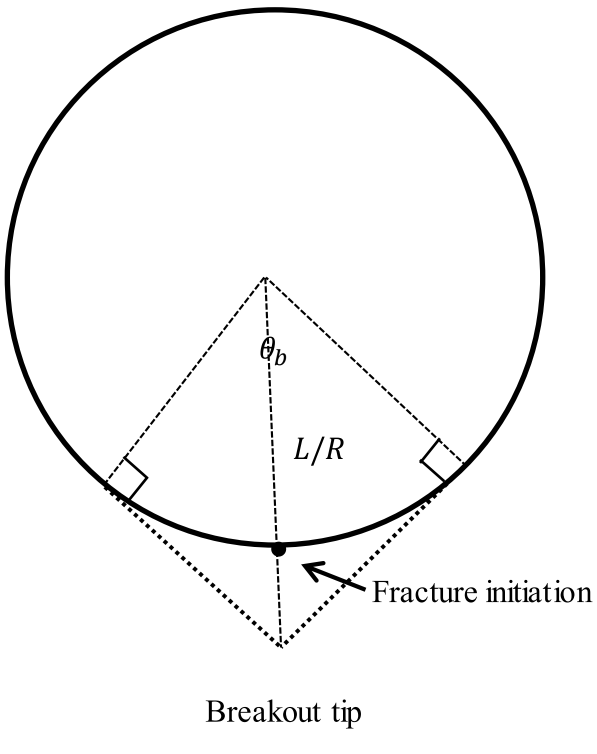

Figure 3.16 Shear fractures from Gough and Bell (1982)

Current analytical solutions cannot effectively predict the relationship between breakout depth and horizontal stress ratio, and it is therefore only possible to determine this relationship from experimental observations. The experimental results presented here, as well as those from previous studies (Haimson and Herrick 1986; Haimson and Herrick 1989; Haimson and Song 1993; Herrick and Haimson 1994; Haimson and Lee 2004; Lee and Haimson 2006), all show that breakout depth increases with the increasing horizontal stress ratio and σ_H. This indicates that breakout depth should increase with the horizontal stress ratio.

3.1.2.4.3 The relationship between breakout geometries

As discussed earlier, some researchers suggest that both breakout geometries are dependent on each other and redundant, and that there is an exclusive relationship between the two geometries that is insensitive to the stress magnitudes. In this case, the estimation of two horizontal stress magnitudes using breakout geometries is not viable. Figure 3.17 shows the relationship between the breakout depth and angular span under various stress conditions and rock types from previous studies. It can be seen that there is an increasing trend between the two geometries although the gradients are very spread out. The relationship between the breakout geometries may be dependent on the material.

Figure 3.18 shows the experimental results from Haimson and Lee (2004). From the illustration, it is clear that the gradients of each set of experiments are different and cannot be constrained in a narrow band although the trends are increasing. A series of very similar breakout depth values (see the red dot horizontal line in the figure) also have significantly different angular span values. This indicates the relationship between the breakout depth and angular span may not be unique. As the laboratory investigation was performed on the same rock properties, the only factors that changed from test to test are the horizontal stress magnitudes. The changes in gradients could only be the results of various horizontal stress magnitudes applied. The results shown here imply that breakout geometries may not be redundant factors for stress estimation as their relationship is heavily influenced by the horizontal stress magnitudes.

As discussed in Section 3.1.2.4.1, the breakout angular span increases with the increasing horizontal stress ratio unless the applied minimum horizontal stress is over half of the BWS value. This is very difficult to observe in the experimental conditions due to the hole size effect. On the other hand, the breakout depth increases with the increasing horizontal stress ratio. This is a rather special case but also shows the non-redundancy between the two breakout geometries and the influence of horizontal stress magnitudes (ratio) on this relationship.

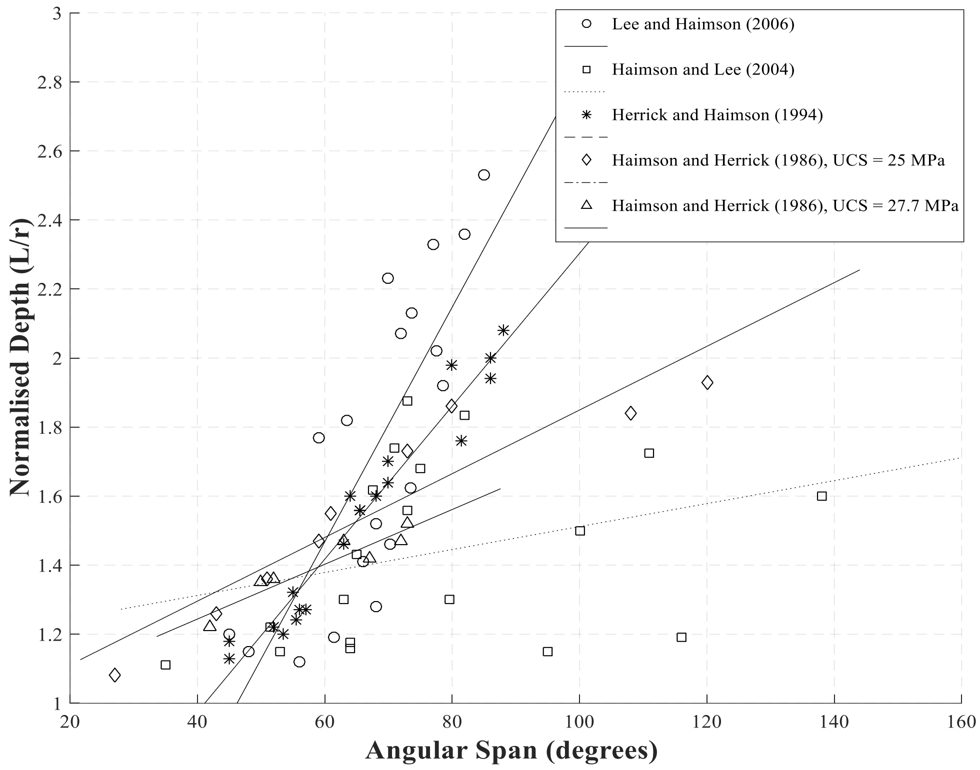

a

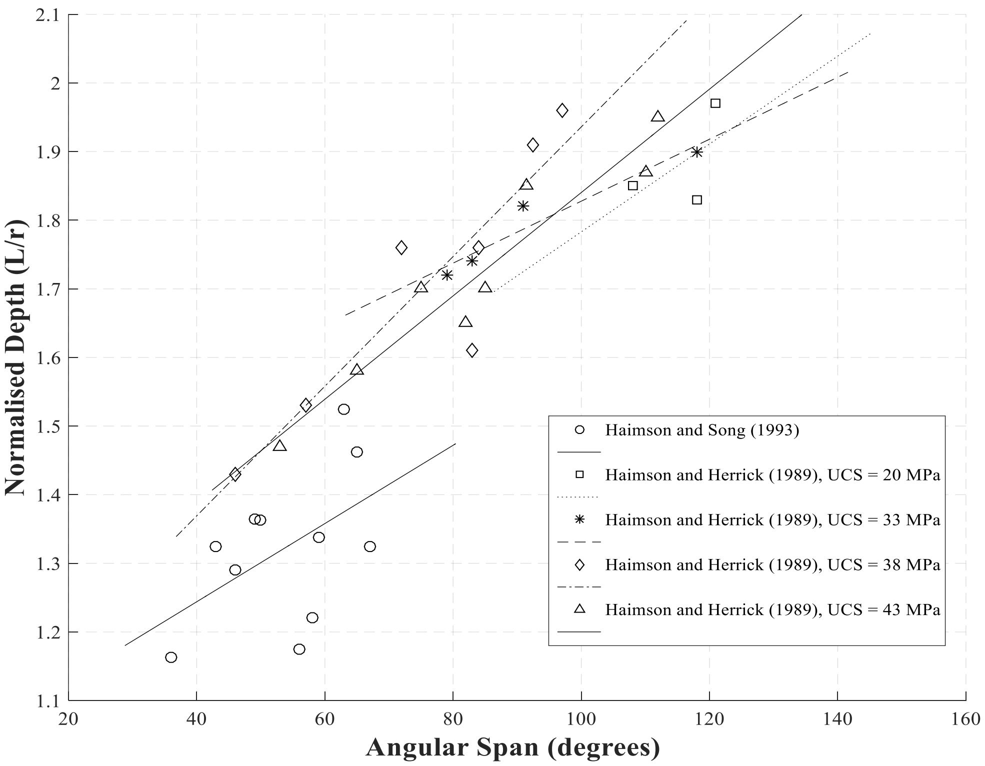

b

Figure 3.17 Previous experimental data on breakout geometries after Lin et al. (2020)

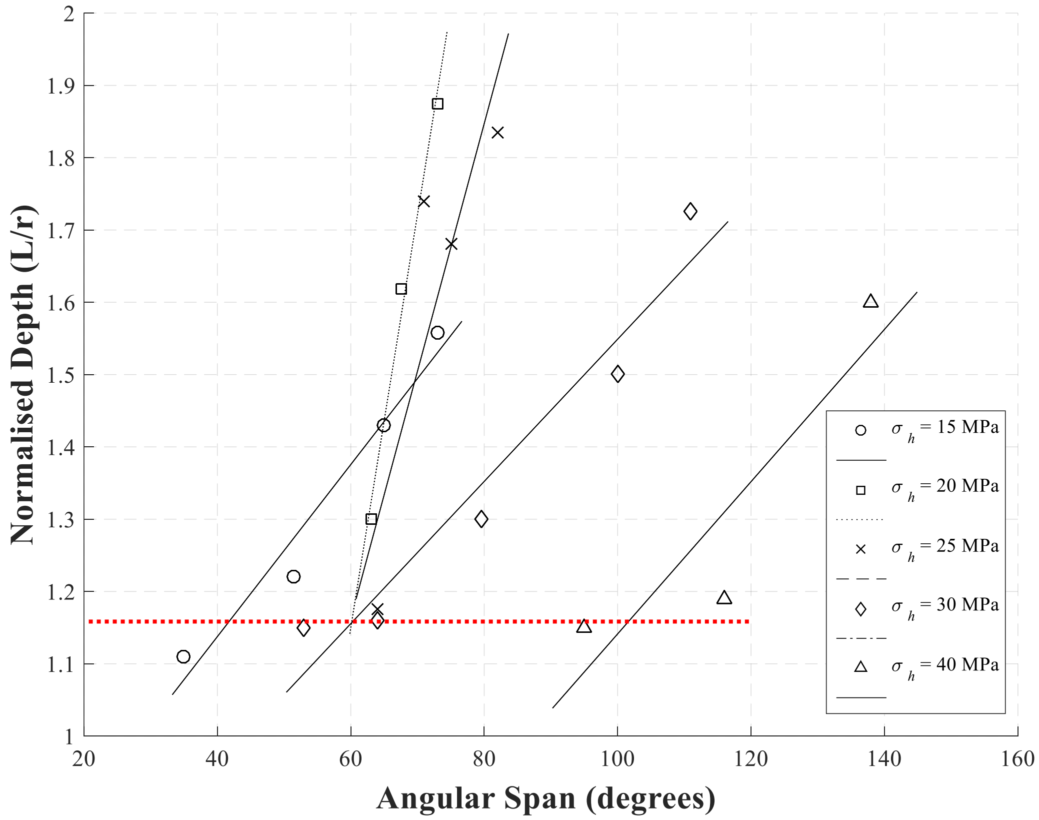

Figure 3.18 Experimental results on breakout geometries from Haimson and Lee (2004)

3.1.3 Conclusion

This chapter presented a set of experimental data on breakout geometries. Results confirm that both angular span and depth are dependent on horizontal stress magnitudes and ratio, which suggest that they can be used for horizontal stress estimation. Under the same stress condition, the comparison between breakout geometries with different hole sizes reveals that hole size has a substantial influence on breakout geometries. Larger hole size tends to yield deeper and wider breakouts, an effect which is not considered by the Kirsch solution or Barton et al. (1988).

The primary reason for this discrepancy is the hole size effect, which has been discussed by several researchers. However, models proposed by Carter (1992) and Bažant et al. (1993) all include empirical parameters which require additional experiments and assumptions. To incorporate this effect in the experimental investigation, this chapter used an empirical relationship between hole size and borehole wall strength that was proposed by Lin et al. (2020). After taking account of the hole size effect, the predictions using Barton et al. (1988) are much closer to the experimental results and reasonable. In general, all existing experimental investigations of hole size effect modify the specimen size with the hole size, i.e. the larger the hole size, the larger the specimen. This is not ideal because the scale effect of rock strength also exists due to the change in specimen dimensions, which the previous experimental results do not take account of when studying the hole size effect. The current study has proposed a series of uniaxial compression tests on block specimens with pre-drilled holes while keeping the specimen dimensions the same. This enables the elimination of the scale effect on specimen dimension changes, and a focus only on the hole size effect.

The analysis on the previous experimental studies found that the relationship between the breakout depth and angular span is not unique although they appear to increase with each other. In fact, the relationship between the two geometries is considerably sensitive to the horizontal stress magnitudes. The analysis performed in this study revealed that the breakout angular span may be narrower if the minimum horizontal stress value is lower than half of the BWS value. However, this is difficult to observe in the experimental conditions due to the hole size effect. Nevertheless, this suggests a very special case where the higher horizontal stress ratio could lead to a narrower but deeper breakout under certain stress–strength conditions. Both arguments indicate that the relationship between two breakout geometries is not unique, but is influenced by the horizontal stress magnitudes, leading to a tentative conclusion that they are not redundant factors for stress estimation.

3.2 HOLE SIZE EFFECT

3.2.1 Experimental procedures

Gosford sandstone, a common construction material in Australia, was obtained from a quarry in the Sydney Basin, Australia. Based on uniaxial compressive tests and Brazilian tests, its material properties are uniaxial compressive strength (UCS) of 37.6 MPa, Young's modulus (E) of 6.0 GPa, Poisson's ratio (v) of 0.23 and tensile strength (σ_T) of 3.1 MPa. Samples were prepared as cubic shapes with circular holes pre-drilled perpendicular to the bedding plane at the centre. To study the influence of borehole size and specimen size on breakout initiation, two series of normal compression tests were carried out at various borehole sizes (6–12.5 mm radii) and specimen sizes ($60 \times 60 \times 60$ mm^3 – $135 \times 135 \times 135$ mm^3). Table 3.1 summarises the sample specifications.

Series 1 constant ratio tests used a constant hole radius to specimen size ratio of 10, whereas specimen dimensions in the Series 2 constant specimen size tests were the same regardless of the borehole size, as shown in Figure 3.19a. This helps isolate specimen size as the only parameter in the experiments to investigate its influence on breakout initiation stress.

Table 3.1 Rock specimen dimensions

Hole Size	Series 1 Specimen Dimensions	Series 2 Specimen Dimensions
6 mm	$60 \times 60 \times 60$ mm^3	$135 \times 135 \times 135$ mm^3
8 mm	$80 \times 80 \times 80$ mm^3	$135 \times 135 \times 135$ mm^3
11 mm	$110 \times 110 \times 110$ mm^3	$135 \times 135 \times 135$ mm^3
12.5 mm	$125 \times 125 \times 125$ mm^3	$135 \times 135 \times 135$ mm^3

Normal compression tests were performed on cubic sandstone specimens via a MTS machine. To ensure the experimental results were not biased, tests under each condition were repeated three times. In total, 24 tests were conducted. Figure 3.19b shows a typical experimental setup. For each test, three strain gauges were mounted inside the hole to detect the on-set breakout initiation. A pair of strain gauges was glued in the hole sidewall that was orthogonal to the axial compressive stress direction, aiming to measure the circumferential deformation, while the remaining gauge was placed along the hole direction to monitor the axial strain. Strain gauges were pre-calibrated against the National Instrument (NI) based on their standard resistance and the strain change during normal compression test was continuously collected using LabVIEW software.

a b

Figure 3.19 a) Specimen dimensions, b) a normal compression test with three strain gauges mounted inside the hole

3.2.2 Results and discussion

3.2.2.1 Experimental results

Fractures initiate and develop around the borehole prior to the sample failure due to local stress concentration. In general, three fracture locations are investigated in previous studies: the primary fracture, remote fracture and sidewall fracture (Carter et al. 1991). This study only focuses on sidewall fracture as it explicitly indicates the on-set breakout initiation. As suggested by numerous researchers, the sudden decrease in stress–strain curves of strain gauges after the linear elastic stage can be considered as the critical axial stress for breakout initiation (σ_P^*) (Nesetova and Lajtai 1973; Haimson and Herrick 1989; Carter 1992; Dzik and Lajtai 1996; Dresen et al. 2010; Meier et al. 2013). Figure 3.20a shows the strain gauge recordings of the constant specimen size (Series 2) specimen with 11 mm borehole radius. In the figure, a deflection point can be observed, indicating the breakout initiation stress. The stress–strain curves of circumferential strain gauges show similar behaviour as the data presented in previous laboratory studies (Carter 1992; Dzik and Lajtai 1996; Dresen et al. 2010; Meier et al. 2013), suggesting the breakout initiation stresses collected from this study are reasonable. In addition, the gradient of the axial strain gauge is rather smooth, and the deflection point is difficult to determine accurately. In this case, the breakout initiation stress was solely extracted from the recordings of circumferential strain gauges. This approach was also undertaken by Dresen et al. (2010) and Meier et al. (2013).

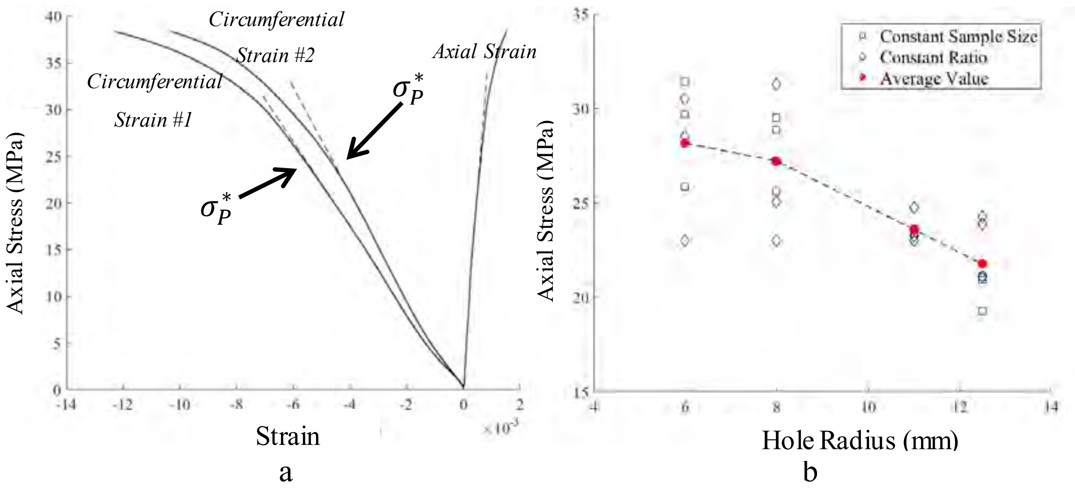

Figure 3.20 a) Strain gauge recordings under 11 mm borehole radius with constant specimen size; b) experimental results of breakout initiation stress, where the red dots represent the average stress at each borehole radius

Figure 3.20b displays the experimental results of two series of tests: Series 1 constant ratio and Series 2 constant specimen size. As illustrated in the figure, there is no clear difference between the two series of tests. This implies that the specimen size may not have a significant influence on the borehole size effect tests, such that both test approaches can be used for future studies. The average values at each borehole size show a decreasing trend as the hole radius increases. This is in good agreement with the popular argument that the larger the borehole size, the lower the stress required to initiate borehole breakout (Bažant et al. 1993; Van den Hoek et al. 1994; Leriche 2017).

According to the Kirsch solution (Jaeger et al. 2009), the critical tangential stress for breakout initiation can be expressed as:

$$\boldsymbol{\sigma_\theta^* = S_H + S_h - 2(S_H - S_h)cos2\theta = 3S_H - S_h} \tag{3.23}$$

where σ_θ = tangential stress around the borehole, σ_H and σ_h = maximum and minimum horizontal stresses, θ = angle from σ_H direction. In this chapter, experiments were carried out under uniaxial compression, such that σ_H is equal to the axial stress applied and σ_h = 0. Hence, the critical tangential stress (σ_θ^*) for breakout initiation is:

$$\boldsymbol{\sigma_\theta^* = 3\sigma_H = 3\sigma_P^*} \tag{3.24}$$

Based on Eq. (3.24), the σ_θ^*/UCS ratio for each test was calculated. Results are shown in Figure 3.21a, together with data in the literature collected from normal compression tests and hollow cylinder tests.

Experimental results show that the experimentally studied breakout initiation stresses are generally higher than those of the UCS values. This implies that this borehole wall strength (Walton et al. 2015; Leriche 2017) amplification requires careful consideration while investigating the influence of stress magnitudes on borehole breakout geometries (Lin et al. 2019). The similar trends observed from both experiments and previous studies confirm that there is a definite relationship between the breakout initiation stress and borehole radius in laboratory conditions. On the other hand, the breakout initiation stress tends to be equal to the UCS value as the borehole radius is approximately 40 mm and remains constant as the borehole radius increases. In mining conditions, the standard exploration borehole radii are usually 37.85 mm (NQ) and 48 mm (HQ), which shows that this phenomenon can be neglected in field breakout analysis.

From the figure, it is clear the σ_θ^*/UCS ratios obtained from normal compression tests are always lower than 3, whereas the ratios in hollow cylinder tests are usually greater than 3. This is because the confining pressure plays a critical role in hollow cylinder tests rather than in normal compression tests. If the σ_θ^*/UCS ratio approaches 3, Eq. (3.24) has to satisfy that:

$$\boldsymbol{\sigma_\theta^* = 3UCS = 3\sigma_P^*} \tag{3.25}$$

Such that the UCS equals the critical axial stress for breakout initiation:

$$\boldsymbol{UCS = \sigma_P^*} \tag{3.26}$$

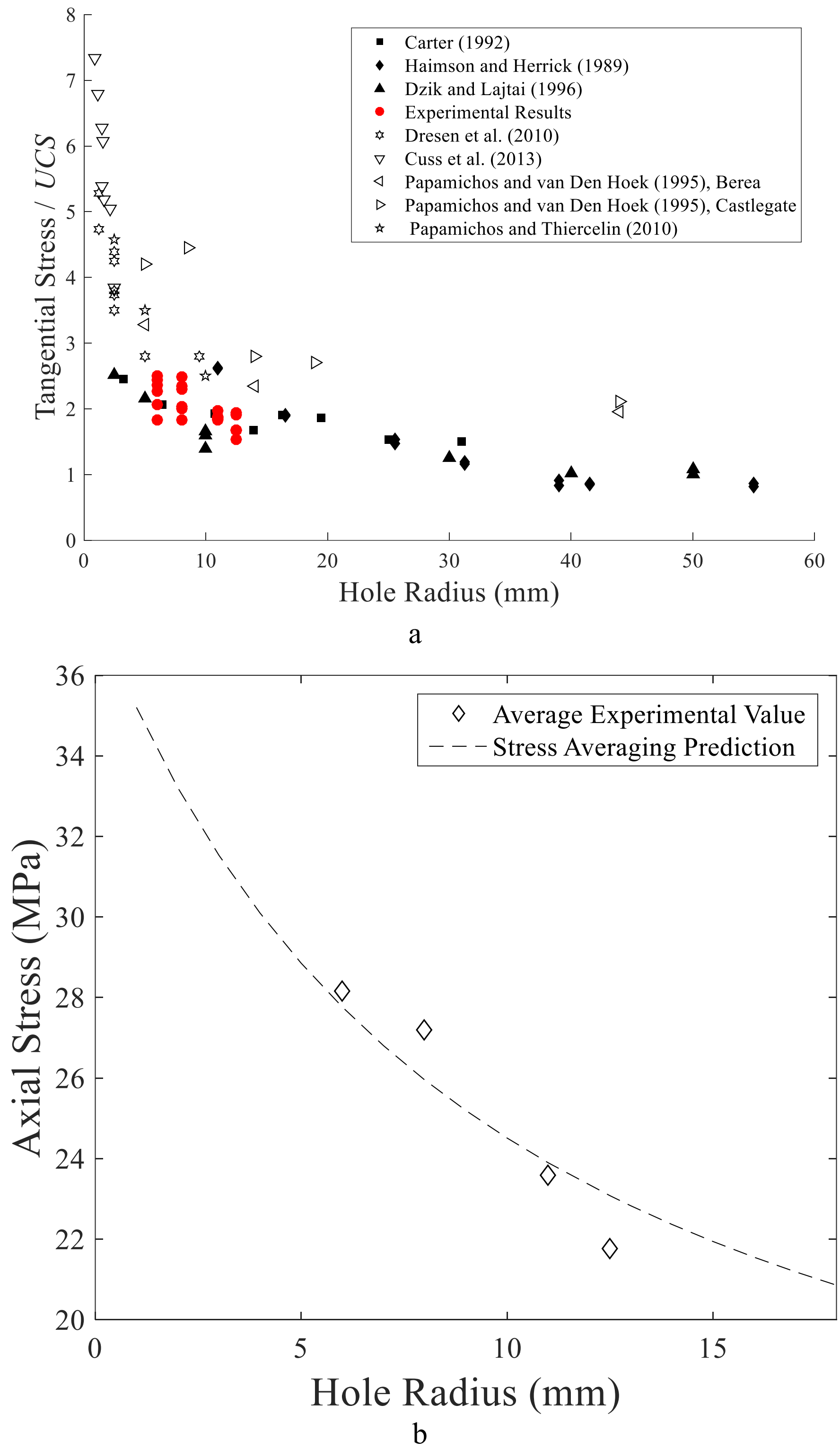

Figure 3.21 a) Experimental results against data in the literature, where the solid markers represent the normal compression tests, and the unfilled markers represent the hollow cylinder tests; b) prediction using the stress averaging concept against the experimental data

This is practically impossible to achieve as the sample at this point has failed as the axial compressive stress exceeded the rock strength. On the other hand, the hollow cylinder test applies hydrostatic pressure around the cylindrical specimen, in which the rock specimen is subjected to equal all-around stress instead of pure axial loading which leads to breakout nucleation prior to sample failure.

3.2.2.2 Prediction on experimental data

3.2.2.2.1 Stress averaging

To model the relationship between the breakout initiation stress and radius, Lajtai (1972) proposed that the stress may be effectively averaged over a critical distance if the area is subjected to high stress gradients. This stress averaging concept was later extended by Carter (1992), suggesting that the critical axial stress for breakout initiation can be estimated by assuming the rock near the borehole is subjected to a uniaxial stress condition:

$$\boldsymbol{\sigma_P^*} = \frac{\boldsymbol{d \times UCS}}{(\boldsymbol{R}+\boldsymbol{d})(\boldsymbol{1}-\frac{\boldsymbol{R^2}}{\boldsymbol{2(R+d)^2}}-\frac{\boldsymbol{R^4}}{\boldsymbol{2(R+d)^4}})} \tag{3.27}$$

where d = material constant which represents the ability of redistributing stress concentration and R = borehole radius. This formula is used in this study to predict the critical axial stress for breakout initiation assuming d = 14.2 mm, which was determined by the curve fitting procedures proposed by Carter (1992). Figure 3.21b shows the model results against the experimental data in this study. The prediction values are quite close to the experimental results, and both indicate a decreasing trend with larger borehole radius. Based on Eq. (3.27), the maximum σ_P^* would occur when R = 0 mm as the equation shows a monotone decreasing trend:

$$\boldsymbol{\sigma_P^*} = \frac{\boldsymbol{d \times UCS}}{(\boldsymbol{0}+\boldsymbol{d})(\boldsymbol{1}-\frac{\boldsymbol{0^2}}{\boldsymbol{2(0+d)^2}}-\frac{\boldsymbol{0^4}}{\boldsymbol{2(0+d)^4}})} = \boldsymbol{UCS} \tag{3.28}$$

At R = 0 mm, the borehole does not exist which means that the critical axial stress (σ_P^*) for breakout initiation calculated from the stress averaging concept should always be smaller than the UCS, as discussed in the previous section for Eq. (3.26). Although the prediction is well aligned with the experimental results, a 14.2 mm stress averaging constant, d, seems like an extended distance which may not be appropriate for the calculation providing the hole radii used in the experimental investigation were smaller than 14.2 mm. If a 14.2 mm critical stress averaging distance is considered, the radial stress (σ_r) should not be negligible, such that the breakout initiation is no longer governed by the simple uniaxial compressive condition. The concept hence should either consider a shorter d for the uniaxial compressive condition, or take account of the influence of σ_r.

Figure 3.22a illustrates the relationship between the critical axial stress for breakout initiation (σ_P^*) and the stress averaging distance (d) at various borehole radii. In the figure, it is clear that shorter d always leads to lower σ_P^*, such that it provides a worse prediction of the experimental data presented in this study. This is mainly because the tangential stress is averaged over a longer distance, d. The results here indicate that this approach may not be applicable and the radial stress should be considered during the analysis.

As d is a material property (Lajtai 1972), any stress within the distance should be effectively averaged. This means not only the mean tangential stress ($\overline{\sigma_\theta}$), but also the mean radial stress ($\overline{\sigma_r}$) should be used over d. The equations of each stress can be expressed as (Carter 1992):

$$\overline{\boldsymbol{\sigma_\theta}} = \frac{\boldsymbol{\sigma_P^*}}{\boldsymbol{d}}(\boldsymbol{R}+\boldsymbol{d})(\mathbf{1}-\frac{\boldsymbol{R}^2}{2(\boldsymbol{R}+\boldsymbol{d})^2}-\frac{\boldsymbol{R}^4}{2(\boldsymbol{R}+\boldsymbol{d})^4}) \tag{3.29}$$

$$\overline{\boldsymbol{\sigma_r}} = \frac{\boldsymbol{\sigma_P^*}\times\boldsymbol{R}}{\boldsymbol{d}}(\mathbf{1}-\frac{3\boldsymbol{R}}{2(\boldsymbol{R}+\boldsymbol{d})}+\frac{\boldsymbol{R}^3}{2(\boldsymbol{R}+\boldsymbol{d})^3}) \tag{3.30}$$

As the secondary stress ($\overline{\sigma_r}$) cannot be neglected around the borehole, a commonly used failure criterion, i.e. Mohr–Coulomb, is considered as the governing equation, in which the critical failure state can be defined as:

$$\boldsymbol{\sigma_1} = \boldsymbol{UCS}+\boldsymbol{\sigma_3 tan\psi} \tag{3.31}$$

where σ_1 and σ_3 = major and minor stresses, $tan\psi = \frac{1+sin\phi}{1-sin\phi}$, ϕ = friction angle. For the stress state around the borehole, it can be assumed that $\overline{\sigma_\theta}$ and $\overline{\sigma_r}$ are major and minor stresses, respectively and Eq. (3.31) is rearranged as:

$$\overline{\sigma_\theta} = UCS + \overline{\sigma_r} tan\psi \quad (3.32)$$

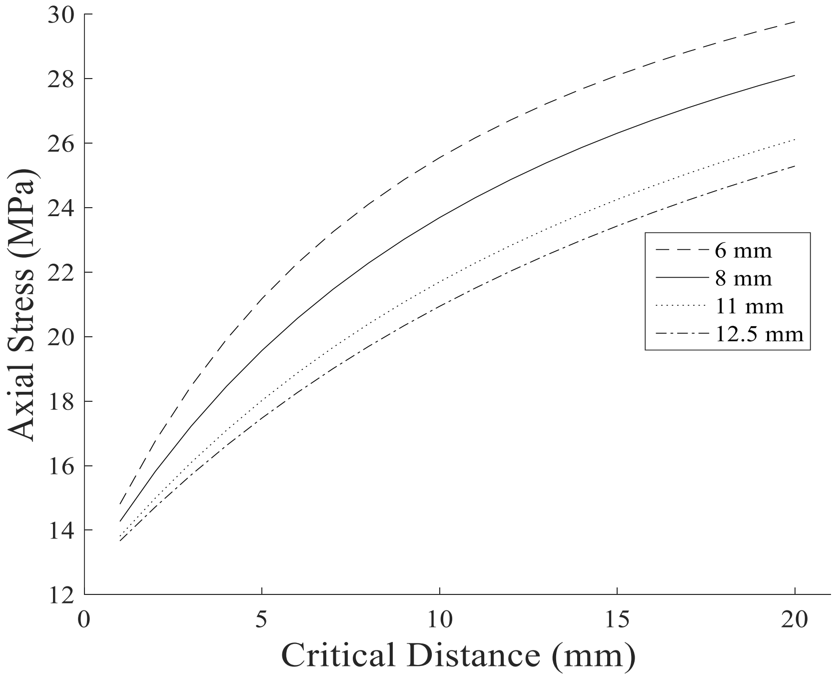

a

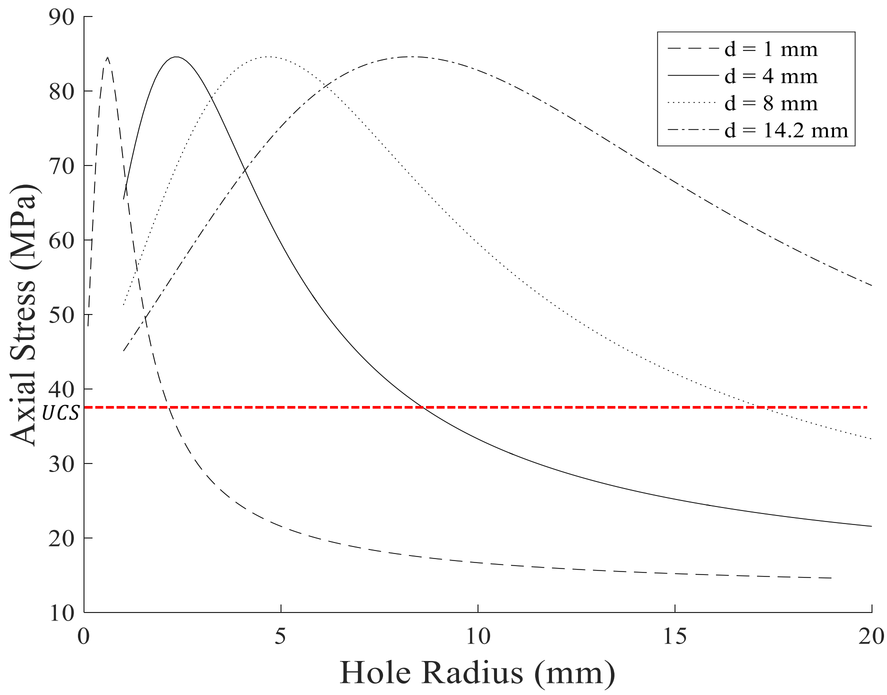

b

Figure 3.22 a) Critical axial stress vs critical distance at various borehole sizes; b) prediction of critical axial stress using the stress averaging concept incorporating Mohr–Coulomb failure criterion at various stress averaging distances

By substituting Eq. (3.29) and Eq. (3.30) into Eq. (3.32), the critical axial stress for breakout initiation can be obtained:

$$\boldsymbol{\sigma_P^*} = \frac{\boldsymbol{d \times UCS}}{-\boldsymbol{tan\psi \times R}\left[\boldsymbol{1 - \frac{3R}{2(R+d)} + \frac{R^3}{2(R+d)^3}}\right] + \boldsymbol{(R+d)}\left[\boldsymbol{1 - \frac{R^2}{2(R+d)^2} - \frac{R^4}{2(R+d)^4}}\right]} \tag{3.33}$$

Figure 3.22b displays the prediction results using the stress averaging concept and Mohr–Coulomb failure criterion, given the friction angle of Gosford sandstone is 35° (Lin et al. 2019), where the horizontal red line indicates the UCS value of the rock specimen. The prediction results should always be lower than the UCS value otherwise the rock sample will fail. The figure shows that σ_P^* first increases then decreases as the borehole size gets longer at various d, which does not match with the experimental observations from this study as well as other studies (Haimson and Herrick 1989; Carter 1992; Dzik and Lajtai 1996) under normal compression tests. In addition, predictions in Figure 3.22b are practically impossible to achieve as the critical axial stress for breakout initiation should not be higher than the UCS value of the rock specimen, as indicated by the horizontal red line in the figure. This is because the rock sample will fail under the uniaxial compressive condition, as discussed in the previous section. Results here suggest the approach does not reliably estimate the borehole size effect, likely due to two reasons: i) the failure criterion is not appropriate for the borehole size analysis, and different failure criteria may change the prediction curve; and ii) the stress that is parallel to the borehole axis is not recognised. To more precisely consider the stress condition around the borehole, this stress should not be neglected and needs to be considered for rock failure. A detailed study on various failure criteria should be carried out to determine the most suitable criterion given the influence of tertiary stress that is parallel to the borehole axis.

3.2.2.2.2 Failure criteria considering pressure-dependency

Based on a series of triaxial compression tests, Santarelli et al. (1986) observed that the Young's modulus of the specimen changes with the applied confinement such that higher confinement leads to higher Young's modulus. Santarelli et al. (1986) argued that the stress–strain relationship around the borehole is not simply linear elastic but rather pressure-dependent due to change in the radial stress (confinement) around the circle. Using this postulation, this study suggested that the maximum tangential stress around the borehole is no longer at the borehole wall but at a distance into the rock (Δr), which the borehole breakout will initiate at some distance away from the borehole wall (Santarelli and Brown 1989). This phenomenon has also been reported by numerous researchers in their experimental studies (Zaitsev 1985; Haimson and Song 1993; Lee and Haimson 1993; Cuss et al. 2003). However, the approach does not provide direct estimation of σ_P^*, given that maximum tangential stress at the breakout initiation location is unknown.

Instead, this study simply uses the Kirsch solution to represent σ_θ^* at the breakout initiation distance ($\Delta r + R$) to predict σ_P^*; this assumption has been implemented previously by Dresen et al. (2010) and Meier et al. (2013) in their predictions on hollow cylinder tests. According to the Kirsch solution (Jaeger et al. 2009), the stress conditions around the borehole can be expressed as:

$$\boldsymbol{\sigma_\theta = \frac{1}{2}(\sigma_H + \sigma_h)\left(1 + \frac{R^2}{r^2}\right) - \frac{1}{2}(\sigma_H - \sigma_h)\left(1 + 3\frac{R^4}{r^4}\right)cos2\theta} \tag{3.34}$$

$$\boldsymbol{\sigma_r = \frac{1}{2}(\sigma_H + \sigma_h)\left(1 - \frac{R^2}{r^2}\right) + \frac{1}{2}(\sigma_H - \sigma_h)\left(1 - 4\frac{R^2}{r^2} + 3\frac{R^4}{r^4}\right)cos2\theta} \tag{3.35}$$

$$\boldsymbol{\sigma_z = \sigma_v - 2v(\sigma_H - \sigma_h)(\frac{R^2}{r^2})cos2\theta} \tag{3.36}$$

where r = point of interest from the centre of the borehole and σ_z = vertical stress around the borehole. Since breakout is initiated at the location along the minimum horizontal stress direction, θ = 90° and $cos2\theta$ = -1. Eq. (3.34)–Eq. (3.36) can thus be rearranged as:

$$\boldsymbol{\sigma_\theta = \frac{1}{2}(\sigma_H + \sigma_h)\left(1 + \frac{R^2}{r^2}\right) + \frac{1}{2}(\sigma_H - \sigma_h)\left(1 + 3\frac{R^4}{r^4}\right)} \tag{3.37}$$

$$\boldsymbol{\sigma_r = \frac{1}{2}(\sigma_H + \sigma_h)\left(1 - \frac{R^2}{r^2}\right) - \frac{1}{2}(\sigma_H - \sigma_h)\left(1 - 4\frac{R^2}{r^2} + 3\frac{R^4}{r^4}\right)} \tag{3.38}$$

$$\boldsymbol{\sigma_z = \sigma_v - 2v(\sigma_H - \sigma_h)(\frac{R^2}{r^2})} \tag{3.39}$$

In the normal compression test, axial stress is the only stress applied to the sample, which means σ_v and σ_h = 0, and $\sigma_H = \sigma_P^*$:

$$\sigma_\theta = \frac{1}{2}\sigma_P^*\left(1+\frac{R^2}{r^2}\right)+\frac{1}{2}\sigma_P^*\left(1+3\frac{R^4}{r^4}\right) \tag{3.40}$$

$$\sigma_r = \frac{1}{2}\sigma_P^*\left(1-\frac{R^2}{r^2}\right)-\frac{1}{2}\sigma_P^*\left(1-4\frac{R^2}{r^2}+3\frac{R^4}{r^4}\right) \tag{3.41}$$

$$\sigma_z = 2v\sigma_P^*\left(\frac{R^2}{r^2}\right) \tag{3.42}$$

The major, intermediate and minor stresses (σ_1-σ_3) can be expressed in terms of σ_θ, σ_r and σ_z at the breakout initiation location. Therefore, the fracture initiation distance from the centre of the borehole ($r = R + \Delta r$) was assumed to be 0.185 mm, as suggested by Dresen et al. (2010) in their study on sandstone. In this study, a number of failure criteria were tested to predict σ_P^* for breakout initiation.

Mohr–Coulomb was the first failure criterion examined, and σ_1 and σ_3 were replaced by σ_θ and σ_r in Eq. (3.31) which can be rearranged as:

$$\sigma_P^* = \frac{2 \times UCS \times r^4}{3 \times R^4 tan\psi + 3 \times R^4 + 2 \times r^4 + R^2 \times r^2 - 3 \times R^2 \times r^2 \times tan\psi} \tag{3.43}$$

A similar approach was taken for other failure criteria including Mogi–Coulomb (Mogi 1967), Murrell (Murrell 1963), Stassi D'Alia (Stassi-D'Alia 1967) and linear fracture initiation (Ashby et al. 1986). Table 3.2 summarises the governing equations. It is noted that for the linear fracture initiation criterion, the stress intensity factor (K_{IC}) and half of the defect length (c) are required. K_{IC} of coarse grained sandstone was determined earlier as approximately 1.46 MPa $\sqrt{\text{m}}$ by Clifton et al. (1976) using internally pressurised, pre-notched, thick-walled cylinder tests (IPPTWC). As discussed by Meier et al. (2013), c can be represented by the pore radius; a 0.04 mm half defect length was selected from previous measurement (Klein and Reuschlé 2003).

Figure 3.23 displays the prediction results of five failure criteria. From the figure, it is clear that the Mohr–Coulomb criterion yielded the worst prediction results, with its estimation approximately 1.8 times lower than the experimental results. The Stassi D'Alia and Murrell criteria predicted similar results, both underestimating σ_P^* considerably, whereas the Mogi–Coulomb criterion was more accurate. The implication is that the vertical stress should be taken into account from a rock mechanics point of view as the failure criteria considering intermediate stress had better predictions than those which did not. On the other hand, the linear fracture initiation criterion provided the best estimation results among the failure criteria, although the vertical stress was not incorporated in the model. This failure criterion was also examined by Dresen et al. (2010) and Meier et al. (2013) in hollow cylinder tests where stress conditions were different. Compared to the other four criteria, the linear fracture initiation criterion is based on fracture mechanics, indicating that this concept might be appropriate to explain the borehole size effect in laboratory conditions.

Table 3.2 Governing equations

Failure Criteria	Governing Equation
Mogi–Coulomb	$\boldsymbol{\tau_{oct}} = \frac{\mathbf{2\sqrt{2}}}{\mathbf{3}} \frac{\boldsymbol{UCS}}{\boldsymbol{tan\psi} + \mathbf{1}} + \frac{\mathbf{2\sqrt{2}}}{\mathbf{3}} \frac{\boldsymbol{tan\psi} - \mathbf{1}}{\boldsymbol{tan\psi} + \mathbf{1}} \sigma_{m.2}$
Murrell	$(\boldsymbol{\sigma_1} - \boldsymbol{\sigma_3})^2 + (\boldsymbol{\sigma_1} - \boldsymbol{\sigma_2})^2 + (\boldsymbol{\sigma_2} - \boldsymbol{\sigma_3})^2 = \mathbf{24}\boldsymbol{\sigma_T}(\boldsymbol{\sigma_1} + \boldsymbol{\sigma_2} + \boldsymbol{\sigma_3})$
Stassi D'Alia	$(\boldsymbol{\sigma_1} - \boldsymbol{\sigma_3})^2 + (\boldsymbol{\sigma_1} - \boldsymbol{\sigma_2})^2 + (\boldsymbol{\sigma_2} - \boldsymbol{\sigma_3})^2 = 2(\boldsymbol{UCS} - \boldsymbol{\sigma_T})(\boldsymbol{\sigma_1} + \boldsymbol{\sigma_2} + \boldsymbol{\sigma_3}) + \mathbf{2}\boldsymbol{UCS} \times \boldsymbol{\sigma_T}$
Linear fracture initiation	$\boldsymbol{\sigma_1} = \boldsymbol{\sigma_3} \frac{(\mathbf{1} + \boldsymbol{u}^2)^{1/2} + \boldsymbol{u}}{(\mathbf{1} + \boldsymbol{u}^2)^{1/2} - \boldsymbol{u}} + [\frac{\sqrt{\mathbf{3}}}{(\mathbf{1} + \boldsymbol{u}^2)^{\frac{1}{2}} - \boldsymbol{u}}](\frac{\boldsymbol{K_{IC}}}{\sqrt{\boldsymbol{\pi c}}})$

where $\tau_{oct} = \frac{1}{3}\sqrt{(\sigma_1 - \sigma_2)^2 + (\sigma_1 - \sigma_3)^2 + (\sigma_2 - \sigma_3)^2}$ = octahedral shear stress, $\sigma_{m.2} = \frac{1}{2}(\sigma_1 + \sigma_3)$ = mean normal stress, K_{IC} = stress intensity factor, c = half of defect length.

3.2.2.2.3 Empirical relationship

To provide a simple and effective method to calculate the critical axial stress for breakout initiation under the normal compression test, Lin et al. (2020) proposed an empirical formula based on existing laboratory data:

$$\boldsymbol{\sigma_P^*} = (\mathbf{0.0005}\boldsymbol{R}^2 - \mathbf{0.0638}\boldsymbol{R} + \mathbf{2.7885}) \times \frac{\boldsymbol{UCS}}{\mathbf{3}} \tag{3.44}$$

Figure 3.23 (diamond points) illustrates the prediction results on the laboratory data. Good agreement can be observed between the estimated and experimental values, although there is an overall overestimation of the critical stress, with an average error rate of 11.9%. The approach has also been implemented in studying the relationship between laboratory borehole breakout geometries and horizontal stress analysis and showed promising results on various rock types including sandstone and limestone (Lin et al. 2019; Lin et al. 2020). However, further validation of the formula is required.

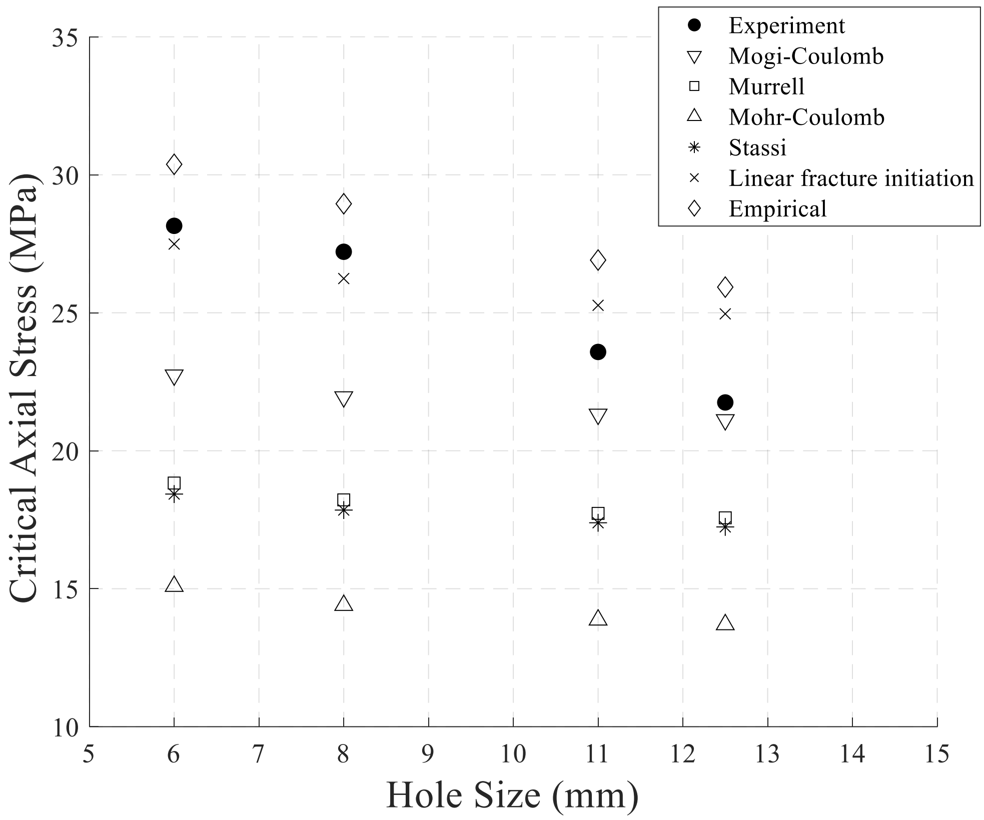

Figure 3.23 Prediction of critical axial stress using various methods

3.2.3 Conclusions

Based on the experimental results from normal compression tests, the specimen size does not have an obvious influence on the breakout initiation stress under the same borehole radius, and constant specimen size and constant borehole–specimen ratio specimens are both suitable for borehole size investigation. Results are also in good agreement with previous studies, confirming that larger borehole size would lead to lower breakout initiation stress given the same rock properties. This indicates that all data from previous tests and in this study are valid and may be used for future borehole size effect studies, which in turn can enhance the understanding of relationships between breakout geometries, rock strength and horizontal stress magnitudes.

The previous assumption of the stress averaging concept to neglect the influence of radial stress may not be fully representative of the local stress condition considering its long critical stress averaging distance (14.2 mm), despite its close prediction results. Instead, this study considered the averaged radial stress and incorporated Mohr–Coulomb failure criterion to estimate critical axial stress for borehole breakout initiation. The proposed model shows unrealistic prediction of the critical axial stress, such that the estimation results were higher than the UCS value. It is likely that this unreasonable prediction may be due to either the selected failure criterion or not recognising the stress that is along the borehole axis, suggesting that detailed investigation is required to consider these parameters.

Based on the pressure-dependent model, breakout initiation would occur inside the rock instead of at the surface of the borehole wall. A comparative analysis of five different failure criteria showed that the linear fracture initiation criterion provided the most accurate results, indicating fracture mechanics theory might be able to address this phenomenon. Although this failure criterion may be used to estimate critical axial stress, it requires parameters that are generally difficult to obtain, i.e. K_{IC} and c; as well as a dubious assumption on the breakout initiation distance (Δr). These assumptions may limit the applicability of this approach.

On the other hand, the empirical relationship proposed by Lin et al. (2020) provides reasonable estimation of the experimental data. Given its simplicity and accuracy, this approach could be adopted if the experimental rock types are similar to the existing laboratory data in the empirical model. Additional experimental data can be included in the model and may improve its reliability. Further validation is also necessary considering the limited data in this study.

4 ESTIMATION OF MAXIMUM HORIZONTAL STRESS MAGNITUDE FROM KRIGING

Currently, the most popular stress estimation technique using breakout data is the stress polygon technique (Barton et al. 1988; Zoback et al. 2003; Chang et al. 2010; Kim et al. 2017). It can either provide the possible ranges of two horizontal stress magnitudes or predict the maximum horizontal stress given the minimum horizontal stress. This is primarily due to the belief that the two breakout geometries are dependent, thus only breakout angular span was used as the input parameter for stress estimation while neglecting breakout depth (Herrick and Haimson 1994; Lee and Haimson 2006; Sahara et al. 2017).

Based on the experimental and analytical investigation of experimental results, Chapter 3 demonstrated that the two breakout geometries are in fact not dependent on each other, indicating it is possible to use breakout depth as an input parameter for horizontal stress estimation. However, the explicit relationship between breakout depth and horizontal stress magnitudes is complex and difficult to model from a constitutional relationship, as discussed in Section 3.1.2.

As reviewed in Section 2.4, the Kriging technique, a category of machine learning, can model non-linearity problems that may not be solved by a closed-form solution. It has also been successfully used in many geotechnical conditions to estimate important parameters, including rock porosity (Yao et al. 1999) and Rock Mass Rating (Choi and Lee 2007). Considering its reliability and applicability in the rock mechanics field, Kriging is used in this study to model the relationship between breakout geometries and horizontal stress magnitudes.

Section 4.1 describes the basic concept and calculation scheme of Kriging, and provides the reasons for selecting the technique. Section 4.2 presents the training and validation data collected from the laboratory and field, respectively. The section also further explores the relationship between the two breakout geometries as well as the influence of horizontal stress magnitudes, to verify the argument from Section 2.2.1 and Section 3.1.2. The Kriging model generation process is provided in Section 4.3, together with the validation results against laboratory data through the 'leave-one-out cross-validation' technique and independent field data. This model is only applied to maximum horizontal stress estimation, with its limitation on minimum horizontal stress also discussed in Section 4.3.

4.1 KRIGING INTERPOLATION

Kriging is a semi-parametric interpolation technique, which predicts the unknown responses of input parameters based on a given dataset. The theory was first developed by Krige (1951) for mining resource estimations and completed by Matheron (1973). The key assumption in Kriging is that a performance function can be represented by a stochastic Gaussian process, $\mathrm{G}(\mathrm{x})$, which is represented as:

$$\mathbf{G}(\mathbf{x}) = \mathbf{F}(\mathbf{x}, \mathbf{b}) + \mathbf{Z}(\mathbf{x}) \tag{4.1}$$

where $\mathrm{F}(\mathrm{x}, \mathrm{b})$ = the deterministic mean function describing the mean trend of the outputs, $\mathrm{Z}(\mathrm{x})$ = a stationary Gaussian process function with zero mean and autocovariance, x = a vector of random variables, and b = a vector of regression coefficients = $[\mathrm{b}_1, \ldots, \mathrm{b}_\mathrm{k}]^T$.

The first term in Eq. (4.1), the deterministic mean function, is defined as:

$$\mathbf{F}(\mathbf{x}, \mathbf{b}) = \mathbf{f}(\mathbf{x})^{\boldsymbol{T}}\mathbf{b} \tag{4.2}$$

where f(x) = a vector with $[f_1(\mathrm{x}), \ldots, f_k(\mathrm{x})]^\mathrm{T}$ and $f(\cdot)$= a scalar or polynomial with multiple variables.

The second term in Eq. (4.1), the Gaussian process function $\mathrm{Z}(\mathbf{x})$, is represented by:

$$\mathbf{Z}(\mathbf{x}) = \boldsymbol{\sigma}_{\boldsymbol{Z}}^{\mathbf{2}}\boldsymbol{R}(\mathbf{x}, \mathbf{x}'; \boldsymbol{\theta}) \tag{4.3}$$

in which σ_Z = the process variance, $R(\mathrm{x}, \mathrm{x}')$ = the auto-correlation function, and θ = a vector of hyper parameters defining the auto-correlation function. The auto-correlation function can flexibly represent nonlinearity of the performance function (Kaymaz 2005). Various types of auto-correlation functions are available including Gaussian, low order polynomial, and exponential functions, and an exponential auto-correlation function is used in this study assuming that the physical phenomena under the observed data show a linear behaviour near the origin (Isaaks and Srivastava 1989).

Given a design of experiment points and the corresponding outcomes of the performance function, b and σ_Z are estimated as follows (Jones et al. 1998):

$$\hat{\mathbf{b}} = (\mathbf{F}^T\mathbf{R}^{-1}\mathbf{F})^{-1}\mathbf{F}^T\mathbf{R}^{-1}\mathbf{G} \tag{4.4}$$

where F = the vector of $f(\mathrm{x})$ at the experimental points, G = the vector of outputs evaluated at the experimental points, and R = the auto-correlation matrix at combinations of design points.

$$\hat{\sigma}_Z^2 = \frac{1}{N}\left(\mathbf{G} - \mathbf{F}\hat{\mathbf{b}}\right)^T \mathbf{R}^{-1}(\mathbf{G} - \mathbf{F}\hat{\mathbf{b}}) \tag{4.5}$$

where N = the number of experimental points. The unknown θ in the auto-correlation matrix R is commonly calculated using the maximum likelihood estimation method as follows:

$$\hat{\boldsymbol{\theta}} = \arg\min_{\theta}[\hat{\sigma}_Z^2 \det(\mathbf{R})^{\frac{1}{N}}] \tag{4.6}$$

In this study, Kriging has been adopted to predict σ_H due to the following reasons: (i) the database used in this study has clear positive linear relationships between the input parameters and output values. Also, the deviation parts from these linear trends are highly non-linear and difficult to fit with conventional polynomial-based regression models. (ii) Once a Kriging model is developed, the model can be further improved by collecting more training (laboratory) data, and the prediction accuracy can be further improved. (iii) in contrast to other regression techniques, Kriging is an interpolation method, and the predictions at the training data points have no error. Therefore, the training data points can be exactly recycled in future predictions.

4.2 Data Collection

As discussed in the previous section, the Kriging technique requires training data to produce a reliable model for in-situ horizontal stress estimation. A total number of 106 laboratory and 23 field data are collected for model generation and validation, respectively. The laboratory data are used for training because they are carefully monitored, parameters can be collected on a reliable standard, and statistically meaningful numbers of data are available. The field data are independently used only for validation to mitigate the correlation between training and validation, so that the developed model is more practically applicable.

4.2.1 Laboratory data collection

Under field conditions, borehole breakouts can occur at different layers where rock is not sufficiently strong to withstand in-situ stresses near the borehole wall. However, it is difficult to obtain the stress magnitudes in that strata, whereas both stresses and breakout geometries can be easily controlled and measured in the laboratory with a repeatable process to gain more data at various stress magnitudes. For a particular breakout test, true triaxial stresses ($\sigma_H \neq \sigma_h \neq \sigma_v$) are applied to the rock sample up to the required stress levels. Drilling is then conducted to create a hole in the centre of the sample to closely simulate practical conditions. Acoustic sensors are used to carefully observe the breakout process. The sample is kept under the same confinement after completion of drilling for another 20 to 30 minutes to enable full development and stabilisation of breakout (Lee et al. 2016). Eventually, it is filled with epoxy and cut into pieces for geometrical investigation.

A total of 106 laboratory breakout data were collected from literature (Haimson and Herrick 1986; Haimson and Herrick 1989; Haimson and Song 1993; Herrick and Haimson 1994; Haimson and Lee 2004; Lee and Haimson 2006) on sandstone and limestone samples. All experimental data revealed that when σ_v and σ_h are constant, the increasing σ_H results in wider θ_b and longer normalised breakout depth (L/r), which confirms that there is a correlation between σ_H and breakout geometries. As suggested by Haimson et al. (1991), there is a unique relationship between L/r and θ_b regardless of the stress magnitudes, i.e. the wider the θ_b the deeper the L/r. The implication here is, for the same rock properties, if the same θ_b are obtained under different horizontal stress magnitudes, their associated L/r should also be the same. Therefore, more than one pair of horizontal stress magnitudes can be derived from the breakout geometries. The knowledge of one horizontal stress has to be provided in order to compute the other. This argument has also been addressed both experimentally and numerically by some researchers (Herrick and Haimson 1994; Haimson and Lee 2004; Lee and Haimson 2006; Sahara et al. 2017). Figure 4.1 shows L/r against θ_b for reviewed studies where stress magnitudes are not considered. An overall increasing trend can be observed between L/r and θ_b, which follows the postulation from Haimson et al. (1991), except the scatter results reported by Haimson and Song (1993) and Haimson and Herrick (1989) with 20 MPa UCS and Haimson and Lee (2004), where their correlation coefficients are 0.25, 0.33 and 0.1. This is due to insufficient data or the scattering of results, whereas the other datasets have correlation coefficients above 0.64. Although experimental trends have a reasonable agreement with the hypothesis, the gradient of each trend varies significantly from study to study, which indicates L/r does not simply depend on θ_b but may rely on other factors such as rock properties.

To examine the influence of rock properties on the gradient between L/r and θ_b, the easiest way is to study data from the same rock type. Assuming that rock is homogenous and isotropic, its mechanical properties should be consistent and insensitive to experimental conditions. Experimental data from Haimson and Lee (2004) is presented in Figure 4.2. It is clear that even for the same rock properties, the relationship between L/r and θ_b still varies in different test series, which is shown in the difference between gradients. This reveals that the change in relationship is not only due to rock properties, but influenced by applied horizontal stress magnitudes since they are the only variables between tests. It implies that the same θ_b resulting from different horizontal stress magnitudes does not necessarily refer to the same L/r under the same rock properties, so that a unique stress pair can be potentially derived solely from breakout geometries. However, this is purely based on experimental observations and further investigation on theories has to be taken.

A broad range of horizontal stress ratios (σ_H/σ_h) was explored in these experiments, which covers possible field scenarios. In practice, due to the frictional faulting equilibrium, the majority of σ_H/σ_h are less than 3.0 (Brace and Kohlstedt 1980), whereas over half of the experimental σ_H/σ_h are greater than the typical values in the field conditions. The large differential stress due to high σ_H/σ_h should display a much wider and deeper breakout than observed.

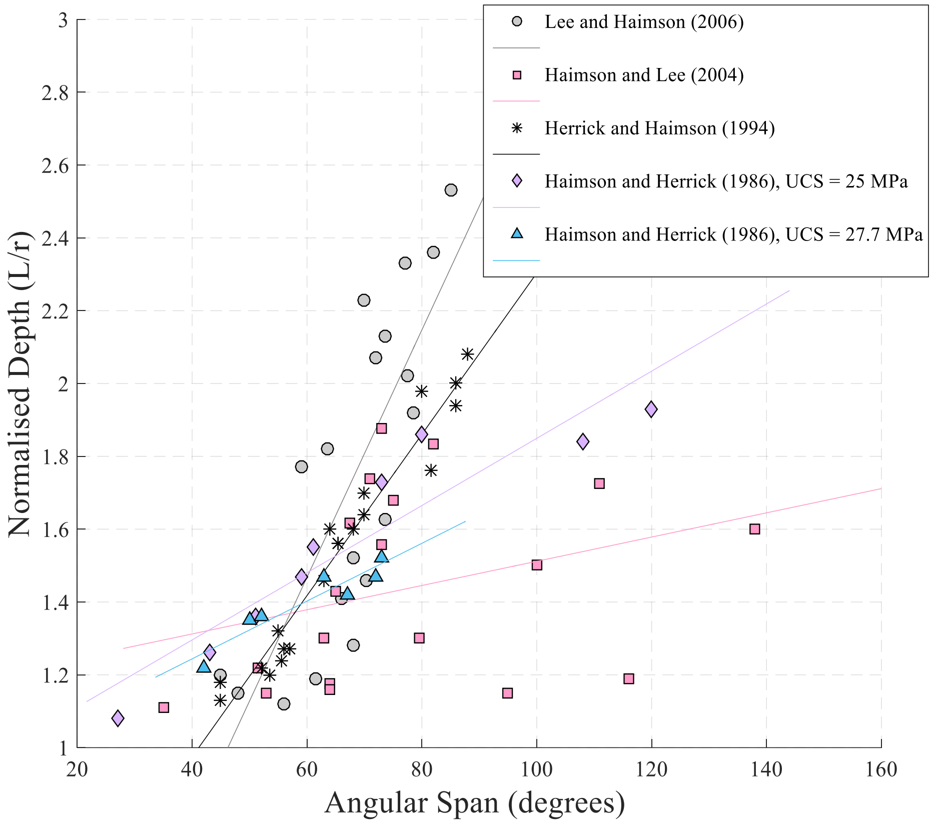

a

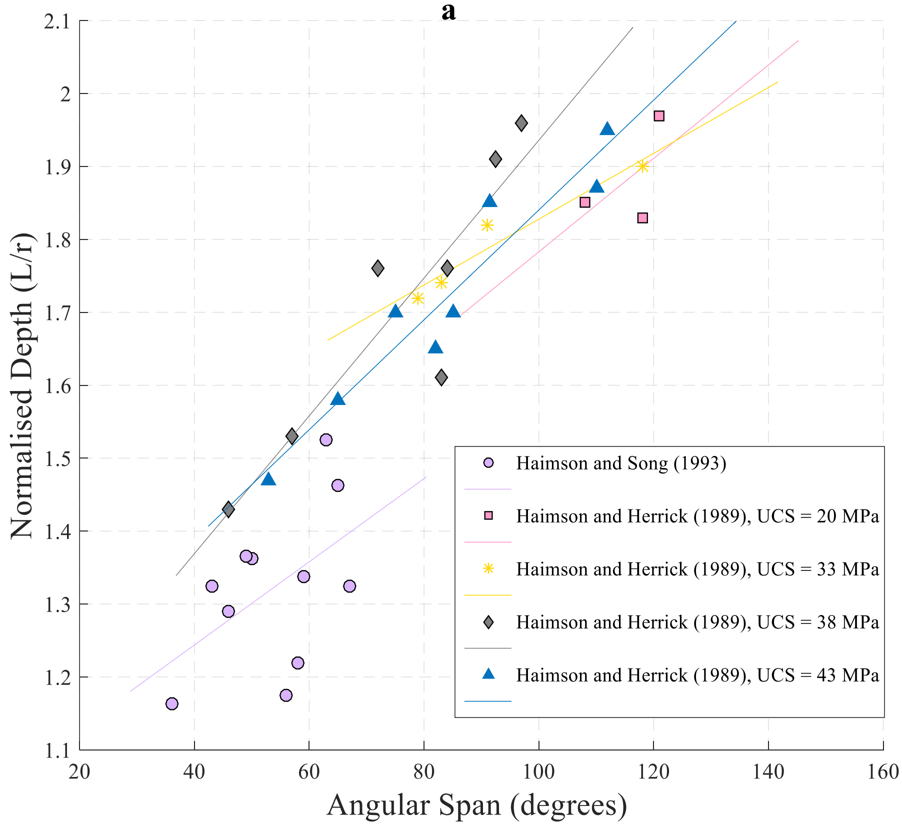

b

Figure 4.1 The relationship between breakout geometries at various rock strengths

Haimson and Herrick (1989) conducted a series of uniaxial compressive tests on limestone blocks with pre-drilled borehole radius ranging from 10 mm to 60 mm to study this observation. The ratio between borehole diameter and block width was kept at 5 to avoid any boundary effect. To have consistency throughout the experiment, the limestone used in their study was the same as the limestone used in breakout tests. They monitored breakout initiations using strain gauges and recorded the corresponding stresses. Results showed that the breakout initiation occurred at much higher horizontal stresses than theoretically estimated values. Thereby, as the borehole radius decreased, the initiation stresses increased dramatically. It reduced to the laboratory UCS until the borehole radius increased to 37.5 mm. Instead of using UCS for breakout study, it was replaced by a more representative factor – borehole wall strength (BWS) (Walton et al. 2015; LeRiche et al. 2017). A similar phenomenon was observed by Carter (1992) on limestone with borehole radius from 3.2 mm to 31 mm. The experimental results are displayed in Figure 4.3, in which the vertical axis is the ratio between BWS and UCS, and the horizontal axis is the borehole radius.

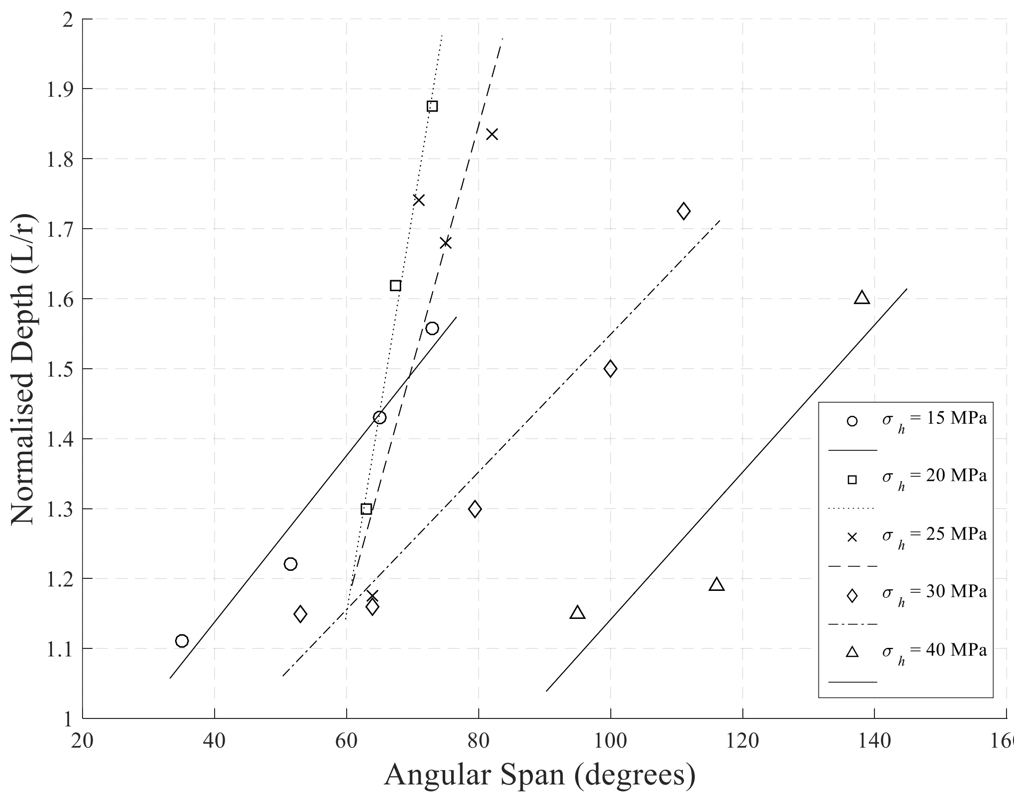

Figure 4.2 The relationships between breakout geometries from Haimson and Lee (2004)

Since both tests were conducted on limestones, an empirical relationship was derived from their experimental results considering their similar lithological features, which was then used to convert UCS to BWS at different borehole radius:

$$\boldsymbol{BWS = (0.0005r^2 - 0.0638r + 2.7885) \times UCS} \tag{4.7}$$

where r = borehole radius. For example, UCS of the rock sample tested by Lee and Haimson (2006) is 35.06 MPa. Since an 11 mm borehole is drilled for breakout experiments, the referred BWS/UCS is 2.1472, as displayed in Figure 4.3 as a red dot. Therefore, the actual strength of the borehole wall, i.e. BWS of this rock sample, is calculated as 75.28 MPa. The summary of BWS conversion for all experiments is provided in Table 4.1, and the full values of geometries and stresses are provided in Appendix Table A1.

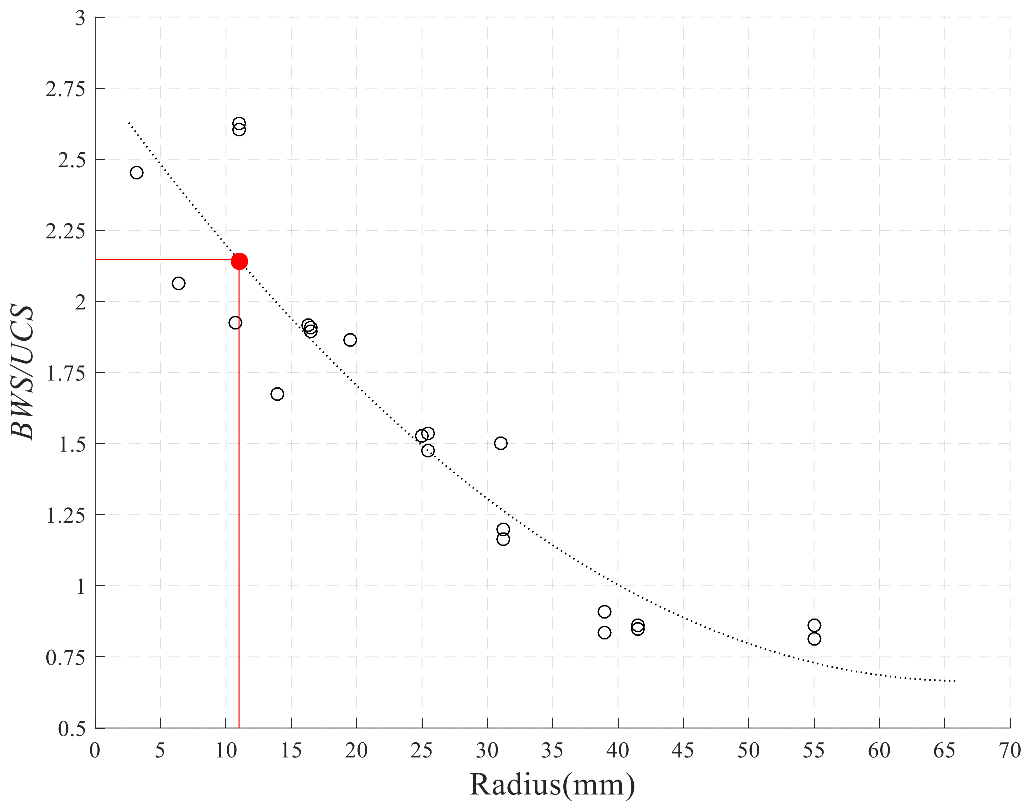

Figure 4.3 The relationships of borehole radius and ratio between BWS and UCS, indicating that the strength of borehole wall increases significantly with decreasing borehole radius

Table 4.1 Laboratory breakout data containing rock types, borehole radius, UCS and BWS

	Rock Type	No. of samples	Sample Radius (mm)	Sample UCS (MPa)	BWS (MPa)
Haimson and Herrick (1986)	Indiana limestone	16	10.7	25, 27.7	54.08, 59.92
Haimson and Herrick (1989)	Indiana limestone & Alabama limestone	22	10	20, 33, 38, 43	44.01, 72.62, 83.62, 94.62
Haimson and Song (1993)	Cordova Cream limestone	11	11	13	27.91
Herrick and Haimson (1994)	Alabama limestone	20	11	43	92.33
Haimson and Lee (2004)	Tablerock sandstone	19	11	39	83.74
Lee and Haimson (2006)	Tenino sandstone	19	11	35.06	75.28

4.2.2 Field data collection

Due to the development of a borehole televiewer (Zemanek et al. 1969), fractures around a borehole can be precisely detected and analysed. This technique has enabled the confirmation of horizontal stress orientations using a four-armed caliper (Plumb and Hickman 1985). Based on the travel time of acoustic emission, breakout shapes and their geometries can be computed at different depths (Broding 1981; Zoback et al. 1985).

Once the Kriging model is developed, it is required to carry out a validation process to demonstrate the reliability and its associated error. To examine the model without any biases, field breakout data from different locations was collected from the literature together with two unpublished new data provided by mine site A, a coal mine in Australia. All breakout data was selected where there was a stress measurement (hydraulic fracturing or overcoring) conducted at very near depth, which was used as the output effective horizontal stress magnitudes for comparison with the Kriging predictions. A total of 23 field data were collected as shown in Table 4.2, where 16 measurements are from hydraulic fracturing, and 7 from overcoring.

Table 4.2 Field breakout data collected from literature

Source	Data number	Normalised depth (L/r)	Angular span width (degrees)	BWS (MPa)	Maximum horizontal stress (MPa)	Minimum horizontal stress (MPa)
Zoback et al. (1985)	1	1.04	37	52.00	34.10	15.7
Walton et al. (2015)	2	1.10	48.00	109.05	79.00	56.00
Shen (2008)	3	1.06	67.00	84.00	59.13	46.08
	4	1.08	61.70	84.00	59.36	46.26
	5	1.13	72.00	84.00	59.89	46.67
	6	1.09	61.00	84.00	60.43	47.09
	7	1.14	66.80	84.00	61.62	48.02
	8	1.18	61.70	84.00	62.22	48.49

	9	1.24	61.70	84.00	62.93	49.04
	10	1.17	66.90	84.00	63.38	49.39
	11	1.18	61.70	84.00	63.96	49.85
	12	1.18	61.70	84.00	65.17	50.79
	13	1.22	72.00	84.00	65.36	50.94
	14	1.15	72.00	84.00	65.69	51.20
Klee et al. (2011)	15	1.25	55.50	84.00	66.55	31.88
Shen and Rinne (2011)	16	1.08	25.00	92.40	51.79	22.53
	17	1.16	51.00	92.40	57.82	26.35
Leriche (2017)	18	1.14	42.00	102.20	72.60	37.95
	19	1.12	30.00	112.00	73.85	49.2
	20	1.18	42.00	136.94	67.09	49.49
	21	1.16	27.00	140.00	70.85	47
Mine site A	22	1.23	19.84	18.20	13.74	10.66
	23	1.21	14.17	17.61	10.15	7.39

Drilling mud can induce thermal stresses around the borehole if the mud temperature is cooler than that of the formation temperature and this can reduce the surrounding hoop stress (Moos and Zoback 1990). However, its effect seems to be limited to a 3%–5% change in the hoop stress and the possible underestimation of σ_H by less than a few MPa at 2–3 km depth (Vernik and Zoback 1992). Recent studies for stress estimation using borehole breakout also neglected the influence of the thermal stress (Chang et al.

2010; Huffman and Saffer 2016; Kim et al. 2017; Song and Chang 2018). Therefore, the current study does not include the effect of thermal stresses.

To prevent the formation fluid from getting into the wellbore during drilling, the mud pressure is usually carefully controlled to ensure it is close to the pore pressure. Since the collected field data does not provide information on mud pressure, the mud and pore pressures are assumed to be equal and cancel out each other for the analysis. In addition, the training data collected from the published literature are laboratory data which only includes breakout geometries and BWS. Hence, the Kriging model cannot predict σ_H using the mud pressure, pore pressure or thermal pressure.

Mine site A is located in the Hunter Valley coalfield, north-west of Newcastle, Australia. A series of boreholes was drilled at the site between 2010 and 2012 and geophysical logging and acoustic scanning were also undertaken. Based on the acoustic data, breakouts were found in several locations along boreholes below 260 m depth, especially in the siltstone layer where the rock is extremely weak. In this study, breakout data from borehole RUD027 and RUD028 was selected for field validation as overcoring stress measurements were conducted in these boreholes at nearby breakout depth. A typical cross section of breakout from acoustic data is provided in Figure 4.4.

UCS data from the literature was obtained either from laboratory or sonic velocity. As addressed in the previous section, UCS in laboratory data is much stronger than BWS in field data, therefore a downscale factor is required to convert the laboratory UCS to BWS. Based on experimental observation, Martin (1997) proposed that BWS is either 50% or 70% of laboratory UCS depending on the orientation of the borehole with respect to the stress conditions. This is because the stress concentration around the borehole wall varies at different orientations. Thus, the corresponding correction factors were applied to each case according to their borehole orientations.

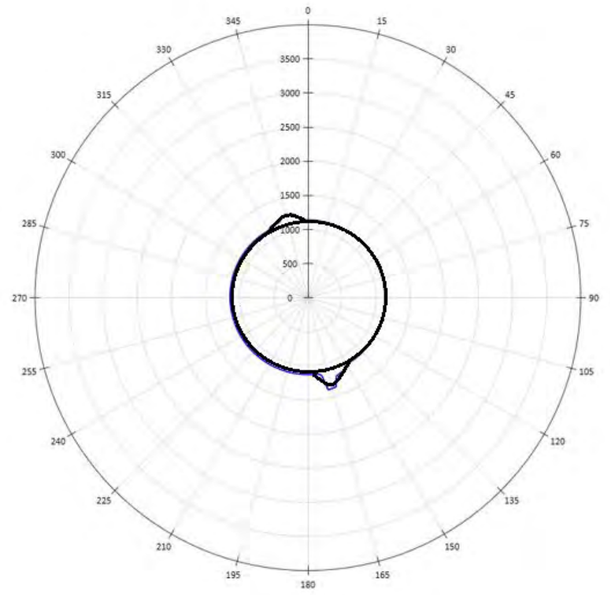

Figure 4.4 A cross-sectional view of breakout at 271.3 m in borehole RUD028, where the minimum horizontal stress direction is approximately at 165°

In practice, unbroken long core samples are sometimes unavailable for laboratory testing to obtain their UCS values, especially in weak strata. Thereby, it is crucial to obtain reasonable rock strength to implement appropriate underground design and control measures. Hence, empirical relationships between in-situ UCS and sonic velocity were constructed and implemented in the mining and petroleum industries (McNally 1987; Entwisle et al. 2005; Chang et al. 2010; Oyler et al. 2010) as sonic velocity can be easily attained from commonly used geophysical logs. Chang et al. (2006) and Azimian et al. (2014) provided summaries of these empirical relations for various rock types. Given the representativeness of sonic velocity on in-situ rock strength, the estimated values are directly used as BWS.

4.3 KRIGING MODEL AND RESULTS

4.3.1 Model generation

4.3.1.1 Deterministic trend analysis

To predict σ_H, the Kriging model in Eq. (4.1) is constructed by defining the following two terms: (i) the deterministic mean function and (ii) the stationary Gaussian process function. The first term can be defined by confirming the deterministic trend of the data along each of the three identified parameters: L/r, θ_b, and BWS. Figure 4.5a shows the relationship between L/r and σ_H for the 106 experimental data points. It clearly shows the positive proportional relationship between σ_H and L/r. The data points are distributed along the least-square linear fitting line, which is shown as a dotted line.

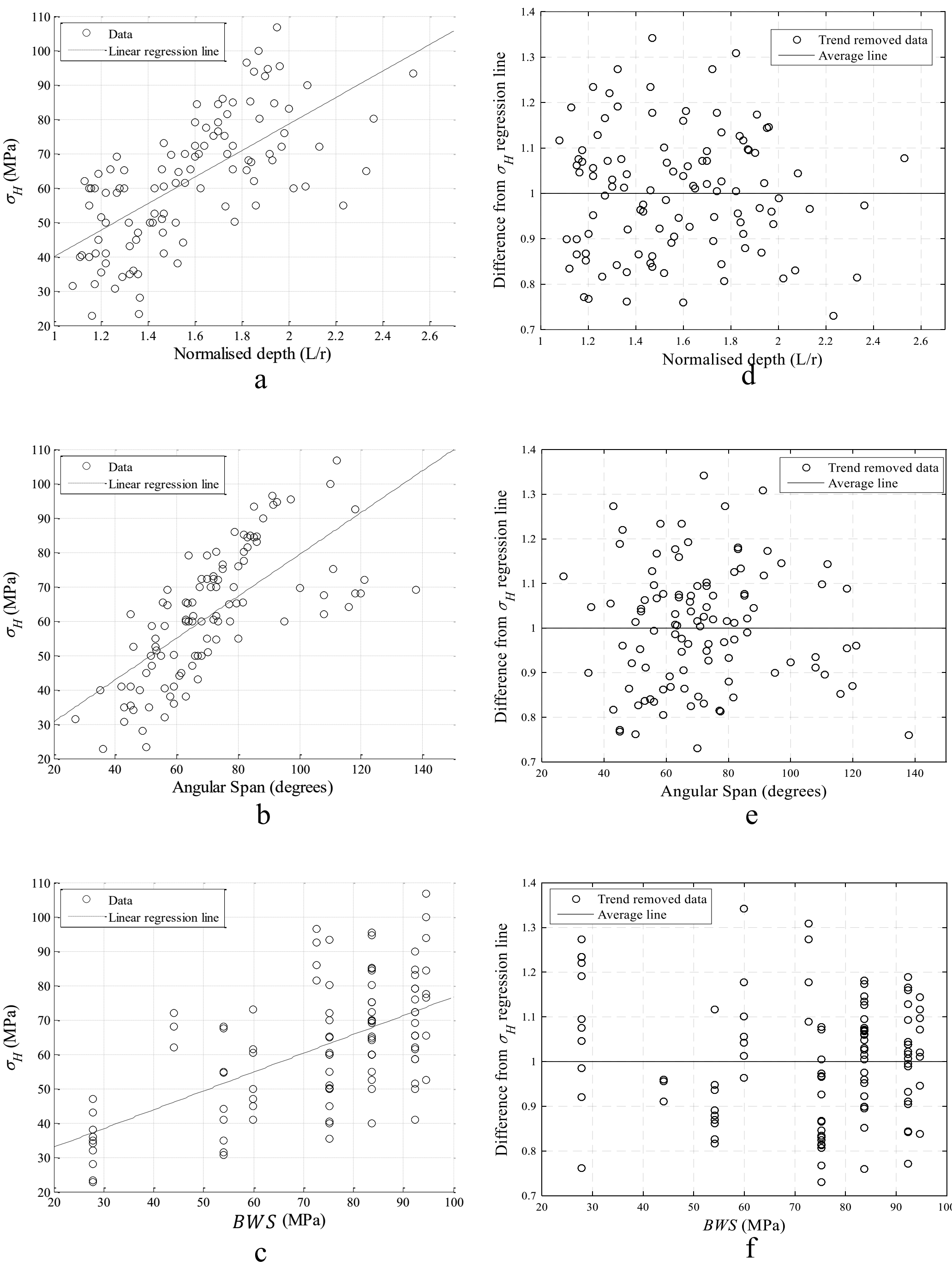

Figure 4.5 a-c) Relationship between σ_H and L/r, θ_b and BWS, respectively; d-f) relationship between residual σ_H and these parameters

To statistically measure the linearity of two parameters, the Pearson correlation coefficient has been used as follows:

$$\boldsymbol{\rho_{x,y}} = \frac{\boldsymbol{COV(x,y)}}{\boldsymbol{\sigma_x \sigma_y}} \tag{4.8}$$

where $\rho_{x,y}$ is the correlation coefficient of two parameters x and y, $COV(x,y)$ is the covariance of x and y, and σ_x and σ_y are standard deviations of x and y. The correlation coefficient has a value between -100% and 100%, where 100% means the positive deterministic linear relationship, 0% means no deterministic relationship, and -100% means the negative deterministic linear relationship between x and y. The correlation coefficient between L/r and σ_H is calculated to be 66.83% showing a moderate positive linear correlation.

Figure 4.5b shows the relationship between the θ_b and σ_H in the experimental database. Similar to L/r, the experimental data are distributed along the least-square linear fitting line shown as a dotted line. The linear relationship is even stronger, and the correlation coefficient is calculated as 69.78%.

As breakout is a phenomenon of rock fracture, the derived σ_H does not simply represent the stress magnitude but is also related to the rock strength. In theory, if other parameters are constant, the higher BWS requires higher σ_H to cause failure of the borehole wall and lead to breakout formation. Figure 4.5c shows the relationship between BWS and σ_H in the experimental database. It shows a positive linear relationship with the correlation coefficient of 60.27%, but due to the nature of the design of the experiments, for fixed values of BWS, multiple σ_H values exist.

From these observations, a least-square linear regression model is used to define the deterministic trend over the identified three parameters: L/r, θ_b and BWS. Then, the deterministic trend of the values of σ_H is removed by dividing the values of σ_H by the linear regression values, and the deterministic term becomes a constant. Only the residuals are used in the Kriging process, where the mean is independent from the data locations. This technique is called the Ordinary Kriging (Matheron 1973). The division form has been used to make the predicted σ_H values always positive that corresponds to reality. The residuals are plotted in Figure 4.5d–f for each of the three identified parameters. Figure 4.5d shows the relationship between L/r and σ_H after dividing the experimental values of σ_H by the linear regression model prediction values. The horizontal line at σ_H value of 1.0 means the deterministic linear relationship between L/r and σ_H. The figure shows the highly nonlinearly distributed residuals along this horizontal line with no constant bias. This is also well observed in the residuals for θ_b and BWS as shown in Figure 4.5e–f, where no constant bias is observed. The residuals have nonlinear relationships with the parameters, and they are predicted by an Ordinary Kriging model represented as the second term only in Eq. (4.1). In this chapter, the Kriging model is defined by extensively utilising a Kriging Toolbox DACE in MATLAB® (Lophaven et al. 2002).

4.3.1.2 Limitation of the experimental database for σ_h prediction

This study limits the scope to the prediction of σ_H and does not attempt to predict σ_h. This is due to the nature of recorded σ_h data in the experimental database, which are difficult to distinguish according to the identified parameters, i.e., L/r, θ_b, and BWS. In Figure 4.6a–c, it is observed that, in many cases, more than one parameter values yield the same σ_h value. For example, in Figure 4.6a, for the same σ_h of 40 MPa, the corresponding L/r values are 1.15, 1.19, 1.28, 1.60, 2.13, 2.36 and 2.53. This is due to the design of the experiments in the database. In many of the studies, the primary interest of the authors was to investigate the influence of σ_H and σ_H/σ_h on breakout geometries. To achieve this aim, σ_h applied to rock samples was fixed, while increasing σ_H for multiple experiments. Because of this, the clear identification of the relationship between σ_h and the parameters is impossible, which makes the prediction of σ_h difficult. Therefore, it is difficult to utilise the collected experimental database for a σ_h prediction, and the scope of this study is limited to the prediction of σ_H.

To improve the reliability of the model and develop its application for σ_h, it is necessary to explore the influence of σ_h on breakout geometries. This can be done by conducting a series of experiments which keep σ_H constant and change the values of σ_h, as opposed to the focus of earlier studies on σ_H.

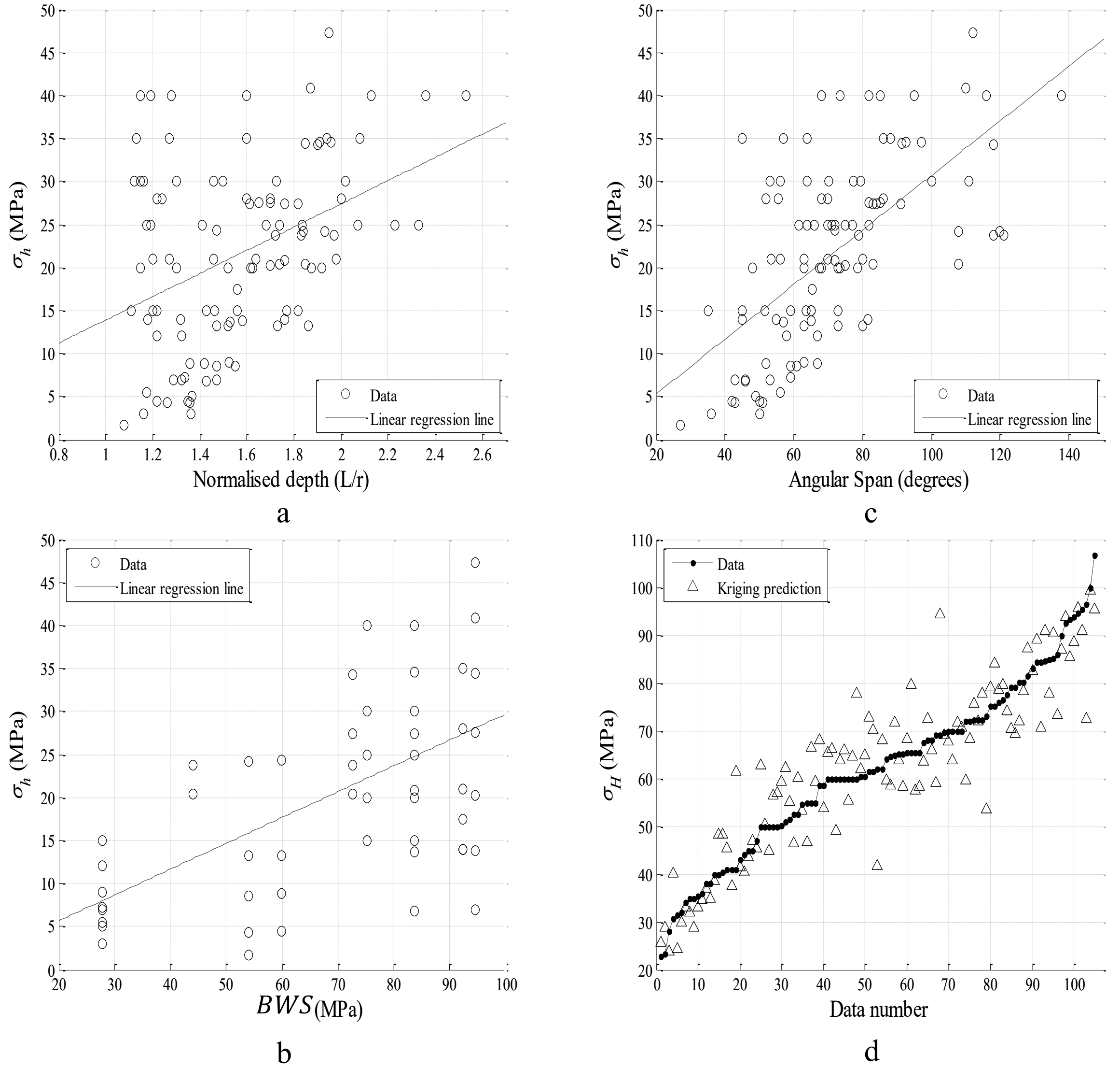

Figure 4.6 a–c) Relationships between σ_h and L/r, θ_b and BWS, respectively; d) σ_H predictions and LOOCV validations

4.3.2 Model validation

4.3.2.1 Validation through leave-one-out cross-validation using experimental data only

The simplest and widely used validation method to test the accuracy of a prediction model is to use the two sets of data: a training set and a test set. The prediction model is constructed based on the training set, and it is validated through the test set. However, because this method uses only a sub-set of the data for training, when the number of data points is limited, this method can limit the prediction capacity and the coverage of the parameter range.

The leave-one-out cross-validation (LOOCV) method (Stone 1974), which is a special case of k-fold cross-validation, is a more appropriate validation method when the number of data is limited. It fully utilises the full set of data for training and validation at the same time. If there are n independent observations, i.e., $y_1,\ldots,y_n$, LOOCV is carried out according to the following steps:

1. Remove one datum, y_i, from the database so that the remaining number of data b ecomes $n - 1$.
2. With the $n - 1$ remaining data, train the prediction model.
3. Validate the model with the removed datum, y_i, and calculate the prediction error.
4. Repeat steps 1–3 for $i = 1,\ldots,n$ and calculate the statistics of the prediction error in step 3.

In this study, a Kriging prediction model is developed by training it with the 106 experimental data points introduced in Section 3.1. To fully utilise the experimental database, LOOCV has been applied for validation, i.e., the model is trained with 105 data and validated for the remaining one data, and this process is repeated for all 106 data. The prediction results are presented in Figure 4.6d, in which the Kriging predictions are compared to the experimental data throughout the leave-one-out process. The relative prediction error is represented by:

$$\boldsymbol{Relative\ error} = \frac{\boldsymbol{Exact - Prediction}}{\boldsymbol{Exact}} \tag{4.9}$$

and its average is calculated as 10.59% for the 106 data. The histogram of the relative errors for 106 data is presented in Figure 4.7a. Although most of the relative errors are skewed towards less than 10% error, there are several high relative prediction errors greater than 30%. These points are not outliers but are important data that must be included in the training. Missing those data significantly reduces the prediction accuracy.

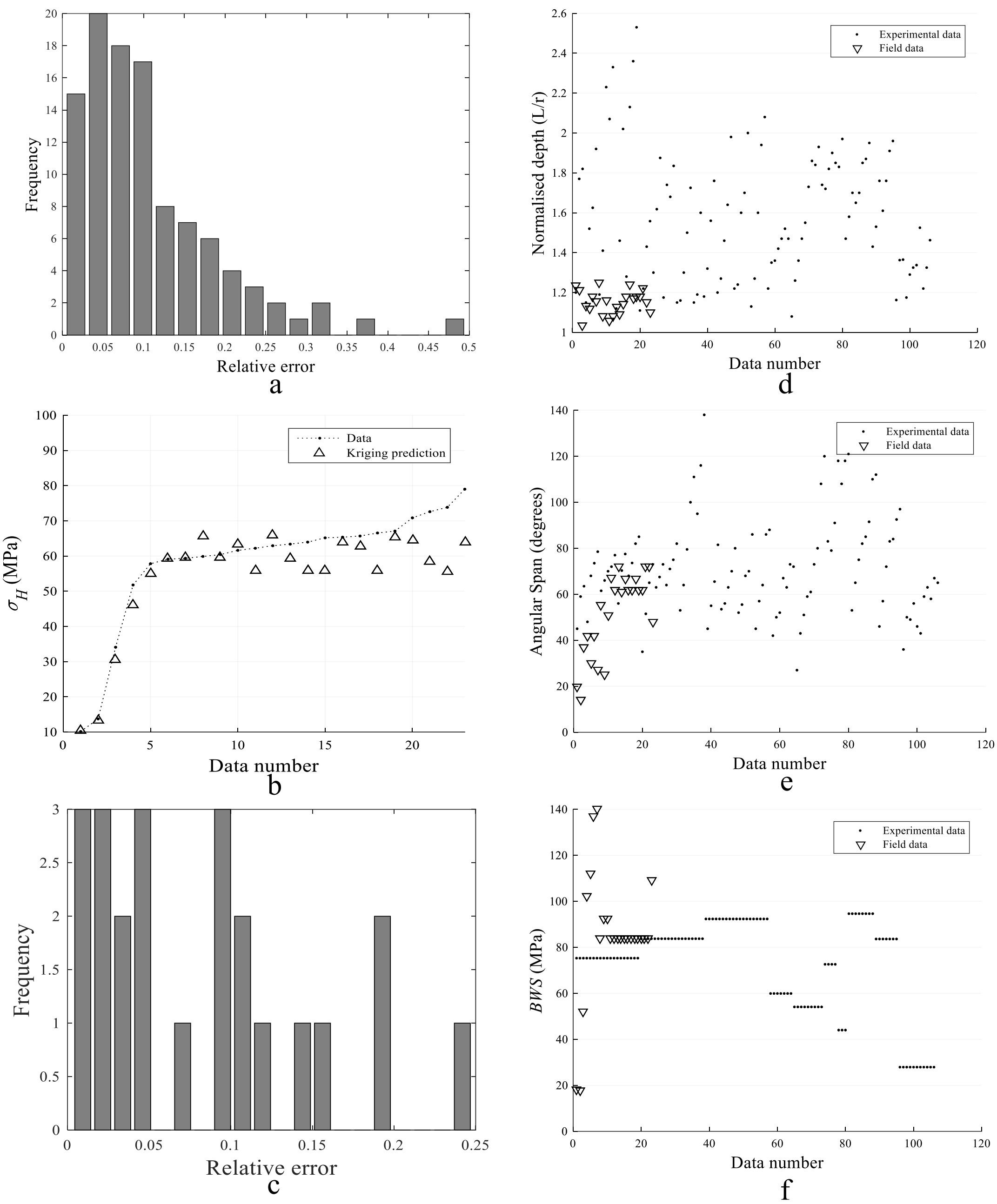

Figure 4.7 a) Histogram of relative prediction errors for 106 experimental data; b) σ_H predictions and validations with the field data; c) histogram of the relative prediction errors for the 23 field data; (d–f) the values of each parameter in the experimental and field data

4.3.2.2 Validation through field data

Although the proposed Kriging model was validated through experimental data in the previous section by showing remarkable accuracy, the use of the model can still be restricted within the range of the parameter values in the training database. To extensively examine the prediction performance of the proposed Kriging model for a practical use, the model is again validated using the 23 field data introduced in Section 3.2 that is independent of the laboratory data. The field data includes two unpublished new data collected from mine site A, and the remaining data are extracted from the literature. All the field data are used only for validation, and they are not used for the training of Kriging model. The validation process is conducted by directly comparing the predicted σ_H values and the field data values, and therefore, LOOCV is not needed.

The Kriging predictions are represented in Figure 4.7b, where the predicted values and the available field data values are compared. The Kriging predictions vary along the data points, and the average relative error is statistically estimated as 8.4% that is close to field measurements. In reality, there are some inherent errors associated with stress measurements, and it is impossible to obtain true/exact values with zero errors. This means that the proposed Kriging model shows similar predictions to field measurements. This method provides high quality estimations considering its utilisation on existing borehole scanning data rather than expensive measurements from ancillary equipment.

Better accuracy has been achieved with the field data because the average relative error in the previous section with LOOCV validations was affected by the cases with missing important data points. However, in this field data validation, the full set of 106 experimental data points is used, and those important data points are included in the training of the Kriging model. Figure 4.7c shows the histogram of the absolute values of the relative errors for the 23 field data and the maximum error was 24.8% that is much lower than 49.59% in the LOOCV validation with experimental data. The histogram is well skewed towards the values less than 10%. The predicted values and the relative errors for the 23 field data are fully reported in Table 4.3.

In field conditions, σ_h can be more reliably obtained than σ_H. For instance, hydraulic fracturing only measures σ_h, whereas its σ_H calculation relies on σ_h as a parameter. This yields a less reliable σ_H estimation where the accuracy can be more than ± 20% (Ljunggren et al. 2003). In contrast, overcoring can directly predict σ_H but it is based on the theory of elasticity, which is difficult to achieve in deep locations due to the lamination or fracture of rock (Gaines et al. 2012). Given the 70% success rate of

SIGRA In-situ Stress Testing (IST) overcoring (Gray and See 2007) and around 20% associated error from experience, 10.59% error on laboratory σ_H predictions from this Kriging model is remarkable.

Table 4.3 Predicted σ_H and their prediction errors for the 23 field data

Data number	Maximum horizontal stress (MPa)	Predicted maximum horizontal stress (MPa)	Relative error
1	34.10	30.63	0.109
2	79.00	63.86	0.192
3	59.13	59.37	-0.004
4	59.36	59.55	-0.003
5	59.89	65.75	-0.098
6	60.43	59.51	0.015
7	61.62	63.43	-0.029
8	62.22	56.00	0.100
9	62.93	65.81	-0.046
10	63.38	59.21	0.066
11	63.96	56.00	0.124
12	65.17	56.00	0.141
13	65.36	63.90	0.022
14	65.69	62.87	0.043

15	66.55	55.89	0.160
16	51.79	46.03	0.111
17	57.82	55.01	0.049
18	72.60	58.39	0.196
19	73.85	55.54	0.248
20	67.09	65.35	0.026
21	70.85	64.37	0.091
22	13.74	13.44	0.022
23	10.15	10.52	-0.037
		Average	0.084

To compare the data distributions of the training data and validation data, the laboratory and field databases are compared in terms of the input parameters Figure 4.7d–f show the comparison of each parameter values between the 106 experimental data and the 23 field data. In Figure 4.7d, it is seen that the range of L/r in the experimental data is from 1.08 to 2.53 while that in the field data is from 1.036 to 1.25. Higher differential stress and weak rock strengths are two major reasons that can lead to longer L/r. Figure 4.8 shows that some σ_H/σ_h applied in experimental conditions are beyond those in the field data, and the absolute stress magnitudes are close, which indicates their differential stress is greater. Although a group of field data has very high absolute stress magnitudes, their σ_H/σ_h is low and so is the differential stress. The size of dots represents the intensity of the rock strength, and it is clear that the majority of the field conditions have similar or stronger rock compared to experiments, which again shows that experimental data should produce longer L/r than field data. Therefore, the broader coverage of σ_H/σ_h in experimental conditions yields a wider range of L/r.

The difference between field and experimental data shows that many of the field data exist outside the range of the experimental data but the overall prediction accuracy has even been improved. One of the main reasons for this is because the deterministic trend function in the Kriging model well predicts the overall trend in the outside range of the training data, and the residuals are also well predicted by the trained Kriging model. This is again seen in Figure 4.7e where the range of θ_b in the experimental data is from 27 to 138 while the range of the field data is from 14.17 to 72. Similarly, this observation can be explained by the difference in differential stress and rock strength between two types of data. This means that some field data points have values lower than the minimum value in the experimental data but the overall prediction of the proposed Kriging model is still accurate. Moreover, Figure 4.7f shows the range of the BWS values in the experimental data from 27.91 to 94.62 while that of the field data is from 17.61 to 140.00, which has wider bounds.

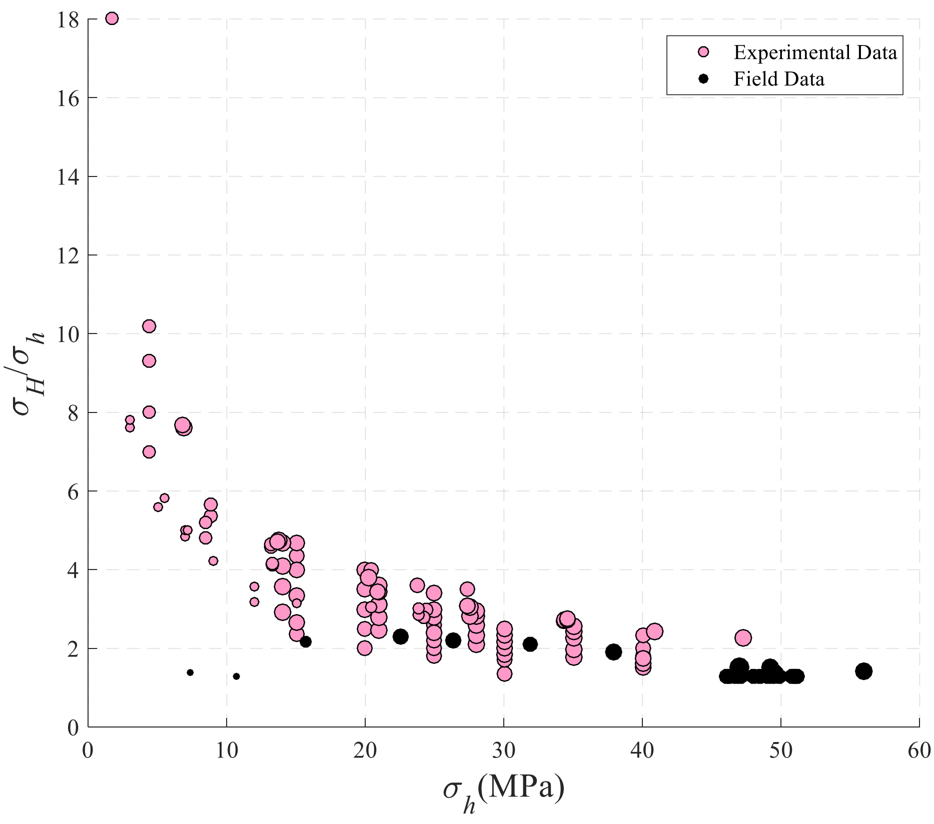

Figure 4.8 σ_H/σ_h vs σ_h for both field and experimental data, where the size of the dot represent strength of the rock. It is observed that experimental data has a much wider coverage of σ_H/σ_h

To further investigate the reasons behind the Kriging prediction accuracy, the input parameter values of field data and their nearby σ_H experimental data points are compared at the data points with relatively high and low prediction accuracies. Figure 4.9 shows the values of L/r, θ_b and BWS, and σ_H at four field data points with the highest prediction accuracy. To have a clear observation on L/r, the values presented in the figures are 10 times the original values. These values are compared with those at the nearest experimental data points. Due to the interpolating nature of the Kriging, the nearest training points should affect the prediction accuracy of the Kriging model. In Figure 4.9a–c, the values of L/r, θ_b, BWS and σ_H at the three best prediction points are represented as white bars, and those of the nearest experimental data points are represented as black bars. In all of these sub-figures, the values of the white and black bars are almost the same, which means that the values of L/r, θ_b and BWS, and σ_H are nearly identical in the field data points and the nearest experimental data points. This yields very accurate interpolations. On the other hand, Figure 4.9d shows the fourth accurate data point, where the white and black bars show a big difference especially for the parameters of θ_b and BWS. This means that the field data point is not located within the range of the experimental database, and the nearest experimental data point has much greater θ_b and BWS. However, σ_H values for those data points are also greater, and this well represents the positive linear proportional trend between the parameters and σ_H. Therefore, the prediction at this field data point is quite accurate although the data point is located outside the range of the experimental database. This is because, for a particular pair of L/r and θ_b at given BWS, there should be only a unique solution of corresponding horizontal stress magnitudes for vertical boreholes. If the input parameters have very close values against training data, the estimated σ_H should also be very accurate.

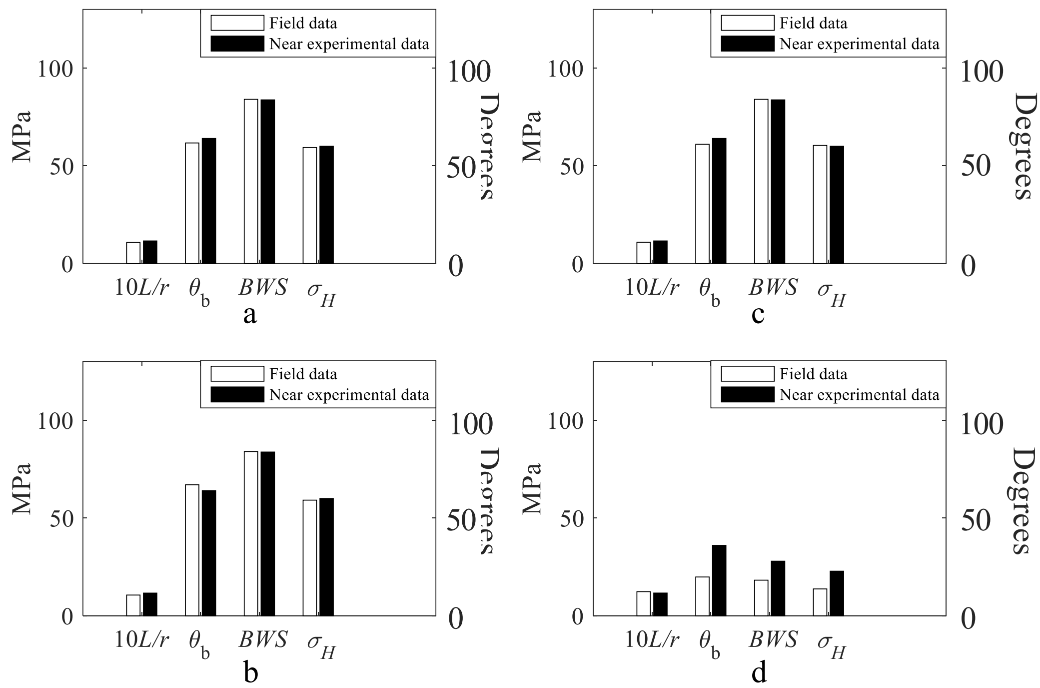

Figure 4.9 The four field data points with the highest prediction accuracy and the comparison with the nearest experimental data points. BWS and σ_H are in MPa, θ_b is in degrees and L/r is a ratio: a) prediction error = -0.3%; b) prediction error = -0.4%; c) prediction error = 1.5%; d) prediction error = 2.2%

Figure 4.10 shows the four field data points with the worst prediction accuracy. In all four sub-figures in Figure 4.10, the nearest experimental data points do not have similar input parameter values. The differences in each parameter for both the four best data and worst data are displayed in Table 4.4. This means that the predictions are interpolated from far-distance data points. Also, there is no positive linear relationship observed between the field and nearest experimental data points for their parameter values. This means that the field data do not follow the general trend of the nearest experimental data, and this affects the accuracy of the predictions. For example, in Figure 4.10a, it is found that, the field data has higher θ_b with lower BWS at 16.67% and 25.23%, but its σ_H value is 45.84% smaller than the nearest experimental data. This shows the inconsistency between the experimental and field data points, and this makes the prediction inconsistent. Similar inconsistencies in terms of their values or trends are found in the other sub-figures. Although these points yield the worst predictions, their accuracies are still reasonable considering the maximum error is only 24.8%. By collecting more data, the prediction errors are expected to be further reduced.

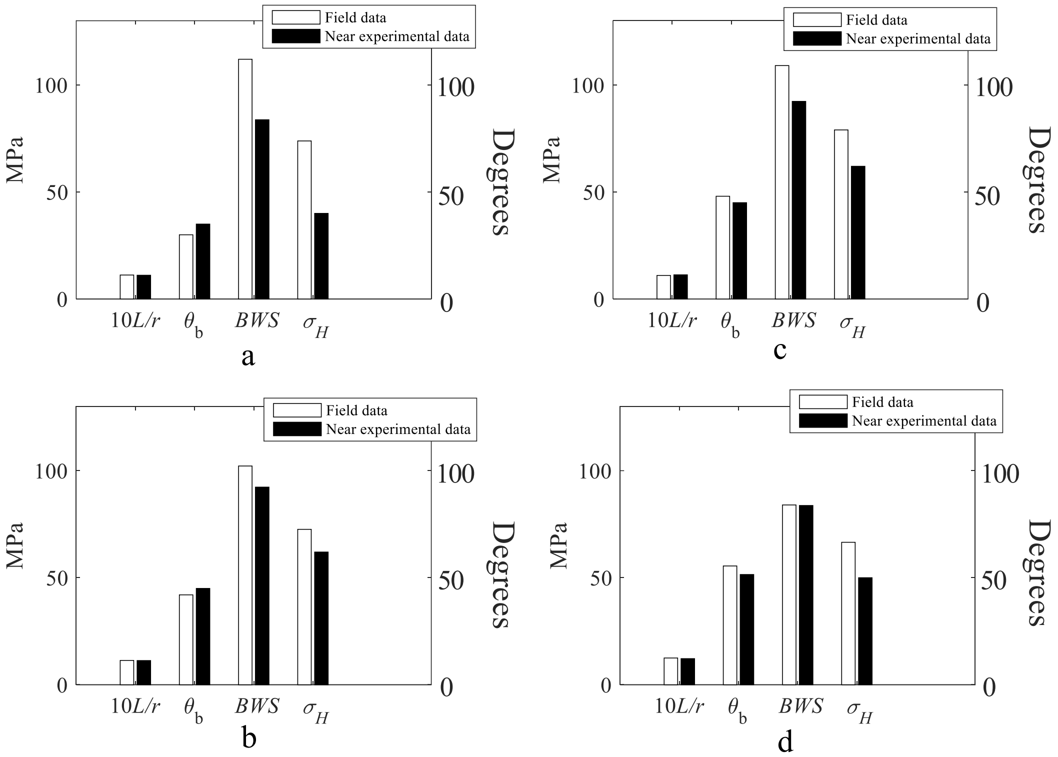

Figure 4.10 The four field data points with the lowest prediction accuracy and the comparison with the nearest experimental data points. BWS and σ_H are in MPa, θ_b is in degrees and L/r is a ratio: a) prediction error = 24.8%; b) prediction error = 19.6%; c) prediction error = 19.2%; d) prediction error = 16%

Table 4.4 Difference between input parameters for best and worst predictions, where % indicates the percentage difference between the field data and the nearest experimental data

Data number	Normalised depth (%)	Angular span, width (%)	BWS (%)	Maximum horizontal stress (%)
1	7.41%	3.73%	-0.31%	1.07%
2	9.43%	-4.48%	-0.31%	1.48%
3	6.42%	4.92%	-0.31%	-0.71%

4	-5.82%	81.45%	53.37%	65.94%
5	-0.89%	16.67%	-25.23%	-45.84%
6	-0.44%	7.14%	-9.66%	-14.60%
7	2.73%	-6.25%	-15.33%	-21.52%
8	-2.40%	-7.21%	-0.31%	-24.87%

4.4 CONCLUSIONS

This study proposes a machine learning-based meta-model using Kriging and breakout data to predict the maximum in-situ horizontal stress. To identify the important parameters used in this Kriging model, the relationships between various breakout parameters were investigated. The results indicated that the relationship between breakout geometries is sensitive to the change in the horizontal stress magnitudes, which also implied that the horizontal stress magnitudes can be estimated from breakout geometries and rock strength if an appropriate technique is implemented. In addition, previous experimental data showed that the strength of the borehole wall depends on the radius of the borehole. The borehole wall strengthens dramatically when the borehole radius decreases, which can be over 2.5 times the UCS. In field conditions, this phenomenon is not observed because the borehole radius is large enough. However, borehole size effect is particularly important when generating a Kriging model, since the rock strength from both field and laboratory data has to be on the same scale to produce reliable estimation. Therefore, it is suggested to carry out further study on borehole radius to investigate the mechanism while quantifying this relationship. Through analysis of laboratory data, the three most influential breakout parameters were identified for horizontal stress estimation: L/r, θ_b and BWS.

A Kriging model was constructed based on the identified parameters and trained using 106 experimental data. Leave-one-out cross-validation was used to validate the prediction accuracy of the proposed Kriging model, and it provided the average Kriging prediction errors of 10.59% on experimental data and 8.4% for the field data based on a direct validation. Compared to other existing stress measurement techniques, which have high σ_H estimation error rates, the proposed Kriging model is simple, accurate and cost-effective. The reasons behind the Kriging prediction error were also investigated by comparing the input parameter values of the field data and their nearby experimental data points when relatively high and low prediction accuracies were observed. The proposed Kriging model did not aim to predict σ_h due to the nature of the experimental design of the data used for training, in which the trend of σ_h values was unclear. It is expected that collecting a broader range of databases will further improve the accuracy and the prediction coverage of the proposed Kriging model in practical conditions.

5 NUMERICAL SIMULATION OF BOREHOLE BREAKOUT AND BOREHOLE SIZE EFFECT USING DISCRETE ELEMENT METHOD

As discussed by a number of researchers, breakout angular span is a more reliable parameter than its depth for horizontal stress estimation (Zoback et al. 1985; Barton et al. 1988; Lee et al. 2016). This is because breakout angular span forms at the initial stage of borehole breakout and remains constant, and is followed by the subsequent elongation in the minimum horizontal stress direction (Sahara et al. 2017). However, this process is difficult to observe in experimental conditions since the specimen is sealed with pressure applied from all conditions.

Numerical analysis is a powerful tool which can simulate different rock mechanics scenarios. As reviewed in Section 2.3, the Discrete Element Method (DEM) software, Particle Flow Code (PFC), is a promising technique to simulate borehole breakout behaviour, especially for micro-mechanical investigation and breakout formation analysis (Fakhimi et al. 2002; Li et al. 2006; Lee et al. 2016). To enhance the understanding of breakout development and critical parameters, borehole breakout is simulated by PFC under different stress conditions.

Section 5.1 discusses the experimental breakouts that were simulated. The calibration process and simulation procedures are provided in Section 5.2, including the micro-mechanical properties in the model. Section 5.3.1 and Section 5.3.2 present the simulation results from Section 5.2, including breakout development, different horizontal stress conditions and borehole size effect.

As mineral resources at shallow depths are being extracted to meet the increasing global demand, exploration and exploitation activities at deeper locations have gained considerable attention (Nickless 2016). For instance, the current geothermal wells have been carried out at depths of up to 5000 m (Ranjith et al. 2017), and mining operations occur at more than 1000 m depth in many countries including China, South Africa and Ukraine (Xie et al. 2015; Al Sayed et al. 2016; Xie 2017; Gürtunca 2018). In deep locations, the temperature is usually high and can have an impact on the mechanical properties of rock (Yang et al. 2017). This thermal effect may also influence the breakout geometries and thus affect the horizontal stress estimation. Due to limitations in laboratory conditions, it is difficult to perform true triaxial tests on samples under various temperatures. PFC has an embedded model to investigate the thermal effect, which has been used by numerous researchers in rock mechanics problems (Wanne and Young 2008; Zhao 2016; Zhao et al. 2019). In Section 5.3.3, the influence of temperature on breakout geometries and borehole size effect is studied. The other parameters that are considered include horizontal stress conditions and borehole radius.

5.1 Experimental Data

Existing experimental data was used in this study to validate the numerical simulation results. Cubic Gosford sandstone samples (120 × 120 × 120 mm^3) with pre-drilled holes (8 mm, 11 mm and 15 mm radii) were loaded under true triaxial stress conditions ($\sigma_H > \sigma_h > \sigma_v$) using a specially designed confinement cell at room temperature to mimic field scenarios, as shown in Figure 5.1. The experiments applied various maximum horizontal stresses while keeping the minimum horizontal and vertical stress magnitudes at the same level. At the completion of experiments, samples were cut in half along the maximum horizontal stress direction and underwent optical scanning to precisely measure the breakout geometries. A detailed description of the experimental procedures is given in Lin et al. (2019).

Figure 5.1 UNSW confinement cell (Lin et al. 2019)

The interpretation of experimental results suggests that both breakout geometries are dependent on the maximum horizontal stress magnitudes, where higher maximum horizontal stress led to wider and longer breakouts. This can be seen in Figure 5.2. Results showed an overall agreement with previous research (Haimson et al. 1991; Haimson and Song 1998; Haimson and Lee 2004; Lee and Haimson 2006), indicating there is a definite relationship between breakout geometries and horizontal stress magnitudes. It can also be seen that the larger hole size resulted in wider and deeper breakouts under the same stress conditions. This is also in line with the observations from Haimson and Herrick (1989), Carter (1992) and Bažant et al. (1993), where the stress required to initiate borehole breakout is much higher for smaller borehole size than for the larger boreholes. In addition, the angular expansion and deepening rate of breakouts with 8 mm and 11 mm borehole radii appear steady and similar with increasing maximum horizontal stress, whereas the rate at 15 mm borehole radius is much higher.

5.2 NUMERICAL SIMULATION

5.2.1 Particle Flow Code

Although breakout geometries under different stress conditions were investigated in the laboratory, the formation mechanism cannot be effectively studied due to the limitation of the equipment. It is not possible to capture the breakout geometries at various stages of the experiment unless the sample is taken out of the equipment for CT-scanning numerous times during the test. To overcome the shortcomings of the experimental work and study breakout geometries in detail, two-dimensional Particle Flow Code (PFC2D) was implemented in this study to reproduce the laboratory results. PFC2D is software developed by Itasca Group using the DEM in which the rock is represented by an assembly of solid particles that are bonded by the cementing material in between (Itasca 2018). Cracking occurs at the contact bonds if the associated tensile or shear force exceeds the corresponding strengths, while the coalescence of bond breakages can represent the macro-fracture initiation and development. The governing fracture criterion is Mohr–Coulomb.

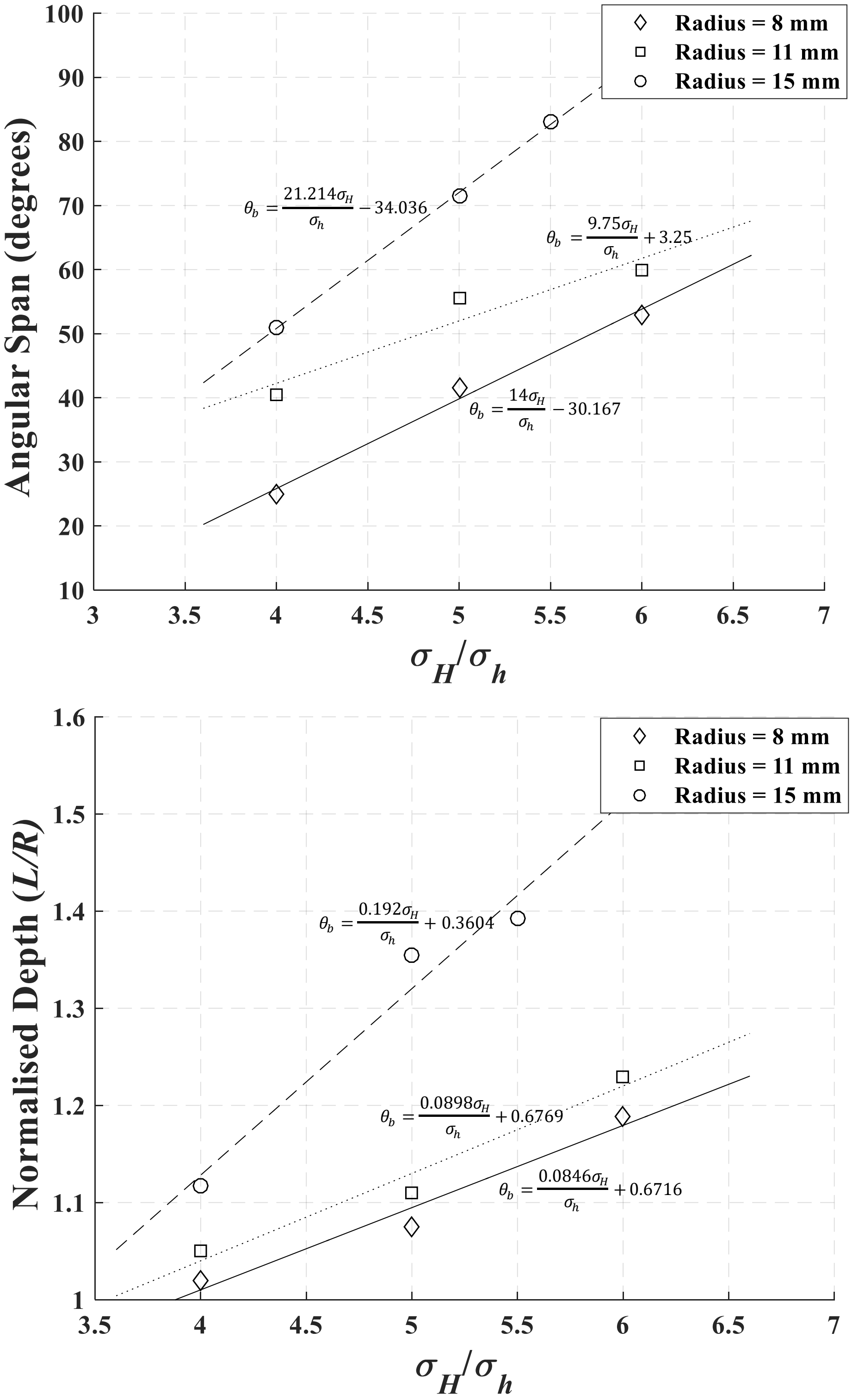

Figure 5.2 Breakout geometries vs horizontal stress ratio after Lin et al. (2019)

In general, there are two basic bond models: contact bond (CB) and parallel bond (PB) models. The CB model is considered as a ‘point of contact’ between particles whereas the PB model is envisioned as a beam distributed along a rectangular area and centered at the point of contact. In recent years, the flat-joint model has also gained significant attention in simulating rock behaviour (Vallejos et al. 2017; Bahaaddini et al. 2019). In this study, the PB model was adopted to closely simulate the breakout phenomenon, primarily due to its popularity in previous numerical investigation of borehole related studies (Peter-Borie et al. 2015; Duan and Kwok 2016; Lee et al. 2016; Zhao 2016; Zhou et al. 2016)

5.2.2 Model calibration

In PFC2D, the physical properties cannot be directly assigned to the synthetic sample and a 'trial and error' process is required to calibrate the micro-mechanical properties of synthetic rock against the macro-responses of Gosford sandstone. For this purpose, a 42 × 100 mm^2 specimen was generated in the model with the particle radius ranging from 0.2 mm to 0.28 mm. Based on the calibration methodology proposed by Potyondy and Cundall (2004), the uniaxial compressive strength (UCS), Young's modulus (E) and Poisson's ratio (v) of the synthetic rock were matched against the laboratory results. Correspondingly, the appropriate micro-mechanical properties of the particles and parallel bonds were determined (Yoon 2007; Bahaaddini et al. 2013), as summarised in Table 5.1.

Table 5.1 Micro-mechanical properties of particles and bonds

Particle micro-mechanical properties		Parallel bond micro-mechanical properties	
Density (kg/m^3)	2650	Young's modulus (GPa)	3
Young's modulus (GPa)	3	Normal strength (MPa)	27 ± 6
Coefficient of friction (MPa)	0.58	Shear strength (MPa)	27 ± 6
Stiffness ratio (k_n/k_s)	1.5	Stiffness ratio (k_n/k_s)	1.5

Table 5.2 shows the macro-mechanical properties of both synthetic and experimental rock samples, which indicate that the synthetic specimen was properly calibrated.

Table 5.2 Physical and numerical rock properties

	Experimental	Numerical
UCS (MPa)	42.3	43.0
Young's modulus (GPa)	7.5	7.54
Poisson's ratio	0.18	0.182

5.2.3 Simulation procedures

Based on the calibration results, a rock specimen with dimensions of 120 × 120 mm^2, which consists of a total of 70,930 particles, was generated with the micro-properties listed in Table 5.1. In laboratory conditions, boreholes (8 mm, 11 mm and 15 mm radii) were drilled prior to the loading phase. To closely simulate the experiment, holes were also created in the centre of the sample before applying stresses. Figure 5.3 illustrates the specimen setup and loading directions.

In the model, horizontal stresses were applied by moving the platens inwards, governed by a servo-control mechanism. The mechanism auto-corrects the applied stresses by adjusting the velocities of boundary walls so that the pre-set stresses can be reached and maintained throughout the test (Itasca 2018). Initially, both σ_H and σ_h were increased simultaneously until 10 MPa. After that, σ_h was kept at the same level while increasing σ_H to the target value to allow the development of borehole breakout.

Figure 5.4 shows a simulation result of borehole breakout with 11 mm borehole radius, where σ_H = 50 MPa and σ_h = 10 MPa. The breakout tip is sub-parallel to the lateral direction, showing that the borehole breakout depth is in line with the minimum horizontal stress direction. This suggests that the breakout depth can be used as a reliable indicator of the horizontal stress orientation, which has been used extensively in field studies (Stock et al. 1985; Zoback et al. 2003; Fowler and Weir 2007; Lin et al. 2010; Ask et al. 2015; Malinverno et al. 2016). The contact between particles can be broken by either shear or tensile failure, as shown by the red and black dashes in the vicinity of the borehole. The figure shows the majority of micro-cracks were formed in tensile failure whereas only a few were formed due to shear failure (Duan and Kwok 2016; Lee et al. 2016). As the micro-cracks coalesce and intersect with each other, a 'dog-ear' shaped breakout was created, which is consistent with experimental observations.

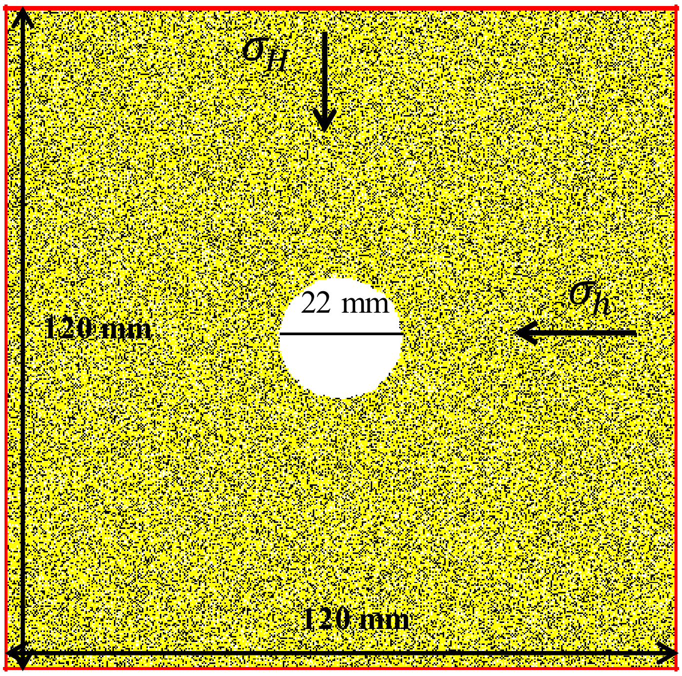

Figure 5.3 Illustration of the numerical simulation

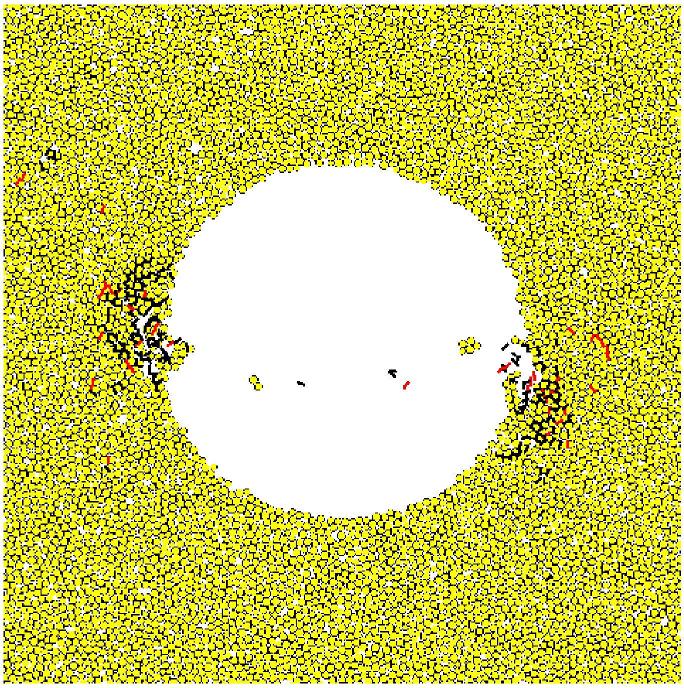

Figure 5.4 Borehole breakout simulated under σ_H = 50 MPa and σ_h = 10 MPa with 11 mm radius, where tensile failure is represented by a black dash and shear failure is represented by a red dash

5.3 Simulation Results and Discussion

5.3.1 *Borehole breakout under various horizontal stress magnitudes*

A series of numerical simulations were carried out on synthetic Gosford sandstone to study the behaviour of borehole breakout. Figure 5.5a–f illustrate the breakout development of a 15 mm radius borehole under σ_H = 50 MPa and σ_h = 10 MPa. As shown in Figure 5.5a–b, breakout initially formed as rock slabs which are sub-parallel to the maximum horizontal stress direction and subsequently spalled off towards the centre of the borehole, indicated by the movement of detached particles. By then, a fracture plane formed along the borehole breakout propagation direction from the maximum point of the fracture at the borehole wall to the breakout tip, see Figure 5.5c–d. Eventually, fractures were localised at the tip of the breakout and induced minor breakout propagation due to the stress re-distribution and concentration from the failure zone, as shown in Figure 5.5e–f. The progress of breakout development followed the same pattern as discussed by Cuss et al. (2003) from their experimental observations on Tennessee sandstone. Numerical results imply that breakout is caused by the combination of shear and tensile failures.

Based on the figure, it can be seen that there were only minor changes in the breakout angular span throughout the process. This indicates that the breakout angular span may form quickly at an early stage of the breakout and does not widen significantly with time. The observation here agrees with earlier studies in which breakout angular span can be assumed constant and considered as a reliable parameter for horizontal stress estimation (Mastin 1984; Zoback et al. 1985; Zheng et al. 1989; Herrick and Haimson 1994; Cuss et al. 2003; Schoenball et al. 2014). Following the approach proposed by Barton et al. (1988), the breakout angular span has been widely used to constrain or compute the horizontal stress magnitudes provided that downhole logging data is available (Barton et al. 1988; Zoback and Healy 1992; Vernik and Zoback 1992; Brudy et al. 1997; Zoback et al. 2003; Yaghoubi and Zeinali 2009; Chang et al. 2010; Huffman and Saffer 2016; Nian et al. 2016; Kim et al. 2017; Molaghab et al. 2017; Song and Chang 2018).

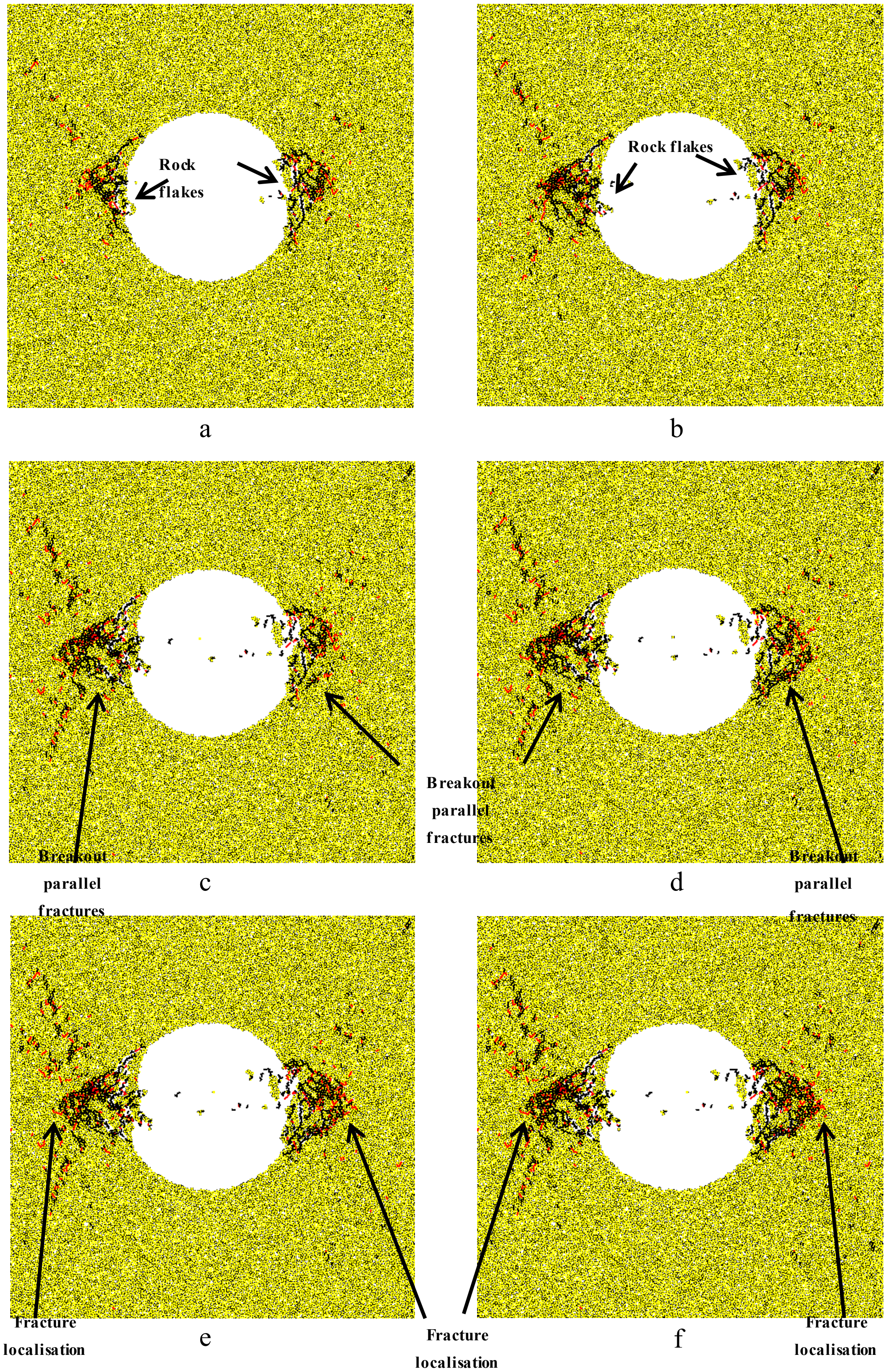

Figure 5.5 Breakout development at various stages under σ_H = 50 MPa and σ_h = 10 MPa with 15 mm radius: a) timestep = 3.2×10^4; b) timestep = 3.6×10^4; c) timestep = 4.4×10^4; d) timestep = 4.7×10^4; e) timestep = 5.0×10^4; f) timestep = 5.2×10^4

Unlike the breakout angular span, the breakout depth tended to propagate along the σ_h direction and elongated at various stages of the simulation, see Figure 5.5a–f. The breakout tip gradually got narrower and finally formed a 'V-shaped' or 'dog-ear' shaped breakout. The progressive breakout development agrees with various researchers (Zoback et al. 1985; Barton et al. 1988; Bažant et al. 1993; Shen et al. 2002; Duan and Kwok 2016; Lee et al. 2016) and a similar phenomenon was reported in both laboratory and field cases (Mastin 1984; Plumb and Hickman 1985; Kessels 1989). Breakout depth may not be an effective parameter for stress estimation based on a simple elastic solution, such as the Kirsch solution, as it is practically impossible to measure the breakout depth when it was just formed. Zoback et al. (1985) and Barton et al. (1988) have also discussed this limitation in their studies. Hence, an unconventional methodology, e.g. machine learning or neural network, may utilize the breakout depth data and solve this problem. Lin et al. (2020) have collected extensive laboratory and field data from the literature and a mine site for this purpose. Figure 5.6 shows the angular span obtained from numerical simulation against the experimental data. As illustrated in the figure, the numerical angular span follows a similar trend as the laboratory investigation, i.e. the higher stress ratio (the higher maximum horizontal stress) would result in a wider breakout angular span given the constant minimum horizontal and vertical stresses. Results again confirm that there is a definite relationship between the maximum horizontal stress and angular span.

It is noteworthy that the breakout angular spans produced with different borehole radii were different under the exact same stress conditions: the larger borehole radius yields a wider breakout. This is also in line with the experimental observation, which contradicts the Kirsch solution as the stress conditions at a given point along the borehole wall should be the same if the same boundary stresses are applied. As discussed earlier, the phenomenon is primarily due to the influence of the borehole size, in which smaller borehole size requires higher stress concentration to nucleate breakout (Carter et al. 1991; Carter 1992; Bažant et al. 1993; Walton et al. 2015; Duan and Kwok 2016; Leriche 2017). Therefore, the simulation results show that the PFC2D can effectively take account of the borehole size effect, as discussed in the section below.

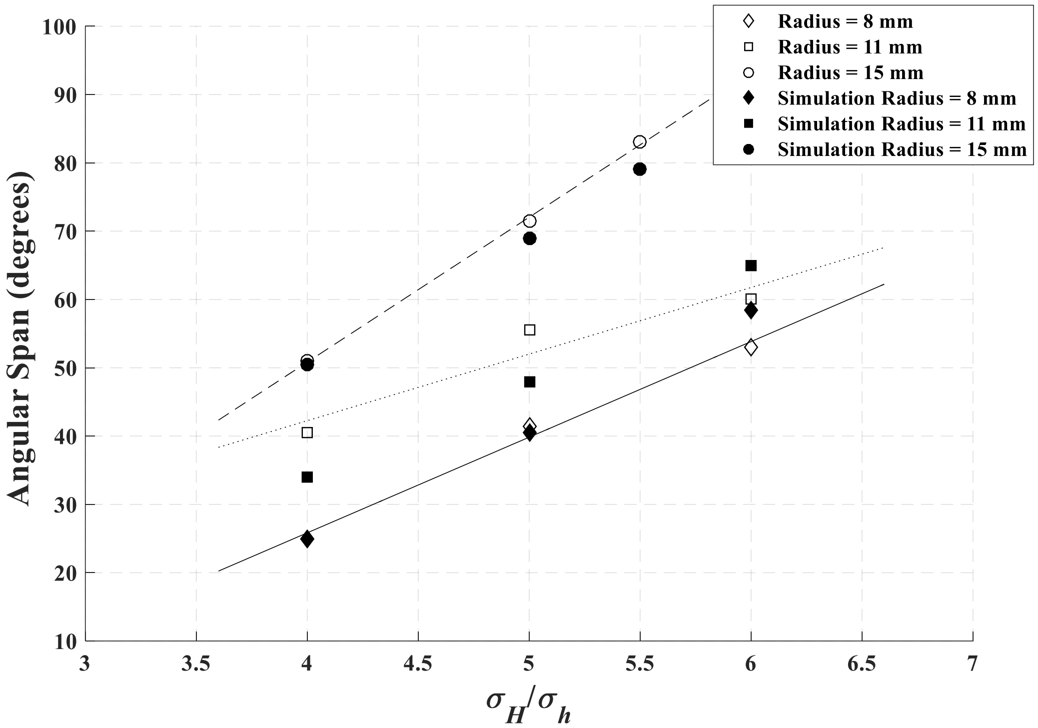

Figure 5.6 Simulation results on breakout angular span vs the experimental results

5.3.2 Borehole size effect

Borehole size is an important parameter that should be considered in laboratory study as it can significantly intensify the stress required for breakout initiation (Leriche 2017). A series of studies have attempted to investigate this mechanism (Haimson and Herrick 1989; Van den Hoek et al. 1994; Papamichos and van Den Hoek 1995; Van den Hoek et al. 1996; Papanastasiou and Thiercelin 2010), with popular explanations including the stress averaging concept (Lajtai 1972; Nesetova and Lajtai 1973; Carter et al. 1991; Elkadi and Van Mier 2006), fracture mechanics (Sammis and Ashby 1986) and conservation of energy (Bažant et al. 1993). As observed previously, the horizontal stress ratios used in laboratory conditions were generally greater than the field conditions unless the ratio is under high differential stress. For instance, Haimson and Herrick (1986) applied a horizontal stress ratio over 10 in some of their experimental work. This is highly unlikely to be seen in the field.

5.3.2.1 Simulation procedures and breakout initiation stress

A numerical study on borehole size effect was also carried out in PFC2D where the pre-drilled specimen was loaded under a hydrostatic compressive condition. In total, six different borehole radii, ranging from 2 mm to 12 mm, were investigated. As suggested by Lotidis et al. (2017), the on-set breakout initiation in PFC2D can be defined when there is a non-linear deflection in the stress–strain curve combined with a sudden increase in cumulative micro-crack numbers. In laboratory conditions, this is generally defined by strain gauges and acoustic emission (Carter et al. 1991; Carter 1992; Dzik and Lajtai 1996; Dresen et al. 2010; Meier et al. 2013; Choens et al. 2018). The same approach was also adopted in the numerical simulation via PFC2D by Duan and Kwok (2016).

According to the Kirsch solution (Jaeger et al. 2009), the stress around a borehole can be expressed as follows:

$$\boldsymbol{\sigma_r = \frac{1}{2}(\sigma_H + \sigma_h)\left(1 - \frac{R^2}{r^2}\right) + \frac{1}{2}(\sigma_H - \sigma_h)\left(1 - 4\frac{R^2}{r^2} + 3\frac{R^4}{r^4}\right)cos2\theta + \Delta P\frac{R^2}{r^2}} \tag{5.1}$$

$$\boldsymbol{\sigma_\theta = \frac{1}{2}(\sigma_H + \sigma_h)\left(1 + \frac{R^2}{r^2}\right) - \frac{1}{2}(\sigma_H - \sigma_h)\left(1 + 3\frac{R^4}{r^4}\right)cos2\theta - \Delta P\frac{R^2}{r^2}} \tag{5.2}$$

where σ_θ = tangential stress, σ_r = radial stress, R = borehole size, r = distance from the centre of the borehole to the point of interest, ΔP = difference between mud pressure and pore pressure. A series of researchers have argued that the breakout would initiate at the maximum tangential stress concentration location (Haimson and Herrick 1986; Haimson and Herrick 1989; Carter 1992; Lin et al. 2019), where the tangential stress can be estimated as:

$$\boldsymbol{\sigma_\theta = 3\sigma_H - \sigma_h} \tag{5.3}$$

Under hydrostatic conditions, the tangential stress around the borehole can be simplified as:

$$\boldsymbol{\sigma_\theta = \frac{1}{2}(\sigma_H + \sigma_h)\left(1 + \frac{R^2}{r^2}\right) = 2\sigma_P} \tag{5.4}$$

where σ_P = hydrostatic pressure applied in the model. For an isotropic material, the breakout would initiate around the borehole at the same time. Figure 5.7a illustrates the simulation of 6 mm borehole radius and the breakout initiation stress (58.7 MPa) is labelled. A non-linear deflection can be observed at the stress, indicating the on-set breakout initiation (Dresen et al. 2010; Meier et al. 2013; Duan and Kwok 2016; Lotidis et al. 2017). At the same time, crack numbers around the borehole increased substantially, as seen in Figure 5.7b. This is in good agreement with the simulation from Duan and Kwok (2016). Figure 5.7c–d show the model states prior and after the breakout initiation, respectively. It can be found that extensive cracks generated after the initiation stress, which was dominated by tensile cracks. This was in good agreement with Figure 5.7a–b, confirming that the stress–strain curve deflection can be used as the indication of breakout initiation. It is worth noting that the cracks are not uniformly distributed around the borehole, mainly due to the heterogeneity of the DEM model.

Although Duan and Kwok (2016) also investigated borehole size effect using PFC, the maximum borehole diameter used was 16 mm, which was almost one third of their specimen length of 50 mm. Boundary effect can have a significant effect under this ratio and considerably influence the breakout initiation stress. Therefore, the conclusions from Duan and Kwok (2016) might be tentative, especially for boreholes with diameters over 10 mm. This might explain the lower breakout initiation stresses observed by Duan and Kwok (2016) compared to experimental studies. On the other hand, the numerical simulation on borehole size effect in this study covered a wider range of borehole diameters up to 24 mm while keeping the ratio between borehole diameter and specimen length under 0.2. In this case, the boundary effect on simulation results can be eliminated.

5.3.2.2 Implications on stress averaging model

As proposed by Lajtai (1972) and Carter (1992), the intensification of breakout initiation stress is due to the stress averaging concept, in which the stress under the high gradient is redistributed towards the lower area over a distance. This critical distance (d) is considered as a material constant and is determined based on the curve fitting data. As suggested by Carter et al. (1992), the critical distance varies from 2 mm to 3.5 mm for ductile to brittle material. Although the stress averaging phenomenon can be identified through strain distributions obtained from strain gauges at the surface of the borehole (Carter 1992), it does not explicitly show the stress transfer along the distance. The measurement circle function embedded in PFC measures the stress change within the pre-defined circle during the simulation process. Hence, three 1 mm diameter measurement circles were assigned parallel and perpendicular to the minimum horizontal stress direction to cover the possible averaging distance and monitor the stress averaging phenomenon numerically, as illustrated in Figure 5.8.

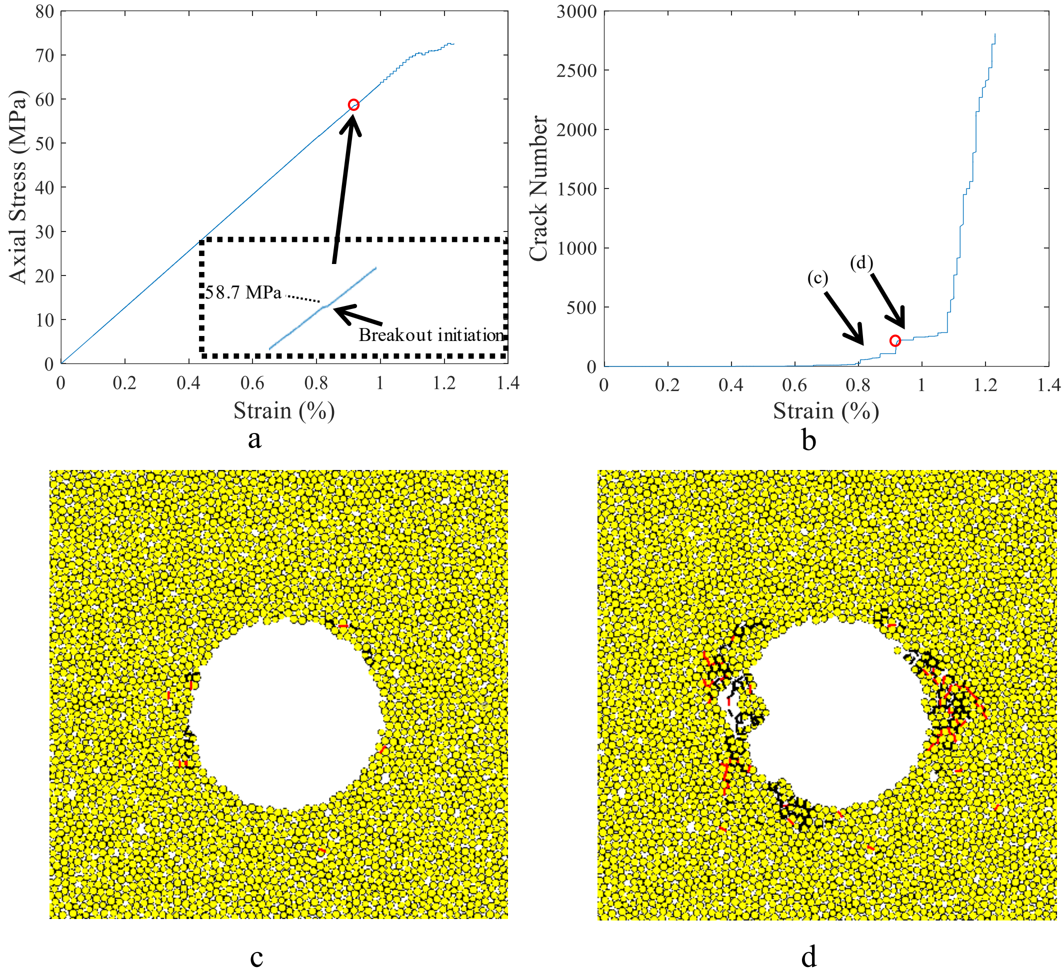

Figure 5.7 Borehole size test at 6 mm borehole radius: a) axial stress vs axial strain curve, where the red circled point is the breakout initiation stress of 58.7 MPa; b) crack numbers vs axial strain curve; c) borehole prior to breakout initiation; d) borehole after breakout initiation

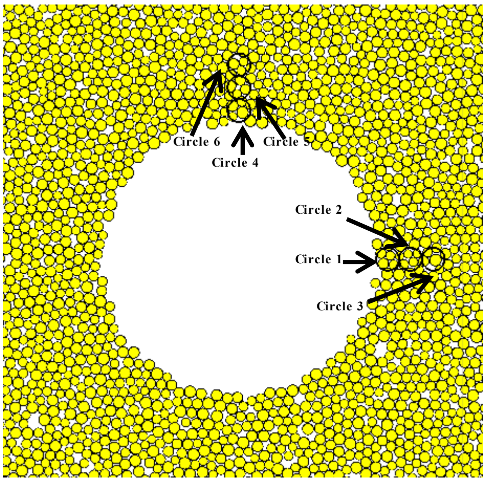

Figure 5.8 Stress measurement circles positions around 6 mm radius borehole

Figure 5.9a shows the tangential stress in measurement circles 1–3. Based on the figure, it can be seen that the tangential stress in circle 1 was approximately double that of the applied hydrostatic stress (σ_P) prior to point A, which agrees with Eq. (5.4). Clear stress re-distribution between circles can be observed after this point and eventually led to substantial stress reduction in circle 1 at point B; this point also happens to be the breakout initiation stress point in Figure 5.7a, which further confirms this methodology of analysing borehole size effect through PFC. On the other hand, stress averaging seems to be taking place between the two points as the tangential stress within circles tend to approach similar values. It is also worth noting that the deflections in stress–strain curves correspond to the formation of micro-cracks since the deflection points in Figure 5.9a are well matched with increasing crack numbers in Figure 5.7b, such that the measurement circle might also be used as a complementary indication tool for breakout initiation detection in PFC. The implication here is that the stress averaging is perhaps due to the energy release through micro-cracking, which was also discussed by some studies (Labuz et al. 1985; Ortiz 1988).

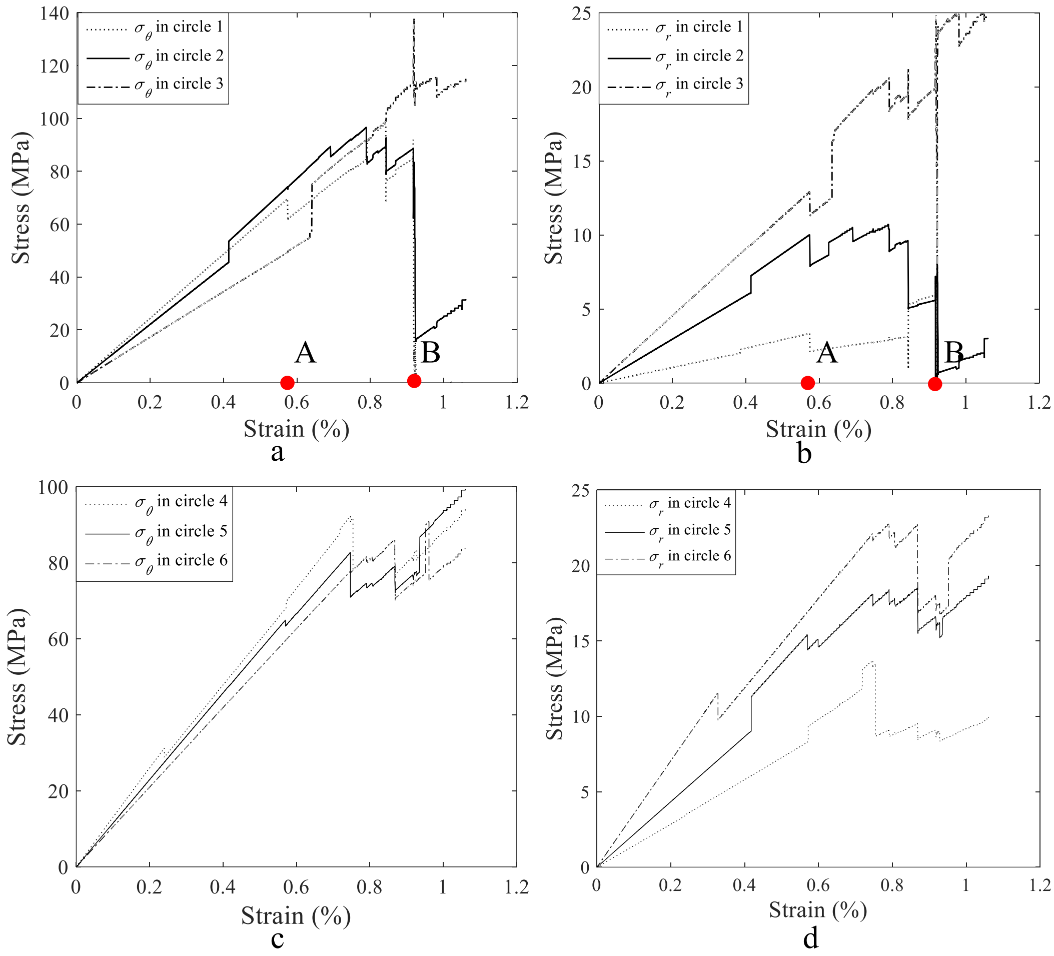

Figure 5.9 a)-d) Tangential and radial stresses within the measurement circles

Figure 5.9b illustrates the radial stress in measurement circles 1–3. The magnitude of radial stress in circle 1 was relatively small compared to other stresses, which is consistent with Eq. (5.1). Some degree of stress transfer between circles can also be found after the same point A in Figure 5.9a, although the radial stress magnitude in circle 3 was marginally greater than that of circle 1 and circle 2. Based on the results in Figure 5.9a and Figure 5.9b, it implies that the stress averaging distance of the material might be within the distance of 2–3 mm, which is in good agreement with the experimental observations from Carter et al. (1992). Similar to the tangential stress, there is also a significant drop in radial stress at point B, which again indicates the on-set breakout initiation. The magnitude of radial stress can be as high as 10 to 20 MPa prior to the on-set breakout initiation, as shown in Figure 5.9b. Hence, it is important to consider the influence of radial stress when estimating breakout initiation stress from the stress averaging concept. In addition, the numerical model may be further improved to simulate the phenomenon in more detail since it only considers the failure of bonding material instead of particle breakage. A grain-based model incorporating both intra- and extra-granular failure should be implemented in future studies to take account of micro-cracks within the grain.

Figure 5.9c–d show the tangential and radial stresses in measurement circles 4–6. An overall agreement can be observed between stresses in circles 1–3 and circle 4–6, in which stress redistribution started at about point A with lower change in magnitudes. There was no significant stress reduction at point B and breakout initiation occurred at the left and right sides of the borehole first, see Figure 5.7d. This is because the DEM model is heterogeneous and stress is not evenly distributed around the borehole.

5.3.2.3 Implications for pressure-dependent linear elastic model

Santarelli et al. (1986) suggested that Young's modulus of rock is not constant but rather depends on the confinement. In this case, the Young's modulus is higher in the rock due to higher radial stress. This leads to relocation of the maximum tangential stress from the borehole wall to the rock, namely, a pressure-dependent linear elastic model. Hence, Santarelli and Brown (1989) suggested that breakout initiation should occur at some distance from the borehole wall instead of the surface of the borehole.

Figure 5.9a shows that the tangential stress in circle 2 surpassed that in circle 1 during the loading stage prior to any cracking and the substantial stress reduction happened in both circles 1 and 2 at the same time. This might indicate the maximum tangential stress relocation around the borehole and breakout initiation at some distance from the borehole. However, this was not observed in measurement circles 4–6. Thereby, it is noticed that the majority of micro-cracking started around the borehole at the borehole wall rather than some distance into the rock, see Figure 5.9c–d. This is not in line with the proposed breakout initiation location from the pressure-dependent linear elastic model.

Although there might be tangential stress relocation due to change in Young's modulus, it is practically difficult to have fracture initiation into the rock due to the stress state. As presented by Santarelli et al. (1986), for 100 MPa hydrostatic pressure, the maximum tangential stress would be approximately 125 MPa at the distance that is 1.5 times the radius away from the centre of the borehole based on the model, whereas the tangential stress at the borehole wall is 100 MPa. However, the radial stresses at the two locations are considerably different under 100 MPa pressure. At the borehole wall, the radial stress can be neglected, whereas at the maximum tangential stress location, the magnitude of radial stress can be over 50 MPa based on the Kirsch solution. This means the breakout initiation would occur at the borehole wall due to its low confinement even considering the pressure-dependent linear elastic model. On the other hand, the breakout initiation might happen at a location into the rock if the distance is very small from the borehole wall, so that the magnitude of radial stress is minimal and can be neglected. This distance is rather difficult to determine and requires further investigation.

5.3.2.4 Comparison with experimental results

Figure 5.10 displays the simulation results against the previous experimental studies from normal compression and hollow cylinder tests, where the critical tangential stresses were estimated from Eq. (5.3) and Eq. (5.4). The figure shows that the simulation results are well aligned with literature data, which shows a decreasing trend with larger borehole radius. The decreasing trend tends to be steadier once the borehole radius is greater than 6 mm, whereas a sharper drop can be seen at smaller radii. As observed in the trend, it might be possible to derive an empirical relationship to estimate the breakout initiation stress based on two sets of data (normal compression and hollow cylinder tests).

In addition, it seems that the ratios obtained from normal compression tests are slightly lower than those from the hollow cylinder tests given the same borehole radius. This may be due to the size of the rock sample. In hollow cylinder tests, the specimen size is usually fixed with various borehole sizes. On the other hand, different specimen sizes were used in the normal compression tests, i.e. the larger the borehole radius, the larger the sample size. As discussed in many studies, different sample sizes already include the rock strength reduction due to the scale effect, in which smaller samples have higher strength than larger samples (Hunt 1973; Bažant 1984; Bažant and Xi 1991). Correspondingly, this may influence the borehole size effect investigation and increase the critical breakout initiation stress for smaller specimens. To verify the influence of the sample size and isolate the borehole size parameter, a systematic laboratory study was carried out in Section 3.2.

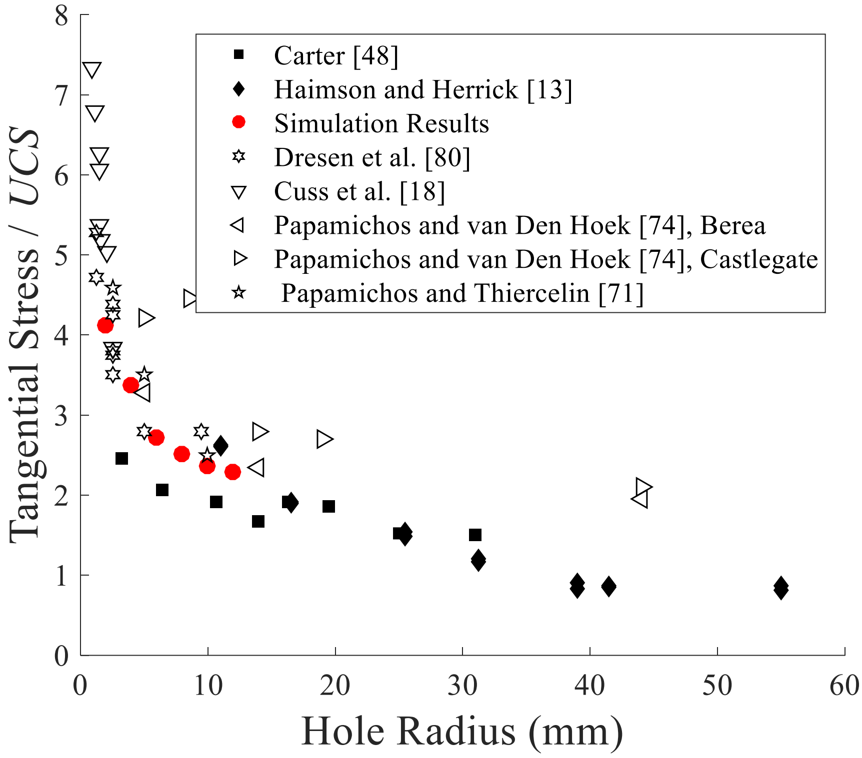

Figure 5.10 The ratio between critical tangential stress at breakout initiation vs UCS from both literature and numerical simulation, where the black filled markers are normal compression test data

5.3.3 Thermal effects on borehole size and borehole breakout

As exploitation activities including mining and geothermal wells are inevitably going deeper, the surrounding rock temperature also increases accordingly (Al Sayed et al. 2016; Gürtunca 2018). As discussed by a series of researchers (Heuze 1983; Keshavarz et al. 2010; Yavuz et al. 2010; Zhang et al. 2016), the temperature has an impact on the rock mechanical behaviour. It is suspected that the borehole breakout initiation stress and breakout angular span may also be affected by high temperature and affect the horizontal stress estimation. However, it is difficult to perform triaxial tests under high temperature in a laboratory environment. Previous thermal related studies on rock specimens have been carried out via PFC2D. Therefore, PFC2D was also used to investigate the breakout angular span under various temperatures.

5.3.3.1 Thermal contact model

In PFC2D, the thermal analysis does not require any calibration of micro-parameters and these parameters can be directly assigned to the synthetic specimen. The thermal material consists of a network of 'heat reservoirs (particles)' that are connected by 'thermal pipes (contacts)'. The thermal pipes enable the heat transfer between reservoirs through heat conduction and are governed by the thermal pipe contact model. In the model, each pipe can be represented by a one-dimensional entity with associated power (Q) to reflect the heat flux (Wanne and Young 2008; Itasca 2018). Q can be calculated and updated by:

$$\boldsymbol{Q = \frac{\Delta T}{\eta L}} \tag{5.5}$$

where ΔT = temperature difference between the two reservoirs connected by a pipe; L = length of the pipe; η = thermal resistance per unit length, which is used to describe the macro-isotropic thermal conductivity (k) of a material. The relationship between the two parameters can be expressed as:

$$\boldsymbol{\eta = \frac{1}{2k}\left(\frac{1-n}{\sum_{N_b} V_b}\right)\sum_{N_p} l_p} \tag{5.6}$$

where n = porosity in the volume of interest; N_b = number of particles within the region; N_p = number of thermal pipes within the region; V_b = volume of a particle; l_p = length of a thermal pipe. The heat-conduction equation for each reservoir is defined as:

$$\boldsymbol{-\sum_{p=1}^{N} Q_p + Q_v = mC_v\frac{\partial T}{\partial t}} \tag{5.7}$$

where Q_v = the heat-source power; Q_p= power of each thermal pipe that is flowing out of the reservoir; m = thermal mass; C_v = the specific heat. In PFC2D, the thermally induced change of particle size and bonding forces are considered to represent the thermal strain. The temperature variation results in the particle radius expansion, which can be calculated by:

$$\boldsymbol{\Delta R = \alpha R \Delta T} \tag{5.8}$$

where ΔR = change in particle radius due to temperature change, α = thermal expansion coefficient of particles. The thermal expansion of the bonding material can be denoted as the change in the normal force ($\overline{F_n}$) of the bond:

$$\Delta\overline{F_n} = -k_n A(\bar{\alpha}\bar{L}\Delta T) \tag{5.9}$$

where k_n = normal stiffness of the bond; A = cross-section area of the bond; $\bar{\alpha}$ = the average thermal expansion coefficients of the two particles on each end of the bond; $\bar{L}$ = the bond length.

5.3.3.2 Simulation procedures

To accurately simulate the breakout generated under the thermal effect, the appropriate thermal properties of Gosford sandstone were selected. The specific heat was assigned to be 790 J/kg˚C and the thermal expansion coefficient was $1.3\times10^{-5}K^{-1}$ (Kirk and Williamson 2012). Based on Abdulagatova et al. (2009), the thermal conductivity of the specimen was chosen as 3.75 $Wm^{-1}K^{-1}$. Once the rock was created, it was gradually heated inwards to reach the pre-set temperature, see Figure 5.11. The standard procedures discussed in Section 5.2.3 and Section 5.3.2 were then followed to apply horizontal stresses to the sample to maintain consistency between simulations and directly compare the results produced with and without the thermal effect. To investigate the corresponding thermal effect that could possibly be encountered at deep locations, four scenarios were considered with temperatures ranging from 100 ˚C to 400 ˚C.

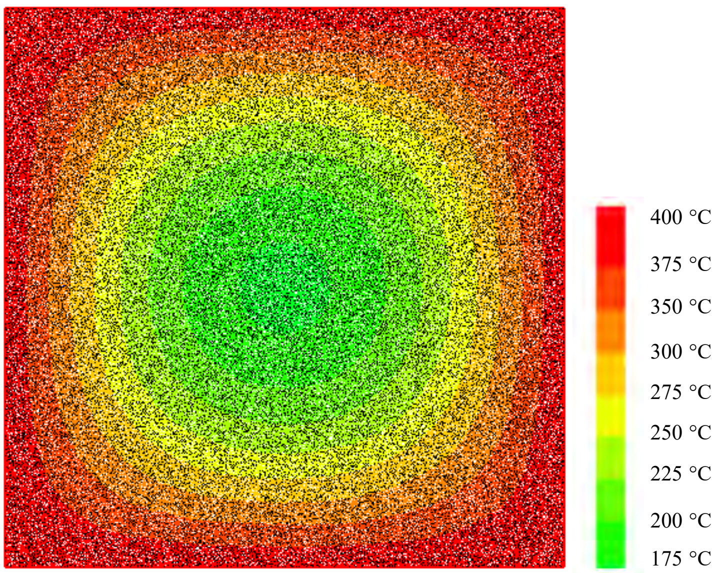

Figure 5.11 Sample heating at 400 ˚C temperature, with different colour layers representing the temperature (the red colour layer is at 400 ˚C)

5.3.3.3 Thermal influence on borehole size effect

A total number of 20 simulations were conducted from 4 mm to 12 mm borehole sizes to investigate the influence of temperature on breakout initiation stress. Figure 5.12 shows the results obtained from the numerical simulation. Overall, a decreasing trend of breakout initiation stresses with increasing temperatures can be observed. The rates of reduction are higher for 4 mm and 6 mm borehole sizes compared to the larger borehole sizes, suggesting the temperature has some degree of influence on breakout initiation stress, especially for smaller borehole size. On the other hand, the changes in the stress in larger borehole sizes (8–12 mm) are minimal and may be neglected since the reduction can be as small as 5%. The axial stress required for 8 mm was higher than 6 mm under 300 ˚C and 400 ˚C. As discussed earlier, the synthetic rock generated in the DEM model is not isotropic. Due to the randomness of particle size distribution, there are locations around the borehole that contained larger particles, so that micro-cracking will occur in these locations first, as shown in Figure 5.7c–d. Under the temperature effect, particles expanded and created additional contact force to bonds. This can induce stress localisation at places where particles are larger, so that the breakout initiation can occur at lower stress for 6 mm borehole radius under higher temperature.

Figure 5.13a–e displays the proportion of tensile to shear cracks under different temperatures. A general decreasing trend of the ratio can be seen from the figure, implying that as temperature increases, the micro-cracking mode gradually transfers from tensile cracking to shear cracking; except for under 10 mm borehole size, where the ratio fluctuated with temperature. Similar to the breakout initiation stress, the decrease in ratio is more significant for 4 mm and 6 mm borehole size than for larger borehole sizes. The implication here is there might be a correlation with the two parameters, although further investigation is required. Figure 5.13f shows the crack ratio with different borehole size neglecting the influence of temperature. It is noted that the crack ratio for 4 mm borehole size is substantially lower than the others, whereas the ratios for other borehole sizes are quite consistent with minor differences. This is also true for the ratios under other temperatures, as shown in Figure 5.13a–e. It is suspected that this low crack ratio might contribute to the breakout imitation stress since the stress required to initiate breakout for 4 mm borehole size is marginally higher than that of other sizes, as shown in Figure 5.12. However, further study is also required to confirm this hypothesis. Overall, it can be seen that the temperature has an influence on the micro-cracking mode, which may subsequently affect the breakout initiation stress.

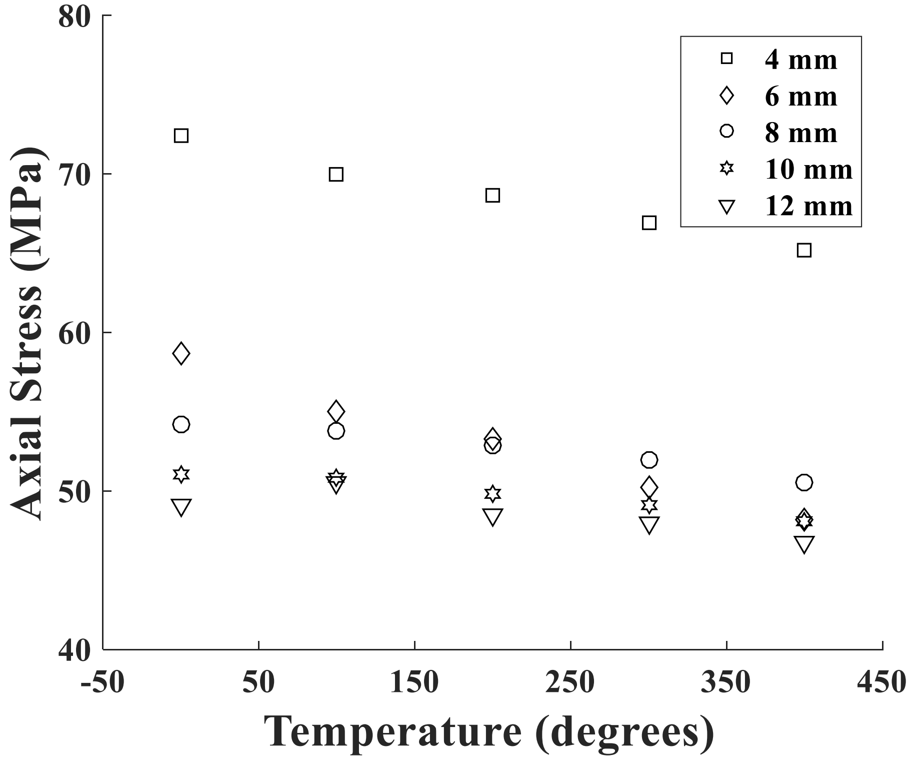

Figure 5.12 Axial stresses for on-set breakout initiation under various temperatures

The above section analysed the initiation stress, whereas this section focuses on the influence on breakout angular span as it is the most critical parameter for horizontal stress constraint and estimation. Numerical simulations were conducted under different temperatures and results are in Figure 5.14. Under lower σ_H (40 MPa), the breakout angular span remains relatively constant regardless of the temperature change, whereas the breakout angular span increased considerably at 300 ˚C and 400 ˚C for higher σ_H (50 MPa). The change between 300 ˚C and 400 ˚C is minimal. This implies that the thermal effect may influence the breakout angular span under a higher horizontal stress condition when the temperature is over 300 ˚C.

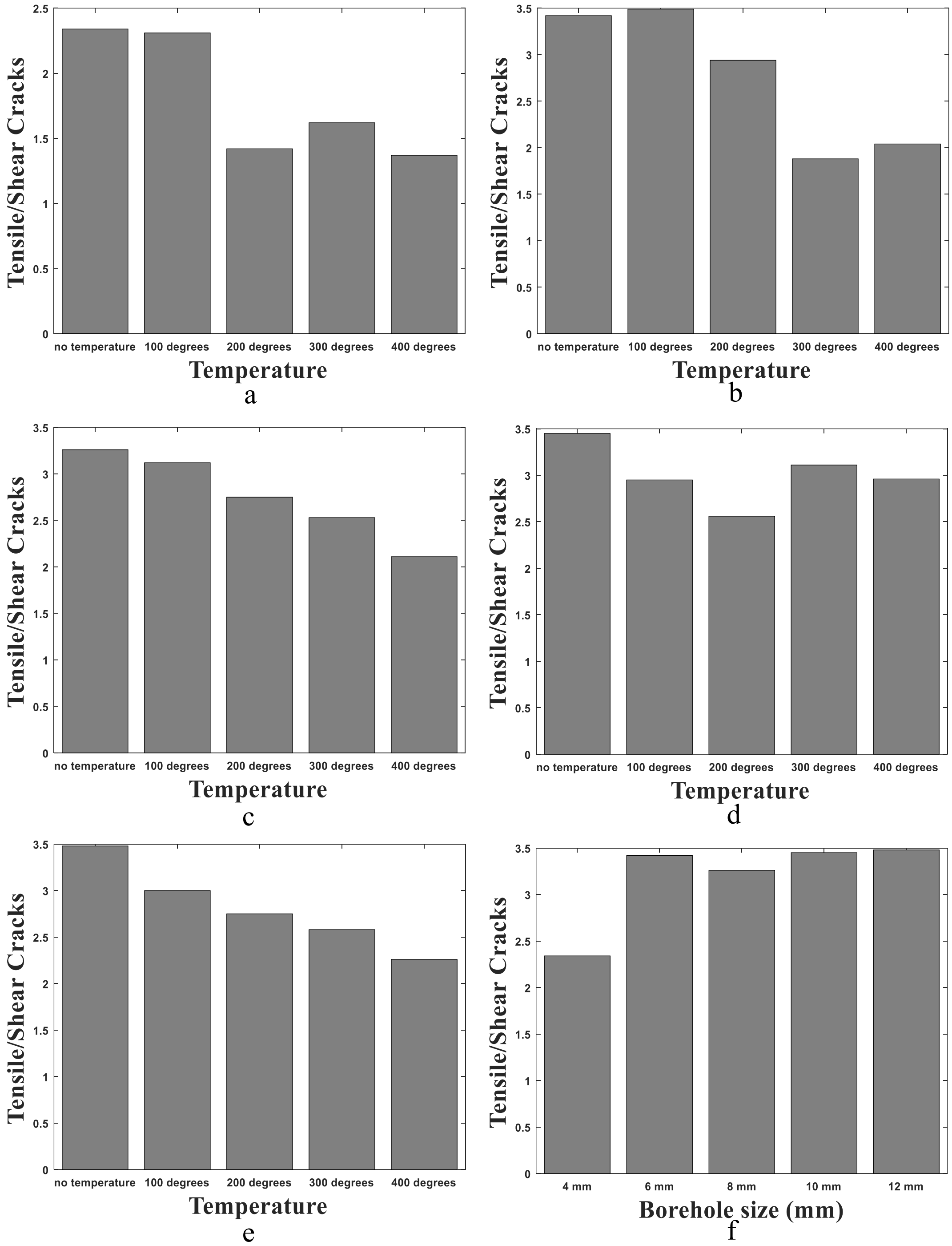

Figure 5.13 a)–e) tensile/shear cracks ratio at 4 -12 mm radius at various temperatures; f) tensile/shear cracks ratio by different borehole sizes without temperature

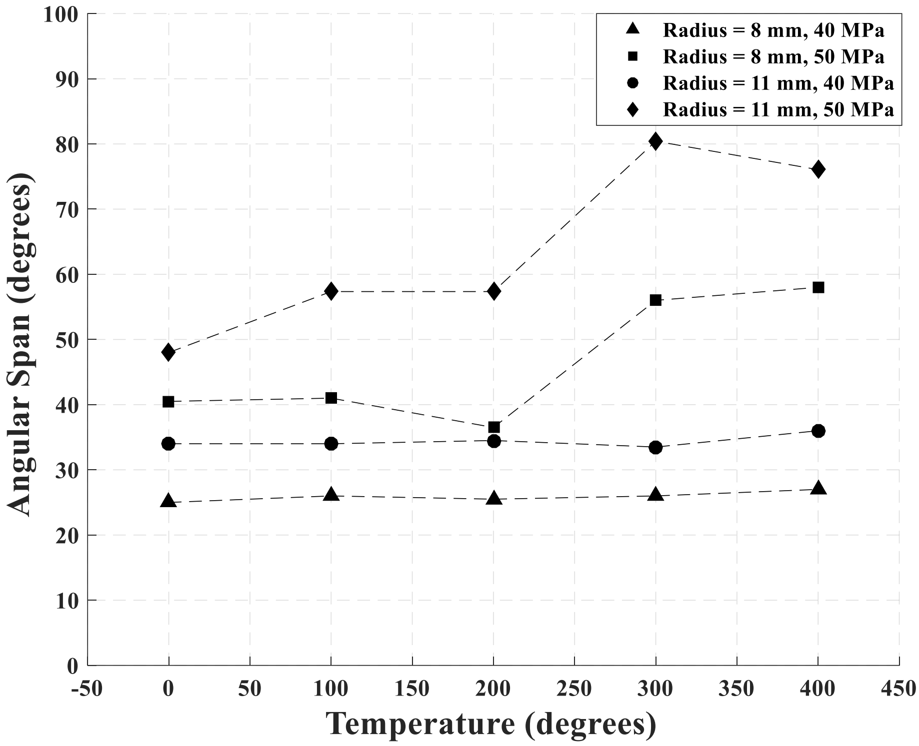

Figure 5.14 Simulation results under various conditions

Figure 5.15 shows the simulation results with 11 mm borehole size under 50 MPa of σ_H, where the base case (no temperature) is displayed in Figure 5.4. The breakout orientations under 100 ˚C and 200 ˚C (see Figure 5.15a–b) are consistent with the simulation without the temperature. However, the breakout orientation changed under the higher temperature, see Figure 5.15c–d. A similar orientation change was also observed with 8 mm borehole size under 50 MPa of σ_H. This is perhaps due to the thermal related micro-cracks generated during the breakout formation, as particles expand during the heating process which may lead to increased contact force in local areas. For instance, micro-cracks started to appear and become dense around the top right side of the borehole as temperature increases, which was not observed under 0 ˚C and 100 ˚C. Hence, the local micro-cracking due to the temperature effect subsequently altered the breakout orientations as well as angular span under higher temperature. The implication here is that the temperature might be considered for the determination of horizontal stress orientation and magnitudes for borehole breakout collected from geothermal wells.

The simulation shows that there might be some degree of influence on breakout angular span and orientation under the high temperature (300 ˚C) and high horizontal stress condition (50 MPa), although this requires further investigation and consideration, especially for deep geothermal wells where the temperature can be as high as 500 ˚C (Ikeuchi et al. 1998). On the other hand, the underground temperatures in coal mining areas are relatively low. For instance, He (2009) reported that the average temperature in 33 coal mines with depth of cover over 1000 m is between 30 ˚C to 40 ˚C, whereas Xiaojie et al. (2011) summarised the information in numerous studies in China, as shown in Table 5.3. Therefore, thermal effect on breakout angular span may not need to be considered under these scenarios.

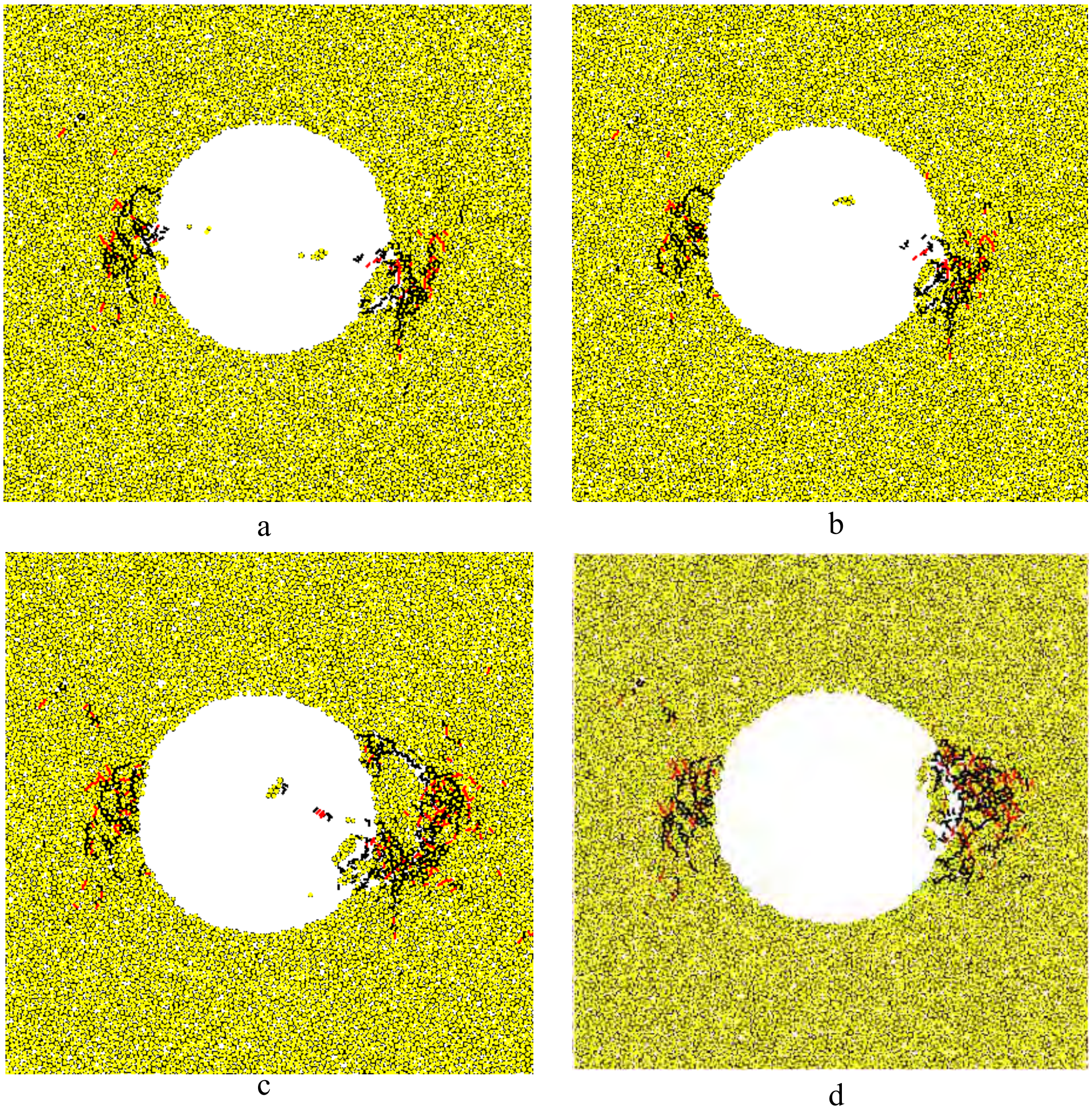

Figure 5.15 Breakout generated under different temperatures at 11 mm borehole radius: a) 100 ˚C; b) 200 ˚C; c) 300 ˚C; d) 400 ˚C

Table 5.3 Mine site temperature collected from literature by Xiaojie et al. (2011)

Mine Site Name	Depth of Cover (m)	Underground Temperature (˚C)
Sanhejian	1300	56
Jiahe	800	32–34
Zhangshuanglou	1000	34–36
Zhangxiaolou	1125	30
Jisan	785	31–51
Wobei	640	35–37
Yongchuan	800	29.3–31.5

5.4 CONCLUSIONS

Breakout geometrical variation under different stress conditions was studied numerically. Laboratory results revealed that breakout geometries are closely related to horizontal stress magnitudes as well as the borehole size. Both higher maximum horizontal stress and larger borehole radius can result in deeper and wider breakout given the same other parameters. The implication is that there is a relationship between breakout geometries and horizontal stress magnitudes.

The DEM model result shows similar breakout behaviour as discussed above. Based on the numerical simulations, it is clear that the breakout angular span forms at a very early stage of the breakout and does not widen significantly, which is then followed by subsequent fracture propagation along the minimum horizontal stress direction. The results agree with the argument noted in various studies and indicate that breakout angular span can be used as a reliable indicator of horizontal stress estimation. Due to the complexity of breakout depth development and its relationship with horizontal stress magnitudes, it is difficult to derive a simple analytical method for stress estimation and compare it against the experimental measurements. Therefore, it may be useful to consider an unconventional approach either through time-dependent numerical simulations or advanced computer techniques, including machine learning or neural networks. For instance, given the vast breakout data available, a massive database could be used to train a model to correlate breakout depth and horizontal stress magnitudes.

In addition, the relationship between breakout initiation stress and borehole size was also investigated in this study. Simulation results are well in line with the previous experimental observations in which smaller borehole size can considerably amplify the breakout initiation stress. The stress analysis around the borehole also shows some degree of stress averaging from micro-cracking and the importance of radial stress. Therefore, borehole size is a critical parameter in laboratory borehole breakout studies and the stress averaging approach should not ignore the influence of radial stress.

It is worth noting that micro-cracking occurred at the borehole wall rather than some distance into the rock and borehole breakout initiation is likely to occur at the borehole wall even considering the pressure-dependent linear elastic model. However, further investigation is required to confirm this observation.

Based on the analysis of literature data, it was found that the ratios of breakout initiation and UCS in normal compression tests were slightly lower than ratios in hollow cylinder tests. It might be resulted from the rock strength variation due to the scale effect as the normal compression tests used various specimen sizes. However, due to the limited data observations, this conclusion is tentative. A systematic laboratory approach was undertaken to study the influence of specimen size on the breakout initiation stress, as discussed in Section 3.2.

This study investigated the thermal effect on borehole size and borehole breakout. Results showed that the breakout initiation stress reduces with increasing temperature, although it may be neglected for borehole size over 6 mm. A higher proportion of shear cracks was induced as temperature increases, which may also contribute to the decrease in breakout initiation stress. For the thermal effect on borehole breakout, under the lower maximum horizontal stress, the temperature only has a minor influence on breakout. Conversely, the higher horizontal stress resulted in a significantly wider breakout angular span when the temperature is over 300 °C. The corresponding breakout orientation also varies under these scenarios. This implies that the thermal effect may need to be taken into account under high temperature and high horizontal stress conditions when using breakout angular span for horizontal stress constraint or estimation, especially in geothermal wells. However, the temperature in most underground coal mines is relatively low, suggesting the thermal effect may be neglected in this case.

6 EXPERIMENTAL STUDY AND COMBINED HORIZONTAL STRESS MAGNITUDE ESTIMATION FROM ARTIFICIAL NEURAL NETWORK AND CONSTITUTIVE MODELLING

The literature review in Chapter 2 revealed that the majority of the experimental studies focused on the influence of maximum horizontal stress on breakout geometries, whereas the minimum horizontal and vertical stresses were rarely investigated (Haimson and Herrick 1986; Herrick and Haimson 1994; Haimson and Lee 2004; Lee et al. 2016). However, in field conditions, in-situ stress is always three-dimensional and the intermediate stress has significant influence on rock failure (Murrell 1963; Stacey and De Jongh 1977). To study the effect of two principal stresses, a series of laboratory breakout tests are conducted and the results are presented in Section 6.1 and Section 6.2.

In Chapter 4, an approach to maximum horizontal stress magnitude estimation from borehole breakout was developed based on the Kriging technique. This method showed remarkable accuracy on both laboratory and field data. Section 6.3 attempted to use the stress polygon (derived from a constitutive relationship) technique to predict minimum horizontal stress given the maximum horizontal stress can be derived from Kriging. Nine failure criteria were examined against 79 experimental data on the reliability of minimum horizontal estimation, in which eight failure criteria considered the effect of the intermediate stress. However, due to the sensitivity of minimum horizontal stress (as detailed in Section 6.3), none of the constitutive models yielded reliable results.

To overcome this limitation, an Artificial Neural Network (ANN) model is introduced in Section 6.4 to estimate the minimum horizontal stress from borehole breakout. ANN is a powerful computer algorithm to mimic the human nervous system, which recognises complex patterns and provides estimations (Chen et al. 2019). This technique has been implemented in the rock mechanics field in many cases (Yilmaz and Yuksek 2008; Qi et al. 2018; Moon et al. 2019). The ANN model is constructed based on training, validation and testing on 79 laboratory data, and independently validated against 23 field data as discussed in Section 6.5.1. Section 6.5.2 provides a comparative analysis of the prediction of maximum horizontal stress through various approaches including ANN, stress polygon and Kriging. In addition, a sensitivity analysis of input parameters is conducted for the ANN model in Section 6.5.3.

Based on the findings of Chapter 6, a new technique for horizontal stress estimation from borehole breakout is developed, which can, in turn, enhance the understanding of local stress environments from existing downhole logging data.

6.1 EXPERIMENTAL SETUP

In this study, Hydrostone-TB was used as the casting rock specimen with a mixing material-to-water ratio of 0.375. All samples were prepared as cubes with dimensions of 120 × 120 × 120 mm^3 and cured at room temperature for 14 days. Based on laboratory rock property testing, the mechanical properties of Hydrostone-TB are summarised in Table 6.1. Holes of 22 mm diameter were drilled at the centre of the specimens before the start of the experiment. In past experimental studies, researchers focused mainly on the relationships between σ_H and breakout geometries by altering the magnitude of σ_H (Haimson and Herrick 1986; Haimson and Herrick 1989; Haimson and Song 1993; Herrick and Haimson 1994; Haimson and Lee 2004; Lee and Haimson 2006; Lee et al. 2016), such that influences of the other two principal stresses on breakout geometries were not investigated in detail. As the two other principal stresses may also have an effect on breakout geometries, two series of experiments were carried out in this study. The first series of experiments varied the magnitude of σ_h at an increment of 5 MPa in each individual test while keeping σ_H and σ_v the same. Similarly, the second series of experiments changed the magnitude of σ_v and kept σ_H and σ_h constant.

Table 6.1 Mechanical properties of Hydrostone-TB

Uniaxial compressive strength (UCS)	Tensile strength (UTS)	Cohesion (MPa)	Friction angle (°)	Poisson's ratio (v)
18.2	2.07	6.7	28	0.19

The laboratory investigation was carried out using a specially designed true triaxial confinement cell, as shown in Figure 6.1a. Vertical and minimum horizontal stresses can be first applied by tensioning bolts on the side plates, and stress levels were monitored by the attached load cells. Then, the maximum horizontal stress was applied in the MTS machine. When the required stresses were achieved, they were maintained on the specimen for another 30 minutes to enable the complete development of borehole breakout to occur (Haimson et al. 1991; Haimson and Kovacich 2003). On completion of the test, specimens were cut along the borehole axis to allow optical scanning to obtain accurate breakout geometrical profiles, see Figure 6.1b. Details of the experimental procedures are summarised in Lin et al. (2019).

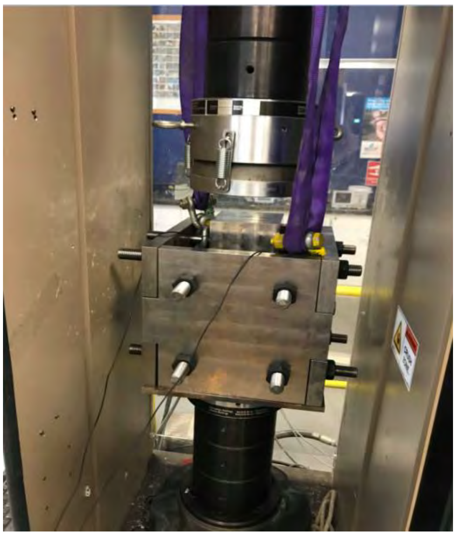

a

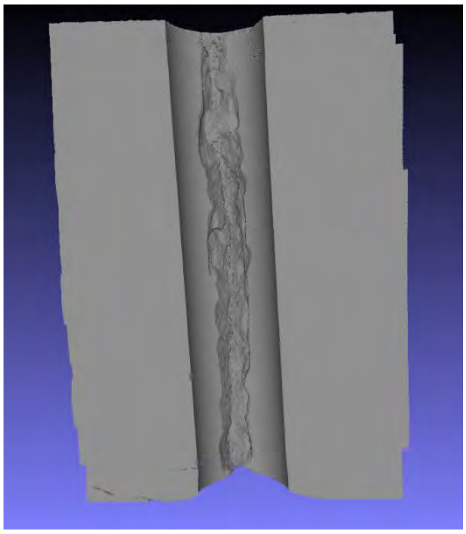

b

Figure 6.1 a) True triaxial test confinement cell (Lin et al. 2019); b) optimal scanning breakout profile on Hydrostone-TB

6.2 Experimental Results and Discussion

Figure 6.2 shows the relationships between breakout geometries and σ_h under the same σ_H and σ_v conditions. From Figure 6.2a, it is clear that the higher σ_h led to shallower normalised breakout depth (L/R). This suggests that L/R may have an inverse relationship with σ_h. It is noted that rates of change in L/R with respect to σ_h were relatively constant and similar in the two series of tests, although the magnitudes of stresses applied were different. Similarly, breakout angular span also decreases with increasing σ_h at a relatively constant rate, as illustrated in Figure 6.2. Results show that breakout geometries are substantially affected by the magnitude of σ_h, indicating that it is possible to derive σ_h from borehole breakout data.

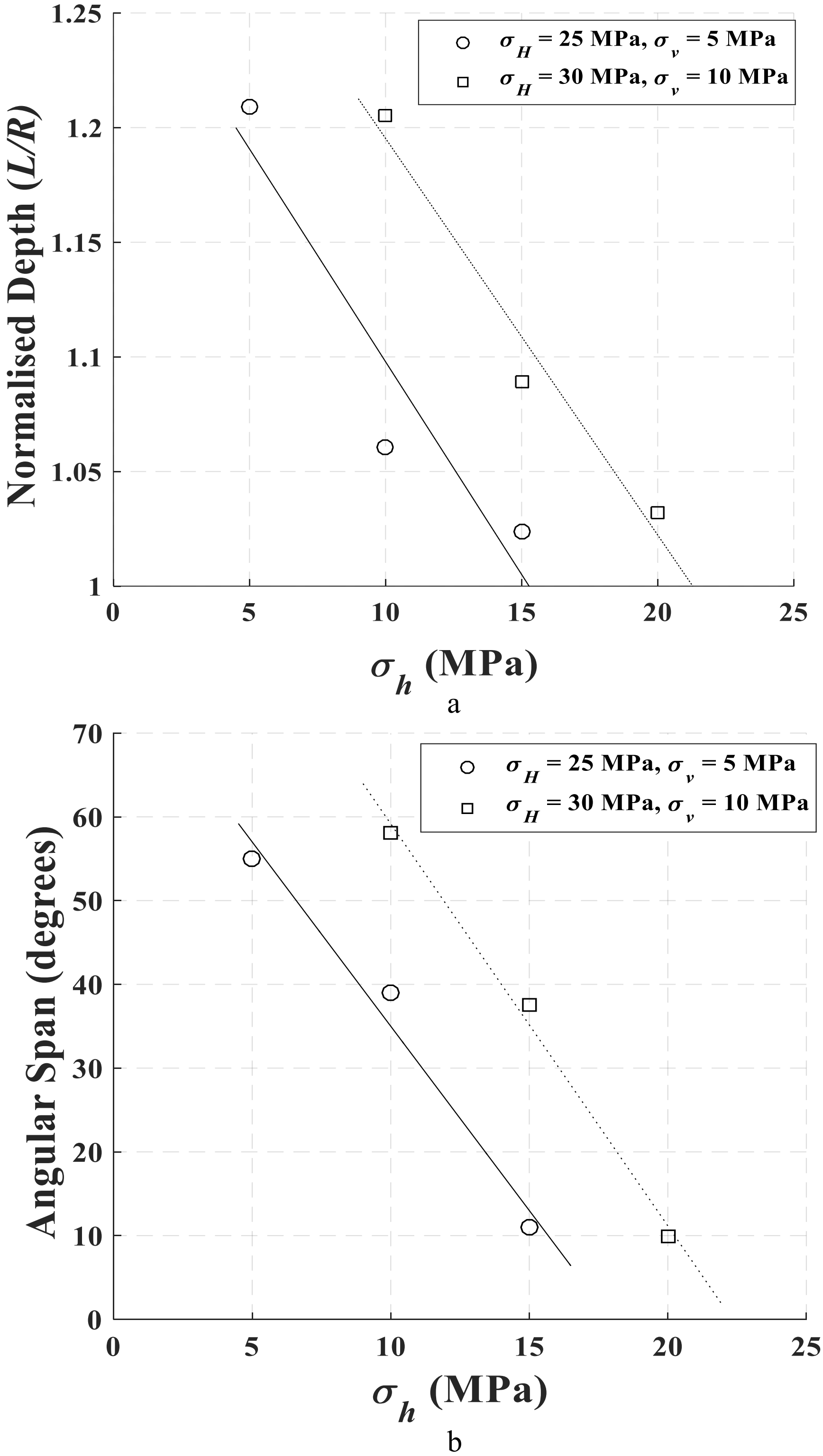

Figure 6.2 a) Minimum horizontal stress vs normalised breakout depth; b) minimum horizontal stress vs breakout angular span

Boreholes in a rock mass are a truly three-dimensional medium in which the axial stress can have significant magnitude. Hence, it is also important to consider the impact of σ_v.

Figure 6.3a–b show the breakout geometries under different σ_v magnitudes. From the figure, it can be observed that both geometries decrease with increasing σ_v, suggesting an inverse correlation between σ_v and breakout geometries. Compared to σ_h, the influence of σ_v is less significant as the gradients of both angular span and normalised breakout depth are flatter than those under various $\sigma_h$values. Results here suggest that when analysing borehole breakout data, it is important to incorporate the influence of σ_v and σ_h since both parameters can have considerable effect on breakout geometries. Therefore, the implication here is that when estimating the magnitude of either σ_H or σ_h, the plane stress condition may not be appropriate as it is critical to take account of σ_v.

6.3 Horizontal Stress Estimation Using Failure Criteria

As discussed in numerous studies, breakout angular span forms at the initial stage of breakout and remains relatively constant as breakout propagates along the σ_h direction (Mastin 1984; Plumb and Hickman 1985; Stock et al. 1985; Barton et al. 1988; Kessels 1989; Duan and Kwok 2016; Lee et al. 2016). This indicates that breakout angular span can be used as a reliable parameter for horizontal stress estimation rather than breakout depth due to its sophisticated formation mechanism (Barton et al. 1988; Chang et al. 2010; Lin et al. 2019). Attempts have been made since the 1980s to either constrain the magnitudes of the two horizontal stresses or to calculate σ_H from breakout angular span based on different failure criteria (Barton et al. 1988; Vernik and Zoback 1992; Zoback et al. 2003; Chang et al. 2010; Lee and Ong 2018; Song and Chang 2018), as one breakout parameter (θ_b) cannot estimate two horizontal stress magnitudes (Lee et al. 2016). To overcome this problem, Lin et al. (2020) proposed a machine learning technique which could estimate the magnitude of σ_H based on borehole breakout depth and angular span. The methodology has been verified against both experimental and field data and presented promising results. Hence, it may be possible to derive the σ_h magnitude from breakout angular span and estimated σ_H.

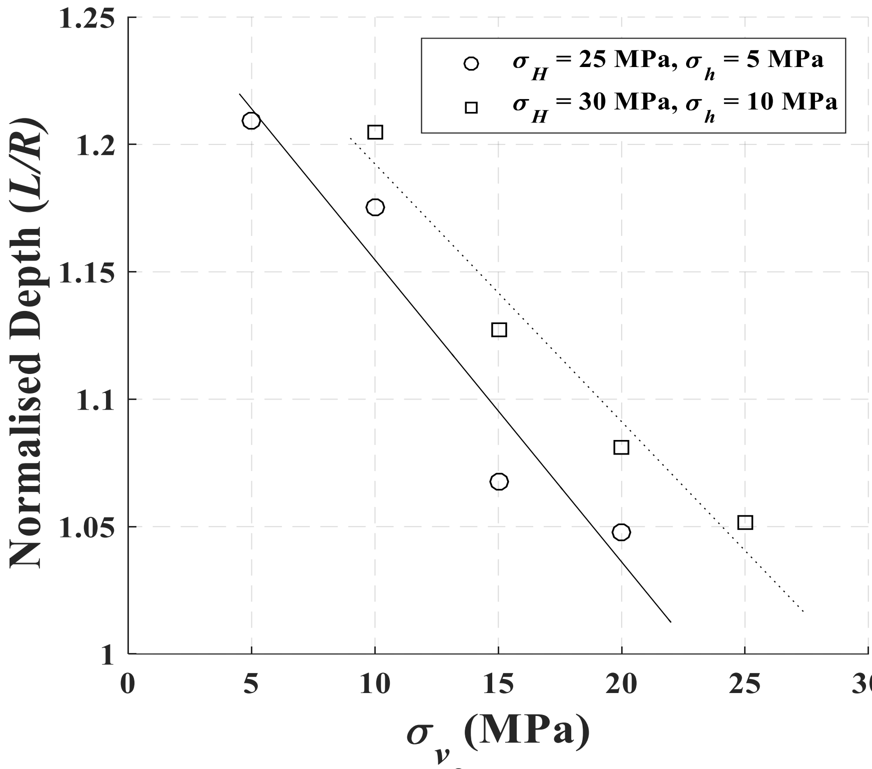

a

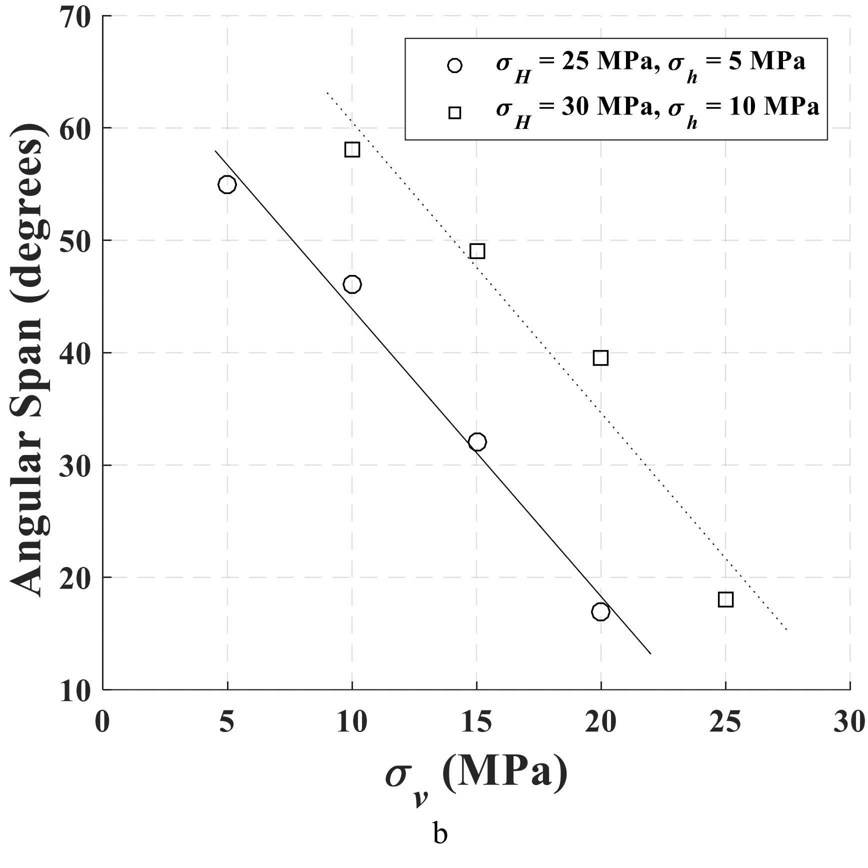

b

Figure 6.3 a) Vertical stress vs normalised breakout depth; b) vertical stress vs breakout angular span

6.3.1 Kirsch solution

Barton et al. (1988) initially proposed that at the breakout angular, the tangential stress (σ_θ) should be equal to the UCS value of rock. Hence, breakout angular span can be used to calculate one horizontal principal stress if the other is given. Since the vertical stress has considerable influence on the breakout geometries, the intermediate stress should also be taken into account during the analysis. In this section, different failure criteria are compared to determine the most appropriate criterion for estimating σ_h based on the experimental data. Based on the famous Kirsch solution (Jaeger et al. 2009), the stress condition around the borehole wall (where L/R = 1) can be expressed as:

$$\boldsymbol{\sigma_\theta = (\sigma_H + \sigma_h) - 2(\sigma_H - \sigma_h)cos2\theta} \tag{6.1}$$

$$\boldsymbol{\sigma_r = 0} \tag{6.2}$$

$$\boldsymbol{\sigma_z = \sigma_v - 2v(\sigma_H - \sigma_h)cos2\theta} \tag{6.3}$$

$$\boldsymbol{\tau_{r\theta} = 0} \tag{6.4}$$

where 2θ = 180 – breakout angular span (θ_b), v = Poisson's ratio, σ_θ = tangential stress, σ_r = radial stress, σ_z = vertical stress and $\tau_{r\theta}$ = shear stress. Considering the rock that is subjected to a triaxial stress condition around the borehole wall, σ_θ, σ_z and σ_r can be denoted as major (σ_1), intermediate (σ_2) and minor (σ_3) principal stresses, respectively.

6.3.2 Rock failure criteria

6.3.2.1 Failure criteria without considering intermediate stress

In general, failure criteria can be classified into two groups, depending on the consideration of the intermediate stress (principal stress acting parallel to the borehole axis) effect. The typical failure criteria without considering intermediate stress include Mohr–Coulomb, Hoek–Brown, Griffith and Tresca. Zoback et al. (1985) attempted to estimate both horizontal stress magnitudes based on breakout geometries and the Mohr–Coulomb failure criterion. Due to the subsequent elongation of breakout depth from inelastic deformation and creep behaviour (Mastin 1984; Barton et al. 1988; Zheng et al.

1989; Schoenball et al. 2014), it is difficult to use this criterion as a reliable parameter in a constitutional relationship. This was one of the major reasons to develop a machine learning model for the maximum horizontal stress estimation from borehole breakout (Lin et al. 2020). Since the minor principal stress ($\sigma_3 = \sigma_r = 0$) is negligible at the borehole wall, the failure criteria which do not incorporate the intermediate stress can all be simplified as the uniaxial compressive stress condition regardless. Hence, rock is only subjected to the tangential stress (σ_θ) at the borehole wall, i.e.

$$\boldsymbol{\sigma_1 = \sigma_\theta = UCS} \tag{6.5}$$

Barton et al. (1988) were the first researchers to introduce this approach, suggesting that the maximum horizontal stress can be estimated given the minimum horizontal stress:

$$\boldsymbol{\sigma_H = \frac{UCS}{(1 - 2cos2\theta)} - \sigma_h \frac{(1 + 2cos2\theta)}{(1 - 2cos2\theta)}} \tag{6.6}$$

where $2\theta = 180^\circ - 2\theta_b$. This method has been implemented in many field conditions and is the basis of the contemporary stress polygon technique to constrain the magnitudes of horizontal stresses in conjunction with Anderson's faulting mechanism (Barton et al. 1988; Zoback et al. 2003; Yaghoubi and Zeinali 2009; Nian et al. 2016; Molaghab et al. 2017). It provides an indication of two horizontal stress magnitudes in the field, although the approach failed to consider the influence of intermediate stress. In order to estimate the magnitude of the minimum horizontal stress, Eq. (6.6) can be rearranged as:

$$\boldsymbol{\sigma_h = \frac{UCS - (1 - 2cos2\theta)\sigma_H}{(1 + 2cos2\theta)}} \tag{6.7}$$

6.3.2.2 Failure criteria considering the intermediate stress

Based on the laboratory results, it is clear that the vertical stress influences breakout angular span; this means that the intermediate stress should be considered in σ_h estimation according to Eq. (6.3). To determine the most reliable criteria for calculating σ_h from breakout angular span, several failure criteria are summarised and discussed in the following section. Since the approach is developed for practical application, it is important to use common parameters including UCS, UTS, cohesion (c) and friction angle (ϕ), rather than other empirical parameters which are difficult to collect in the field. Table 6.2 presents the failure criteria that are studied in this chapter.

Table 6.2 Failure criteria with intermediate stress

Failure Criteria	Governing Equation
Mogi–Coulomb	$\tau_{oct} = a + b\sigma_{m.2}$
Modified Wiebols–Cook	$J_2^{1/2} = A + BJ_1 + CJ_1^2$
Von Mises	$J_2^{1/2} = \frac{UCS}{3} = \sqrt{\frac{1}{6}((\sigma_1 - \sigma_2)^2 + (\sigma_2 - \sigma_3)^2 + (\sigma_3 - \sigma_1)^2)}$
Inscribed Drucker–Prager	$J_2^{1/2} = \frac{3UCS \times cos\phi}{2\sqrt{q}\sqrt{9 + 3sin^2\phi}} + \frac{3sin\phi}{\sqrt{9 + 3sin^2\phi}}J_1$
Circumscribed Drucker–Prager	$J_2^{1/2} = \frac{\sqrt{3}UCS \times cos\phi}{\sqrt{q}(3 - 3sin\phi)} + \frac{6sin\phi}{\sqrt{3}(3 - 3sin\phi)}J_1$
Modified Lade	$\frac{(I_1')^3}{I_3'} = 27 + \eta$
Murrell	$(\sigma_1 - \sigma_3)^2 + (\sigma_1 - \sigma_2)^2 + (\sigma_2 - \sigma_3)^2 = 24T(\sigma_1 + \sigma_2 + \sigma_3)$
Stassi D'Alia	$(\sigma_1 - \sigma_3)^2 + (\sigma_1 - \sigma_2)^2 + (\sigma_2 - \sigma_3)^2 = 2(UCS - T)(\sigma_1 + \sigma_2 + \sigma_3) + 2UCS \times T$

6.3.2.2.1 Mogi–Coulomb

Based on a series of polyaxial tests on various hard rocks using a customised apparatus, Mogi (1971) investigated the effect of intermediate and minor stresses on the ultimate strength of rock. Results showed that both stresses affected the rock failure strength, and Mogi (1971) proposed an empirical relationship to incorporate these stresses:

$$\tau_{oct} = f(\sigma_{m.2}) \tag{6.8}$$

where $\tau_{oct} = \frac{1}{3}\sqrt{(\sigma_1 - \sigma_2)^2 + (\sigma_1 - \sigma_3)^2 + (\sigma_2 - \sigma_3)^2}$ = octahedral shear stress, $\sigma_{m.2} = \frac{1}{2}(\sigma_1 + \sigma_3)$ = mean normal stress and f = a monotonically increasing function with a power-fit on $\sigma_{m.2}$, i.e. $\sigma_{m.2}^n$; where n is obtained from curve fitting of experimental data. This failure criterion was implemented by Haimson and Song (1995) and Song and Haimson (1997) on σ_H estimation with given σ_h, angular span and rock information prior to the introduction of Mohr–Coulomb parameters to Mogi–Coulomb. Results suggested that Mogi–Coulomb is a reliable failure criterion for σ_H estimation.

Al-Ajmi and Zimmerman (2005) subsequently argued that this power-fit Mogi–Coulomb function can be replaced with a linear function, and its parameters can be obtained from Mohr–Coulomb according to polyaxial test data, such that the equation was modified as:

$$\tau_{oct} = a + b\sigma_{m.2} \tag{6. 9}$$

with

$$a = \frac{2\sqrt{2}}{3}\frac{UCS}{q+1}$$

$$b = \frac{2\sqrt{2}}{3}\frac{q-1}{q+1}$$

$$q = (1 + sin\phi)/(1 - sin\phi)$$

The Mogi–Coulomb failure criterion has also been regarded as a reliable failure criterion for wellbore stability analysis (Zhang et al. 2010; Rahimi and Nygaard 2015).

6.3.2.2.2 Modified Wiebols–Cook

Zhou (1994) proposed a failure criterion to model the initial borehole breakout shape, which was developed as an extension of the Drucker–Prager criterion (Bradley 1979). Since this model has similar characteristics to Wiebols–Cook (Wiebols and Cook 1968), it was later named the modified Wiebols–Cook failure criterion. The governing equation of the modified Wiebols–Cook is presented below:

$$J_2^{1/2} = A + BJ_1 + CJ_1^2 \tag{6.10}$$

where

$$J_1 = \frac{1}{3}(\sigma_1 + \sigma_2 + \sigma_3)$$

$$J_2^{\frac{1}{2}} = \sqrt{((\sigma_1 - \sigma_2)^2 + (\sigma_2 - \sigma_3)^2 + (\sigma_3 - \sigma_1)^2)\frac{1}{6}}$$

$$A = \frac{UCS}{\sqrt{3}} - \frac{UCS}{3}B - \left(\frac{UCS}{3}\right)^2 C$$

$$B = \frac{\sqrt{3}(q-1)}{q+2} - \frac{C}{3}(2UCS + (q+2)\sigma_3)$$

$$C = \frac{\sqrt{27}}{(2C_1 + (q-1)\sigma_3 - UCS)} \times \left(\frac{C_1 + (q-1)\sigma_3 - UCS}{2C_1 + (2q+1)\sigma_3 - UCS} - \frac{q-1}{q+2}\right)$$

$$C_1 = (1 + 0.6tan\phi)UCS$$

J_1 = mean effective confining stress and J_2 = second deviatoric stress invariant. While the governing equation seems complicated and involves a number of sub-equations including A, B and C, these sub-equations can be simply represented by two commonly used parameters, i.e. UCS and ϕ. Similar to Mogi–Coulomb, this failure criterion has been applied in the field conditions of two constraining horizontal stresses based on breakout angular span (Chang et al. 2010; Huffman and Saffer 2016).

6.3.2.2.3 Von Mises

Prior to true triaxial test equipment development, the importance of the intermediate stress on rock failure was not studied experimentally. Based on the energy distortion in the material, Von Mises (1913) was one of the early researchers who theoretically proposed an equation to incorporate the influence of intermediate stress:

$$J_2^{1/2} = \frac{UCS}{3} = \sqrt{((\sigma_1 - \sigma_2)^2 + (\sigma_2 - \sigma_3)^2 + (\sigma_3 - \sigma_1)^2)\frac{1}{6}} \tag{6.11}$$

Since the failure criterion was developed from the theory of plasticity, it is more suitable for materials with ductile behaviours, such as metals.

6.3.2.2.4 Drucker–Prager

Due to the limited applicability of the Von Mises criterion to different material types, Drucker and Prager (1952) later extended the failure criterion to soil mechanics by considering the influence of mean effective confining stress:

$$\boldsymbol{J_2^{1/2} = k + \alpha J_1} \tag{6.12}$$

where k and α are material constants that can be determined from $J_2^{1/2}$ and J_1 relationship. Based on the intersections with the Mohr–Coulomb failure criterion from inner and outer boundaries, Drucker–Prager can be further divided into two categories: inscribed Drucker–Prager, which touches the inner bound of the Mohr–Coulomb, and circumscribed Drucker–Prager, which touches the outer bound of the Mohr–Coulomb. Since both categories were compared to Mohr–Coulomb, its material constants k and α can be represented in terms of cohesion and friction angle, respectively.

The material constants of Inscribed Drucker–Prager can be expressed as (McLean and Addis 1990):

$$\boldsymbol{\alpha = \frac{3sin\phi}{\sqrt{9 + 3sin^2\phi}}}$$

$$\boldsymbol{k = \frac{3UCS \times cos\phi}{2\sqrt{q}\sqrt{9 + 3sin^2\phi}}}$$

The material constants of Circumscribed Drucker–Prager criterion are obtained as (Zhou 1994):

$$\boldsymbol{\alpha = \frac{6sin\phi}{\sqrt{3}(3 - 3sin\phi)}}$$

$$\boldsymbol{k = \frac{\sqrt{3}UCS \times cos\phi}{\sqrt{q}(3 - 3sin\phi)}}$$

6.3.2.2.5 Modified Lade

Based on elasto-plastic stress–strain theory, Lade (1977) developed a three-dimensional failure criterion for cohesionless soil with curved failure envelopes. Its equation can be written as:

$$\left(\left(\frac{I_1^3}{I_3}\right) - 27\right)\left(\frac{I_1}{p_a}\right)^{m'} = \eta_1 \tag{6.13}$$

with

$$I_1 = \sigma_1 + \sigma_2 + \sigma_3$$

$$I_3 = \sigma_1\sigma_2\sigma_3$$

where I_1 = first stress invariant, I_3= third stress invariant, p_a = atmospheric pressure, m' and η_1 are material constants. Ewy (1999) later attempted to modify the Lade criterion so that it can incorporate the increasing relationship between I_1 and linear shear strength. By assuming m' = 0, Eq. (6.13) can be modified as:

$$\frac{(I_1')^3}{I_3'} = 27 + \eta \tag{6.14}$$

where

$$I_1' = (\sigma_1 + S) + (\sigma_2 + S) + (\sigma_3 + S)$$

$$I_3 = (\sigma_1 + S)(\sigma_2 + S)(\sigma_3 + S)$$

Compared to the original Lade criterion, the modified Lade criterion considers the effect of intermediate stress more reasonably in borehole stability analysis (Ewy 1999). Its material constants η and S can also be obtained from Mohr–Coulomb parameters:

$$S = \frac{c}{tan\phi}$$

$$\eta = \frac{4tan^2\phi(9 - 7sin\phi)}{1 - sin\phi}$$

6.3.2.2.6 Murrell

Murrell (1963) extended the Griffith criterion (Griffith 1921) to a three-dimensional stress distribution to take account of the effect of intermediate stress, and the relationship can be presented as the following:

$$(\sigma_1 - \sigma_3)^2 + (\sigma_1 - \sigma_2)^2 + (\sigma_2 - \sigma_3)^2 = 24T(\sigma_1 + \sigma_2 + \sigma_3) \tag{6.15}$$

where $T = \frac{UCS}{12}$. The Murrell criterion used a higher ratio of UCS/UTS than the Griffith criterion, to match typical experimental results (Fjar et al. 2008). The criterion may also be written in terms of normal (σ) and shear (τ) stresses:

$$\boldsymbol{\tau^2 + 12T\sigma = 36T} \tag{6.16}$$

6.3.2.2.7 Stassi D'Alia

Stassi-D'Alia (1967) developed a failure criterion from the plasticisation condition by considering the inherent resistance of material to tension and compression:

$$\begin{aligned}\boldsymbol{(\sigma_1 - \sigma_3)^2 + (\sigma_1 - \sigma_2)^2 + (\sigma_2 - \sigma_3)^2} \\ \boldsymbol{= 2(UCS - UTS)(\sigma_1 + \sigma_2 + \sigma_3) + 2UCS \times UTS}\end{aligned} \tag{6.17}$$

Compared to the Murrell criterion, Stassi D'Alia may be more practically reliable as it uses both UCS and UTS values instead of assuming a constant ratio. In addition, it does not require Mohr–Coulomb parameters to evaluate the equation.

6.3.2.3 Laboratory data

To determine the most reliable failure criterion for σ_h estimation, it is essential to have sufficient laboratory data. Table 6.3 presents a list of experimental studies on borehole breakout including their rock mechanical properties. As the friction angle for Tenino sandstone was not provided, a reasonable assumption of 36° was used in the analysis. It is noted that a sensitivity analysis of friction angle on the most appropriate failure criterion was conducted, as described in Section 6.5.3 below. Results indicated that predictions were not sensitive to the change in this parameter. Since the modified Lade criterion was the only criterion that used cohesion directly for its parameter, it was replaced with the following equation for simplicity:

$$\boldsymbol{c = \frac{UCS}{2\sqrt{(1 + sin\phi)/(1 - sin\phi)}}} \tag{6.18}$$

As discussed by a significant body of research, the stress required for breakout initiation in the laboratory is substantially higher than in the field (Haimson and Herrick 1989; Carter et al. 1991; Carter 1992; Papanastasiou and Thiercelin 2010; Lin et al. 2019). In some experimental cases, the horizontal stress ratio applied can be as high as 8, which is practically impossible in the field. Later, it was realised this was due to the size of the borehole, where the stress required for borehole breakout initiation is inversely proportional to the borehole size used in the laboratory (Haimson and Herrick 1989; Lee and Haimson 1993; Herrick and Haimson 1994; Lin et al. 2019). To incorporate this effect in the experiments, some studies suggested replacing UCS with a more representative parameter, i.e. borehole wall strength (BWS) (Walton et al. 2015; LeRiche et al. 2017). This is also one of the reasons to replace cohesion with UCS from Eq. (6.18) to take account of this effect for the modified Lade criterion. Lin et al. (2020) proposed an empirical relationship to quantify this relationship, which was reliable in laboratory conditions. Similarly, it is essential to upscale UTS in the laboratory condition as it is also borehole size dependent (Carter et al. 1991; Carter 1992; Carter et al. 1992), namely, borehole tensile strength (BTS). Hence, this study also summarised a simple and effective empirical relationship on UTS based on the experimental data from Carter (1992):

$$\frac{\boldsymbol{BTS}}{\boldsymbol{UTS}} = \mathbf{0.0076}\boldsymbol{R}^{\mathbf{2}} - \mathbf{0.5532}\boldsymbol{R} + \mathbf{11.701} \tag{6.19}$$

Table 6.4 summarises the breakout angular span, stress conditions and BWS and BTS for each experimental data from the literature. In total, there are 79 data collected for the examination of failure criteria. From the table, it is clear that, apart from this study, all other studies investigated mainly the influence of σ_H on breakout geometries. Based on the data obtained, it can be concluded that increasing σ_H will lead to larger breakout angular span when σ_h and σ_v are constant.

Table 6.3 Rock properties from literature and experimental data

Source	Rock Type	UCS (MPa)	UTS (MPa)	Friction angle (°)	Poisson's ratio
Herrick and Haimson	Alabama limestone	43	2.5[a]	18	0.27

(1994)					
Haimson and Lee (2004)	Tablerock sandstone	39	4.4	39.7	0.2
Lee and Haimson (2006)	Tenino sandstone	35.06	2.47	36[b]	0.22
Lin et al. (2019)	Gosford sandstone	42.3	2.8	35	0.17
This study	Hydrostone-TB	18.2	2.07	28	0.19

6.3.3 *Examination of failure criterion on estimating σ_h*

By submitting Eq. (6.1)–(6.3) into each rock failure criterion governing equation, σ_h can be estimated by providing maximum horizontal and vertical stresses, rock and breakout information. The 79 laboratory data summarised above were used to examine the reliability of each model, and the average errors were compared. Interestingly, unreasonable prediction results were obtained from all failure criteria. Some predictions even yielded negative results or were simply unsolvable. It was later noted that this is because of the nature of the governing equations. For instance, Figure 6.4 shows the relationships between horizontal stress magnitudes derived from different failure criteria according to Data 5 in Table 6.4. For this particular set of data, the modified Wiebols–Cook criterion did not provide a closed-form relationship, whereas modified Lade yielded eigenvalues in the relationship. To estimate σ_h, a horizontal line is first drawn from the y-axis given the magnitude of σ_H. Then, the intersection between the σ_H line and the failure criterion line can be determined. A vertical line can then be drawn down to the x-axis to determine the predicted $\sigma_h$value, as illustrated in Figure 6.5.

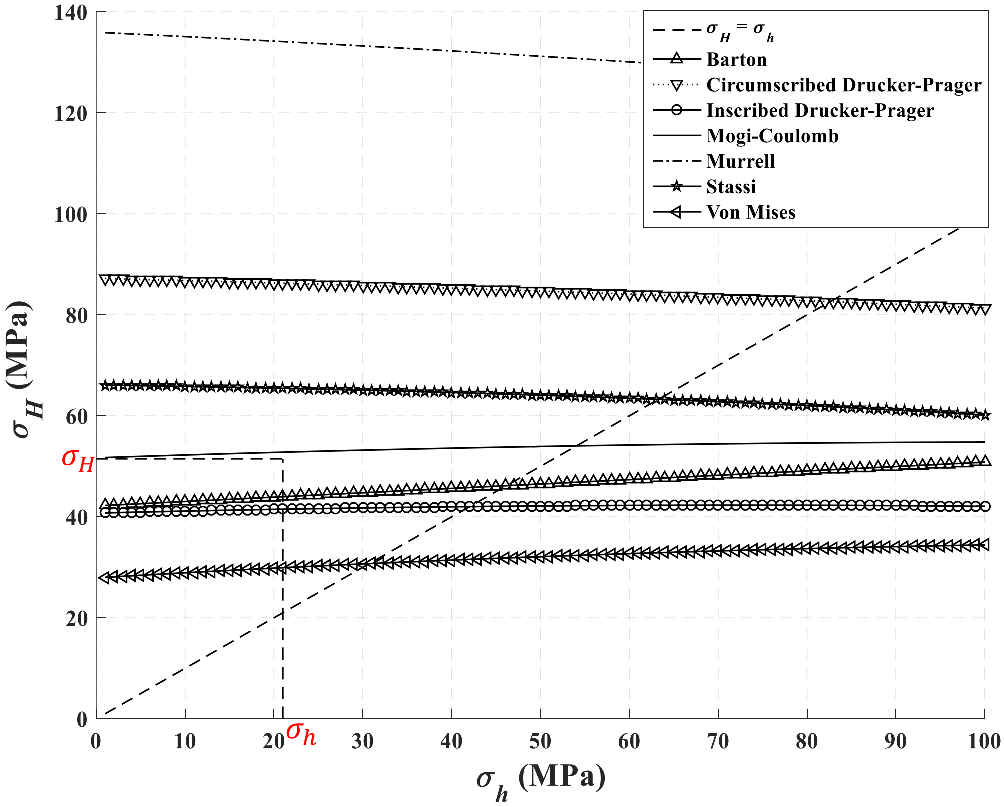

Figure 6.4 Illustration of data 5 from different failure criteria. The black dot line represents $\sigma_H = \sigma_h$; the intersections between the axes and black dot lines refer to the laboratory applied horizontal stress values

The black dotted lines in Figure 6.4 represent the horizontal stress magnitudes applied in data 5. As displayed in the figure, the σ_H line does not meet any of the failure criterion lines, suggesting that there is no solution for σ_h. This is the reason why unreasonable prediction results were observed during estimation of σ_h. According to the figure, it can also be seen that the relationships between horizontal stress magnitudes can be significantly different for different failure criteria. This suggests that the prediction results for σ_h will also vary, depending on the failure criterion. Although failure criteria do not intersect with the σ_H line, the Mogi–Coulomb criterion is the closest distance from the line. Compared to the other criteria, the Von Mises criterion requires the lowest σ_H to predict the same σ_h value, whereas the Murrell criterion needs the highest σ_H to obtain the same σ_h value.

Figure 6.4 also shows that the gradients of relationships for failure criteria are relatively flat, indicating that the magnitude of σ_h is very sensitive to the input σ_H. Conversely, this means that the magnitude of σ_H is not as sensitive as σ_h. The implication here is that it may be more appropriate to estimate σ_H from given σ_h as the vertical σ_h line from Figure 6.4 can intersect with all failure criteria.

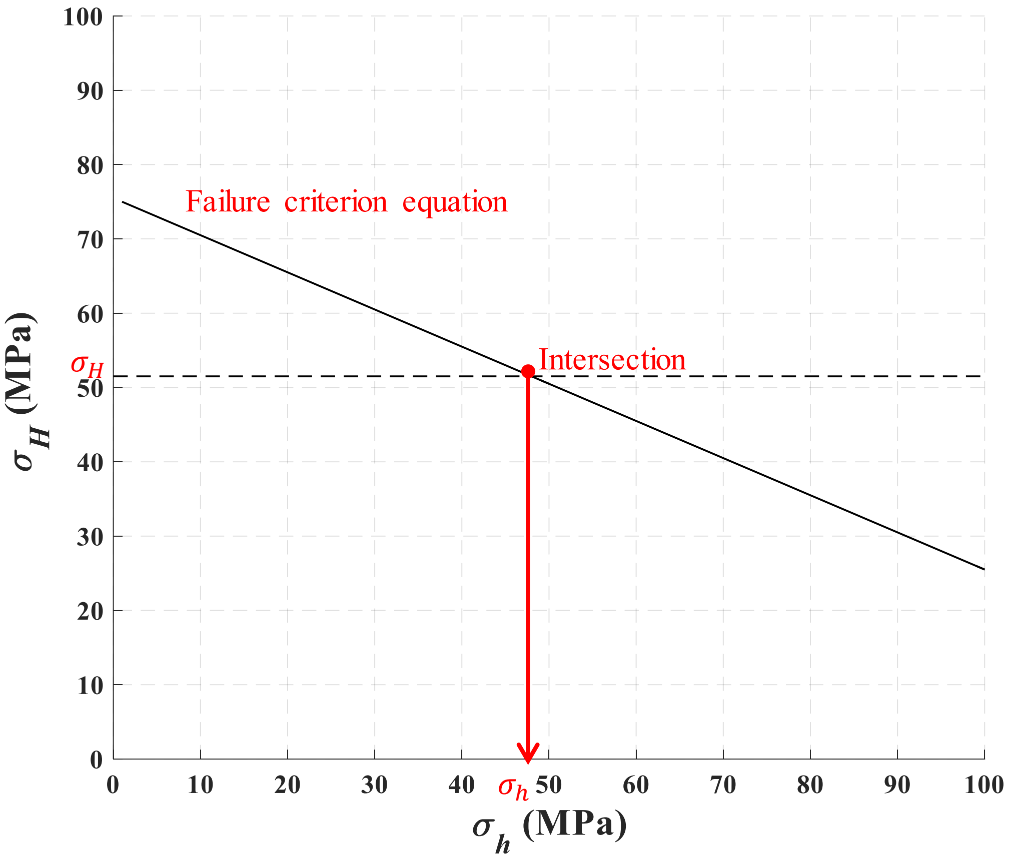

Figure 6.5 Illustration of the estimation process

Table 6.4 Stress and associated rock information from literature and experimental data

Literature	Data	σ_H (MPa)	σ_h (MPa)	σ_v (MPa)	θ_b(°)	BWS (MPa)	BTS (MPa)
Herrick and Haimson (1994)	1	41	14	21	45	92.33	16.34
	2	50	14	21	55	92.33	16.34
	3	57.5	14	21	65.5	92.33	16.34
	4	65.5	14	21	81.5	92.33	16.34

	5	51.5	21	28	53.5	92.33	16.34
	6	58.5	21	28	56	92.33	16.34
	7	65.5	21	28	63	92.33	16.34
	8	65.5	21	28	65.5	92.33	16.34
	9	72.2	21	28	70	92.33	16.34
	10	75.8	21	28	80	92.33	16.34
	11	58.5	28	3s5	52	92.33	16.34
	12	65.5	28	35	55.5	92.33	16.34
	13	72.2	28	35	68	92.33	16.34
	14	79	28	35	70	92.33	16.34
	15	83	28	35	86	92.33	16.34
	16	62	35	42	45	92.33	16.34
	17	69	35	42	57	92.33	16.34
	18	79	35	42	64	92.33	16.34
	19	84.5	35	42	86	92.33	16.34
	20	90	35	42	88	92.33	16.34
Haimson and Lee (2004)	21	40	15	30	35	83.74	28.76
	22	50	15	30	51.5	83.74	28.76
	23	60	15	30	65	83.74	28.76
	24	70	15	30	73	83.74	28.76
	25	60	20	40	63	83.74	28.76
	26	70	20	40	67.5	83.74	28.76
	27	80	20	40	73	83.74	28.76
	28	60	25	40	64	83.74	28.76

	29	70	25	40	71	83.74	28.76
	30	75	25	40	75	83.74	28.76
	31	85	25	40	82	83.74	28.76
	32	54.9	30	40	53	83.74	28.76
	33	60	30	40	64	83.74	28.76
	34	65.1	30	40	79.5	83.74	28.76
	35	69.6	30	40	100	83.74	28.76
	36	75	30	40	111	83.74	28.76
	37	60	40	50	95	83.74	28.76
	38	64	40	50	116	83.74	28.76
	39	69.2	40	50	138	83.74	28.76
Lee and Haimson (2006)	40	35.4	15	25	45	75.28	16.14
	41	50.25	15	25	59	75.28	16.14
	42	65.25	15	25	63.5	75.28	16.14
	43	40	20	30	48	75.28	16.14
	44	50	20	30	68	75.28	16.14
	45	60	20	30	73.5	75.28	16.14
	46	70	20	30	78.5	75.28	16.14
	47	45	25	35	61.5	75.28	16.14
	48	50	25	35	66	75.28	16.14
	49	55	25	35	70	75.28	16.14
	50	60.5	25	35	72	75.28	16.14
	51	65	25	35	77	75.28	16.14
	52	40.5	30	40	56	75.28	16.14

	53	51	30	40	70.3	75.28	16.14
	54	60	30	40	77.5	75.28	16.14
	55	60	40	50	68	75.28	16.14
	56	72	40	50	73.6	75.28	16.14
	57	80	40	50	82	75.28	16.14
	58	93.2	40	50	85	75.28	16.14
Lin et al. (2019)	59	40	10	5	25	97.72	19.17
	60	50	10	5	41.5	97.72	19.17
	61	60	10	5	53	97.72	19.17
	62	40	10	5	40.5	90.83	16.14
	63	50	10	5	55.5	90.83	16.14
	64	60	10	5	60	90.83	16.14
	65	40	10	5	51	82.23	12.63
	66	50	10	5	71.5	82.23	12.63
	67	55	10	5	83	82.23	12.63
This study	68	25	5	5	55	39.08	10.58
	69	25	5	10	46	39.08	10.58
	70	25	5	15	32	39.08	10.58
	71	25	5	20	17	39.08	10.58
	72	25	10	5	39	39.08	10.58
	73	25	15	5	11	39.08	10.58
	74	30	10	10	58	39.08	10.58
	75	30	10	15	49	39.08	10.58
	76	30	10	20	39.5	39.08	10.58

77	30	10	25	18	39.08	10.58
78	30	15	10	37.5	39.08	10.58
79	30	20	10	10	39.08	10.58

6.3.4 Examination of failure criterion on estimating σ_H

A similar approach was conducted to estimate σ_H when σ_h, σ_v, rock and breakout information are provided. Figure 6.6 presents the estimation results from six rock failure criteria. Circumscribed Drucker–Prager, modified Lade and modified Wiebols–Cook are not included, since they cannot predict some data points due to the nature of their equations for the reasons given in Section 4.3. It was also noted that Von Mises also cannot estimate data 38.

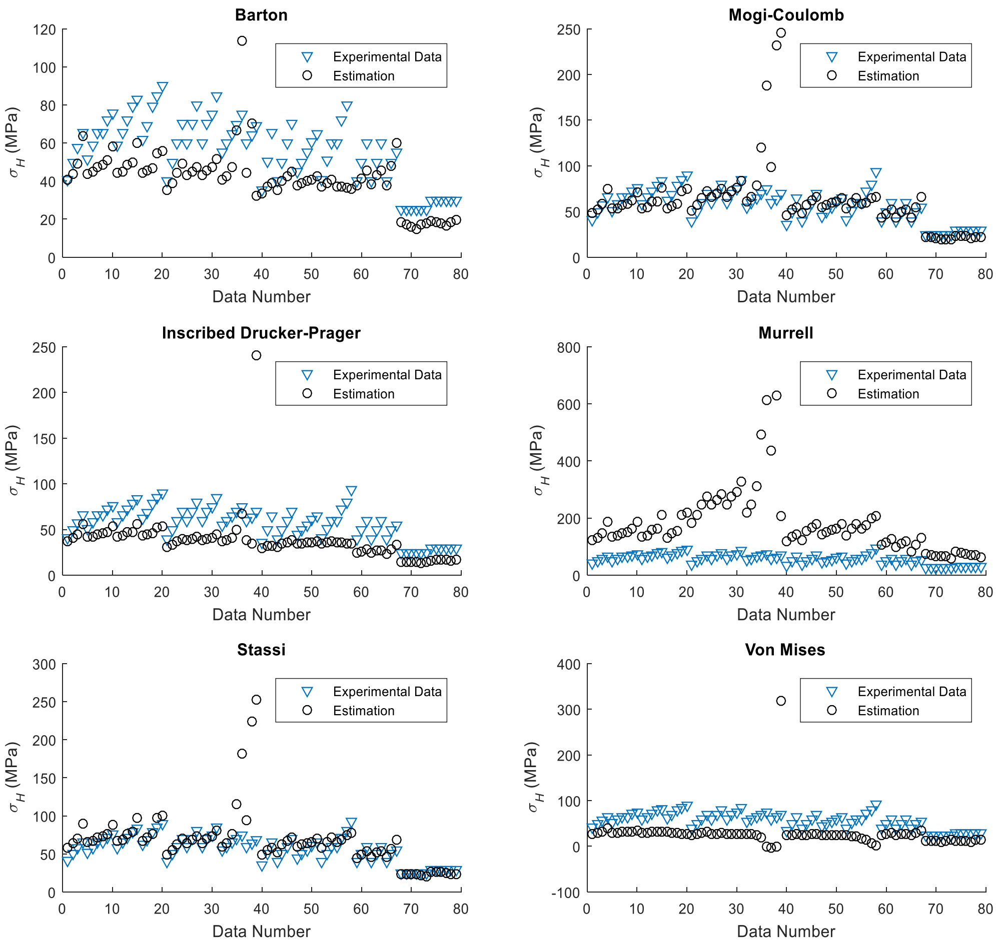

Figure 6.6 σ_H prediction on laboratory data

Table 6.5 σ_H estimation for each laboratory data

Data	Barton	Mogi–Coulomb	Inscribed Drucker–Prager	Murrell	Stassi D'Alia	Von Mises
1	40.65	48.12	37.57	121.27	58.64	27.81
2	43.96	52.18	40.32	132.29	63.50	29.51
3	49.16	58.44	44.56	148.60	70.82	32.16
4	63.65	75.17	55.80	187.77	89.29	39.43
5	43.99	52.82	41.47	134.10	65.45	29.93
6	44.76	53.85	42.13	137.25	66.77	30.23
7	47.38	57.32	44.32	147.64	71.15	31.25
8	48.51	58.81	45.26	151.99	73.01	31.69
9	50.89	61.90	47.20	160.83	76.82	32.61
10	58.36	71.42	53.18	186.24	88.15	35.50
11	44.28	53.54	42.67	135.94	67.39	30.36
12	45.03	54.69	43.32	140.11	69.01	30.47
13	48.77	60.33	46.50	159.86	76.83	31.02
14	49.57	61.53	47.18	163.89	78.46	31.14
15	59.88	76.51	55.55	209.19	97.69	32.68
16	44.25	53.21	43.40	132.60	67.50	31.02
17	45.69	55.98	44.66	145.40	72.05	30.38
18	46.90	58.31	45.72	155.69	75.77	29.84
19	54.60	72.72	52.19	211.53	97.30	26.28
20	55.87	75.04	53.23	219.30	100.53	25.67
21	35.37	50.85	30.38	184.47	49.44	24.66

22	38.94	56.75	32.90	210.28	55.10	26.37
23	44.12	65.12	36.47	245.80	63.12	28.86
24	48.91	72.60	39.67	276.51	70.31	31.17
25	42.92	66.25	38.71	246.17	64.55	26.92
26	44.78	69.76	40.12	261.47	67.90	27.50
27	47.60	75.05	42.24	283.98	72.94	28.41
28	42.98	66.38	38.38	248.31	64.61	26.91
29	45.43	71.67	40.07	273.50	69.61	27.19
30	47.23	75.47	41.29	291.15	73.22	27.39
31	51.39	84.06	44.06	329.59	81.35	27.87
32	40.77	60.74	36.66	219.31	59.22	27.27
33	42.65	65.79	37.75	247.26	63.97	26.77
34	47.40	78.10	40.40	311.69	75.55	25.49
35	66.37	120.53	49.76	490.51	115.72	19.95
36	113.81	187.44	66.65	614.88	182.01	0.36
37	44.53	98.17	38.80	437.87	94.50	-3.11
38	70.34	231.32	34.98	629.15	223.80	N/A
39	32.31	245.80	240.53	205.91	252.34	318.68
40	33.76	46.17	29.06	118.03	49.38	23.33
41	37.30	51.69	31.52	134.63	55.28	24.91
42	38.93	54.17	32.62	141.93	57.92	25.64
43	35.09	48.71	31.28	123.84	52.44	24.12
44	40.17	57.76	34.78	152.99	62.28	25.54
45	42.50	61.79	36.34	165.43	66.61	26.20

46	45.22	66.41	38.12	179.24	71.53	26.97
47	37.94	54.86	34.43	143.74	59.69	24.33
48	38.94	57.06	35.11	151.51	62.14	24.28
49	40.01	59.38	35.83	159.57	64.71	24.22
50	40.62	60.70	36.24	164.07	66.17	24.19
51	42.44	64.55	37.43	176.97	70.40	24.09
52	37.21	53.58	34.96	138.40	58.78	23.92
53	39.13	59.57	36.20	162.44	65.73	22.20
54	40.66	64.27	37.16	180.41	71.10	20.78
55	37.30	57.94	36.34	161.97	65.85	17.15
56	36.98	60.03	35.93	173.95	68.65	13.90
57	36.31	64.42	35.07	197.83	74.42	6.24
58	35.98	66.52	34.65	208.65	77.13	1.94
59	37.63	43.31	24.32	105.20	45.03	24.42
60	41.11	47.21	25.99	115.79	49.04	26.18
61	45.27	51.79	27.93	128.04	53.72	28.28
62	38.10	43.82	24.27	97.43	45.73	24.38
63	43.21	49.47	26.63	111.16	51.53	26.92
64	45.42	51.86	27.63	116.89	53.97	28.00
65	37.55	43.20	23.60	83.90	45.31	23.70
66	48.07	54.51	28.20	107.16	56.86	28.72
67	60.03	66.52	33.07	130.50	68.81	34.28
68	18.54	21.75	14.20	75.23	23.36	12.04
69	17.17	21.41	14.89	72.35	23.71	11.70

70	15.79	20.34	14.84	68.18	23.20	10.80
71	14.98	19.51	14.75	66.21	23.02	9.59
72	17.47	19.98	13.52	65.76	21.25	11.89
73	18.06	19.97	14.30	59.80	20.95	13.11
74	19.26	23.80	16.20	81.03	26.17	12.87
75	18.25	23.34	16.86	77.49	26.36	12.54
76	17.50	22.63	17.07	74.71	26.32	11.65
77	16.57	21.04	16.56	69.60	25.33	9.69
78	18.51	21.98	15.82	68.67	23.81	13.36
79	19.69	22.49	17.02	63.41	23.95	15.12

According to the figure, it can be seen that both Mogi–Coulomb and Stassi D'Alia yielded the most reliable results, with an average error rate of 22.69% and 22.75%, respectively. Murrell significantly overestimated σ_H while Von Mises and Inscribed Drucker–Prager underestimated σ_H. As displayed in the figure, there are five over-predictions in Mogi–Coulomb and Stassi D'Alia, which also happened to be the only five data (Data 35–39) which have angular spans over 90°. In field conditions, it is rare to have a breakout angular span that is greater than 90°, and thus these five data may be neglected. The average error rates of the two failure criteria are 13.37% and 13.74% after removing the five data. Thus, the two failure criteria are the most reliable approaches to estimate σ_H. Table 6.5 and Table 6.6 show the magnitudes of each σ_H prediction as well as the error rate, respectively (Shen et al. 2002; Shen 2008; Klee et al. 2011; Leriche 2017).

Table 6.6 Estimation error for each data

Data	Barton	Mogi–Coulomb	Inscribed Drucker–Prager	Murrell	Stassi D'Alia	Von Mises
1	-0.86%	17.38%	-8.37%	195.78%	43.03%	-32.17%
2	-12.08%	4.35%	-19.36%	164.59%	27.00%	-40.98%

3	-14.50%	1.63%	-22.51%	158.43%	23.17%	-44.07%
4	-2.82%	14.77%	-14.80%	186.67%	36.33%	-39.80%
5	-14.59%	2.57%	-19.47%	160.39%	27.08%	-41.88%
6	-23.49%	-7.94%	-27.99%	134.62%	14.13%	-48.32%
7	-27.67%	-12.49%	-32.34%	125.41%	8.63%	-52.29%
8	-25.94%	-10.22%	-30.91%	132.05%	11.46%	-51.62%
9	-29.52%	-14.26%	-34.62%	122.76%	6.40%	-54.83%
10	-23.01%	-5.77%	-29.85%	145.70%	16.29%	-53.17%
11	-24.30%	-8.47%	-27.05%	132.37%	15.20%	-48.10%
12	-31.25%	-16.51%	-33.86%	113.91%	5.37%	-53.48%
13	-32.45%	-16.44%	-35.59%	121.41%	6.41%	-57.04%
14	-37.25%	-22.11%	-40.28%	107.46%	-0.69%	-60.58%
15	-27.85%	-7.82%	-33.07%	152.03%	17.70%	-60.63%
16	-28.63%	-14.18%	-30.00%	113.87%	8.88%	-49.97%
17	-33.79%	-18.86%	-35.27%	110.72%	4.42%	-55.97%
18	-40.64%	-26.19%	-42.13%	97.07%	-4.09%	-62.23%
19	-35.39%	-13.95%	-38.23%	150.33%	15.15%	-68.90%
20	-37.92%	-16.63%	-40.85%	143.67%	11.70%	-71.48%
21	-11.58%	27.12%	-24.05%	361.19%	23.61%	-38.35%
22	-22.13%	13.50%	-34.20%	320.57%	10.20%	-47.26%
23	-26.46%	8.53%	-39.21%	309.66%	5.20%	-51.90%
24	-30.13%	3.72%	-43.32%	295.02%	0.45%	-55.47%
25	-28.46%	10.41%	-35.49%	310.29%	7.58%	-55.13%
26	-36.03%	-0.34%	-42.69%	273.53%	-3.00%	-60.71%

27	-40.50%	-6.18%	-47.20%	254.97%	-8.83%	-64.49%
28	-28.37%	10.64%	-36.04%	313.85%	7.68%	-55.15%
29	-35.09%	2.38%	-42.76%	290.71%	-0.55%	-61.16%
30	-37.02%	0.63%	-44.94%	288.20%	-2.38%	-63.48%
31	-39.54%	-1.11%	-48.17%	287.76%	-4.29%	-67.21%
32	-25.73%	10.64%	-33.22%	299.48%	7.86%	-50.33%
33	-28.92%	9.64%	-37.09%	312.10%	6.62%	-55.38%
34	-27.19%	19.96%	-37.95%	378.79%	16.05%	-60.84%
35	-4.64%	73.17%	-28.51%	604.75%	66.26%	-71.34%
36	51.74%	149.92%	-11.13%	719.84%	142.68%	-99.52%
37	-25.78%	63.61%	-35.33%	629.79%	57.50%	-105.18%
38	9.91%	261.44%	-45.34%	883.05%	249.69%	N/A
39	-53.31%	255.20%	247.59%	197.55%	264.65%	360.52%
40	-4.65%	30.42%	-17.91%	233.42%	39.48%	-34.10%
41	-25.76%	2.87%	-37.28%	167.92%	10.01%	-50.43%
42	-40.34%	-16.98%	-50.01%	117.51%	-11.24%	-60.70%
43	-12.28%	21.78%	-21.79%	209.59%	31.11%	-39.70%
44	-19.66%	15.52%	-30.44%	205.99%	24.57%	-48.92%
45	-29.17%	2.99%	-39.44%	175.72%	11.02%	-56.33%
46	-35.40%	-5.13%	-45.55%	156.06%	2.19%	-61.47%
47	-15.70%	21.91%	-23.50%	219.43%	32.64%	-45.93%
48	-22.12%	14.11%	-29.78%	203.02%	24.27%	-51.44%
49	-27.25%	7.96%	-34.86%	190.12%	17.66%	-55.96%
50	-32.85%	0.33%	-40.10%	171.19%	9.37%	-60.02%

51	-34.71%	-0.69%	-42.41%	172.26%	8.30%	-62.94%
52	-8.12%	32.29%	-13.68%	241.72%	45.12%	-40.94%
53	-23.28%	16.80%	-29.03%	218.52%	28.87%	-56.47%
54	-32.23%	7.12%	-38.06%	200.68%	18.50%	-65.37%
55	-37.83%	-3.43%	-39.43%	169.95%	9.75%	-71.42%
56	-48.63%	-16.63%	-50.10%	141.60%	-4.66%	-80.69%
57	-54.62%	-19.48%	-56.17%	147.29%	-6.98%	-92.20%
58	-61.39%	-28.63%	-62.82%	123.87%	-17.24%	-97.92%
59	-5.92%	8.28%	-39.20%	162.99%	12.56%	-38.95%
60	-17.77%	-5.57%	-48.03%	131.58%	-1.92%	-47.64%
61	-24.55%	-13.69%	-53.44%	113.40%	-10.47%	-52.87%
62	-4.75%	9.56%	-39.33%	143.57%	14.32%	-39.05%
63	-13.58%	-1.06%	-46.74%	122.33%	3.06%	-46.16%
64	-24.31%	-13.57%	-53.95%	94.82%	-10.05%	-53.33%
65	-6.12%	7.99%	-41.01%	109.76%	13.27%	-40.75%
66	-3.86%	9.03%	-43.61%	114.31%	13.73%	-42.56%
67	9.15%	20.94%	-39.87%	137.27%	25.12%	-37.67%
68	-25.83%	-12.99%	-43.19%	200.91%	-6.57%	-51.84%
69	-31.32%	-14.37%	-40.44%	189.39%	-5.17%	-53.20%
70	-36.86%	-18.65%	-40.63%	172.72%	-7.22%	-56.80%
71	-40.06%	-21.96%	-41.01%	164.82%	-7.91%	-61.64%
72	-30.12%	-20.06%	-45.92%	163.03%	-14.98%	-52.44%
73	-27.74%	-20.10%	-42.82%	139.22%	-16.21%	-47.56%
74	-35.79%	-20.67%	-45.99%	170.11%	-12.78%	-57.10%

75	-39.16%	-22.19%	-43.79%	158.29%	-12.12%	-58.20%
76	-41.66%	-24.56%	-43.09%	149.03%	-12.27%	-61.17%
77	-44.75%	-29.87%	-44.81%	131.99%	-15.58%	-67.70%
78	-38.30%	-26.73%	-47.28%	128.89%	-20.64%	-55.47%
79	-34.37%	-25.04%	-43.25%	111.36%	-20.15%	-49.60%
Average	27.45%	22.69%	39.75%	209.82%	22.75%	59.18%

6.4 ARTIFICIAL NEURAL NETWORK ON CALCULATING σ_h

6.4.1 Artificial neural network

Artificial neural network (ANN) models are a first order mathematical approximation to the human nervous system and are now widely used to solve a variety of problems related to classification, regression and prediction (Chen et al. 2019). ANNs are composed of multiple simple processing units called neurons, which perform computations on numerous input signals to produce an output. Each input to the neuron has associated weight and bias that has decisive impact on the output (Guo et al. 2012). In general, the network architecture of an ANN consists of three layers: an input layer, a hidden layer and an output layer (Srinivasulu and Jain 2006), see Figure 6.7. The input layer comprises of several inputs to the network and no computation is performed in this layer. An intermediate hidden layer is composed of a number of neurons that are arranged in parallel. A network may contain several hidden layers with neurons in each layer connected to the neurons in the preceding and subsequent layers. The output layer produces final predictions and is formed by a weighted summation of outputs from the last layer (Phung and Bouzerdoum 2007). A neuron in the network is identified by the activation or transfer function that is applied to the weighted sum of inputs, and each layer might have different activation functions (Salchenberger et al. 1992; Bashir and El-Hawary 2009). Commonly used activation functions include binary, linear, hyperbolic tangent and sigmoid. Determination of optimal weights and biases in a network is a critical aspect that governs the output and can be obtained using a training dataset i.e. a set of data consisting of inputs and outputs. Hence, the problem reduces to optimisation that involves minimising a specific cost function. The cost function often decomposes as a sum of certain loss functions (such as squared error, negative log likelihood or cross entropy) over training examples. Several methods based on backpropagation (also called learning) are available to solve the optimisation problem of determining weights and biases (Rumelhart et al. 1986).

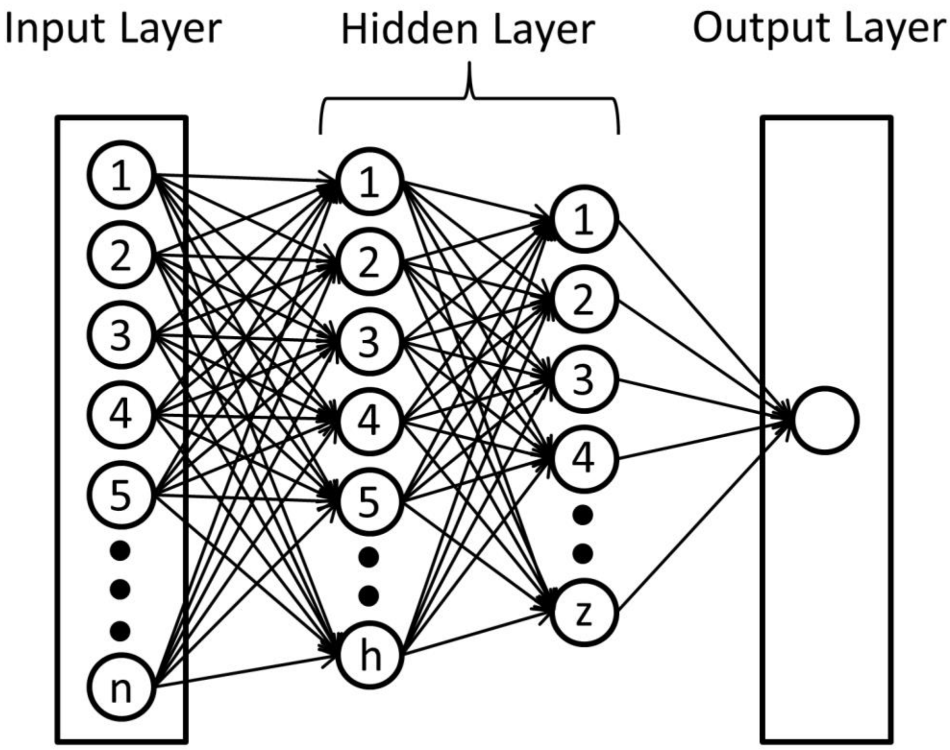

Figure 6.7 General ANN architecture, where n = number of inputs, h and z = number of neurons in each hidden layer

The topology of any given network, also known as network architecture, is defined by neuron connections in different layers. This study used a two-layer feedforward neural network with a sigmoid hidden layer and a scaled conjugate gradient (SCG) backpropagation algorithm (discussed in Section 6.4.3 below). In a feedforward neural network, information flows only in one direction from input to output. The study implemented a sigmoid activation function as it is widely used and employs SCG backpropagation due to its faster convergence of cost function (mean square error in this study) and modest memory requirements (Møller 1990).

In recent years, ANN has gained popularity for parameter predictions in rock mechanics and mining applications (Mia and Dhar 2016; Qi et al. 2018; Nguyen et al. 2019). This resulted from the capability of the model to discern complex patterns in the data and its ability to improve as additional data become available. For example, Esfe et al. (2019) predicted the viscosity of a nano-fluid from a set of 28 experimental data with high accuracy, demonstrating state-of-the-art performance. Similarly, Mia and Dhar (2016) predicted surface roughness using 68 multivariate experimental data respectively. In another study, Yilmaz and Yuksek (2008) used ANN to estimate various mechanical properties of rock based on 39 data. The importance of ANN for different applications ranging from rock engineering to mineral processing in mining was discussed by Kapageridis (2002).

6.4.2 Trend analysis of parameters

To generate a reliable artificial neural network model, 79 laboratory data were collected to be the initial database, as shown in Table 6.3 and Table 6.4. For the experimental data, it is easier to monitor stress magnitudes as well as obtain breakout geometries and rock information in experimental conditions. As discussed in Section 6.3, both σ_v and σ_h are influential for breakout geometries. It has been argued θ_b is a more reliable parameter than L/R because it forms quickly at the initial stage of breakout and does not widen significantly afterwards (Barton et al. 1988; Zheng et al. 1989; Lee and Haimson 2006; Chang et al. 2010; Schoenball et al. 2014; Lee et al. 2016). Hence, three parameters which were considered for this model were BWS, σ_v and θ_b.

Figure 6.8a–c display the relationships between σ_h and the three input parameters, respectively. The R-value lies between '0' and '1', with '1' indicating perfect correlation while '0' indicates that no relationship exists between prediction and measurement. Based on the figures, a positive linear relationship between σ_h and σ_v can be found, with a R^2 value of 0.79. On the other hand, the relationships between σ_h, θ_b and BWS remain unclear due to their low R^2 values, indicating no clear deterministic relationships between the parameters and responses. It was also noticed that there were only limited data points presented in Figure 6.8a and Figure 6.8c, mainly due to the experimental setup in previous studies. As the majority of the focus was on relationships between σ_H and breakout geometries, σ_h and σ_v were kept constant in many cases with varying σ_H. This resulted in difficulty in using Kriging to predict σ_h (Lin et al. 2020).

Unlike the early investigations, this study performed breakout experiments with various σ_h under constant σ_H and σ_v. Results not only confirmed the dependency of breakout geometries on σ_h, but also enriched the previous breakout database for machine learning and have been included as part of the 79 data points. Although supplementary data were added to the σ_h database, they were still not sufficient to establish a reliable Kriging model (Lin et al. 2020). This is one of the main reasons to introduce ANN to overcome this limitation and estimate σ_h.

As discussed earlier, the correlations between σ_h, θ_b and BWS are unclear, because the parameters are not independent factors and influenced by σ_v. For instance, θ_b is also related to σ_v apart from σ_h, which has been demonstrated in the experimental results. It requires different σ_h and σ_v combinations to initiate borehole breakout for constant BWS. Hence, interaction terms are introduced to take account of this effect. The interaction terms are used when one variable is dependent on the other variable for the same response, such that an interaction variable should be included (Altman and Matthews 1996; Matthews and Altman 1996). For example, a general regression model with two variables (x_1 and x_2) can be expressed as:

$$\boldsymbol{Y = a_1 x_1 + a_2 x_2 + a_3 + error} \tag{6.20}$$

where Y = model response, a_1, a_2 and a_3 are constants determined by regression. When the interaction terms are introduced, the model becomes:

$$\boldsymbol{Y = a_1 x_1 + a_2 x_2 + a_3 + a_4 (x_1 \times x_2) + error} \tag{6.21}$$

in which $x_1 \times x_2$ is the interaction term. By applying this concept to the database, three new interaction terms were introduced to the model, as displayed in Figure 6.8a–f.

As shown in Figure 6.8f, the correlation between $BWS \times \theta_b$ and σ_h does not improve significantly compared to the singular term θ_b (Figure 6.8b) and still shows poor correlation. Hence, this interaction term was neglected. Instead, the other two newly introduced terms ($\sigma_v \times BWS$ and $\sigma_v \times \theta_b$) exhibit significantly improved correlations with σ_h, compared to that of the original terms. To make the ANN training and prediction more effective, instead of using three terms for artificial neural network training, this study trained the model with five terms derived from the three parameters suggested earlier.

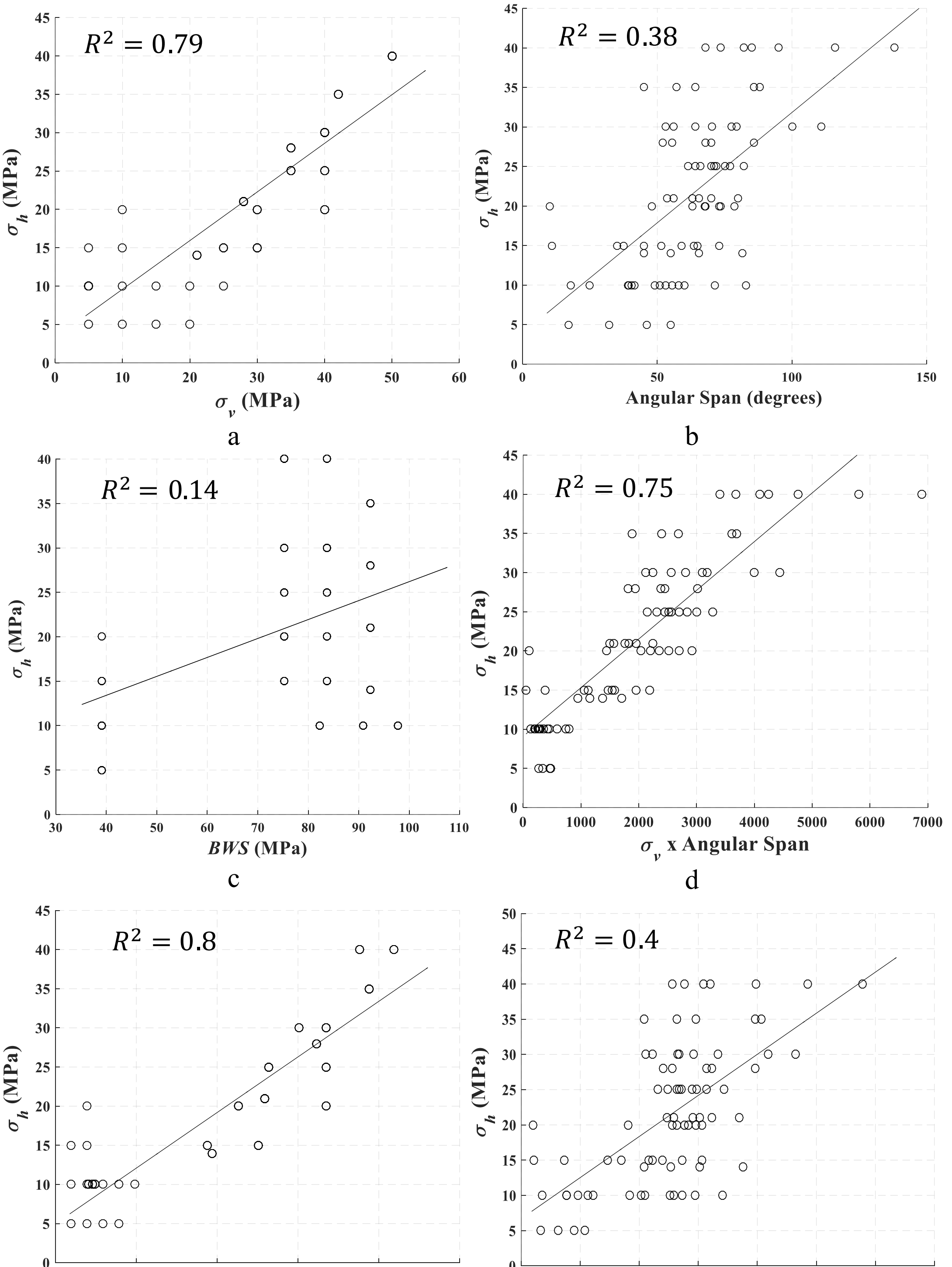

Figure 6.8 ANN trend analysis on σ_H with respect to different parameters

6.4.3 ANN modelling

The ANN modelling is outlined in Figure 6.9. This study used MATLAB 2019b neural fitting tool (nftool) to create, train and test the neural network. To train the neural network the entire dataset consisting of 79 sample data was divided into three categories: training, validation and testing. The training dataset was used to train the network, which was adjusted based on the obtained mean square error (MSE). The validation dataset was used to measure network generalisation to check the network performance on an independent dataset. The network was modified repeatedly until the generalisation stops improving. Finally, the test dataset was used to provide a performance measure after the network is generalised. The entire process was repeated again until the error in all three datasets was optimised to a minimum. This study used 70% training data, 15% validation data and 15% test data which corresponds to 55, 12 and 12 data points respectively (Zain et al. 2010; Gholami et al. 2016; Mia and Dhar 2016).

Various possible network architectures with variable hidden layers and number of neurons were tested to determine the most reliable combination. A low number of neurons may reduce analysis capability while an excessively high number of neurons might overtrain the network resulting in output with high error. A trial and error approach was adopted in this study where the number of neurons was varied in the range of 1–100 in the hidden layer. The threshold where performance (MSE) became consistent (20 neurons in this study) regardless of neuron numbers was selected. The number of hidden layers was restricted to one based on numerous past case studies (Zain et al. 2010; Mia and Dhar 2016; Moon et al. 2019). Several optimisation methods are provided in the toolbox such as Levenberg–Marquardt, Bayesian regularisation and SCG which have competitive advantages over one another. SCG was preferred due to its faster convergence and modest memory requirements. Figure 6.10 illustrates the prediction capability of the trained network corresponding to various datasets in terms of correlation coefficient (R-value). The solid line in the figure represents fit while the dashed line represents identical predicted and measured values. Figure 6.10 shows strong correlation between prediction and measurement in the dataset used.

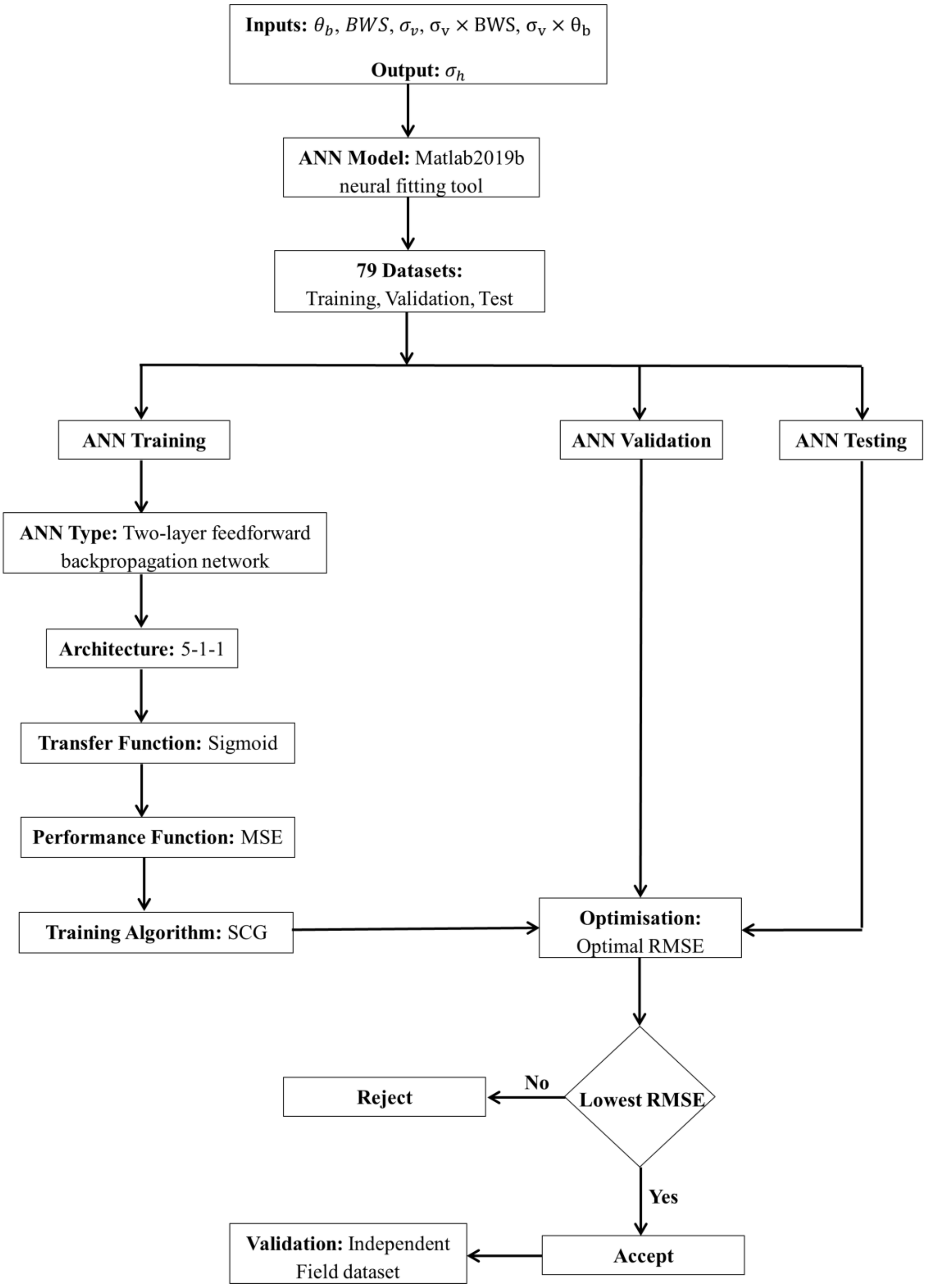

Figure 6.9 ANN process

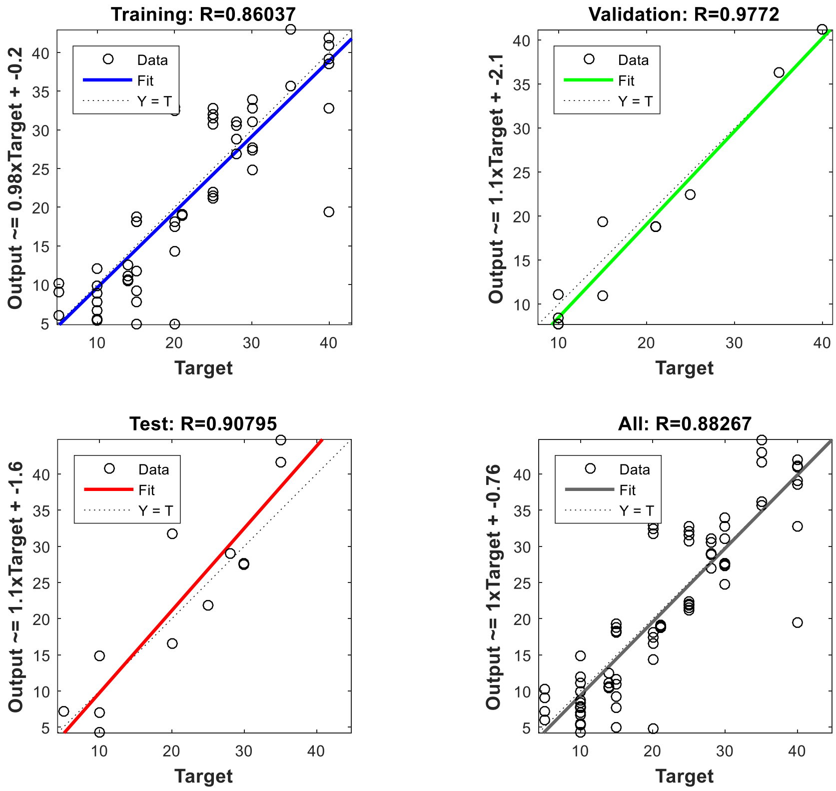

Figure 6.10 Correlation between prediction and measurement after application of trained neural network on various datasets

6.5 Validation on Field Data

As the model has been trained, validated and tested during the model construction process, it is deemed to be a completed artificial neural network model. However, its prediction accuracy in the field remains a question. To examine the applicability of the model, 23 field data samples were collected, as summarised earlier by Lin et al. (2020), and shown in Table 6.7. The vertical stresses from data 1–20 were provided in the published studies, whereas the vertical stresses from data 21–23 were estimated from a constant 0.025 MN/m³ unit weight ratio between vertical stress and depth of cover, as suggested by numerous studies (Alehossein and Poulsen 2010; Yang et al. 2011; Suchowerska et al. 2013) .

Table 6.7 Field data collected by Lin et al. (2020)

Literature Source	Data	σ_H (MPa)	σ_h (MPa)	σ_v (MPa)	BWS (MPa)	θ_b (°)
Zoback et al. (1985)	1	34.1	15.7	23	52	37
Leriche (2017)	2	72.60	37.95	35.70	102.2	42
	3	73.85	49.20	39.65	112	30
	4	67.09	49.49	41.21	136.94	42
	5	70.85	47.00	34.90	140	27
Klee et al. (2011)	6	66.55	31.88	36.65	84	55.5
Shen et al. (2002)	7	51.79	22.53	28.77	92.4	25
	8	57.82	26.35	32.12	92.4	51
Shen (2008)	9	59.13	46.08	41.20	84	67
	10	59.36	46.26	41.37	84	61.7
	11	59.89	46.67	41.73	84	72
	12	60.43	47.09	42.11	84	61
	13	61.62	48.02	42.94	84	66.8
	14	62.22	48.49	43.36	84	61.7
	15	62.93	49.04	43.86	84	61.7
	16	63.38	49.39	44.16	84	66.9
	17	63.96	49.85	44.57	84	61.7

	18	65.17	50.79	45.41	84	61.7
	19	65.36	50.94	45.55	84	72
	20	65.69	51.20	45.78	84	72
Walton et al. (2015)	21	79.00	56.00	43.23	109.05	48
Lin et al. (2020)	22	13.74	10.66	6.78	18.2	19.84
	23	10.15	7.39	6.90	17.61	14.17

6.5.1 Estimation of σ_h

Figure 6.11a shows the prediction results, using the Artificial Neural Network model, on collected field data. Apart from Data 1, other estimations which have high discrepancy in σ_h magnitudes from field measurements were for Data 9–20. This set of data also happened to be collected from one source (Shen 2008), where the depths of breakout data ranged from 3700 m to 4150 m. Given the deep locations of the data, it is likely that temperature may influence breakout geometries as high temperatures can result in change in rock mechanical properties (Yang et al. 2017). Although the difference in σ_h magnitudes was relatively large in these data, the associated errors were still reasonable. Overall, the estimation yielded an average error rate of 15.88%.

Considering that this approach does not require any ancillary equipment or additional cost, the error rate is acceptable. Because of the nature of the ANN model, it is possible to improve the reliability by providing additional training data. Detailed predictions on each data point are in Table 6.8.

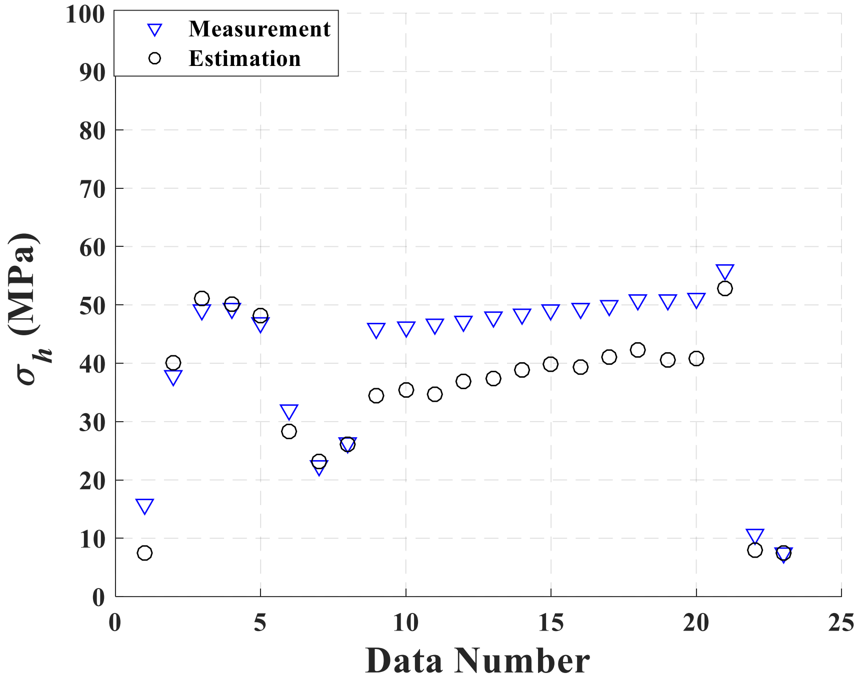

a

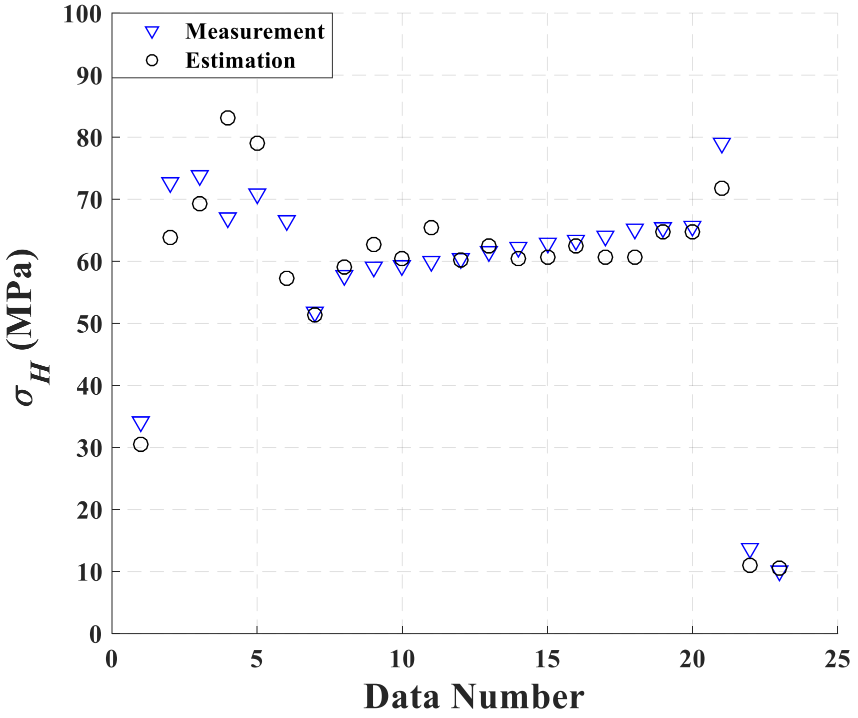

b

Figure 6.11 a) σ_h prediction by Artificial Neural Network against field measurements; b) σ_H prediction by Artificial Neural Network against field measurements

Table 6.8 Estimation results on σ_h

Data	σ_h (MPa) measured	σ_h (MPa) estimated	Error
1	15.70	7.38	-52.99%
2	37.95	40.17	5.85%
3	49.20	51.08	3.82%
4	49.49	50.12	1.26%
5	47.00	48.17	2.49%
6	31.88	28.22	-11.48%
7	22.53	23.06	2.36%
8	26.35	26.08	-1.01%
9	46.08	34.54	-25.05%
10	46.26	35.51	-23.25%
11	46.67	34.66	-25.74%
12	47.09	36.86	-21.73%
13	48.02	37.39	-22.14%
14	48.49	38.89	-19.80%
15	49.04	39.73	-18.99%
16	49.39	39.37	-20.29%

17	49.85	40.94	-17.86%
18	50.79	42.34	-16.62%
19	50.94	40.57	-20.36%
20	51.20	40.93	-20.06%
21	56.00	52.77	-5.77%
22	10.66	7.90	-25.92%
23	7.39	7.36	-0.43%
		Average	**15.88%**

6.5.2 Estimation of σ_H

As discussed earlier, the Mogi–Coulomb criterion provides the most reliable estimation of σ_H based on 79 laboratory data with given σ_h. Thus, the same approach was implemented to estimate σ_H from field data from estimated σ_h. As in-situ rock properties were not available in the field data, Poisson's ratio (v) and friction angle (ϕ) were assumed to be 0.2 and 35°, respectively. Assumptions were reasonable as these values are common in the field. By substituting Eq. (6.1)–(6.3) into Eq. (6. 9) and solving for σ_H, estimations can be obtained, as shown in Figure 6.11b. Table 6.9 shows the estimation error on each data value. The average error rate on σ_H was 6.82% through the Mogi–Coulomb approach, which is better than the Kriging approach presented by Lin et al. (2020) in an earlier study on the same dataset (8.4%). Another advantage of this approach over Kriging is that Mogi–Coulomb does not require breakout depth as an input parameter. As discussed by Schoenball et al. (2014), breakout depth exhibits creep behaviour and might not be a reliable parameter to use in horizontal stress estimation.

On the other hand, the Stassi D'Alia criterion was also validated against field data. Since tensile strengths were not available, three UCS/UTS ratios were used in this analysis, including 8, 10 and 12. Average error rates on σ_H were calculated to be

13.13%, 14.07% and 14.81%, respectively, suggesting that Mogi–Coulomb provides higher accuracy compared to Stassi D'Alia on the given dataset.

Table 6.9 Estimation results on σ_H

Data	σ_H (MPa) measured	σ_H (MPa) estimated	Error
1	34.10	30.40	10.84%
2	72.60	63.75	12.19%
3	73.85	69.24	6.24%
4	67.09	83.19	24.00%
5	70.85	79.10	11.64%
6	66.55	57.21	14.03%
7	51.79	51.42	0.72%
8	57.82	59.06	2.14%
9	59.13	62.70	6.04%
10	59.36	60.35	1.67%
11	59.89	65.50	9.37%
12	60.43	60.17	0.43%
13	61.62	62.53	1.48%
14	62.22	60.52	2.73%
15	62.93	60.56	3.77%

16	63.38	62.51	1.37%
17	63.96	60.61	5.24%
18	65.17	60.67	6.90%
19	65.36	64.76	0.92%
20	65.69	64.71	1.49%
21	79.00	71.69	9.26%
22	13.74	11.08	19.39%
23	10.15	10.65	4.89%
		Average	**6.82%**

In addition, an ANN model was also constructed based on the same experimental data to estimate σ_H. Similar to the procedures in Section 6.4, the relationships between σ_H and each individual parameter including their interaction terms were plotted, see Figure 6.12. The interaction term, $\sigma_v \times \theta_b$ (Figure 6.12d) showed lower R^2 value than θ_b (Figure 6.12), such that this parameter was excluded in ANN training. On the other hand, the other two parameters, $\sigma_v \times BWS$ and $\theta_b \times BWS$ displayed improved correlations, as shown in Figure 6.12e–f, and were considered as input parameters for the ANN model.

After the same model construction process, the optimised ANN model was used to predict 23 field data on σ_H, as seen in Figure 6.13. The average error rate using the ANN model is 13.89%, which is not as accurate as the Mogi–Coulomb approach discussed above. However, more validation is expected to be conducted to further compare these approaches.

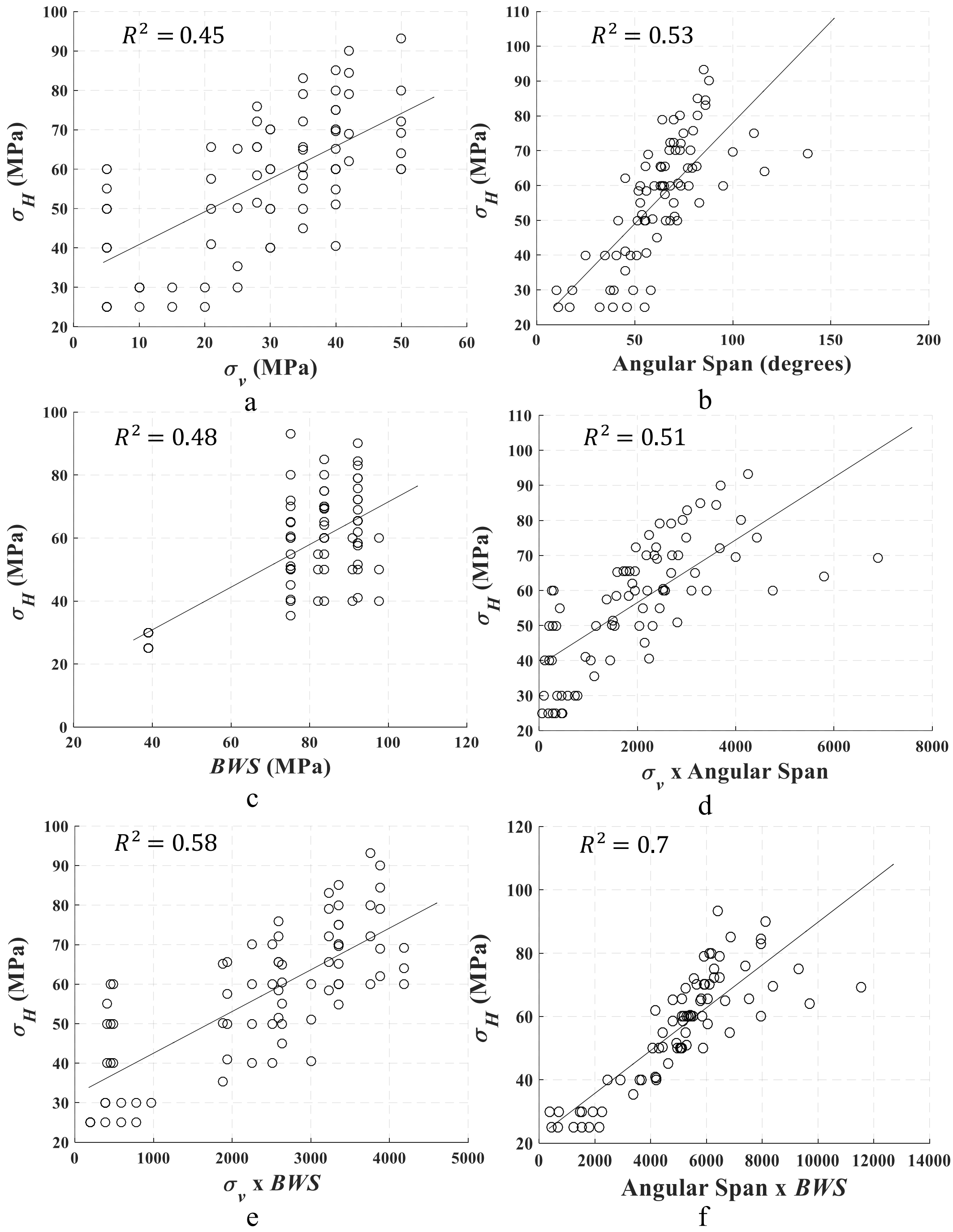

Figure 6.12 ANN trend analysis on σ_H with respect to different parameters

6.5.3 Sensitivity analysis of friction angle and Poisson's ratio

The sensitivity of Mogi–Coulomb was examined against ϕ and ν. Figure 6.14a displays the estimated σ_H values based on three ϕ values ranging from 30° to 40°. It can be seen that the higher ϕ values led to increased σ_H magnitudes, although changes in σ_H values were insignificant. Overall, the average error rates of 30° and 40° friction angles on field data are 9.1% and 8.9%, respectively, which are slightly higher than for the 35° friction angle. The implication here is that ϕ values do not influence estimation results significantly, such that appropriate assumptions can be made in the field when the parameter is unknown.

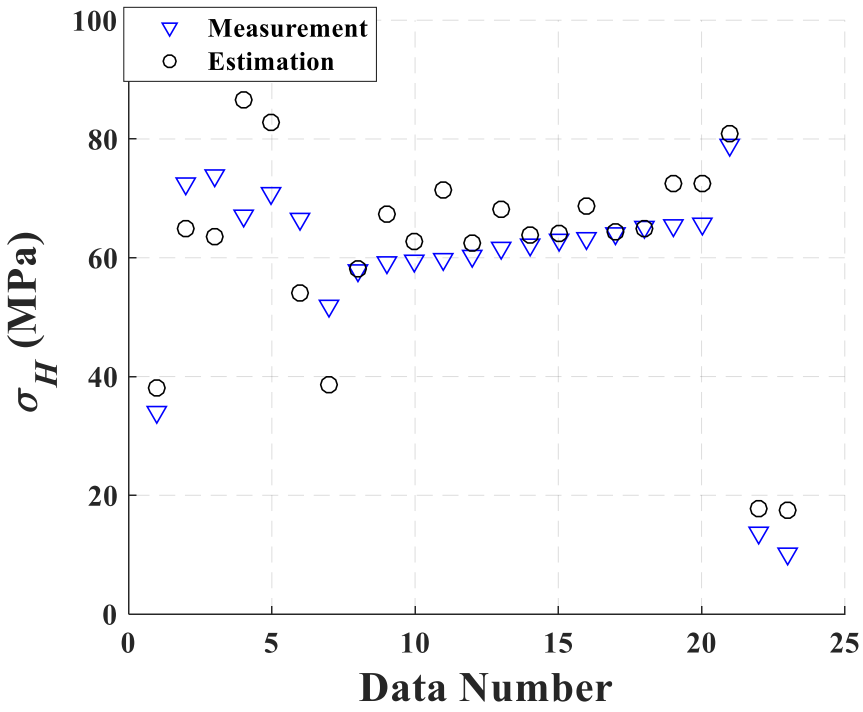

Figure 6.13 ANN estimation on σ_H

Figure 6.14b reveals that the calculated σ_H increased with increasing v (from 0.15–0.25). However, this increment is minimal as the average rate of change is less than 1%. This is mainly because the magnitude of v is nominal and it is only considered in the intermediate stress in Eq. (6.3). Therefore, the influence of v can be neglected and simply assumed as 0.2 in field applications.

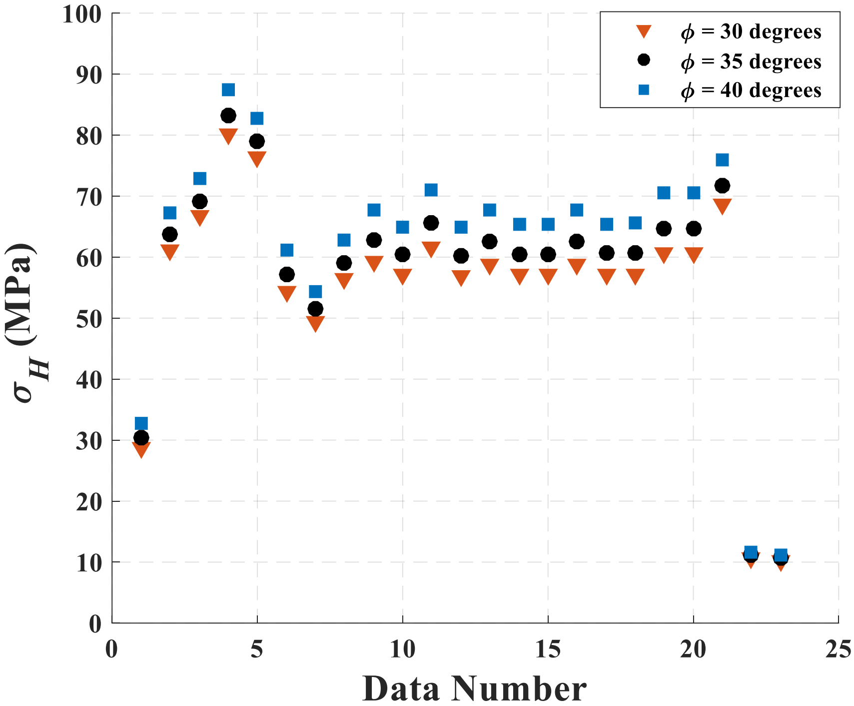

a

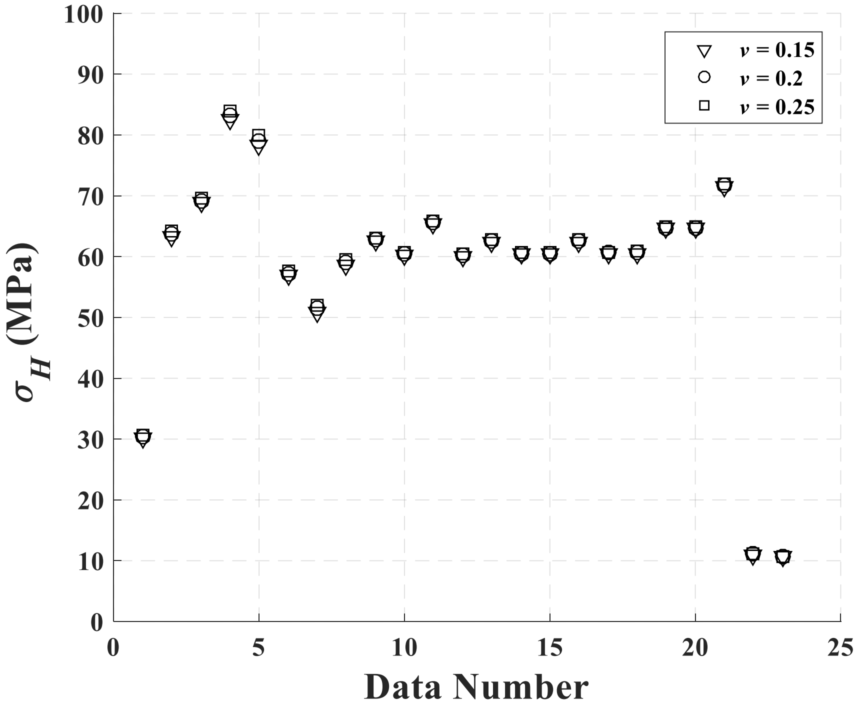

b

Figure 6.14 Sensitivity analysis on a) friction angle; b) Poisson's ratio

6.6 Discussion and Conclusions

This study presented experimental breakout data under various stress combinations. Results show that both σ_h and σ_v influence breakout geometries, in which higher σ_h and σ_v lead to narrower and shorter breakout geometries. It is noted that the influence of σ_h is more significant than that of σ_v. The implication here is that σ_v should be considered during estimation of horizontal stress magnitudes.

Since σ_H was able to be estimated from Kriging, the focus of this study was initially on the estimation of σ_h. Analytical investigation of nine failure criteria using σ_H, σ_v, θ_b and rock information was carried out against 79 laboratory data. Results revealed that σ_h prediction values are sensitive to σ_H, so that it is not possible to estimate a reasonable value of σ_h using σ_H and rock information. Instead, estimation of σ_H from given σ_h is viable through Mogi–Coulomb and Stassi D'Alia failure criteria, which yielded 22.69% and 22.75% average error rates on 79 laboratory data points, respectively. Five data points (Data 35–39) with θ_b over 90° produced high level errors in both criteria. In field conditions, it is rare to encounter θ_b that is greater than 90°, and therefore these five data points were excluded. After excluding these data, the average error rates of Mogi–Coulomb and Stassi D'Alia on σ_H improved to 13.37% and 13.74%.

To overcome difficulties and to estimate both horizontal stress magnitudes from borehole breakout data only, an ANN model was proposed based on the 79 laboratory data to estimate σ_h. The model was optimised based on a training, validation and testing process. Based on an independent validation against 23 field data, it was found that the ANN model produced a 15.88% average error rate on σ_h.

Since σ_h can be estimated from the ANN model, σ_H prediction using borehole breakout was also conducted on 23 field data points using the three approaches of Mogi–Coulomb, Stassi D'Alia and ANN to compare to the Kriging technique. Results showed that Mogi–Coulomb provided the most reliable estimation, with an average error rate of 6.82% whereas Stassi D'Alia provided higher error rates ranging from 13.13% to 14.81% on σ_H with different UCS/UTS ratios (8–12). Although Kriging also produced a competitive accuracy of 8.4%, it was not as favourable as Mogi–Coulomb because Kriging used breakout depth as an input parameter and this parameter is subject to a rock creep phenomenon which might influence the prediction results. Consideration of this parameter may therefore cause a misleading estimation due to its time-dependent behaviour. Estimation of σ_H using θ_b, BWS, σ_v and two interaction terms was also carried out and exhibited a higher error rate of 13.89% on the same dataset. In addition, a sensitivity analysis on Mogi–Coulomb suggested that assumptions on ϕ and v are reasonable. This indicates that the Mogi–Coulomb approach for horizontal stress estimation from borehole breakout data is reliable.

Overall, the proposed 'ANN'-'Mogi-Coulomb' method provided an innovative approach to horizontal stress magnitude estimation via borehole breakout. Although the error of σ_h was only acceptable, the technique provides a number of competitive advantages over commonly used techniques including hydraulic fracturing and overcoring. Firstly, hydraulic fracturing and overcoring require the borehole wall at the measurement point to be elastic; this is difficult in weak layers where rock experiences high stress concentrations and these layers are important to be considered. Further, in higher stress, brittle rock conditions, stress fracturing around and ahead of the borehole will affect overcoring measurement results. The borehole breakout phenomenon is usually observed in these locations and can be used to estimate horizontal stress magnitudes. Secondly, σ_H estimation from borehole breakout presented very promising results on field data. Thirdly, this approach can produce a stress profile along the borehole if breakout exists in multiple layers, whereas hydraulic fracturing and overcoring only provide measurements at required depths. Lastly, and most importantly, borehole breakout data can be easily accessed as borehole imaging is compulsory in many countries. This means the approach can theoretically provide horizontal estimation at "no" cost compared to traditional stress measurement techniques.

7 APPLICABILITY OF THE DEVELOPED MODELS TO FIELD CASES: ADDITIONAL DATA COLLECTION AND VALIDATION

Chapter 6 presented a newly proposed technique to estimate horizontal stress magnitudes based on borehole breakout data. This approach is a combination of an Artificial Neural Network (ANN) and a constitutive relationship (the Mogi–Coulomb failure criterion), in which the minimum horizontal stress (σ_h) is estimated from the ANN model and the maximum horizontal stress (σ_H) is calculated subsequently. A comparison between various proposed models (Kriging, ANN and constitutive relationship) on predicting σ_H was also discussed in the previous chapter. The accuracy of these models was examined against 23 field data from the literature and mine site A. The comparison results revealed that the constitutive relationship yielded the most reliable estimations on σ_H, with an average error rate of 6.82%. However, further comparison between these methods is necessary since both the ANN and Kriging models also had acceptable error rates on the same field data, at 8.4% and 13.89% respectively.

In this chapter, downhole logging data from the field is provided from four underground coal mines in eastern Australia (mine sites A–D). In field conditions, borehole breakout geometries cannot be directly obtained and numerous processing steps are required. Section 7.1 presents procedures to identify and extract breakout occurrences and geometries from the Borehole Televiewer (BHTV). Then, the estimation of rock strengths at breakout locations from sonic velocity data or cored samples is discussed. Since the horizontal stress magnitudes are required for the validation of models, stress measurement reports at nearby depths of breakouts are also used. Where horizontal stress measurements are not available, the stress maps in the mining regions constructed by Hillis et al. (1999) are used as the reference for the local stress environment.

Section 7.2 discusses the locations of mine sites and compares the models against the data processed in Section 7.1. As the data from mine site A has been used in Chapter 4 and Chapter 6, only the datasets collected from the other three sites are used here (mine sites B–D). The most reliable model for σ_H prediction will be determined based on the examinations in Chapter 6 and in this section. In addition, the ANN model on σ_h

estimation is also tested using the field data. Overall, this chapter provides further validation of the proposed model in Chapter 6 and examines its applicability to underground mines in different regions.

7.1 DATA COLLECTION AND PROCESSING

With the development of the BHTV (Zemanek et al. 1969), the conditions of rock around the borehole can be visually inspected and evaluated. This revolutionary technique has also enabled the confirmation of alignments between horizontal stress orientations and breakout depths, which was not clear using four-armed calliper data (Plumb and Hickman 1985). As the BHTV can provide images of fractures at the borehole wall and the raw data can be converted to digitised form, it is also capable of identifying and extracting borehole breakout data. Based on the travel time of elastic waves through the formation from the BHTV, breakout shapes and geometries can be computed at various depths (Broding 1981; Zoback et al. 1985; Walton et al. 2015; Leriche 2017).

This section first provides the procedures for breakout identification and extraction from travel time data. Then, the rock strength calculation at the breakout location and horizontal stress measurements are presented.

7.1.1 Breakout identification

The BHTV is an acoustic logging tool that provides an image of the surrounding rock in the scanning borehole along the depth at 360°. It was initially implemented in the petroleum industry for observation of the borehole environment (Zemanek et al. 1969). The BHTV uses a transducer to transmit the acoustic pulse to the borehole and records amplitude and travel time of the wave once it reflects back to the device. The data is then processed into image format, which can be displayed as unfolded boreholes. Depending on the equipment type (e.g. Schlumberger and Mount Sopris Instruments), the number of scans per unit length can also vary. The data provided by mine sites has different scanning frequency, ranging from 2 to 5 mm per record. The intervals between measurement points at the same level during each scan are also different between mine sites, ranging from 1.4° to 2.5°.

To identify borehole breakouts, the travel time data of acoustic pulses from the BHTV is used (Zoback et al. 1985; Tingay et al. 2008; Walton et al. 2015; LeRiche et al.

2017). In this study, the BHTV data is visualised in WellCAD software developed by Advanced Logic Technology (ALT). If the borehole wall is relatively intact with no observable fractures, the time required for an elastic wave travelling from the transducer to the borehole and reflecting back to the transducer should be similar, see Figure 7.1a. On the other hand, the travel time required when encountering borehole breakouts should be significantly longer since additional travel distance has been created by the formation of V-shaped voids (Faraguna et al. 1989; Zemanek et al. 1990). Hence, breakouts can be identified as the increased travel time at opposite sides of the borehole from BHTV data (Tingay et al. 2008), as shown in Figure 7.1b.

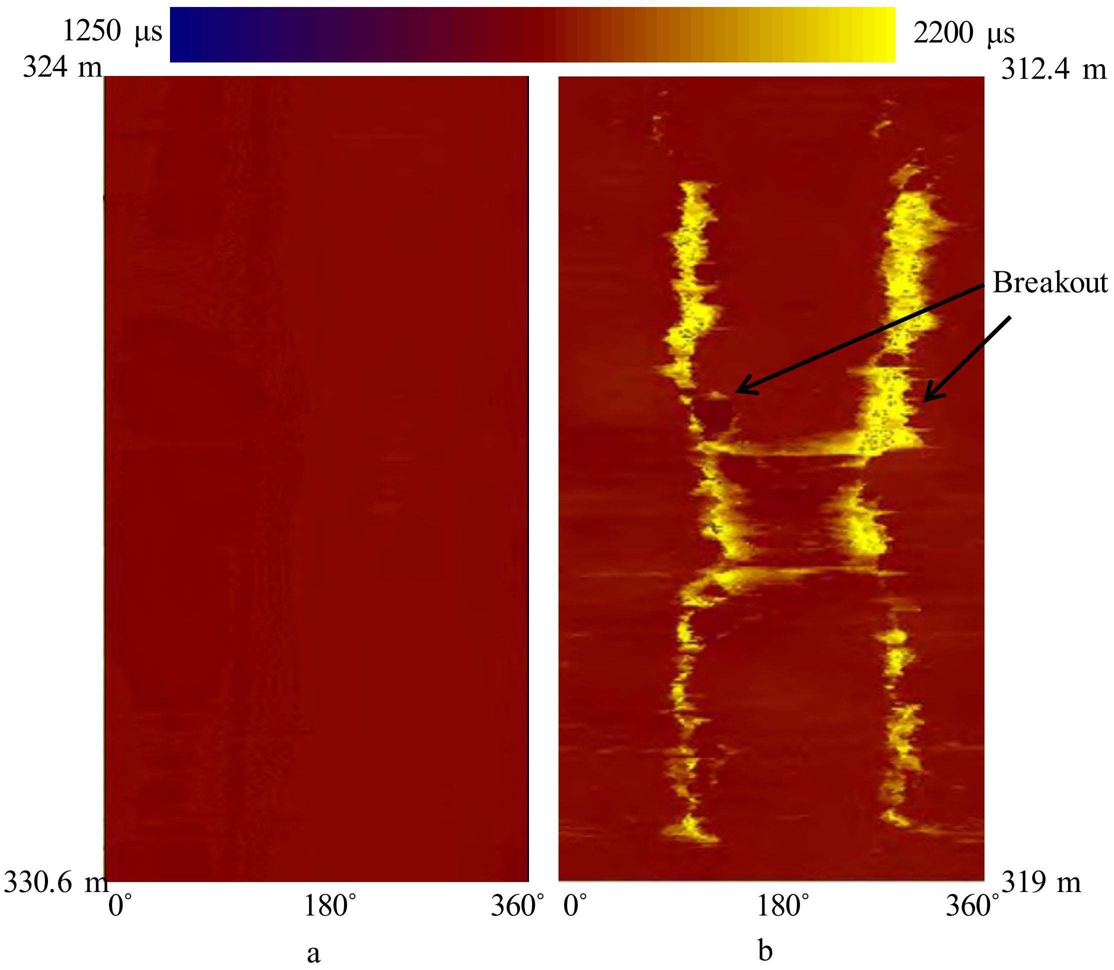

Figure 7.1 a) Travel time data from 324 m to 330.6 m in a borehole provided by mine site B, b) Travel time data from 312.4 m to 319 m in the same borehole, where the yellow colour indicates borehole breakout.

Although the travel time data distinguishes the borehole breakout areas from an un-fractured borehole wall based on the colour difference, it is still difficult to visually observe the borehole breakout. To provide a clear image of breakout, the ‘cross-section’ view function of WellCAD was used. Based on the function, the borehole breakout shape at 316 m in Figure 7.1b was extracted and shown in Figure 7.2. The figure shows that the breakout shape at this level is a ‘V-shaped’ breakout, which occurred symmetrically at the angles approximately between 85˚–127˚ and 265˚–290˚. As the travel time data is indicative of the distance from the transducer to the rock surface around the borehole, it can also represent the borehole radius and breakout depth. Figure 7.2 shows that the borehole radius and breakout depth require approximate travel time of 1750 µs and 1900 µs, respectively. Therefore, based on the combination of unfolded and cross-sectional views of the borehole, the breakout occurrence can be confirmed at this location.

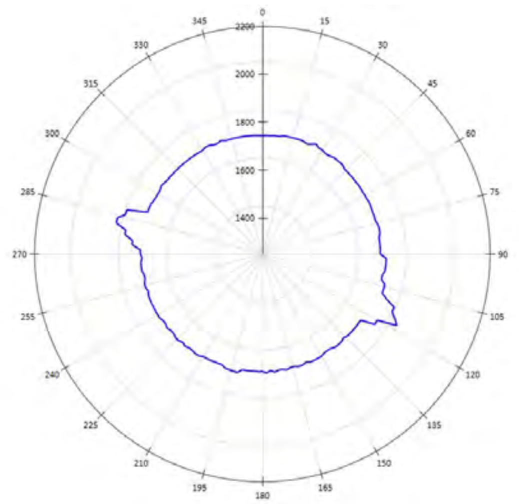

Figure 7.2 A ‘cross-section’ view of the borehole at 316 m depth

Once the borehole is drilled, the stress re-distribution can be influenced by the existence of discontinuities including fissures and joints, which may in turn impact the breakout geometries and orientations (Maloney and Kaiser 1989). This can lead to misinterpretation of the local stress field estimated from borehole breakouts (Kwong and Kaiser 1989). For instance, breakout features can be disturbed by the foliation or bedding plane that is parallel to the borehole axis (Duan and Kwok 2016; LeRiche et al. 2017). To mitigate this uncertainty, it is important to select borehole breakouts that do not intersect with these discontinuities (Leriche 2017). Another selection criterion is to distinguish borehole breakouts from other borehole failures, such as washouts and key seats. A washout is 360˚ borehole enlargement due to the instability of surrounding rock when the mud weight is not sufficient to stabilise the borehole (Zoback 2010;

Mansourizadeh et al. 2016). Figure 7.3a shows a typical washout. As suggested by Zoback (2010), if the initial breakout angular span is over 120°, the borehole is likely to be unstable and consequently results in washouts. For this reason, field data observations with breakouts under such conditions were excluded. On the other hand, key seats are a groove at the borehole, as displayed in Figure 7.3b. Unlike breakouts or washouts, the formation of this phenomenon is not related to stress but due to the artefact of drilling pipe rotation (Etchecopar et al. 2013). Thus, the existence of key seats is not informative for stress magnitudes and can also be excluded.

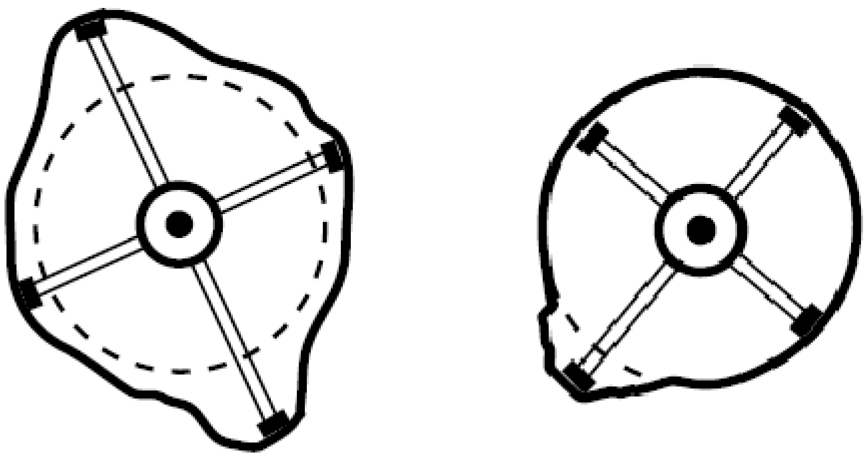

a b

Figure 7.3 a) Borehole washout; b) key seat (Zoback 2010)

Since the purpose of this chapter is to validate the proposed models, the breakout data collected from mine sites should have corresponding horizontal stress magnitudes for direct comparison. However, only a limited number of breakout data observations met this criterion. For mine sites A and D, five breakout data points were selected in total as they have stress measurements available at the nearby depths. In contrast, mine sites B and C did not have stress measurement reports at the breakout locations. To effectively use the data collected from these mine sites, local stress maps in the regions were used for validation (Hillis et al. 1999).

7.1.2 Breakout geometrical extraction

Once the breakout was identified from the travel time data, the next step was to extract its geometries. Breakout angular span is relatively simple to measure. In WellCAD, this measurement was achieved directly by inserting 'breakout log'. The log function allows users to define the breakout areas (yellow areas in Figure 7.1b) on the travel time image and estimates the 'widths' (angles) of these areas. The average angle of two sides was taken and used as the final breakout angular span, which is 44.5°. Then, the length of breakout along the borehole axis can also be obtained from this log, which is 5 m. This was later used for breakout depth extraction. Since each measurement point was taken at 1.4°–2.5° intervals at different mine sites, the breakout angle between the intervals cannot be captured. This might result in minor underestimations of breakout angular span measurements, which can be neglected during horizontal stress estimation.

Measurement of breakout depth is rather complicated and requires multiple steps. Since the travel time data was displayed in the form of an image using WellCAD, it was not possible to derive the breakout depth directly. To conduct the depth measurement, it was essential to convert the image data to digitised data. The travel time data was initially exported from WellCAD to Excel, so that the travel time at each borehole angle and depth could be presented. For instance, a total number of 180 data points (2° interval) can be collected per 2 mm depth at mine site B. This means, over a 1 m borehole breakout length along the borehole axis, there are 500 sets of data to analyse.

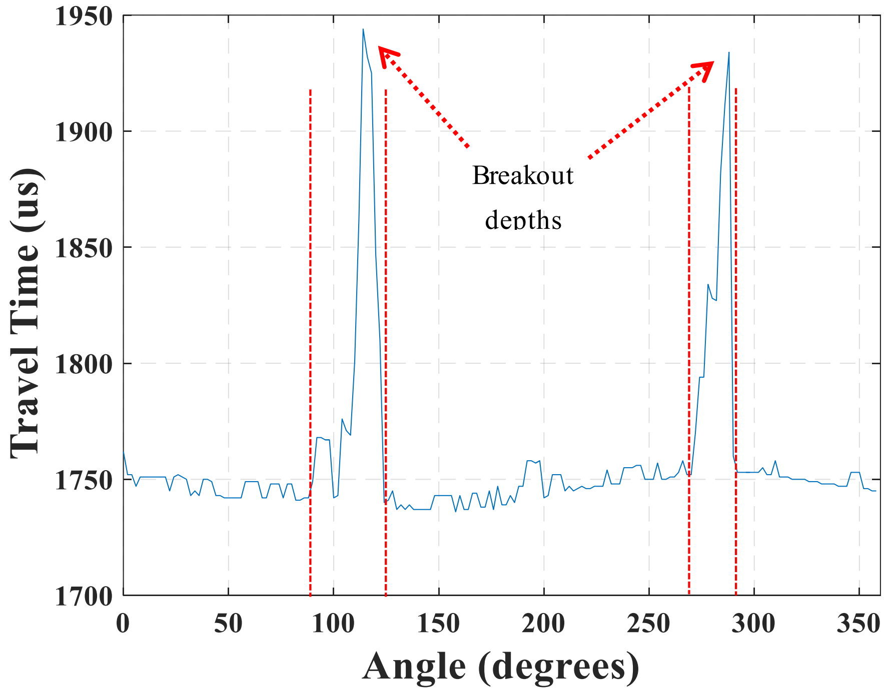

Figure 7.4 Digitised travel time data of Figure 7.2

Since every set of data has same number of data points, the extraction process can be semi-automated. Hence, the next step was to extract breakout depth from a single dataset. Figure 7.4 shows the digitised travel time data at each angle of the cross-sectional area in Figure 7.2 after processing using Excel. It can be seen that the travel time outside the bounded areas is approximately the same (1750 μs), indicating that the borehole wall at these orientations is competent and not fractured. Conversely, the travel time within the areas continuously increases until the peak points, then decreases back to 1750 μs travel time. These areas can be classified as breakout regions and the peak points can be referred to as the breakout depths at this level. Breakout depths at every 2 mm interval were then calculated along the 5 m breakout length, as measured earlier. Consequently, the final breakout depth was estimated at 2030 μs based on the average of breakout depths at each level.

Although the breakout depth was able to be derived from the digitised data, it still did not represent the actual elongation length but the time required for the acoustic wave to travel to the breakout tip and reflect back to the transducer. As discussed in previous chapters, this parameter is usually normalised by the borehole radius, i.e. breakout depth/borehole radius. Hence, the normalised breakout depth can be estimated as long as the travel time of the borehole radius is available.

To determine the travel time of the borehole radius, the appropriate sections of the borehole should be selected. To precisely calculate the borehole radius, the borehole wall should be relatively intact so that the travel time data is not disturbed. When the borehole section does not contain any fractures, the travel time around the borehole at the same level is supposed to be similar. Based on the selection condition, two sections were chosen between 310.4–310.9 m and 320–320.5 m in Figure 7.5, which were above and below the identified breakout regions. The travel time data in these regions was then interpreted in Excel using the same approach above and the average value was obtained. Hence, the travel time of the borehole radius for this particular breakout was estimated as 1753 μs. Subsequently, the normalised breakout depth can be calculated as 1.16.

The use of travel time for the computation of borehole radius was more favourable than for the actual length. This is because the drilling process itself involves some uncertainties as the diameter of the borehole is usually greater than the drill bit (Hickman et al. 1984). The indication here is that the drill bit size may not be truly representative of the borehole diameter. This error can result in significantly shorter normalised breakout depth, which will in turn lead to unreliable horizontal stress estimation results. Therefore, calculation from travel time can provide more reliable breakout depth measurements.

The same procedures were repeated on the other breakout data to extract their geometric attributes. The extracted data is presented in Table 7.1.

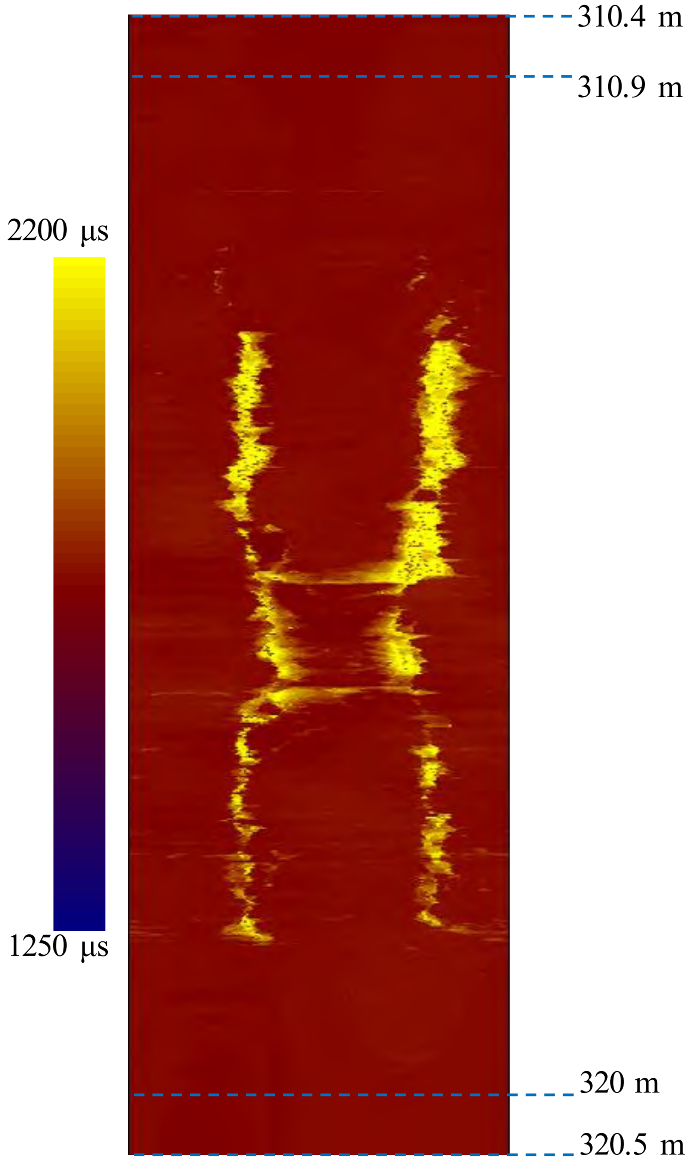

Figure 7.5 Travel time data from 310.4 m to 320.5 m in the same borehole from Figure 7.1b, where the yellow colour indicates borehole breakout

7.1.3 Rock strength estimation

Uniaxial compressive strength (UCS) is a critical parameter that should be considered during breakout analysis (Haimson and Herrick 1986; Barton et al. 1988). In theory, a higher UCS value will result in narrower and shallower borehole breakouts under the same stress levels. In field conditions, cored samples are not always available at various borehole depths, such that the magnitudes of UCS may not be directly provided in many breakout locations. To overcome this limitation and make effective use of the downhole logging data, the empirical relationship between UCS and sonic velocity has been introduced to represent in-situ rock strengths. To date, the empirical relationship is implemented extensively in both mining and petroleum engineering (Chang et al. 2006; Chang et al. 2010; Azimian et al. 2014). Therefore, this methodology was applied at mine sites A–C where the cored samples were not available.

Sonic log is one type of geophysical log which emits the sound waves travelling from the device into the rock formation and returning back to the source. Its data, sonic velocity, is usually recorded as the travelling speed (e.g. VL2F) or travel time (e.g. MC2F) of the wave during this cycle (MacGregor 2003). Sonic velocity data provided from the mine sites was saved in 'LAS' files, which had to be imported and processed via Excel. Similar to the process of extracting breakout depth, the sonic velocity of a breakout section was calculated by averaging the sonic velocity data within the breakout length. As suggested in Chapters 4 and 6, the borehole wall strength (BWS) should be used to represent the in-situ rock strength rather than UCS and this parameter can be estimated from sonic velocity or UCS. Based on the empirical equations provided by mine sites A–C, the corresponding BWS values can be converted from sonic velocity, i.e.

$$\boldsymbol{BWS = 3.689\mathrm{exp}(0.000684 \times VL2F)} \text{ – mine site A} \tag{7.1}$$

$$\boldsymbol{BWS = 897.75\mathrm{exp}(-0.037 \times MC2F)} \text{ – mine site B} \tag{7.2}$$

$$\boldsymbol{BWS = 2.7996\mathrm{exp}(0.0008 \times VL2F)} \text{ – mine site C} \tag{7.3}$$

Rock strengths at mine site D were provided directly. According to the mine site, the UCS values were estimated from the point load tests since the sonic velocity data was not available and the following equation was used for the conversion:

$$\boldsymbol{UCS = 21 \times F \times P \times 1000/D_e^2} \text{ – mine site D} \tag{7.4}$$

F = size correction factor = 1.12, P = point failure load (kN) and D_e^2 = 4A/π. Mo (2019) analysed the rock strength data at the same mine site and suggested that the UCS values estimated from the point load index tests should be downgraded with a factor of 0.58 to represent BWS (Galvin 2016). Thus, this factor was also used in this thesis to estimate the in-situ rock strengths at mine site D.

There are also other parameters that should be considered in the ANN model on σ_h, including Poisson's ratio (v) and friction angle (ϕ). However, these parameters were not collected as there were no cored samples at the required locations. Based on the sensitivity analysis of the v and ϕ on σ_h prediction results in Chapter 6, it can be seen that the influences of the two parameters are not significant. Therefore, the values of v and ϕ were assumed to be 0.2 and 35°, which were justified as reasonable assumptions in Chapter 6. Overall, the UCS values estimated for all mine sites are summarised in Table 7.1.

7.1.4 Summary of data

Based on the procedures described, breakout geometries and rock strength data at the mine sites were extracted. Since the data from mine site A has already been shown and discussed in Chapters 4 and 6, only the data from mine sites B–D is presented in this section. Similar to Chapter 6, the vertical stress (σ_v) was estimated using the unit weight of overburden, which is 0.025 MN/m^3 (Alehossein and Poulsen 2010; Suchowerska et al. 2013; Yang et al. 2011).

A summary of data is provided in Table 7.1. It is noted that some travel time data files provided by mine sites C and D were corrupted, such that the data could not be exported to Excel. This means the Kriging model cannot be examined against these data due to lack of breakout depths, but the data can still be used for other models. As mentioned in Section 7.1.1, there are stress measurement reports available at mine site D near the breakout occurrence depths and these data points are presented in Table 7.2.

Table 7.1 Breakout data collected from mine sites B–D

Site	Data	Breakout length (m)	Normalised breakout depth (L/R)	Breakout angular span, θ_b (°)	BWS (MPa)	σ_v (MPa)
Mine site B	1	179.4–180.9	1.05	25.8	33.53	4.50
	2	219.3–219.6	1.04	40.2	20.80	5.49
	3	243–243.6	1.01	18.6	33.98	6.08
	4	245.8–246.1	1.05	36.1	21.88	6.15
	5	275.1–275.6	1.04	38.4	24.71	6.88
	6	298.7–299.9	1.02	24.7	22.20	7.48
	7	313.1–318.1	1.16	44.5	5.68	7.89
	8	327.1–327.4	1.05	32	32.86	8.18
	9	331.9–332.4	1.04	33.5	31.02	8.30
Mine site C	1	375.6–379.1	1.16	47.7	26.7	9.43
	2	473.2–473.6	1.04	28.5	35.1	11.83
	3	537.5–537.7	1.04	48.8	32.9	13.44
	4	542.7–542.9	N/A	40.5	26.1	13.57
	5	556.1–556.5	1.08	51.8	33.5	13.91
	6	562.7–563	1.02	79.8	25.5	14.07
	7	563.8–564	1.12	73.2	27.2	14.10

	8	564.1–564.1	N/A	60.4	26.1	14.11
	9	567.7–568.3	N/A	56.9	28.3	14.20
	10	590.2–590.6	N/A	45.3	39.2	14.76
	11	649.2–650	1.15	57.7	28.1	16.24
	12	674.2–675	1.28	65.5	37.8	16.87
Mine site D	1	263.6–263.8	N/A	37.17	18.59	6.59
	2	318.7–319.2	N/A	41.09	20.1	7.97
	3	350.4–350.8	N/A	46.95	24.65	8.77

Table 7.2 Horizontal stress measurements at mine site D corresponding to the breakout data

Site	Data	Measurement depth (m)	σ_H (MPa)	σ_h (MPa)
Mine site D	1	261.6	13.8	10.7
	2	307.2	11	9.7
	3	353.2	14.6	12.4

7.2 VALIDATION AGAINST PROPOSED MODEL

This section presents the validation against the proposed models in Chapter 6 using the field data collected in Section 7.1. Since the field data from mine site A has already been used in Chapters 4 and 6, it is not discussed here. Based on the validation results, a further comparison between proposed models on σ_H estimation is provided. In addition, the reliability of the ANN model on σ_h prediction is also examined in this section.

7.2.1 Mine site B

Mine site B is an underground coking coal mine located in the Northern Bowen Basin Queensland, Australia. Based on the selection criteria, nine breakout data points were identified and processed, ranging from 179.4 m to 332.4 m depths of cover. Since the mine site does not have any stress measurement reports available, the local stress map constructed by Hillis et al. (1999) is used for prediction validation.

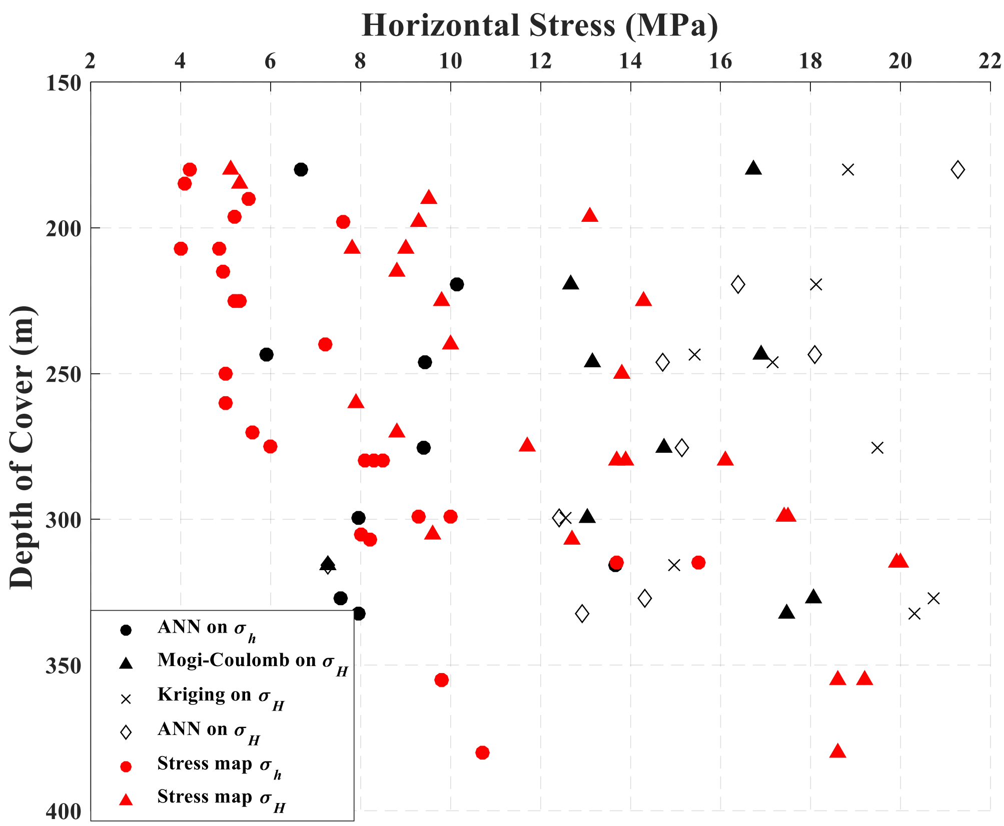

Figure 7.6 Prediction results on mine site B, red symbols represent the historical stress measurements in the region summarised by Hillis et al. (1999)

Figure 7.6 presents the estimation results on mine site B as well as the historical stress measurement results in the region from the local stress map (Hillis et al. 1999). According to the figure, it is clear that the Mogi–Coulomb approach provided the closest prediction on σ_H against the historical data, whereas the ANN model had worse predictions on σ_H than the Mogi–Coulomb, which agrees with Chapter 6. The Kriging model provided overestimation on σ_H as its prediction results yielded the highest values among the three models. It is noted that for data 7, there was significant underestimation of σ_H produced by the Mogi–Coulomb and the ANN models, in which the magnitude of

σ_H was even lower than that of σ_h. This is because of its extremely low BWS value (5.68 MPa). As the BWS value was estimated using the empirical relationship, there might be inevitable errors in the equation (Chang et al. 2006). The surrounding rock is likely to be unstable and results in washout with such low rock strength at 300 m deep, instead of forming a borehole breakout. Therefore, the results from data 7 were ignored.

Based on the estimation results, it can also be seen that the ANN model yielded reasonable σ_h values. This indicates that the ANN model might be considered as an estimation technique for σ_h. Overall, the proposed 'ANN'–'Mogi–Coulomb' method presented the most reliable prediction results against mine site B data, which is consistent with the conclusion drawn from Chapter 6.

Table 7.3 Prediction results on mine site B

Data	Kriging on σ_H (MPa)	ANN on σ_H (MPa)	Mogi–Coulomb on σ_H (MPa)	ANN on σ_h (MPa)
1	18.84	21.28	16.73	6.66
2	18.11	16.38	12.68	10.14
3	15.43	18.10	16.90	5.92
4	17.15	14.72	13.16	9.42
5	19.49	15.13	14.73	9.39
6	12.56	12.42	13.03	7.95
7	14.97	7.28	5.44	13.65
8	20.73	14.32	18.07	7.54
9	20.32	12.92	17.46	7.95

7.2.2 Mine site C

Mine site C is an underground coking coal mine located in the Sydney–Wollongong Basin, New South Wales, Australia. It is currently operating at 650 m depth of cover and it is planned to extend the operation to deeper locations. Based on the selection process, there were 12 borehole breakout data points identified and extracted, from 375.6 m to 675 m. The mine site has two horizontal stress measurements from overcoring at 750 m. Due to the depth differences between stress measurements and breakouts, overcoring results were only used as referencing points. As discussed in Section 7.1.4, some of the travel time data files provided by the mine site were corrupted such that breakout depths could not be extracted. Therefore, the Kriging model was only validated against the other eight data points.

Figure 7.7 presents the estimation results using the proposed models. Similar to mine site B, it can be seen that the Kriging model overestimated the magnitudes of σ_H. Based on the figure, the Mogi–Coulomb approach again had the best alignment with the historical measurements in the region, whereas the ANN model yielded higher σ_H predictions on the data. This further confirms the reliability of the Mogi–Coulomb approach. Table 7.4 summarises the prediction results. Figure 7.7 also shows that the ANN model produced slightly lower estimations on σ_h than the historical data, although the differences are not significant. Thus, this model on σ_h prediction requires more validation.

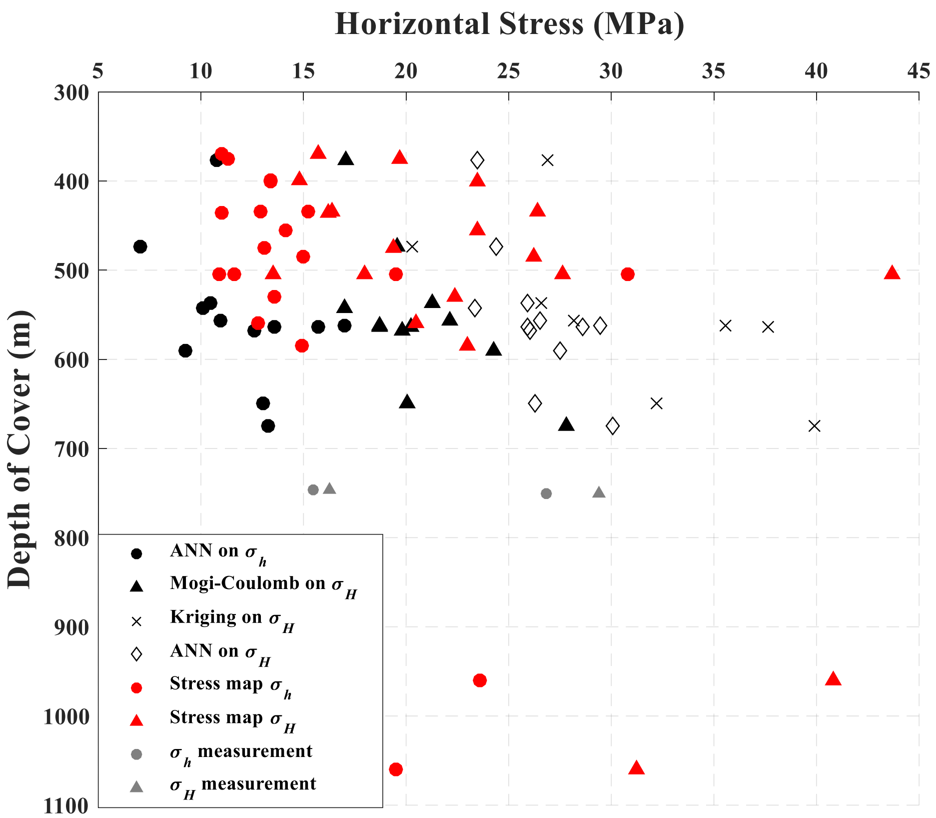

Figure 7.7 Prediction results on mine site C, red symbols represent the historical stress measurements in the region summarised by Hillis et al. (1999)

Table 7.4 Prediction results on mine site C

Data	Kriging on σ_H (MPa)	ANN on σ_H (MPa)	Mogi–Coulomb on σ_H (MPa)	ANN on σ_h (MPa)
1	26.91	23.48	17.05	10.75
2	20.27	24.38	19.55	7.05
3	26.61	25.93	21.30	10.45
4	N/A	23.35	16.98	10.07
5	28.18	26.53	22.14	10.94
6	35.59	29.43	18.71	17.03
7	37.66	28.61	20.23	15.72
8	N/A	25.92	18.72	13.57
9	N/A	26.01	19.83	12.62
10	N/A	27.52	24.27	9.22
11	32.20	26.27	20.08	13.03
12	39.90	30.08	27.82	13.28

7.2.3 Mine site D

Mine site D is an underground thermal coal located in the Central Coast, New South Wales, Australia. Based on the selection criteria, three borehole breakout data points were chosen with corresponding horizontal stress measurements at nearby depths. The breakout locations are from 263.6 m to 350.8 m. Since the travel time data files were damaged, borehole breakout depths could not be extracted.

Figure 7.8 shows the prediction of σ_H using the ANN and the Mogi–Coulomb models based on 23 field data points from Chapter 4 and three data points, 24–26, from mine site D. Results revealed that the Mogi–Coulomb approach yielded an average error rate of 7.62%. Although there is slight increase in the error rate compared to that in Chapter 6, the model still provided accurate σ_H values. On the other hand, the average error rate of the ANN model against the same dataset is 19.03%; it also increased from the value of 13.89% obtained in Chapter 6. Therefore, the error rate of the ANN model is considerably higher than that of the Mogi–Coulomb model. This agrees with the previous comparisons, suggesting that the Mogi–Coulomb model is the most reliable technique for σ_H estimation.

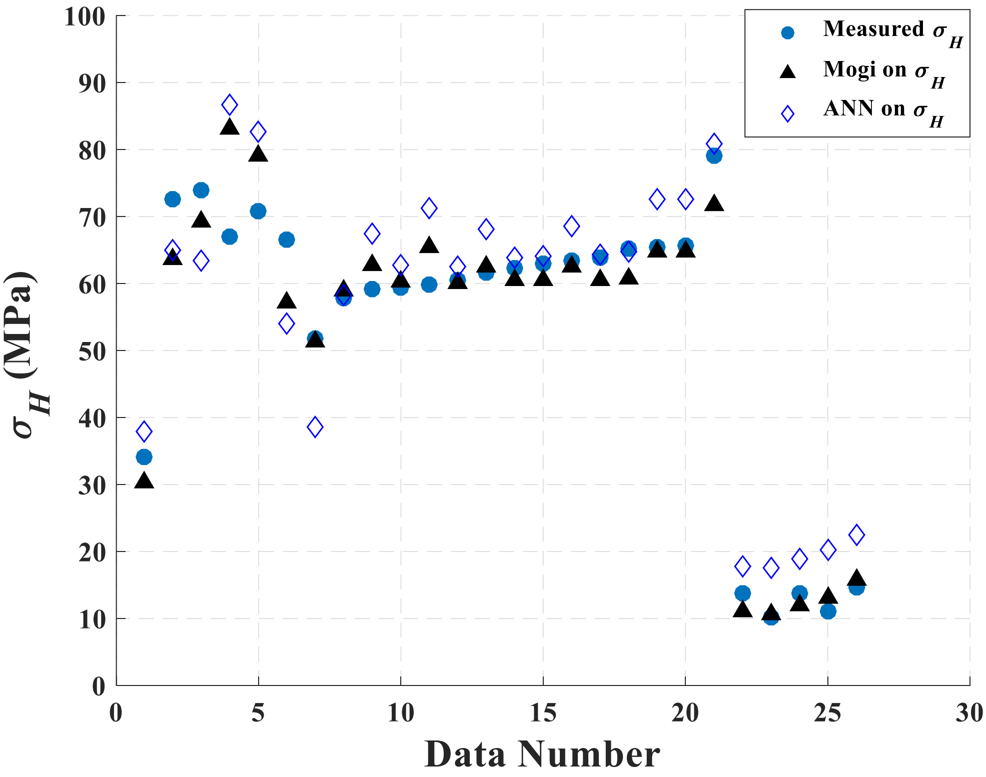

Figure 7.8 Prediction of σ_H on mine site D and field data from Chapter 4

The ANN model on σ_h prediction was also examined against the same dataset, as shown in Figure 7.9. Based on the results, the average error rate decreased from 15.88% in Chapter 6 to 15.05% in this section. The implication here is that this approach is capable of providing reasonable estimations on σ_h in different field cases.

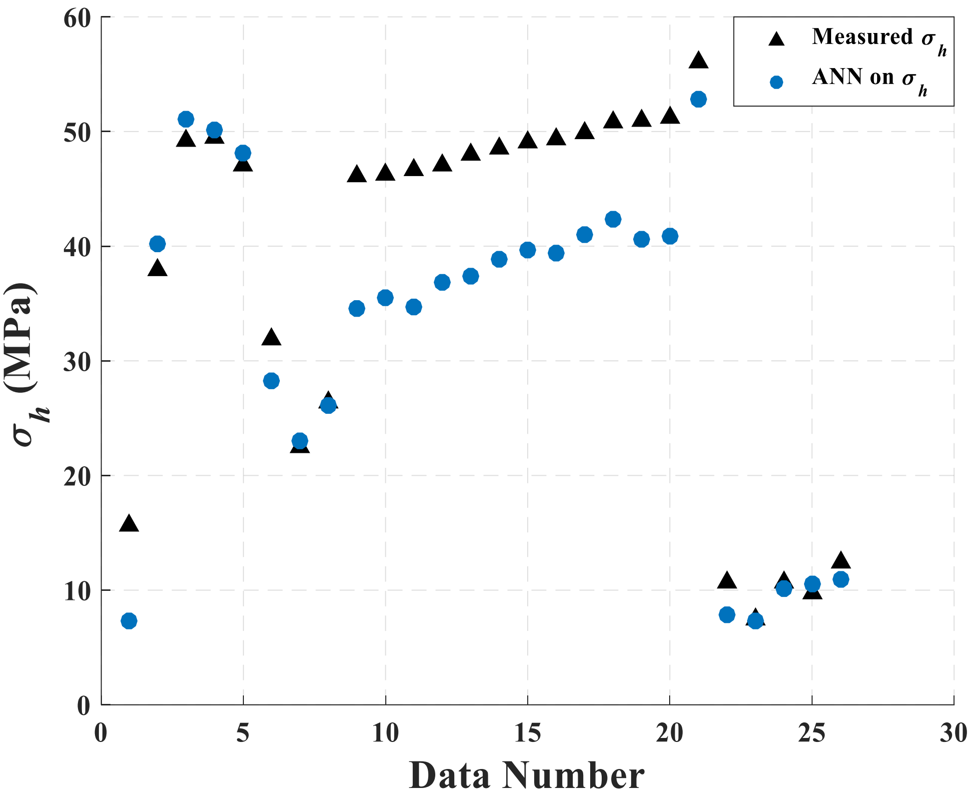

Figure 7.9 Prediction of σ_h on mine site D and field data from Chapter 4

Table 7.5 summarises the prediction results based on each individual model. From the table, it is clear that the estimation of σ_H using the ANN model yielded substantially higher magnitudes compared to the Mogi–Coulomb approach as well as the corresponding horizontal stress measurements.

Table 7.5 Prediction results on mine site D

Data	ANN on σ_H (MPa)	Mogi–Coulomb on σ_H (MPa)	ANN on σ_h (MPa)
1	18.9	11.9	10.1
2	20.2	13.1	10.5
3	22.5	15.8	10.9

7.3 CONCLUSIONS

This chapter provided the procedures to extract breakout information from downhole logging data. The process involves identifying breakout occurrences, extracting the breakout geometries from the travel time data, and estimating rock strength using sonic log or point load tests. The corresponding horizontal stress magnitudes for each breakout data point were either provided by the mine sites or obtained from historical stress measurements in the region.

Based on the extracted breakouts from mine sites B–C, a further evaluation on models proposed in Chapter 6 was carried out. The comparison between three models on σ_H prediction revealed that the Mogi–Coulomb approach provided the most reliable results, whereas the ANN and Kriging models tend to overestimate the magnitudes of σ_H. The reliability of the ANN model for σ_h was also examined. The validation shows that the predictions using the ANN model are also in line with the historical measurements, suggesting this model is capable of estimating σ_h. It is noted that the Kriging model was not examined against all field data due to data file corruption and the horizontal stresses were from the local stress map rather than the measurements at the mine sites. Hence, more field data is required for direct comparisons in the future.

The evaluation of models was also conducted using data from mine site D, where direct stress measurements are available. By combining the data from Chapter 6 and this chapter, the average error rates of the proposed 'ANN–'Mogi–Coulomb' model were 15.05% and 7.62% on σ_h and σ_H, respectively; whereas the average error rate of the ANN model on σ_H against the same dataset is 19.03%. This confirms that the proposed technique is reliable and applicable to multiple field cases.

8 CONCLUSIONS AND RECOMMENDATIONS

The magnitude and orientation of horizontal stresses is one of the most, if not the most, important consideration in the layout and support designs for underground excavations. Due to the increasing depth of cover of mining activities, there is a greater need to obtain reliable horizontal stress magnitudes. However, the conventional estimation methods of hydraulic fracturing and overcoring, struggle to reliably predict horizontal stress magnitudes at these locations at reasonable cost, particularly in weak strata where the rock is likely to be fractured. A new accurate horizontal stress magnitude estimation method is therefore crucial for support design and to minimise production delays due to unexpected rock fall while maintaining the safety of the workforce.

To overcome the limitations of existing stress measurement methods, this study proposed a new estimation technique of horizontal stress magnitudes based on freely accessible borehole breakout data. The technique was developed by a combination of research methods, including experimental studies, numerical simulation, machine learning and constitutive modelling. The back analysis using field data revealed that the proposed approach is capable of providing reliable predictions against other horizontal stress measurement data at no cost, which is of great value to the mining and petroleum industries.

The conclusions and contributions of each chapter are outlined in Section 8.1, and recommendations for future research directions are discussed in Section 8.2.

8.1 CONCLUSIONS AND CONTRIBUTIONS OF THE RESEARCH

8.1.1 Experimental study on borehole breakout and borehole size effect

To closely simulate the true triaxial stress conditions in the field, specially designed laboratory equipment, the UNSW variable confinement cell, was used to conduct breakout tests. Experimental results revealed that the larger and deeper breakouts were observed under a higher horizontal stress ratio (higher σ_H), confirming that they can be used for horizontal stress estimation.

One of the major limitations that prevents the estimation of both horizontal stress magnitudes from borehole breakout data is the absence of a secondary breakout parameter, i.e. breakout depth. This is based on the belief that there is a unique relationship between breakout geometries and this relationship is insensitive to the change in horizontal stress magnitudes (Haimson and Herrick 1989; Haimson et al. 1991; Haimson and Song 1993; Herrick and Haimson 1994; Haimson and Lee 2004; Lee and Haimson 2006; Sahara et al. 2017). However, this conclusion was drawn from experimental observations and lacks theoretical support. An in-depth investigation of breakout geometries based on the famous model proposed by Barton et al. (1988) and existing laboratory data showed that the relationship between the two breakout geometries is in fact not unique and is heavily influenced by horizontal stress magnitudes. Therefore, the findings here suggest it is viable to derive two horizontal stress magnitudes solely from borehole breakout data.

It was also noticed that the breakout geometries not only varied with the horizontal stress magnitudes, but were also influenced by the size of borehole, such that a larger borehole radius (borehole size) resulted in greater breakout geometries under the same stress condition. This phenomenon is the so-called ‘borehole size effect’.However, previous studies (Haimson and Herrick 1989; Carter 1992) on the topic used a constant borehole–specimen ratio (1:5) rather than a constant specimen dimension. This might impact the rock strength of the specimen due to the scale effect, so that the borehole size effect may not be explicitly studied.

Two series of normal compression tests (constant borehole–specimen ratio and constant specimen size) at various borehole sizes were proposed to examine the influence of specimen dimension. Results produced under both constant ratio and constant size were similar. Hence, the experimental results from previous studies are valid and therefore can be used for further breakout study. In addition, this chapter also compared a number of approaches to estimate the breakout initiation stress. The comparative analysis showed that the stress averaging concept was not reliable even considering the effect of radial stress. On the other hand, the linear fracture initiation criterion produced the most accurate results given the validity of the pressure-dependent linear elastic model, although its parameters are dubious and difficult to obtain. An empirical relationship, derived from data in the literature under normal compression tests, also showed promising results in estimating breakout initiation stress. Due to its simplicity and reliability, it was considered for later studies.

8.1.2 *Estimation of maximum horizontal stress magnitude from Kriging*

As breakout depth is a more complex parameter than the angular span due to its sophisticated formation mechanism, a machine learning-based meta-modelling technique, i.e. Kriging, was implemented to estimate σ_H. Based on the analysis of existing laboratory data, three input parameters were determined: normalised breakout depth, breakout angular span and borehole wall strength. The model was generated based on the deterministic mean function and a stationary Gaussian process function derived from 106 data points from published experimental studies. To examine its reliability, a leave-one-out cross validation process was conducted against the published experimental results. The Kriging prediction yielded an average error rate of 10.59% on σ_H. A total of 23 field data were also extracted from both the literature and mine site A with stress measurements available at similar depth. The model provided an average prediction error of 8.4% compared to field stress measurement results on σ_H, which is remarkable considering its simplicity, reliability and low cost.

The scope of this work was limited to the estimation of σ_H due to the nature of the experimental design, in which σ_h and σ_v were kept constant while increasing σ_H. The experimental setup led to the repetition of σ_h in the training data and subsequently resulted in unreliable predictions. Based on the findings here, the later experiments carried out during the research considered the effect of σ_h and σ_v on breakout geometries.

8.1.3 *Numerical simulation on breakout development and borehole size effect*

In experimental conditions, it is not possible to observe the breakout formation process as the rock specimen is sealed inside the loading frame. Hence, Particle Flow Code (PFC) was used to simulate borehole breakouts under various stress combinations. The simulation results are well aligned with the experimental study, such that higher σ_H and larger borehole size will result in larger breakout geometries. This confirms that the horizontal stress magnitudes can be derived from breakout geometries. Based on the geometric changes during the breakout process, it was found that the breakout angular span is constant after the initiation, whereas the breakout depth elongates along the σ_h direction substantially. The results here agree with previous researchers, that the breakout angular span is a more reliable parameter for horizontal stress magnitude estimation.

As PFC is a powerful tool for micro-mechanism investigation, it was also used to study the borehole size effect. Simulation results are also well in line with the experimental observations, in which the larger borehole size can lead to lower breakout initiation stress. PFC was also used to examine the validity of borehole size effect theories since this cannot be conducted in experimental studies. The simulation results indicated that there is some degree of stress averaging due to micro-cracking and the magnitude of radial stress should not be neglected. Interestingly, it was found that the micro-cracking occurred at the borehole wall rather than some distance into the rock. Based on further investigation, the breakout initiation is unlikely to start at some distance from the borehole wall due to the considerably higher radial stress at the location. The findings here do not agree with the pressure-dependent linear elastic model, indicating that the empirical relationship proposed earlier may be appropriate to estimate the breakout initiation stress.

In addition, the numerical simulation incorporated the thermal effect which is widely encountered in deep geothermal wells. Based on the results, higher temperature led to lower breakout initiation stress at the same borehole size, and a higher proportion of shear cracks were generated under higher temperature. This indicates that the temperature might contribute to the micro-fracturing mode and hence influence the horizontal stress estimation results from borehole breakout geometries. Numerical simulation also showed that breakout angular span changed considerably under high stress conditions when the temperature is over 300 °C, suggesting that the temperature influence may need to be considered in stress analysis using borehole breakout in deep geothermal wells. However, this parameter does not need to be taken into account in underground coal mines due to the relatively low temperatures.

8.1.4 Experimental study on combined horizontal stress magnitude estimation from artificial neural network and constitutive modelling

As discussed in Chapter 2, the influences of σ_h and σ_v on breakout geometries have rarely been investigated in experimental conditions. However, they are as equally important as the maximum horizontal stress as the in-situ stress is three-dimensional in the field condition. This research gap was addressed by keeping σ_H constant while changing σ_h or σ_v in proposed breakout tests. Results revealed that both breakout angular span and depth decrease with increasing σ_h or σ_v although the influence of σ_h is more significant. This suggested that the effect of intermediate stress should be considered during stress estimation using borehole breakout data.

Since σ_H can be predicted via Kriging, it is only necessary to estimate the magnitude of σ_h. As breakout angular span is a more reliable parameter for horizontal stress estimation. Hence, analytical investigation on the prediction of σ_h given the value of σ_H and breakout angular span was carried out based on nine failure criteria.

Each constitutive model was examined against 79 laboratory data from the literature and this study. It was found that this approach does not provide reliable estimation of σ_h as it is sensitive to the magnitude of σ_H. On the other hand, the examinations suggested that the Mogi–Coulomb and Stassi D'Alia criteria are capable of predicting σ_H with known σ_h. The average error rates of the two models against the laboratory data were 13.37% and 13.74%, respectively.

To overcome this limitation and estimate both horizontal stress magnitudes, an Artificial Neural Network (ANN) model was introduced to estimate σ_h. The ANN model developed was based on the 79 laboratory data with the use of interaction terms. Once the model was constructed, it was independently validated against 23 field data collected in Chapter 4. The ANN model yielded an acceptable average error rate of 15.88% on σ_h prediction.

To determine the most reliable technique for σ_H estimation, a comparison analysis was carried out on Mogi–Coulomb, Stassi D'Alia, Kriging and ANN models. Results revealed that the Mogi–Coulomb failure criterion is the most reliable approach for σ_H estimation against 23 field data, with an average error rate of 6.82%, whereas Stassi D'Alia yielded average error rates from 13.13% to 14.81% depending on the ratio between uniaxial compressive strength and tensile strength. In addition, the ANN model on σ_H estimation had an average error rate of 13.89%. Based on the comparison, the Mogi–Coulomb (6.82%) approach and the Kriging (8.4%) model provided the most accurate estimation results. However, borehole breakout is subject to creeping behaviour, such that its depth might be elongated with time. This might result in misleading estimation of the Kriging model on σ_H. Therefore, the 'ANN'–'Mogi–Coulomb' model is the most reliable approach to estimate horizontal stress magnitudes from borehole breakout data.

Since the proposed technique uses existing borehole breakout data, it incurs no cost in practice. The phenomenon can also be observed in weak strata where rock experiences high stress concentrations. This is advantageous compared to conventional stress measurements since those techniques require the borehole wall to be elastic. In addition, the model also shows promising results on σ_H estimation and a stress profile can be derived if there are sufficient breakout data in different layers. Hence, the developed technique is a useful and competitive tool for horizontal stress magnitude estimation in underground excavations.

8.1.5 Applicability of the developed models to field cases: additional data collection and validation

To further compare the reliability of proposed techniques, additional field data were acquired from three mine sites B–D. A systematic approach to extract breakout geometries and rock information from borehole imaging and logging data was presented. Since mine sites B and C did not have stress measurement reports near the breakout locations, local stress maps were used for validation. It is noted that the Kriging model was not examined against all field data due to data file corruption, although the model overestimates the magnitude of σ_H in the majority of the cases. The comparison agrees with the comparison in Chapter 6, in which the 'ANN'–'Mogi–Coulomb' approach showed the most promising prediction results against the selected field data.

At mine site D, there were stress measurements available at the nearby breakout locations, such that direct verification could be conducted using the breakout data extracted from the site. By combining the field estimation results together with Chapter 6, the ANN model on σ_H estimation yielded an average error rate of 19.03%. On the other hand, the Mogi–Coulomb model had a rate of 7.62% against the same dataset, and the error rate of the ANN model on σ_h decreased to 15.05%. Therefore, the conclusion drawn from this chapter is in line with that from Chapter 6 that the 'ANN'–'Mogi–Coulomb' approach provides the most accurate prediction results on various field cases.

8.2 RECOMMENDATIONS FOR FUTURE WORK

The findings and contributions of this study are encouraging and present significant value to the mining and petroleum industries considering the reliability, applicability and cost of the proposed horizontal stress measurement technique. Although the model has shown promising prediction results, there is still room for improvement beyond this thesis research. Therefore, a number of recommendations are outlined for future research.

8.2.1 Experimental apparatus modification

An important issue in borehole breakout study is the difficulty of observing the breakout formation process because the rock specimen is sealed when triaxial loading is applied. The technical challenge might be overcome by modifying the current experimental apparatus. It is possible to design a hole at the centre of the loading frame, such that this hole is aligned with the pre-drilled borehole in the rock specimen. With the existence of this opening, a borehole camera could be placed inside the borehole during the experimental stage to record the breakout evolution. A complementary tool, strain gauges, can be mounted at the borehole wall to monitor the breakout propagation. Thereby, the micro-mechanism of breakout development could be studied via CT-scan. This modification is expected to capture breakout evolution and improve knowledge in this research area.

In addition, it is also recommended the capacity of the loading frame is upgraded, so that higher ranges of σ_h and σ_v can be studied.

8.2.2 Further experimental studies

In future research, it is recommended additional laboratory breakout tests are conducted, especially on various σ_h and σ_v combinations using other rock types. This will not only improve the understanding of the effect of σ_h and σ_v on breakout geometries, but also provide data to examine the Mogi–Coulomb model. In addition, the data can be used to enrich the training database of the ANN model, which can in turn improve the reliability of the proposed technique.

8.2.3 3D numerical simulation

As demonstrated in this research, σ_v is a critical parameter for breakout development which should not be ignored. A three-dimensional numerical simulation on breakout should be conducted via PFC3D, to cover a wider range of scenarios given the difficulties in achieving certain specimen conditions in the laboratory. The experiments conducted in this thesis used pre-drilled specimens, whereas the drilling process takes place with the existing in-situ stress in the field. Therefore, it is worth investigating the difference in breakout geometries under pre-drilling and post-drilling conditions. This research can be conducted using numerical simulation.

The time dependency of borehole breakout geometric attributes is a critical topic which should be investigated as it may substantially influence the estimation results. However, due to the equipment capacity and laboratory restrictions, it is difficult to conduct this type of experiment in the laboratory. To explore this phenomenon, the 'stress corrosion' model in PFC3D can be implemented. In this model, the contact bonding strength gradually degrades by removing the contacting material at a specific rate if the contact force is above the pre-defined micro-activation force (Potyondy 2007). Findings based on this simulation may determine whether time is an influential factor that should be considered in breakout analysis.

8.2.4 Machine learning model improvement

Although the proposed ANN model showed an acceptable error rate on field data, it might be possible to increase its prediction accuracy in two ways:

- Expand the existing training database. The 26 field data collected with corresponding horizontal stress measurements can be used as part of the database in conjunction with additional experimental studies. Based on the extended database, the reliability of the proposed ANN model can be further improved. The numerical simulation results might also be considered as part of the training database.
- Implement other machine learning techniques. If the database is sufficiently large, it is worth examining other machine learning techniques on σ_h prediction, such as deep learning.

8.2.5 Field data analysis

Additional field breakout data with horizontal stress measurements can be highly beneficial as some model validations carried out in this thesis were against the local stress maps rather than direct stress measurement. The data can provide more examination of the proposed model while enriching the ANN training database.

8.2.6 Consideration on effect of loading procedures

In experiments, borehole was drilled prior to the loading stage due to the experimental equipment limitation; whereas, borehole was drilled under the in-situ stress state. This might result in some degree of difference in breakout geometries created under both circumstances, although a number of researchers have adopted the same procedures as this study to investigate borehole breakout (Van den Hoek et al., 1994; Cuss et al., 2003; Meier et al., 2013; Duan and Kowk, 2016; Li et al, 2020).

- To examine whether there is any difference of breakout geometries under pre-drilling and post-drilling conditions, it is recommended to carry out the following two analyses: Conduct breakout simulation via PFC3D with pre-drilled and post-drilled cases and compare the numerical results of breakout geometries.
- Upgrade the equipment such that it is capable of drilling the specimen under true tri-axial loading; compare the experimental results of breakout geometries under both scenarios.

REFERENCES

Abdideh M, Mahmoudi N, Moghadasi J, 2014. Geostatistical analysis of the uniaxial compressive strength (UCS) of reservoir rock by petrophysical information. *Energy Sources, Part A: Recovery, Utilization, and Environmental Effects* 36:2320-2327.

Abdulagatova Z, Abdulagatov I, Emirov V, 2009. Effect of temperature and pressure on the thermal conductivity of sandstone. *International Journal of Rock Mechanics and Mining Sciences* 46:1055-1071.

Ageton RW, 1967. Deep mine stress determinations using flatjack and borehole deformation methods, vol 6887. vol Series, 6887, US Department of the Interior, Bureau of Mines.

Al-Ajmi AM, Zimmerman RW, 2005. Relation between the Mogi and the Coulomb failure criteria. *International Journal of Rock Mechanics and Mining Sciences* 42:431-439.

Al Sayed C, Vinches L, Hallé S, 2016. Towards optimizing a personal cooling garment for hot and humid deep mining conditions. *Open Journal of Optimization* 5:35.

Alehossein H, Poulsen BA, 2010. Stress analysis of longwall top coal caving. *International Journal of Rock Mechanics and Mining Sciences* 47:30-41.

Altman DG, Matthews JN, 1996. Statistics notes: interaction 1: heterogeneity of effects. *Bmj* 313:486.

Amadei B, Stephansson O, 1997. Rock stress and its measurement, vol Series, Springer Science & Business Media.

Amari S-i, 1993. Backpropagation and stochastic gradient descent method. *Neurocomputing* 5:185-196.

Amato A, Montone P, Cesaro M, 1995. State of stress in Southern Italy from borehole breakout and focal mechanism data. *Geophysical Research Letters* 22:3119-3122.

Amitrano D, Helmstetter A, 2006. Brittle creep, damage, and time to failure in rocks. *Journal of Geophysical Research: Solid Earth* 111.

Anderson EM, 1951. The dynamics of faulting and dyke formation with applications to Britain, vol Series, Hafner Pub. Co.

Ashby MF, amp, Hallam S, 1986. The failure of brittle solids containing small cracks under compressive stress states. *Acta metallurgica* 34:497-510.

Ask D, 2006. Measurement-related uncertainties in overcoring data at the Äspö HRL, Sweden. Part 2: Biaxial tests of CSIRO HI overcore samples. *International Journal of Rock Mechanics and Mining Sciences* 43:127-138.

Ask MV, Ask D, Elvebakk H, Olesen O, 2015. Stress Analysis in Boreholes Drag Bh and Leknes Bh, Nordland, North Norway. *Rock Mechanics and Rock Engineering* 48:1475-1484.

Azimian A, Ajalloeian R, Fatehi L, 2014. An empirical correlation of uniaxial compressive strength with P-wave velocity and point load strength index on marly rocks using statistical method. *Geotechnical and Geological Engineering* 32:205-214.

Babcock E, 1978. Measurement of subsurface fractures from dipmeter logs. *AAPG Bulletin* 62:1111-1126.

Bahaaddini M, Sharrock G, Hebblewhite B, 2013. Numerical direct shear tests to model the shear behaviour of rock joints. *Computers and Geotechnics* 51:101-115.

Bahaaddini M, Sheikhpourkhani AM, Mansouri H, 2019. Flat-joint model to reproduce the mechanical behaviour of intact rocks. *European Journal of Environmental and Civil Engineering* 1-22.

Bankwitz P, Bankwitz E, 1997. Fractographic features on joints in KTB drill cores as indicators of the contemporary stress orientation. *Geologische Rundschau* 86:S34-S44.

Barton CA, Zoback MD, Burns KL, 1988. In‐situ stress orientation and magnitude at the Fenton Geothermal Site, New Mexico, determined from wellbore breakouts. *Geophysical Research Letters* 15:467-470.

Bashir Z, El-Hawary M, 2009. Applying wavelets to short-term load forecasting using PSO-based neural networks. *IEEE transactions on power systems* 24:20-27.

Bažant ZP, 1984. Size effect in blunt fracture: concrete, rock, metal. *Journal of engineering mechanics* 110:518-535.

Bažant ZP, Lin FB, Lippmann H, 1993. Fracture energy release and size effect in borehole breakout. *International Journal for Numerical and Analytical Methods in Geomechanics* 17:1-14.

Bažant ZP, Xi Y, 1991. Statistical size effect in quasi-brittle structures: II. Nonlocal theory. *Journal of Engineering Mechanics* 117:2623-2640.

Bažant ZP, Yavari A, 2005. Is the cause of size effect on structural strength fractal or energetic–statistical? *Engineering fracture mechanics* 72:1-31.

Becker A, Werner D, 1994. Strain measurements with the borehole slotter. *Terra Nova* 6:608-617.

Bell J, Gough D, 1979. Northeast-southwest compressive stress in Alberta evidence from oil wells. *Earth and planetary science letters* 45:475-482.

Bigg GR, 1991. Kriging and intraregional rainfall variability in England. *International Journal of Climatology* 11:663-675.

Bock H, Foruria V, A recoverable borehole slotting instrument for in-situ stress measurements in rock not requiring overcoring, In: *International Symposium on Field Measurement in Geomechanics, Zurich*. pp 15-29.

Bock HF, 1993. Measuring in situ rock stress by borehole slotting, In: Rock Testing and Site Characterization, Elsevier, pp 433-443.

Brace W, Kohlstedt D, 1980. Limits on lithospheric stress imposed by laboratory experiments. *Journal of Geophysical Research: Solid Earth* 85:6248-6252.

Bradley W, 1979. Failure of inclined boreholes. *Journal of Energy Resources Technology* 101:232-239.

Bredehoeft J, Wolff R, Keys W, Shuter E, 1976. Hydraulic fracturing to determine the regional in situ stress field, Piceance Basin, Colorado. *Geological Society of America Bulletin* 87:250-258.

Broding R, Volumetric scanning well logging, In: *SPWLA 22nd Annual Logging Symposium*. Society of Petrophysicists and Well-Log Analysts.

Brudy M, 1995. Determination of in situ stress magnitude and orientation to 9 km depth at the KTB site. *thesis*, Verlag nicht ermittelbar.

Brudy M, Zoback M, 1999. Drilling-induced tensile wall-fractures: implications for determination of in-situ stress orientation and magnitude. *International Journal of Rock Mechanics and Mining Sciences* 36:191-215.

Brudy M, Zoback M, Fuchs K, Rummel F, Baumgärtner J, 1997. Estimation of the complete stress tensor to 8 km depth in the KTB scientific drill holes: Implications for crustal strength. *Journal of Geophysical Research: Solid Earth* 102:18453-18475.

Byerlee J, 1978. Friction of rocks, In: Rock friction and earthquake prediction, Springer, pp 615-626.

Cai M, Blackwood R, Performance of the USBM borehole deformation gage in different rock conditions, In: *The 28th US Symposium on Rock Mechanics (USRMS)*. American Rock Mechanics Association.

Cai M, Thomas L, A comparison of the USBM gage and the CSIRO cell in various rock conditions, In: *The 32nd US Symposium on Rock Mechanics (USRMS)*. American Rock Mechanics Association.

Carter B, 1992. Size and stress gradient effects on fracture around cavities. *Rock Mechanics and Rock Engineering* 25:167-186.

Carter B, Lajtai E, Petukhov A, 1991. Primary and remote fracture around underground cavities. *International Journal for Numerical and Analytical Methods in Geomechanics* 15:21-40.

Carter BJ, Lajtai EZ, Yuan Y, 1992. Tensile fracture from circular cavities loaded in compression. *International journal of fracture* 57:221-236.

Chang C, McNeill LC, Moore JC, Lin W, Conin M, Yamada Y, 2010. In situ stress state in the Nankai accretionary wedge estimated from borehole wall failures. *Geochemistry, Geophysics, Geosystems* 11.

Chang C, Zoback MD, Khaksar A, 2006. Empirical relations between rock strength and physical properties in sedimentary rocks. *Journal of Petroleum Science and Engineering* 51:223-237.

Chen DS, Jain RC, 1994. A robust backpropagation learning algorithm for function approximation. *IEEE Transactions on Neural Networks* 5:467-479.

Chen Q, Zhu B, Hu H, 2006. Experimental research on measurement of in-situ stress field by Kaiser effect. *Yanshilixue Yu Gongcheng Xuebao/Chinese Journal of Rock Mechanics and Engineering* 25:1370-1376.

Chen Y-Y, Lin Y-H, Kung C-C, Chung M-H, Yen I, 2019. Design and implementation of cloud analytics-assisted smart power meters considering advanced artificial intelligence as edge analytics in demand-side management for smart homes. *Sensors* 19:2047.

Choens RC, Ingraham MD, Lee MY, Yoon H, Dewers T, 2018. Acoustic Emission during Borehole Breakout, In: *52nd US Rock Mechanics/Geomechanics Symposium*. American Rock Mechanics Association.

Choi J-Y, Lee C-I, 2007. An estimation of rock mass rating using 3D indicator kriging approach with uncertainty assessment of rock mass classification, In: *11th ISRM Congress*. International Society for Rock Mechanics and Rock Engineering.

Chou J-S, Thedja JPP, 2016. Metaheuristic optimization within machine learning-based classification system for early warnings related to geotechnical problems. *Automation in Construction* 68:65-80.

Clifton R, Simonson E, Jones A, Green S, 1976. Determination of the critical-stress-intensity factor K Ic from internally pressurized thick-walled vessels. *Experimental Mechanics* 16:233-238.

Coetzer S, 1997. Conceptual development of a method to determine the principal stresses around coal mine workings to ensure safe mine design.

Cornet F, Valette B, 1984. In situ stress determination from hydraulic injection test data. *Journal of Geophysical Research: Solid Earth* 89:11527-11537.

Cornet FH, 1993. Stresses in rock and rock masses. *Comprehensive rock engineering* 3:297-327.

Cox JW, 1970. The high resolution dipmeter reveals dip-related borehole and formation characteristics, In: *SPWLA 11th Annual Logging Symposium*. Society of Petrophysicists and Well-Log Analysts.

Crook T, Willson S, Yu JG, Owen R, 2003. Computational modelling of the localized deformation associated with borehole breakout in quasi-brittle materials. *Journal of Petroleum Science and Engineering* 38:177-186.

Cuss R, Rutter E, Holloway R, 2003. Experimental observations of the mechanics of borehole failure in porous sandstone. *International Journal of Rock Mechanics and Mining Sciences* 40:747-761.

Dougherty M, 1995. A review of neural networks applied to transport. *Transportation Research Part C: Emerging Technologies* 3:247-260.

Dresen G, Stanchits S, Rybacki E, 2010. Borehole breakout evolution through acoustic emission location analysis. *International Journal of Rock Mechanics and Mining Sciences* 47:426-435.

Drucker DC, Prager W, 1952. Soil mechanics and plastic analysis or limit design. *Quarterly of applied mathematics* 10:157-165.

Du W, 1997. Numerical modeling of mixed mode multiple crack propagation and its application to the simulation of nonlinear rock deformation and borehole breakout.

Duan K, Kwok C, 2016. Evolution of stress - induced borehole breakout in inherently anisotropic rock: Insights from discrete element modeling. *Journal of Geophysical Research: Solid Earth* 121:2361-2381.

Dyke C, 1989. Core discing: Its potential as an indicator of principal in situ stress directions, In: *ISRM International Symposium*. International Society for Rock Mechanics.

Dzik E, Lajtai E, 1996. Primary fracture propagation from circular cavities loaded in compression. *International journal of fracture* 79:49-64.

Elkadi A, Van Mier J, 2006. Experimental investigation of size effect in concrete fracture under multiaxial compression. *International journal of fracture* 140:55.

Entwisle D, Hobbs P, Jones L, Gunn D, Raines M, 2005. The relationships between effective porosity, uniaxial compressive strength and sonic velocity of intact Borrowdale Volcanic Group core samples from Sellafield. *Geotechnical & Geological Engineering* 23:793-809.

Esfe MH, Goodarzi M, Reiszadeh M, Afrand M, 2019. Evaluation of MWCNTs-ZnO/5W50 nanolubricant by design of an artificial neural network for predicting viscosity and its optimization. *Journal of Molecular Liquids* 277:921-931.

Eshelby JD, 1957. The determination of the elastic field of an ellipsoidal inclusion, and related problems. *Proc R Soc Lond A* 241:376-396.

Etchecopar A, Yamada T, Cheung P, 2013. Borehole images for assessing present day stresses. *Bulletin de la Société Géologique de France* 184:307-318.

Ewy R, 1999. Wellbore-stability predictions by use of a modified Lade criterion. *SPE Drilling & Completion* 14:85-91.

Ewy R, Cook N, 1989. Fracture processes around highly stressed boreholes, In: *Proc. Drilling Symp. at ETCE*. ASME Houston, TX, pp 63-70.

Faiella D, Manfredini G, Rossi PP, 1983. In situ flat jack tests: analysis of results and critical assessment, vol Series, ISMES.

Fairhurst C, 2003. Stress estimation in rock: a brief history and review. *International Journal of Rock Mechanics and Mining Sciences* 40:957-973.

Fakhimi A, Carvalho F, Ishida T, Labuz JF, 2002. Simulation of failure around a circular opening in rock. *International Journal of Rock Mechanics and Mining Sciences* 39:507-515.

Faraguna J, Chance D, Schmidt M, An improved borehole televiewer system: image acquisition, analysis and integration, In: *SPWLA 30th Annual Logging Symposium*. Society of Petrophysicists and Well-Log Analysts.

Fjar E, Holt RM, Raaen A, Risnes R, Horsrud P, 2008. Petroleum related rock mechanics, vol Series, Elsevier.

Fowler M, Weir F, 2007. The use of borehole breakouts for geotechnical investigation of an open pit mine. *Proc of the 1st SHIRMS* .

Freudenthal AM, 1977. Stresses around spherical and cylindrical cavities in shear dilatant elastic media, In: *The 18th US Symposium on Rock Mechanics (USRMS)*. American Rock Mechanics Association.

Gaines S, Diederichs M, Hutchinson D, 2012. Review of borehole in situ stress measurement techniques for various ground conditions and numerical stress estimation considerations, In: *46th US Rock Mechanics/Geomechanics Symposium*. American Rock Mechanics Association.

Gallagher Jr J, Friedman M, Handin J, Sowers G, 1974. Experimental studies relating to microfracture in sandstone. *Tectonophysics* 21:203-247.

Galvin J, 2016. Ground engineering-principles and practices for underground coal mining, vol Series, Springer.

Gholami A, Bonakdari H, Fenjan SA, Akhtari AA, 2016. Flow variables prediction using experimental, computational fluid dynamic and artificial neural network models in a sharp bend. *International Journal of Engineering* 29:14-22.

Gough D, Bell J, 1981. Stress orientations from oil-well fractures in Alberta and Texas. *Canadian Journal of Earth Sciences* 18:638-645.

Gough D, Bell J, 1982. Stress orientations from borehole wall fractures with examples from Colorado, east Texas, and northern Canada. *Canadian Journal of Earth Sciences* 19:1358-1370.

Gray I, 2003. Report to simrac demonstration of overcore stress measurement from surface using the sigra ist tool, Sigra Pty. Ltd.

Gray I, See L, 2007. The measurement and interpretation of in-situ stress using an overcoring technique from surface, In: *1st Canada-US Rock Mechanics Symposium*. American Rock Mechanics Association,

Gregorczyk P, Lourenço PB, 2000. A review on flat-jack testing.

Griffith AA, 1921. VI. The phenomena of rupture and flow in solids. *Philosophical transactions of the royal society of london Series A, containing papers of a mathematical or physical character* 221:163-198.

Guenot A, 1989. Borehole breakouts and stress fields: Int J Rock Mech Min Sci V26, N3/4, July 1989, P185–195, In: *International Journal of Rock Mechanics and Mining Sciences & Geomechanics Abstracts*, vol 2. Pergamon, p A118.

Guo Z, Zhao W, Lu H, Wang J, 2012. Multi-step forecasting for wind speed using a modified EMD-based artificial neural network model. *Renewable Energy* 37:241-249.

Gürtunca R, 2018. Mining below 3000m and challenges for the South African gold mining industry, In: *Mechanics of Jointed and Faulted Rock*. Routledge, pp 3-10.

Haimson B, 1995. Estimation in situ stress conditions from borehole breakout and core disking experimental results in granite, In: *Proc. Int. Workshop on Rock Stress Measurement at Depth, 1995*. pp 19-24.

Haimson B, 2001. Fracture-like borehole breakouts in high-porosity sandstone: Are they caused by compaction bands? *Physics and Chemistry of the Earth, Part A: Solid Earth and Geodesy* 26:15-20.

Haimson B, 2007. Micromechanisms of borehole instability leading to breakouts in rocks. *International Journal of Rock Mechanics and Mining Sciences* 44:157-173.

Haimson B, Cornet F, 2003. ISRM Suggested Methods for rock stress estimation Part 3: hydraulic fracturing (HF) and/or hydraulic testing of pre-existing fractures (HTPF). *International Journal of Rock Mechanics and Mining Sciences* 40:1011-1020.10.1016/j.ijrmms.2003.08.002.

Haimson B, Herrick C, 1989. Borehole breakouts and in situ stress, In: *12th annual energy-sources technology conference and exhibition, Houston, New York, 1989*. American Society of Mechanical Engineers, pp 17-22.

Haimson B, Kovacich J, 2003. Borehole instability in high-porosity Berea sandstone and factors affecting dimensions and shape of fracture-like breakouts. *Engineering Geology* 69:219-231.

Haimson B, Lee H, 2004. Borehole breakouts and compaction bands in two high-porosity sandstones. *International Journal of Rock Mechanics and Mining Sciences* 41:287-301.

Haimson B, Lee M, Herrick C, 1991. Recent advances in in-situ stress measurements by hydraulic fracturing and borehole breakouts, In: *7th ISRM Congress*. International Society for Rock Mechanics.

Haimson B, Song I, 2002. Laboratory study of borehole breakouts in Cordova Cream: a case of shear failure mechanism, In: *International journal of rock mechanics and mining sciences & geomechanics abstracts*, vol 7. Elsevier, pp 1047-1056.

Haimson BC, Chang C, 2002. True triaxial strength of the KTB amphibolite under borehole wall conditions and its use to estimate the maximum horizontal in situ stress. *Journal of Geophysical Research: Solid Earth* 107:ETG 15-11-ETG 15-14.

Haimson BC, Song I, 1995. A new borehole failure criterion for estimating in situ stress from breakout span, In: *8th ISRM Congress*. International Society for Rock Mechanics.

Haimson BC, Song I, 1998. Borehole breakouts in Berea sandstone: two porosity-dependent distinct shapes and mechanisms of formation, In: *SPE/ISRM Rock Mechanics in Petroleum Engineering*. Society of Petroleum Engineers.

Haimson H, Herrick C, 1986. Borehole breakouts-a new tool for estimating in situ stress?, In: *ISRM International Symposium*. International Society for Rock Mechanics.

Hakala M, Hudson J, Christiansson R, 2003. Quality control of overcoring stress measurement data. *International Journal of Rock Mechanics and Mining Sciences* 40:1141-1159.

Hampson DP, Schuelke JS, Quirein JA, 2001. Use of multiattribute transforms to predict log properties from seismic data. *Geophysics* 66:220-236.

He M-c, 2009. Application of HEMS cooling technology in deep mine heat hazard control. *Mining Science and Technology (China)* 19:269-275.

Herrick CG, Haimson BC, Modeling of episodic failure leading to borehole breakouts in Alabama limestone, In: *1st North American Rock Mechanics Symposium*. American Rock Mechanics Association.

Heuze F, 1983. High-temperature mechanical, physical and thermal properties of granitic rocks—a review, In: *International Journal of Rock Mechanics and Mining Sciences & Geomechanics Abstracts*, vol 1. Elsevier, pp 3-10.

Hickman SH, Svitek JF, Langseth MG, Observatory L-DG, 1984. 7. Borehole televiewer log of hole 395A1.

Hillis R, Enever J, Reynolds S, 1999. In situ stress field of eastern Australia. *Australian Journal of Earth Sciences* 46:813-825.

Hoek E, Diederichs MS, 2006. Empirical estimation of rock mass modulus. *International journal of rock mechanics and mining sciences* 43:203-215.

Hubbert MK, Willis DG, 1957. Mechanics of hydraulic fracturing. *Am Assoc Pet Geol Bulletin* 18:153-168.

Huffman K, Saffer D, 2016. In situ stress magnitudes at the toe of the Nankai Trough Accretionary Prism, offshore Shikoku Island, Japan. *Journal of Geophysical Research: Solid Earth* 121:1202-1217.

Hung J-H, Ma K-F, Wang C-Y, Ito H, Lin W, Yeh E-C, 2009. Subsurface structure, physical properties, fault-zone characteristics and stress state in scientific drill holes of Taiwan Chelungpu Fault Drilling Project. *Tectonophysics* 466:307-321.https://doi.org/10.1016/j.tecto.2007.11.014.

Hunt DD, 1973. The influence of confining pressure on size effect. *thesis*, Massachusetts Institute of Technology.

Ikeuchi K, Doi N, Sakagawa Y, Kamenosono H, Uchida T, 1998. High-temperature measurements in well WD-1a and the thermal structure of the Kakkonda geothermal system, Japan. *Geothermics* 27:591-607.

Ingraffea A, 1979. The strength ratio effect in the fracture of rock structures, In: *20th US Symposium on Rock Mechanics (USRMS)*. American Rock Mechanics Association.

Isaaks EH, Srivastava RM, 1989. An introduction to applied geostatistics, Oxford university press.

Ishida T, Saito T, 1995. Observation of core discing and in situ stress measurements; stress criteria causing core discing. *Rock mechanics and rock engineering* 28:167-182.

Itasca, 2018. PFC 5.0 Documentation.

Jaeger J, Cook N, 1963. Pinching‐off and disking of rocks. *Journal of Geophysical Research* 68:1759-1765.

Jaeger J, Cook N, 1964. Theory and application of curved jacks for measurement of stresses, In: State of Stress in the Earth's Crust, Elsevier NY, pp 381-395.

Jaeger JC, Cook NG, Zimmerman R, 2009. Fundamentals of rock mechanics, vol Series, John Wiley & Sons.

Jones DR, Schonlau M, Welch WJ, 1998. Efficient global optimization of expensive black-box functions. *Journal of Global optimization* 13:455-492.

Kaga N, Matsuki K, Sakaguchi K, 2003. The in situ stress states associated with core discing estimated by analysis of principal tensile stress. *International Journal of Rock Mechanics and Mining Sciences* 40:653-665.

Kaiser J, 1953. Erkenntnisse und Folgerungen aus der Messung von Geräuschen bei Zugbeanspruchung von metallischen Werkstoffen. *Archiv für das Eisenhüttenwesen* 24:43-45.

Kanagawa T, Ashi MH, Kitahara Y, 1981. Acoustic emission and over coring methods for measuring tectonic stresses, In: *ISRM International Symposium*. International Society for Rock Mechanics and Rock Engineering.

Kapageridis IK, 2002. Artificial neural network technology in mining and environmental applications. *Mine Planning and Equipment Selection* 172-179.

Katsman R, Aharonov E, Haimson B, 2009. Compaction bands induced by borehole drilling. *Acta Geotechnica* 4:151-162.

Katsman R, Haimson B, 2011. Modelling partially-emptied compaction bands induced by borehole drilling. *Journal of Structural Geology* 33:690-697.

Kavur B, Cvitanović NŠ, Hrženjak P, 2015. Comparison between plate jacking and large flat jack test results of rock mass deformation modulus. *International Journal of Rock Mechanics and Mining Sciences* 73:102-114.

Kaymaz I, 2005. Application of kriging method to structural reliability problems. *Structural Safety* 27:133-151.

Keshavarz M, Pellet F, Loret B, 2010. Damage and changes in mechanical properties of a gabbro thermally loaded up to 1,000 C. *Pure and Applied Geophysics* 167:1511-1523.

Kessels W, 1989. Observation and interpretation of time-dependent behaviour of boreholes stability in the continental deep drilling pilot borehole, In: *ISRM International Symposium*. International Society for Rock Mechanics.

Khandelwal M, Monjezi M, 2013. Prediction of backbreak in open-pit blasting operations using the machine learning method. *Rock mechanics and rock engineering* 46:389-396.

Khosravi A, Nahavandi S, Creighton D, Atiya AF, 2011. Comprehensive review of neural network-based prediction intervals and new advances. *IEEE Transactions on neural networks* 22:1341-1356.

Kim H, Xie L, Min K-B, Bae S, Stephansson O, 2017. Integrated In Situ Stress Estimation by Hydraulic Fracturing, Borehole Observations and Numerical Analysis at the EXP-1 Borehole in Pohang, Korea. *Rock Mechanics and Rock Engineering* 50:3141-3155.

KIM K, 1993. Design, execution and analysis of a large-scale in situ thermomechanical test for siting high-level nuclear waste repository, In: Rock Testing and Site Characterization, Elsevier, pp 881-913.

Kirk SS, Williamson DM, Structure and thermal properties of porous geological materials, In: *American Institute of Physics Conference Series*. pp 867-870.

Kirsch EG, 1898. Die Theorie der Elastizit t und die Bed rfnisse der Festigkeitslehre. *Zeitshrift des Vereines deutscher Ingenieure* 42:797-807.

Klee G, Bunger A, Meyer G, Rummel F, Shen B, 2011. In situ stresses in borehole Blanche-1/South Australia derived from breakouts, core discing and hydraulic fracturing to 2 km depth. *Rock mechanics and rock engineering* 44:531-540.

Klein E, Reuschlé T, 2003. A model for the mechanical behaviour of Bentheim sandstone in the brittle regime. *pure and applied geophysics* 160:833-849.

Koehler J, Owen A, 1996. Computer experiments. *Handbook of statistics* 13:261-308.

Krige DG, 1951. A statistical approach to some basic mine valuation problems on the Witwatersrand. *Journal of the Southern African Institute of Mining and Metallurgy* 52:119-139.

Kurita K, Fujii N, 1979. Stress memory of crystalline rocks in acoustic emission. *Geophysical Research Letters* 6:9-12.

Kwong A, Kaiser P, Stability of tunnels in rock with localized weaknesses, In: *Proceedings of the international congress on progress innovation in tunneling*. pp 341-358.

Labuz J, Shah SP, Dowding C, 1985. Experimental analysis of crack propagation in granite, In: *International Journal of Rock Mechanics and Mining Sciences & Geomechanics Abstracts*, vol 2. Elsevier, pp 85-98.

Lade PV, 1977. Elasto-plastic stress-strain theory for cohesionless soil with curved yield surfaces. *International Journal of Solids and Structures* 13:1019-1035.

Lajtai E, 1972. Effect of tensile stress gradient on brittle fracture initiation, In: *International Journal of Rock Mechanics and Mining Sciences & Geomechanics Abstracts*, vol 5. Elsevier, pp 569-578.

Lakirouhani A, Detournay E, Bunger A, 2016. A reassessment of in situ stress determination by hydraulic fracturing. *Geophysical Journal International* 205:1859-1873.

Lavrov A, 2003. The Kaiser effect in rocks: principles and stress estimation techniques. *International Journal of Rock Mechanics and Mining Sciences* 40:151-171.

Lee H, Haimson B, 2006. Borehole breakouts and in-situ stress in sandstones, In: *In-Situ Rock Stress: International Symposium on In-Situ Rock Stress, Trondheim, Norway, 19-21 June 2006*. CRC Press, p 201

Lee H, Moon T, Haimson B, 2016. Borehole breakouts induced in arkosic sandstones and a discrete element analysis. *Rock Mechanics and Rock Engineering* 49:1369-1388.

Lee H, Ong SH, 2018. Estimation of In Situ Stresses with Hydro-Fracturing Tests and a Statistical Method. *Rock Mechanics and Rock Engineering* 51:779-799.

Lee M, Haimson B, 1993. Laboratory study of borehole breakouts in Lac du Bonnet granite: a case of extensile failure mechanism, In: *International journal of rock mechanics and mining sciences & geomechanics abstracts*, vol 7. Elsevier, pp 1039-1045.

Leeman E, 1967. The borehole deformation type of rock stress measuring instrument, In: *International Journal of Rock Mechanics and Mining Sciences & Geomechanics Abstracts*, vol 1. Elsevier, pp 23-44.

Lehtonen A, Cosgrove J, Hudson J, Johansson E, 2012. An examination of in situ rock stress estimation using the Kaiser effect. *Engineering Geology* 124:24-37.

Leriche A, 2017. Stress estimation from borehole scans for prediction of excavation overbreak in brittle rock. degree of Master of Applied Science *thesis*, Queen's University.

LeRiche A, Kalenchuk K, Diederichs M, 2017. Estimation of in situ stress from borehole breakout for improved understanding of excavation overbreak in brittle-anisotropic rock.

Li L, Cornet F, 2004. Three dimensional consideration of flat jack tests. *International Journal of Rock Mechanics and Mining Sciences* 41:255-260.

Li L, Papamichos E, Cerasi P, 2006. Investigation of sand production mechanisms using DEM with fluid flow. *Multiphysics Coupling and Long Term Behaviour in Rock Mechanics* 1:241-247.

Li X, Jaffal H, Feng Y, El Mohtar C, Gray K, 2018. Wellbore breakouts: Mohr-Coulomb plastic rock deformation, fluid seepage, and time-dependent mudcake buildup. *Journal of Natural Gas Science and Engineering* 52:515-528.

Lim S, Martin C, 2010. Core disking and its relationship with stress magnitude for Lac du Bonnet granite. *International Journal of Rock Mechanics and Mining Sciences* 47:254-264.

Lin H, Kang W-H, Oh J, Canbulat I, 2020. Estimation of in-situ maximum horizontal principal stress magnitudes from borehole breakout data using machine learning. *International Journal of Rock Mechanics and Mining Sciences* 126:104199.

Lin H, Oh J, Canbulat I, Stacey T, 2019. Experimental and Analytical Investigations of the Effect of Hole Size on Borehole Breakout Geometries for Estimation of In Situ Stresses. *Rock Mechanics and Rock Engineering* 1-18.

Lin W, 2014. Constraining the magnitudes of maximum and minimum horizontal stresses from borehole breakouts–A comparison between different rock failure criteria, In: *ISRM Regional Symposium-EUROCK 2014*. International Society for Rock Mechanics and Rock Engineering.

Lin W et al., 2010. Present‐day principal horizontal stress orientations in the Kumano forearc basin of the southwest Japan subduction zone determined from IODP NanTroSEIZE drilling Site C0009. *Geophysical Research Letters* 37.

Liu H, Kou S, Lindqvist P-A, Tang C, 2002. Numerical simulation of the rock fragmentation process induced by indenters. *International Journal of Rock Mechanics and Mining Sciences* 39:491-505.

Liu Y, Zhou J, Wu S-C, 2007. Micro-numerical simulation of cyclic biaxial test I: results of loose sand [J]. *Chinese Journal of Geotechnical Engineering* 7.

Ljunggren C, Chang Y, Janson T, Christiansson R, 2003. An overview of rock stress measurement methods. *International Journal of Rock Mechanics and Mining Sciences* 40:975-989.

Lophaven SN, Nielsen HB, Søndergaard J, 2002. DACE: a Matlab kriging toolbox, vol 2. vol Series, 2, Citeseer.

Lotidis MA, Nomikos PP, Sofianos AI, 2017. Numerical Simulation of Granite Plates Containing a Cylindrical Opening in Compression. *Procedia Engineering* 191:242-247.

Lu J, Elgamal A, Yan L, Law KH, Conte JP, 2011. Large-scale numerical modeling in geotechnical earthquake engineering. *International Journal of Geomechanics* 11:490-503.

Lund B, Zoback M, 1999. Orientation and magnitude of in situ stress to 6.5 km depth in the Baltic Shield. *International Journal of Rock Mechanics and Mining Sciences* 36:169-190.

MacGregor S, 2003. Maximising In-Situ Stress Measurement Data from Borehole Breakout using Acoustic Scanner and Wireline Tools, ACARP,

Malinverno A, Saito S, Vannucchi P, 2016. Horizontal principal stress orientation in the Costa Rica Seismogenesis Project (CRISP) transect from borehole breakouts. *Geochemistry, Geophysics, Geosystems* 17:65-77.

Maloney S, Kaiser P, 1989. Results of borehole breakout simulation tests, In: *ISRM International Symposium*. International Society for Rock Mechanics and Rock Engineering.

Mansourizadeh M, Jamshidian M, Bazargan P, Mohammadzadeh O, 2016. Wellbore stability analysis and breakout pressure prediction in vertical and deviated boreholes using failure criteria–A case study. *Journal of Petroleum Science and Engineering* 145:482-492.

Martin CD, 1997. Seventeenth Canadian geotechnical colloquium: the effect of cohesion loss and stress path on brittle rock strength. *Canadian Geotechnical Journal* 34:698-725.

Mastin LG, 1984. An analysis of stress-induced elongation of boreholes at depth. *thesis*, MS thesis, Stanford Univ., Stanford, Calif.

Matheron G, 1973. The intrinsic random functions and their applications. *Advances in applied probability* 5:439-468.

Matsuki K, Kaga N, Yokoyama T, Tsuda N, 2004. Determination of three dimensional in situ stress from core discing based on analysis of principal tensile stress. *International Journal of Rock Mechanics and Mining Sciences* 41:1167-1190.

Matthews JN, Altman DG, 1996. Statistics Notes: Interaction 2: compare effect sizes not P values. *BmJ* 313:808.

Mayer A, Habib P, 1951. Marchand R, Mesure en place des pressions de terrains, In: *Proc. Conf. Int. sur les Pressions deTerrains et le Soutènement dans les Chantiers d'Exploration, Liège*. pp 217-221.

McClelland JL, Rumelhart DE, 1988. Training hidden units. *Explorations in parallel distributed processing* 121-160.

McLean M, Addis M, 1990. Wellbore stability: the effect of strength criteria on mud weight recommendations, In: *SPE annual technical conference and exhibition*. Society of Petroleum Engineers.

McNally G, 1987. Estimation of coal measures rock strength using sonic and neutron logs. *Geoexploration* 24:381-395.

Meier T, Rybacki E, Reinicke A, Dresen G, 2013. Influence of borehole diameter on the formation of borehole breakouts in black shale. *International Journal of Rock Mechanics and Mining Sciences* 62:74-85.

Mia M, Dhar NR, 2016. Prediction of surface roughness in hard turning under high pressure coolant using Artificial Neural Network. *Measurement* 92:464-474.

Mises Rv, 1913. Mechanik der festen Körper im plastisch-deformablen Zustand. *Nachrichten von der Gesellschaft der Wissenschaften zu Göttingen, Mathematisch-Physikalische Klasse* 1913:582-592.

Mo S, 2019. Floor heave mechanisms in underground coal mine roadways. Doctor of Philosophy *thesis*, UNSW Sydney.

Mogi K, 1967. Effect of the intermediate principal stress on rock failure. *Journal of Geophysical Research* 72:5117-5131.

Mogi K, 1971. Fracture and flow of rocks under high triaxial compression. *Journal of Geophysical Research* 76:1255-1269.

Molaghab A, Taherynia MH, Aghda SMF, Fahimifar A, 2017. Determination of minimum and maximum stress profiles using wellbore failure evidences: a case study—a deep oil well in the southwest of Iran. *Journal of Petroleum Exploration and Production Technology* 7:707-715.

Mollema P, Antonellini M, 1996. Compaction bands: a structural analog for anti-mode I cracks in aeolian sandstone. *Tectonophysics* 267:209-228.

Møller MF, 1990. A scaled conjugate gradient algorithm for fast supervised learning, vol Series, Aarhus University, Computer Science Department,

Moon HS, Ok S, Chun P-j, Lim YM, 2019. Artificial Neural Network for Vertical Displacement Prediction of a Bridge from Strains (Part 1): Girder Bridge under Moving Vehicles. *Applied Sciences* 9:2881.

Moos D, Zoback MD, 1990. Utilization of observations of well bore failure to constrain the orientation and magnitude of crustal stresses: application to continental, Deep Sea Drilling Project, and Ocean Drilling Program boreholes. *Journal of Geophysical Research: Solid Earth* 95:9305-9325.

Murrell S, 1963. A criterion for brittle fracture of rocks and concrete under triaxial stress and the effect of pore pressure on the criterion. *Rock mechanics* 563-577.

Nelson E, Meyer J, Hillis R, Mildren S, 2005. Transverse drilling-induced tensile fractures in the West Tuna area, Gippsland Basin, Australia: implications for the in situ stress regime. *International Journal of Rock Mechanics and Mining Sciences* 42:361-371.

Nesetova V, Lajtai E, 1973. Fracture from compressive stress concentrations around elastic flaws, In: *International Journal of Rock Mechanics and Mining Sciences & Geomechanics Abstracts*, vol 4. Elsevier, pp 265-284

Nguyen H, Drebenstedt C, Bui X-N, Bui DT, 2019. Prediction of blast-induced ground vibration in an open-pit mine by a novel hybrid model based on clustering and artificial neural network. *Natural Resources Research* 1-19.

Nian T, Wang G, Xiao C, Zhou L, Deng L, Li R, 2016. The in situ stress determination from borehole image logs in the Kuqa Depression. *Journal of Natural Gas Science and Engineering* 34:1077-1084.

Nickless E, 2016. Resourcing future generations: a global effort to meet the world's future needs head-on. *Eur Geol* 42:46-50.

Obert L, Stephenson D, 1965. Stress conditions under which core discing occurs. *Society of Mining Engineers of AIME Transactions* 232:227-235.

Ocak I, Seker SE, 2012. Estimation of elastic modulus of intact rocks by artificial neural network. *Rock mechanics and rock engineering* 45:1047-1054.

Oettl G, Stark R, Hofstetter G, 2004. Numerical simulation of geotechnical problems based on a multi-phase finite element approach. *Computers and Geotechnics* 31:643-664.

Olsson WA, 1999. Theoretical and experimental investigation of compaction bands in porous rock. *Journal of Geophysical Research: Solid Earth* 104:7219-7228.

Ortiz M, 1988. Microcrack coalescence and macroscopic crack growth initiation in brittle solids. *International Journal of Solids and Structures* 24:231-250.

Oyler DC, Mark C, Molinda GM, 2010. In situ estimation of roof rock strength using sonic logging. *International Journal of Coal Geology* 83:484-490.

Papamichos E, van Den Hoek P, 1995. Size dependency of Castlegate and Berea sandstone hollow-cylinder strength on the basis of bifurcation theory, In: *Proc. 35th US Symp. Rock Mechanics*. Balkema Rotterdam, Netherlands, pp 301-306.

Papanastasiou P, Thiercelin M, 2010. Modeling borehole and perforation collapse with the capability of predicting the scale effect. *International Journal of Geomechanics* 11:286-293.

Pestman B, Van Munster J, 1996. An acoustic emission study of damage development and stress-memory effects in sandstone, In: *International journal of rock mechanics and mining sciences & geomechanics abstracts*, vol 6. Elsevier, pp 585-593.

Peter-Borie M, Blaisonneau A, Gentier S, Guillon T, Rachez X, 2015. Study of thermo-mechanical damage around deep geothermal wells: from the micro-processes to macroscopic effects in the near well.

Phung SL, Bouzerdoum A, 2007. A pyramidal neural network for visual pattern recognition. *IEEE transactions on neural networks* 18:329-343.

Plumb RA, Hickman SH, 1985. Stress‐induced borehole elongation: A comparison between the four‐arm dipmeter and the borehole televiewer in the Auburn geothermal well. *Journal of Geophysical Research: Solid Earth* 90:5513-5521.

Potyondy DO, 2007. Simulating stress corrosion with a bonded-particle model for rock. *International Journal of Rock Mechanics and Mining Sciences* 44:677-691.

Potyondy DO, Cundall P, 2004. A bonded-particle model for rock. *International journal of rock mechanics and mining sciences* 41:1329-1364.

Qi C, Fourie A, Chen Q, 2018. Neural network and particle swarm optimization for predicting the unconfined compressive strength of cemented paste backfill. *Construction and Building Materials* 159:473-478.

Qian W, Pedersen LB, 1991. Inversion of borehole breakout orientation data. *Journal of Geophysical Research: Solid Earth* 96:20093-20107.

Rahimi R, Nygaard R, 2015. Comparison of rock failure criteria in predicting borehole shear failure. *International Journal of Rock Mechanics and Mining Sciences* 79:29-40.

Rahmati H, 2013. Micromechanical study of borehole breakout mechanism. PhD *thesis*, University of Alberta.

Rahmati H, Nouri A, Chan D, Vaziri H, 2019. Relationship between rock macro-and micro-properties and wellbore breakout type. *Underground Space*

Ranjith PG, Zhao J, Ju M, De Silva RV, Rathnaweera TD, Bandara AK, 2017. Opportunities and challenges in deep mining: a brief review. *Engineering* 3:546-551.

Rao GRM, 1998. Study of in situ stresses and deformation modulus for underground power house, Srisailam hydroelectric project, Andhra Pradesh *J Eng Geol* 26:41-43.

Rawlings C, Barton N, Bandis S, Addis M, Gutierrez M, 1993. Laboratory and numerical discontinuum modeling of wellbore stability. *Journal of Petroleum Technology* 45:1,086-081,092.

Reinecker J, Stephansson O, Zang A, 2008. Stress analysis from overcoring data. *World Stress Map Project guidelines*.

Rumelhart DE, Hinton GE, Williams RJ, 1986. Learning representations by back-propagating errors. *nature* 323:533-536.

Saati V, Mortazavi A, 2011. Numerical modelling of in situ stress calculation using borehole slotter test. *Tunnelling and underground space technology* 26:172-178.

Sacks J, Schiller S, Welch W, 1989. Designs for computer experiments. Technometrics 31 41–47. *Mathematical Reviews (MathSciNet): MR997669 Digital Object Identifier: doi* 10:10488474.

Sahara DP, Schoenball M, Gerolymatou E, Kohl T, 2017. Analysis of borehole breakout development using continuum damage mechanics. *International Journal of Rock Mechanics and Mining Sciences* 97:134-143.

Salchenberger LM, Cinar EM, Lash NA, 1992. Neural networks: A new tool for predicting thrift failures. *Decision Sciences* 23:899-916.

Sammis C, Ashby M, 1986. The failure of brittle porous solids under compressive stress states. *Acta metallurgica* 34:511-526.

Santarelli F, Brown E, 1989. Failure of three sedimentary rocks in triaxial and hollow cylinder compression tests, In: *International Journal of Rock Mechanics and Mining Sciences & Geomechanics Abstracts*, vol 5. Elsevier, pp 401-413.

Santarelli F, Brown E, Maury V, 1992. Analysis of borehole stresses using pressure-dependent, linear elasticity, In: *International Journal of Rock Mechanics and Mining Sciences & Geomechanics Abstracts*, vol 6. Elsevier, pp 445-449.

Santarelli F, Dahen D, Baroudi H, Sliman K, 1992. Mechanisms of borehole instability in heavily fractured rock media, In: *International journal of rock mechanics and mining sciences & geomechanics abstracts*, vol 5. Elsevier, pp 457-467.

Schafer JN, 1979. A practical method of well evaluation and acreage development for the naturally fractured Austin Chalk formation, In: *SPWLA 20th Annual Logging Symposium*. Society of Petrophysicists and Well-Log Analysts.

Schoenball M, Sahara DP, Kohl T, 2014. Time-dependent brittle creep as a mechanism for time-delayed wellbore failure. *International Journal of Rock Mechanics and Mining Sciences* 70:400-406.

Seto M, Utagawa M, Katsuyama K, Nag DK, Vutukuri V, 1997. In situ stress determination by acoustic emission technique. *International Journal of Rock Mechanics and Mining Sciences* 34:281. e281-281. e216.

Shen B, 2008. Borehole breakouts and in situ stresses. *SHIRMS* 1:407-418.

Shen B, Rinne M, 2011. Estimate In situ Stresses from Borehole Breakout at Blanche 1 Geothermal Well in Australia, Paper presented at the *ITA-AITES World Tunnel Congress*, Helsink, 20-26.5.2011.

Shen B, Stephansson O, 1994. Modification of the G-criterion for crack propagation subjected to compression. *Engineering Fracture Mechanics* 47:177-189.

Shen B, Stephansson O, Rinne M, 2002. Simulation of borehole breakouts using FRACOD2D. *Oil & Gas Science and Technology* 57:579-590.

Singh V, Singh D, Singh T, 2001. Prediction of strength properties of some schistose rocks from petrographic properties using artificial neural networks. *International Journal of Rock Mechanics and Mining Sciences* 38:269-284.

Song I, 1998. Borehole breakouts and core disking in westerly granite: mechanisms of formation and relationship in situ stress, vol Series, University of Wisconsin--Madison, Song I, Chang C, 2018. Stochastic Optimization of In Situ Horizontal Stress Magnitudes Using Probabilistic Model of Rock Failure at Wellbore Breakout Margin. *Rock Mechanics and Rock Engineering* 1-16.

Song I, Haimson BC, 1997. Polyaxial strength criteria and their use in estimating in situ stress magnitudes from borehole breakout dimensions. *International Journal of Rock Mechanics and Mining Sciences* 34:116. e111-116. e116.

Sonmez H, Gokceoglu C, Nefeslioglu H, Kayabasi A, 2006. Estimation of rock modulus: for intact rocks with an artificial neural network and for rock masses with a new empirical equation. *International Journal of Rock Mechanics and Mining Sciences* 43:224-235.

Srinivasulu S, Jain A, 2006. A comparative analysis of training methods for artificial neural network rainfall–runoff models. *Applied Soft Computing* 6:295-306.

Stacey T, De Jongh C, 1977. Stress fracturing around a deep-level bored tunnel. *Journal of the Southern African Institute of Mining and Metallurgy* 78:124-133.

Stassi-D'Alia F, 1967. Flow and fracture of materials according to a new limiting condition of yelding. *Meccanica* 2:178-195.

Stock J, Healy J, Hickman S, Zoback M, 1985. Hydraulic fracturing stress measurements at Yucca Mountain, Nevada, and relationship to the regional stress field. *Journal of Geophysical Research: Solid Earth* 90:8691-8706.

Stone M, 1974. Cross-validatory choice and assessment of statistical predictions. *Journal of the royal statistical society Series B (Methodological)* 111-147.

Suchowerska A, Merifield RS, Carter JP, 2013. Vertical stress changes in multi-seam mining under supercritical longwall panels. *International Journal of Rock Mechanics and Mining Sciences* 61:306-320.

Sugawara K, Kameoka Y, Saito T, Oka Y, Hiramatsu Y, 1978. A study on core discing of rock. *Journal of Japanese Association of Mining* 94:19-25.

Thompson P, Chandler N, 2004. In situ rock stress determinations in deep boreholes at the Underground Research Laboratory. *International Journal of Rock Mechanics and Mining Sciences* 41:1305-1316.

Tincelin E, 1951. Les études de pressions de terrains entreprises dans les mines de fer de Lorraine (France), vol Series, Institut National de L'Industrie Charbonniere,

Tingay M, Reinecker J, Müller B, 2008. Borehole breakout and drilling-induced fracture analysis from image logs. *World Stress Map Project* 1-8.

Tronvoll J, Fjaer E, 1994. Experimental study of sand production from perforation cavities, In: *International journal of rock mechanics and mining sciences & geomechanics abstracts*, vol 5. Elsevier, pp 393-410.

Tu JV, 1996. Advantages and disadvantages of using artificial neural networks versus logistic regression for predicting medical outcomes. *Journal of clinical epidemiology* 49:1225-1231.

Vallejos JA, Salinas JM, Delonca A, Mas Ivars D, 2017. Calibration and verification of two bonded-particle models for simulation of intact rock behavior. *International Journal of Geomechanics* 17:06016030.

Valley B, Evans KF, 2015. Estimation of the stress magnitudes in Basel enhanced geothermal system, In: *Proceedings World Geothermal Congress, Melbourne, Australia*. pp 19-25.

Van den Hoek P, Prediction of different types of cavity failure using bifurcation theory, In: *DC Rocks 2001, The 38th US Symposium on Rock Mechanics (USRMS)*. American Rock Mechanics Association,

Van den Hoek P, Hertogh G, Kooijman A, De Bree P, Kenter C, Papamichos E, A new concept of sand production prediction: theory and laboratory experiments, In: *SPE Annual Technical Conference and Exhibition*. Society of Petroleum Engineers, Van den Hoek P, Smit D-J, Khodaverdian M, Material-dependent size effect of hollow cylinder stability: theory and experiment, In: *1st North American Rock Mechanics Symposium*. American Rock Mechanics Association,

Vernik L, Zoback MD, 1992. Estimation of maximum horizontal principal stress magnitude from stress - induced well bore breakouts in the Cajon Pass scientific research borehole. *Journal of Geophysical Research: Solid Earth* 97:5109-5119.

Villaescusa E, Li J, Seto M, Stress measurements from oriented core in Australia, In: *Proc. 5th Int. Workshop on the Application of Geophysics in Rock Engineering, Toronto, Canada,(2002.)*. p 77

Vogler U, UW V, RD D, 1976. CSIR large flat jack equipment for determining rock mass deformability.

Walton G, Kalenchuk K, Hume C, Diederichs M, Borehole Breakout Analysis to Determine the In-Situ Stress State in Hard Rock, In: *49th US Rock Mechanics/Geomechanics Symposium*. American Rock Mechanics Association,

Wang T, Huang H, Zhang F, Han Y, 2020. DEM-continuum mechanics coupled modeling of slot-shaped breakout in high-porosity sandstone. *Tunnelling and Underground Space Technology* 98:103348.

Wanne T, Young R, 2008. Bonded-particle modeling of thermally fractured granite. *International Journal of Rock mechanics and mining Sciences* 45:789-799.

Webber T, Costa JFCL, Salvadoretti P, 2013. Using borehole geophysical data as soft information in indicator kriging for coal quality estimation. *International journal of coal geology* 112:67-75.

Wiebols G, Cook N, An energy criterion for the strength of rock in polyaxial compression, In: *International Journal of Rock Mechanics and Mining Sciences & Geomechanics Abstracts*, vol 6. Elsevier, pp 529-549

Xiaojie Y, Qiaoyun H, Jiewen P, Xiaowei S, Dinggui H, Chao L, 2011. Progress of heat-hazard treatment in deep mines. *Mining Science and Technology (China)* 21:295-299.

Xie H, 2017. Research framework and anticipated results of deep rock mechanics and mining theory. *Advanced Engineering Sciences* 49:1-16.

Xie H et al., 2015. Quantitative definition and investigation of deep mining. *Journal of China Coal Society* 40:1-10.

Yaghoubi AA, Zeinali M, 2009. Determination of magnitude and orientation of the in-situ stress from borehole breakout and effect of pore pressure on borehole stability—Case study in Cheshmeh Khush oil field of Iran. *Journal of Petroleum Science and Engineering* 67:116-126.

Yamshchikov V, Shkuratnik V, Lykov K, Farafonov V, 1991. Evaluation of the stressed-state of a bed based on emission memory effects of rocks in near-well space. *Journal of Mining Science* 27:100-103.

Yang L, Alec MM, Dariusz W, Rod S, Thushan E, 2017. Effect of high temperatures on sandstone–a computed tomography scan study. *International Journal of Physical Modelling in Geotechnics* 17:75-90.

Yang W, Lin B-q, Qu Y-a, Li Z-w, Zhai C, Jia L-l, Zhao W-q, 2011. Stress evolution with time and space during mining of a coal seam. *International Journal of Rock Mechanics and Mining Sciences* 48:1145-1152.

Yao T, Mukerji T, Journel A, Mavko G, 1999. Scale matching with factorial kriging for improved porosity estimation from seismic data. *Mathematical Geology* 31:23-46.

Yavuz H, Demirdag S, Caran S, 2010. Thermal effect on the physical properties of carbonate rocks. *International Journal of Rock Mechanics and Mining Sciences* 47:94-103.

Yilmaz I, Yuksek A, 2008. An example of artificial neural network (ANN) application for indirect estimation of rock parameters. *Rock Mechanics and Rock Engineering* 41:781.

Yokoyama T, Ogawa K, 2016. New Hydraulic Fracturing System for In-Situ Stress Measurement by Using High Stiffness Mechanism, In: *ISRM International Symposium on In-Situ Rock Stress*. International Society for Rock Mechanics.

Yoon J, 2007. Application of experimental design and optimization to PFC model calibration in uniaxial compression simulation. *International Journal of Rock Mechanics and Mining Sciences* 44:871-889.

Zain AM, Haron H, Sharif S, 2010. Prediction of surface roughness in the end milling machining using Artificial Neural Network. *Expert Systems with Applications* 37:1755-1768.

Zaitsev YV, 1985. Inelastic properties of solids with random cracks, In: Mechanics of geomaterials, Wiley Chicester, pp 89-128

Zemanek J, Caldwell R, Glenn Jr E, Holcomb S, Norton L, Straus A, 1969. The Borehole TeleviewerA New Logging Concept for Fracture Location and Other Types of Borehole Inspection. *Journal of Petroleum Technology* 21:762-774.

Zemanek J, Strozeski B, Wang Z, 1990 The Operational Characteristics of a 250 KHz Focused Borehole Imaging Device, In: *SPWLA 31st Annual Logging Symposium*. Society of Petrophysicists and Well-Log Analysts.

Zhang L, Cao P, Radha K, 2010. Evaluation of rock strength criteria for wellbore stability analysis. *International journal of rock mechanics and mining sciences* 47:1304-1316.

Zhang W, Sun Q, Hao S, Geng J, Lv C, 2016. Experimental study on the variation of physical and mechanical properties of rock after high temperature treatment. *Applied Thermal Engineering* 98:1297-1304.

Zhao X, Xu H, Zhao Z, Guo Z, Cai M, Wang J, 2019. Thermal conductivity of thermally damaged Beishan granite under uniaxial compression. *International Journal of Rock Mechanics and Mining Sciences* 115:121-136.

Zhao Z, 2016. Thermal influence on mechanical properties of granite: a microcracking perspective. *Rock Mechanics and Rock Engineering* 49:747-762.

Zheng Z, Kemeny J, Cook NG, 1989. Analysis of borehole breakouts. *Journal of Geophysical Research: Solid Earth* 94:7171-7182.

Zhou J, Zhang L, Pan Z, Han Z, 2016. Numerical investigation of fluid-driven near-borehole fracture propagation in laminated reservoir rock using PFC2D. *Journal of Natural Gas Science and Engineering* 36:719-733.

Zhou S, 1994. A program to model the initial shape and extent of borehole breakout. *Computers & Geosciences* 20:1143-1160.

Zoback M et al., 2003. Determination of stress orientation and magnitude in deep wells. *International Journal of Rock Mechanics and Mining Sciences* 40:1049-1076.

Zoback M, Mastin L, Barton C, 1986. In-situ stress measurements in deep boreholes using hydraulic fracturing, wellbore breakouts, and stonely wave polarization, In: *ISRM International Symposium*. International Society for Rock Mechanics.

Zoback MD, 2010. Reservoir geomechanics, vol Series, Cambridge University Press,

Zoback MD, Healy JH, 1992. In situ stress measurements to 3.5 km depth in the Cajon Pass scientific research borehole: Implications for the mechanics of crustal faulting. *Journal of Geophysical Research: Solid Earth* 97:5039-5057.

Zoback MD, Moos D, Mastin L, Anderson RN, 1985. Well bore breakouts and in situ stress. *Journal of Geophysical Research: Solid Earth* 90:5523-5530.

Zurada JM, 1992. Introduction to artificial neural systems, vol 8. vol Series, 8, West St. Paul.

APPENDIX

Table A1 Breakout geometries and associated horizontal stress magnitudes applied in experiments

	Maximum Horizontal Stress (MPa)	Minimum Horizontal Stress (MPa)	Normalised depth (L/r)	Angular Span – width (degrees)
Haimson and Herrick (1986)	40.996	4.4	1.22	42
	44.874	4.4	1.35	50
	47.09	8.8	1.36	52
	49.86	8.8	1.42	67
	60.386	13.2	1.47	63
	61.494	13.2	1.52	73
	73.128	24.376	1.47	72
	31.5	1.75	1.08	27
	30.625	4.375	1.26	43
	35	4.375	1.36	51
	40.8	8.5	1.47	59
	44.2	8.5	1.55	61
	54.5	13.25	1.73	73
	55	13.25	1.86	80
	67.5	24.25	1.84	108
	68	24.25	1.93	120
Haimson and Herrick (1989)	81.51	20.46	1.74	83
	85.8	23.76	1.72	79
	96.36	27.39	1.82	91
	92.4	34.32	1.9	118
	62	20.4	1.85	108
	68	23.8	1.83	118
	72	23.8	1.97	121
	52.46	6.88	1.47	53

	65.36	13.76	1.58	65
	76.54	20.21	1.7	75
	77.4	27.52	1.65	82
	84.28	27.52	1.7	85
	93.74	34.4	1.85	91.5
	99.76	40.85	1.87	110
	106.64	47.3	1.95	112
	52.44	6.84	1.43	46
	64.6	13.68	1.53	57
	72.2	20.9	1.76	72
	84.36	27.36	1.61	83
	84.74	27.36	1.76	84
	94.62	34.58	1.91	92.5
	95.38	34.58	1.96	97
Haimson	22.8	3	1.1625	36
and	23.4	3	1.3625	50
Song	28	5	1.365	49
(1993)	32	5.5	1.175	56
	34	7	1.29	46
	35	7	1.325	43
	36	7.2	1.3375	59
	38	9	1.525	63
	38	12	1.22	58
	43	12	1.325	67
	47	15	1.4625	65
Herrick	41	14	1.18	45
and	50	14	1.32	55
Haimson	57.5	14	1.56	65.5
(1994)	65.5	14	1.76	81.5
	51.5	21	1.2	53.5
	58.5	21	1.27	56
	65.5	21	1.46	63
	65.5	21	1.56	65.5

	72.2	21	1.64	70
	75.8	21	1.98	80
	58.5	28	1.22	52
	65.5	28	1.24	55.5
	72.2	28	1.6	68
	79	28	1.7	70
	83	28	2	86
	62	35	1.13	45
	69	35	1.27	57
	79	35	1.6	64
	84.5	35	1.94	86
	90	35	2.08	88
Haimson	40	15	1.11	35
and Lee	50	15	1.22	51.5
(2004)	60	15	1.43	65
	70	15	1.558	73
	60	20	1.3	63
	70	20	1.618	67.5
	80	20	1.875	73
	60	25	1.175	64
	70	25	1.74	71
	75	25	1.68	75
	85	25	1.835	82
	54.9	30	1.15	53
	60	30	1.16	64
	65.1	30	1.3	79.5
	69.6	30	1.5	100
	75	30	1.725	111
	60	40	1.15	95
	64	40	1.19	116
	69.2	40	1.6	138
Lee and	35.4	15	1.2	45
Haimson	50.25	15	1.77	59

(2006)	65.25	15	1.82	63.5
	40	20	1.15	48
	50	20	1.52	68
	60	20	1.625	73.5
	70	20	1.92	78.5
	45	25	1.19	61.5
	50	25	1.41	66
	55	25	2.23	70
	60.5	25	2.07	72
	65	25	2.33	77
	40.5	30	1.12	56
	51	30	1.46	70.3
	60	30	2.02	77.5
	60	40	1.28	68
	72	40	2.13	73.6
	80	40	2.36	82
	93.2	40	2.53	85